

Electronic Thesis and Dissertation Repository

6-13-2017 12:00 AM

Process-Structure-Property relationships for High Pressure Die-cast Magnesium Alloys

Pouya Sharifi, *The University of western Ontario*

Supervisor: Dr Jeffrey Wood, *The University of Western Ontario*

A thesis submitted in partial fulfillment of the requirements for the Doctor of Philosophy degree in Mechanical and Materials Engineering

© Pouya Sharifi 2017

Follow this and additional works at: <https://ir.lib.uwo.ca/etd>



Part of the [Mechanics of Materials Commons](#)

Recommended Citation

Sharifi, Pouya, "Process-Structure-Property relationships for High Pressure Die-cast Magnesium Alloys" (2017). *Electronic Thesis and Dissertation Repository*. 4656.

<https://ir.lib.uwo.ca/etd/4656>

This Dissertation/Thesis is brought to you for free and open access by Scholarship@Western. It has been accepted for inclusion in Electronic Thesis and Dissertation Repository by an authorized administrator of Scholarship@Western. For more information, please contact wlsadmin@uwo.ca.

Abstract

The primary goal of this study was to conduct experiments and simulation modeling to determine the relevant filling and solidification process parameters that influence microstructural features of the high-pressure die-cast magnesium alloy AM60. This work continues from the previous research that has been carried out by Dr. Jeff Wood's research group over the last sixteen years.

Spherical microindentation was used to analyze the influence of microstructural features on the flow stress for both skin (finer grain sizes) and core (larger grain sizes) of high pressure die castings (HPDC), as well as different regions of gravity cast stepped-plate. It was observed that the local yield stress and flow stress of magnesium alloys depend on grain size.

Multiple runs of the commercial casting simulation package, ProCAST™, were used to model the mold filling and solidification events employing a range of interfacial heat transfer coefficient (IHTC) values. The simulation results were used to estimate the centreline cooling curve at various locations through the casting. In this contribution, a new method was developed which employs the knowledge of local cooling rates to predict the grain size and the skin thickness of HPDC magnesium. The local cooling rate was used to calculate the resulting grain size and skin thickness via the established relationships.

A new casting instrument to simulate the important aspects of the HPDC process was designed. The heat flux and IHTC profiles at the metal-die interface in that casting process have been successfully predicted by solving the inverse thermal problem.

Keywords

High pressure die casting (HPDC), process-structure-property relationships, solidification modeling, casting simulation, casting defects, interfacial heat transfer coefficient.

Dedication

I would like to dedicate this thesis to my beloved parents who have loved me unconditionally and stood by me through thick and thin in my life. Without their support and encouragement this wouldn't have been possible. I would specially dedicate this work to my loving wife who gave me the strength to fulfill my career goals. I also dedicate this work to my brother and his family for the love that they have showered upon me in my life and for being there for me whenever needed.

Acknowledgments

I would like to express my deepest sense of gratitude to my research supervisor Dr. Jeff Wood for his kind support, guidance, patience, and friendship during my work at University of Western Ontario. His constant support and encouragement, both in my personal and professional life has been unparalleled and is the reason behind the successful completion of this research.

I would also like to give thanks to Dr. Kumar Sadayappan for his great involvement, exceptional contributions, support and advice during my research at CanmetMaterial. I cannot imagine working in a better environment than the one created by Dr. Kumar Sadayappan.

I would like to thank the staff at CanmetMaterial for the help and materials that assisted me to fulfill the research and in particular, Mr. Gabriel Birsan, and Mr. Frank Benkel, for their valuable contributions in all the casting procedures and experimental setup.

I would like to thank Meridian Technologies Inc., for their contributions in materials and time, especially Mr. John Jekl, Dr. Jon Weiler and Dr. Mehdi Farrokhnejad for knowledge of the process of die-casting of magnesium and run the MAGMASoft simulations that made this research work possible.

This work is jointly supported by NSERC - Automotive Partnership Canada program and NRCan's Office of Energy R&D through the Program on Energy R&D. Technical support from the Magnesium Front End R&D (MFERD) research team at USAMP is appreciated. I would like to gratefully acknowledge the significant contributions of Dr. Robert Klassen in the field of indentation testing. I am grateful to Dr. Anthony Straatman for his valuable contributions in the heat transfer approaches.

I am also thankful to my colleagues Dr. Jamal Jamaloudin, Dr. Ying Fan, Mr. Hooman Baghaei and Mr. Aria Khalili for sharing their rich research experiences at the times of difficulties..

Table of Contents

Abstract	i
Dedication	ii
Acknowledgments.....	iii
Table of Contents.....	iv
List of Tables	viii
List of Figures.....	ix
Symbols	xiv
Chapter 1.....	1
1 INTRODUCTION	1
Chapter 2.....	4
2 LITERATURE REVIEW	4
2.1 Materials Selection.....	5
2.1.1 Physical & Mechanical Properties of Magnesium Alloys	5
2.1.2 Magnesium Alloys	5
2.1.3 Magnesium-Aluminum Phase Diagram.....	6
2.2 Solidification of Alloys.....	9
2.2.1 Equilibrium Solidification.....	11
2.2.2 Non-Equilibrium Solidification	12
2.2.3 Phase Change Problem in Solidification.....	13
2.3 High Pressure Die Cast Process	15
2.3.1 Simulation of Filling and Solidification during HPDC Process	19
2.3.2 Heat Transfer Coefficient in HPDC Process.....	20
2.4 Microstructure of High Pressure Die Casting	24
2.4.1 Different Kind of Defects in the Microstructure of HPDC.....	25
2.4.1.1 Shrinkage and Gas Porosity	25
2.4.1.2 Externally Solidify Crystals (ESGs)	27
2.4.1.3 Defect Band	27
2.4.2 Effect of Process Parameters on the Defect in the HPDC Process	30
2.5 Structure-Property Relationships	31
2.5.1 Effects of Grain Size	31
2.5.1.1 Microindentation Testing.....	37
2.5.1.2 Spherical Indentation	37

2.5.1.3 Analysis of Indentation Load–Depth Curve	39
2.5.1.4 Average Indentation Stress and Strain	42
2.5.2 Effect of Defects on the Mechanical Properties of Die Cast Ductile Metal.....	44
Chapter 3.....	51
3 PREDICTING THE FLOW STRESS OF AS CAST MAGNESIUM ALLOYS	51
3.1 Experimental Procedure	51
3.1.1 Alloys and Casting	51
3.1.2 Microindentation Testing.....	54
3.1.3 Metallography	57
3.2 Experimental Results	58
3.2.1 Microstructural Result.....	58
3.2.2 Indentation Results.....	61
3.3 Discussion	67
3.3.1 Microstructure-dependent local mechanical properties	67
3.3.2 Prediction of local mechanical properties using Hall-Petch relationship	70
Chapter 4.....	76
4 PREDICTION OF THE EFFECTS OF COOLING RATES ON THE MICROSTRUCTURE AND STRENGTH OF HPDC AM60.....	76
4.1 Experimental Procedure	77
4.1.1 Alloys and Casting	77
4.1.2 Computation of Cooling Rate	79
4.1.3 Grain Size Measurement by Image Analysis Software.....	80
4.1.4 Uniaxial Tensile Testing	82
4.2 Modeling of Solidification of Magnesium Alloys in the HPDC.....	83
4.2.1 Simulation of High Pressure Die Cast Process	83
4.2.1.1 Initial Conditions	84
4.2.1.2 Boundary Conditions	86
4.2.2 Predicting of Temperature-Time Distribution	88
4.3 Results.....	92
4.3.1 Cooling Rate- Grain Size Correlation	92
4.3.2 Microstructure of HPDC.....	94
4.3.3 Simulation and Modeling Results	96
4.4 Discussion	105
4.4.1 Effect of Process Parameters on the Grain Size Distribution.....	105
4.4.2 Prediction of Grain Size	107
4.4.3 Prediction of Interfacial Heat Transfer Coefficient	112
4.4.4 Determination of Skin Thickness.....	117

4.4.5 Prediction of Yield Strength for Different Locations	120
4.4.6 Prediction of Elongation	122
Chapter 5.....	127
5 QUANTITATIVE EXPERIMENTAL STUDY OF DEFECTS INDUCED BY PROCESS PARAMETERS IN THE HIGH-PRESSURE DIE CAST PROCESS	127
5.1 Experimental Procedure	128
5.1.1 Shock Tower	128
5.1.2 Production of Top Hat.....	130
5.1.3 Defect Analysis.....	131
5.1.3.1 Optical Microscopic Analysis	131
5.1.3.2 X-ray Tomography Analysis.....	135
5.2 Simulation and Modeling.....	136
5.3 Effect of Process Parameters on the Formation of Defects.....	136
5.3.1 Slow Stage of Piston Velocity Effects	143
5.3.2 Fast Stage of Piston Velocity Effects.....	144
5.3.3 Intensification Pressure Effects.....	145
5.3.4 Die Temperature Effects	146
5.4 Prediction of Defect Band Location in the Complex Geometry	147
5.5 Investigation of Knit Line Impacts on the Formation of Porosity	154
Chapter 6.....	172
6 PREDICTION OF HEAT TRANSFER COEFFICIENT AT METAL/DIE INTERFACE .	172
6.1 Experimental Procedure	173
6.2 Mathematical Modeling of Interfacial Heat Transfer Coefficient	177
6.2.1 Heat Transfer Inside the Die	177
6.2.2 Heat Transfer Inside the Casting.....	180
6.3 Results and Discussion	180
6.3.1 Heat Flux and IHTC Evaluation	180
6.3.1.1 Effect of Pressure on the IHTC Value	183
6.3.2 Microstructural Analysis.....	189
Chapter 7.....	194
7 SUMMARY AND FUTURE WORK.....	194
7.1 Cooling Rate - Grain Size-Local Yield Strength Relationships.....	194
7.2 Prediction of Interfacial Heat Transfer Coefficient between Metal and Die	195
7.3 Quantitative Experimental Study of Defects Induced by Process Parameters in the High Pressure Die Cast Process	196
7.4 Investigation of External Pressure Effects on the IHTC Variation.....	197
7.5 Future Work.....	197

References.....	199
Curriculum Vitae	207

List of Tables

Table 2.1: Physical properties of pure magnesium [11].	5
Table 2.2: The effect of alloying element on the resultant alloy [1, 11].	6
Table 2.3: Aluminum content effects on the mechanical properties of magnesium alloys [2, 11].	9
Table 2.4: The origin and morphology of different defects in HPDC [4, 27, 44-47].	26
Table 2.5: Reported effects of the process parameters on different kinds of defects.	31
Table 3.1: Chemical composition (wt.%) of AZ91, AE44 and AM60 magnesium alloys.	52
Table 3.2: The location of different selected samples for magnesium alloys.	54
Table 3.3: Etchants were applied for three different kinds of magnesium alloys.	58
Table 3.4: The Hall-Petch slope values are determined from microindentation testing and uniaxial tensile testing.	71
Table 4.1: The reference process parameters were used in this study.	77
Table 4.2: The different samples were selected from the instrument panel. These results has been published in the Reference [45].	80
Table 4.3: The values of thermo-physical variables were used.	84
Table 4.4: The characteristic of six location for shock tower which have been performed under the reference process parameter	96
Figure 4.32: Comparison of the measured grain size and predicted values using the modified model for different IHTC value from surface to center for Location 6.	
Table 4.5: IHTC value for casting process in the literature that the pressure is applied.	116
Table 5.1: The different Sets of process parameters.	129
Table 5.2: Quantitative data on the porosity presents in each location using X-ray tomography and optical microscope.	161
Table 5.3: Quantitative data on the porosity presents in each location using X-ray tomography and optical microscope.	165
Table 5.4: Quantitative data on the porosity presents in each location using X-ray tomography and optical microscope.	170

List of Figures

Figure 2.1: Process-structure-property relationship.....	4
Figure 2.2: Magnesium-Aluminum phase diagram [11].....	7
Figure 2.3: Schematic of eutectic microstructure of Mg-Al alloy.	8
Figure 2.4: a) Heterogeneous nucleation of spherical cap on a flat mold wall. b) The excess free energy of solid clusters for homogeneous and heterogeneous nucleation. It should be noted that r^* is independent of the nucleation site. c) Difference of ΔG^* with undercooling (ΔT) for homogeneous and heterogeneous nucleation d) The corresponding nucleation rates assuming the same critical value of ΔG^* [15].	10
Figure 2.5: Equilibrium solidification and distribution of solute content [15].	12
Figure 2.6: Non-equilibrium solidification once there is no diffusion in solid state and complete diffusion in liquid state [15].	13
Figure 2.7: The general form of the one-dimensional solution to the Stefan problem [23].	14
Figure 2.8: Schematics of hot chamber die casting [25].	16
Figure 2.9: Schematics of cold chamber die casting [25].	17
Figure 2.10: Three different stages of the HPDC. The pressure reaches the static point and intensification pressure is applied to maintain the pressure relatively constant in last stage [4]. ...	18
Figure 2.11: (a) The presence of micro gap on the mold wall at the initial stage of casting (b) as solidification progresses, the gap start to expand [4].	21
Figure 2.12: The IHTC (h) and heat flux (q) variation as a function of time [40]. Capital letters are from original reference and not used here.	22
Figure 2.13: Comparison of direct and inverse heat conduction problems [42].	23
Figure 2.14: Typical grain structure in the cross section of casting for samples of die cast.	25
Figure 2.15: Typical defect band in the micrograph of AlSi7Mg, AM60, and AZ91. (a) through (c) are as-polished images and (d) through (f) are etched images revealing the ESGs (large white grains) and macrosegregation. Defect bands are indicated with arrows [26].	28
Figure 2.16: The material as a function of fraction solid, for the two extremes in crystal morphology; large dendritic crystals and small globular crystals [29].	29
Figure 2.17: Hall-Petch relationship for sand-cast magnesium alloy [56].	33
Figure 2.18: Average indentation yield strength as a function of grain size in comparison with published results on similar magnesium alloys [56].	34
Figure 2.19: Variation of microhardness from skin to core for die-cast AZ91D [59].	36
Figure 2.20: Determination of skin thickness using four methods: the hardness profile, the areal percentage of eutectic composition, the average grain size, and the onset of large dendritic structures across the casting thickness [9].	36
Figure 2.21: The compression mechanism of indentation proposed by Mulhearn. The circular continuous line represents the elastic-plastic boundary. The dashed lines indicate several hypothetical plastic shells, and the arrows represent the direction of straining of the shells [65].	39
Figure 2.22: Schematic diagram of the indentation of a material by spherical indenter.	40
Figure 2.23: Schematic representation of plastic zone expansion during spherical indentation and indentation load-depth curves for a) elastic, b) plastic - elastic, c) fully plastic regimes [71].	41
Figure 2.24: Calculating the contact radius without the consideration of the effect of pileup, a^* , at the given load, L.	43
Figure 2.25: The influence of area fraction of porosity on the UTS (a) and elongation (b) for each nominal range of grain size [76].	45
Figure 2.26: Material containing spherical void [45].	47

Figure 3.1: The different regions on step-cast plate.....	53
Figure 3.2: High pressure die casting plate.....	53
Figure 3.3: The Micro materials NanoTest™ microindentation hardness testing apparatus in which the spherical indentation was performed.....	55
Figure 3.4: The NanoTest™ pendulum assembly showing the operation of the indenter.....	56
Figure 3.5: The spherical indenter.....	56
Figure 3.6: Typical microstructures of AE44 alloy for different locations of the step-cast plate..	59
Figure 3.7: Typical microstructures of HPDC a) skin b) core for AE44. In the skin region, the area fraction of β phase is approximately 3.5% and core region contains less than 2%.....	60
Figure 3.8: Three indentations on the surface of location.....	61
Figure 3.9: The typical indentation load-depth curves for HPDC skin region, core region and step-cast sample A for AE44.....	62
Figure 3.10: The constraint factor Ψ , as function of ϕ in the plastic regime in elastic-plastic regime [70].....	63
Figure 3.11: The plasticity parameter, Φ , with respect to average plastic strain for AE44. All tests preform in this study were in elastic-plastic zone.....	64
Figure 3.12: The average indentation stress, σ_{avg} , with respect to average plastic strain, ϵ_{avg} , for the samples indented in the HPDC skin region, core region and sample G from gravity step-cast. Constitutive linear extrapolations are shown to obtain the indentation yield strength.....	65
Figure 3.13: The yield strength, σ_y , with respect to average grain size, $d^{-1/2}$, for the samples indented in the skin region, core region and step-cast sample G from step-cast for AM60. The indentation result of the skin and core regions for HPDC AM60 have been presented in Reference [85].....	66
Figure 3.14: The yield strength, σ_y , with respect to average grain size, $d^{-1/2}$, for the samples indented in the skin region, core region and step-cast sample G from step-cast for AZ91.....	66
Figure 3.15: The yield strength, σ_y , with respect to average grain size, $d^{-1/2}$, for the samples indented in the skin region, core region and step-cast sample G from step-cast for AE44.....	67
Figure 3.16: The intermetallic phase in the HPDC; a) skin region and b) core region.....	69
Figure 3.17: The average indentation stress, σ_{avg} , with respect to average grain size, $d^{-1/2}$ for different levels of plastic strain for AM60.....	73
Figure 3.18: The average indentation stress, σ_{avg} , with respect to average grain size, $d^{-1/2}$ for different levels of plastic strain for AZ91.....	74
Figure 3.19: The average indentation stress, σ_{avg} , with respect to average grain size, $d^{-1/2}$ for different levels of plastic strain for AE44.....	74
Figure 3.20: Hall-Petch slope as a function of $\epsilon^{1/2}$, encountered during indentation testing of wear process.....	75
Figure 4.1: The shock tower and the six selected Locations.....	78
Figure 4.2: Top hat casting and five selected locations.....	79
Figure 4.3: The measurement of variation of average grain size in the cross section of casting using image analysis software.....	81
Figure 4.4: The measurement of area fraction on ESGs in the cross section of casting using image analysis software Clemex.....	82
Figure 4.5: Locations of 12 tensile specimens were cut from a die-cast Top hat from gate to overflow.....	83
Figure 4.6: how to set up the alloy (a) and thermo-physical properties of alloys (b).....	85
Figure 4.7: The determination of interfacial heat transfer coefficient in the ProCAST™.....	87
Figure 4.8: The determination of piston velocity as a function of time.....	87
Figure 4.9: Schematic view for the solidification through the thickness of casting based on the modified heat transfer approach.....	89
Figure 4.10: Grain size as a function of cooling rate.....	93

Figure 4.11: The prediction of grain size along the thickness of the casting for Sample 1. This also shows variation grain structure through the casting cross section.....	94
Figure 4.12: The typical microstrture of six locations.	95
Figure 4.13: Sequence and solidification of shock tower was simulated by ProCAST™.	97
Figure 4.14: Filling sequence and solidification of top hat was simulated by ProCAST™.	98
Figure 4.15: Dependency of the filling time on the variation of fast velocity of piston at a fixed value of IHTC.	99
Figure 4.16: Predicted die surface temperatures in selected locations at IHTC =15000 Wm ⁻² K ⁻¹ , die temperture =200 ⁰ C and fast stage velocity=4m/s. This curve was directly obtained from simulation result.....	100
Figure 4.17: Temperature distribution along the die wall to center with time for Location 1 of shock tower.	101
Figure 4.18: Relationship between cooling rate and IHTC at diffrent locations for a) skin b) core.	102
Figure 4.19: Dependency of average grain size on the variation of die temperture at a) skin regin b) core region.	103
Figure 4.20: Dependency of average grian size on the variation of filling time at a) skin regin b) core region.	104
Figure 4.21: Comparison of the experimental results and predicted values using the modified model in term of grain size from surface to center for Location 1.	108
Figure 4.22: Comparison of the experimental results and predicted values using the modified model in term of grain size from surface to center for Location 2.	109
Figure 4.23: Comparison of the experimental results and predicted values using the modified model in term of grain size from surface to center for Location 3.	109
Figure 4.24: Comparison of the experimental results and predicted values using the modified model in term of grain size from surface to center for Location 4.	110
Figure 4.25: Comparison of the experimental results and predicted values using the modified model in term of grain size from surface to center for Location 5.	110
Figure 4.26: Comparison of the experimental results and predicted values using the modified model in term of grain size from surface to center for Location 6.	111
Figure 4.27: Comparison of the measured grain size and predicted values using the modified model for different IHTC value from surface to center for Location 1.	113
Figure 4.28: Comparison of the measured grain size and predicted values using the modified model for different IHTC value from surface to center for Location 2.	114
Figure 4.29: Comparison of the measured grain size and predicted values using the modified model for different IHTC value from surface to center for Location 3.	114
Figure 4.30: Comparison of the measured grain size and predicted values using the modified model for different IHTC value from surface to center for Location 4.	115
Figure 4.31: Comparison of the measured grain size and predicted values using the modified model for different IHTC value from surface to center for Location 5.	115
Figure 4.32: Comparison of the measured grain size and predicted values using the modified model for different IHTC value from surface to center for Location 6.	116
Table 4.5: IHTC value for casting process in the literature that the pressure is applied.	116
Figure 4.33: Cooling rate variation from mold wall to casting centerline. As shown in Figure 4.17, the cooling rate for each point a cross thickness of die casting sample can be determined.	118
Figure 4.34: Accuracy of predicted skin thickness with different IHTC value.	119
Figure 4.35: Skin thickness as a function of cooling rate. The cooling rate should be higher than 375 °C/s that skin can be formed.	120
Figure 4.36: Accuracy of predicted yield strengths of specimens cut from a Top-Hat die casting.	121

Figure 4.37: a) The presence of porosity and shrinkage into the surface which is close to the fracture surface. b) SEM image of a fracture surface of the HPDC AM60 alloy.	124
Figure 4.38: Predicted tensile elongations as a function of area fraction of porosity using the modified analytical model compared with experimental tensile elongations.	125
Figure 5.1: The shock tower casting with gates and overflow. Selected locations for the characterization are marked from L1 to L6.	129
Figure 5.2: The shot profile of one casting from HPDC.....	130
Figure 5.3: Three different gate configurations to study knit line formation and impact.	131
Figure 5.4: Flowchart algorithm for the separation procedures of gas and shrinkage pore.	133
Figure 5.5: Separation of gas porosity from shrinkage a) Gray scale of typical micro structure magnesium alloy AM60 including gas porosity b) Binary image of the gray scale image. c) Small gas pores and shrinkage porosity. d) Shrinkage porosity.....	134
Figure 5.6: Separation of defect band from gas and shrinkage porosity a) gray scale of 12 montaged picture of microstructure from Location 6 b) defect band c) shrinkage and gas porosity.	135
Figure 5.7: The montage of micrograph covering the thickness of sample cut from locations 1 to 6.	137
Figure 5.8: Filling sequence and solidification conditions predicted in Pro-cast. Arrows show the location of knit lines.....	138
Figure 5.9: The effect of different Sets of process parameters on the amount of various porosities at Location 1. The error bars represent one standard deviation resulting from three shock towers at Location 1.	139
Figure 5.10: The effect of different Sets of process parameters on the amount of various porosities at Location 2. The error bars represent one standard deviation resulting from three shock towers at Location 2.	139
Figure 5.11: The effect of different Sets of process parameters on the amount of various porosities at Location 3. The error bars represent one standard deviation resulting from three shock towers at Location 3.	140
Figure 5.12: The effect of different Sets of process parameters on the amount of various porosities at Location 4. The error bars represent one standard deviation resulting from three shock towers at Location 4.	140
Figure 5.13: The effect of different Sets of process parameters on the amount of various porosities at Location 5. The error bars represent one standard deviation resulting from three shock towers at Location 5.	141
Figure 5.14: The effect of different Sets of process parameters on the amount of various porosities at Location 6. The error bars represent one standard deviation resulting from three shock towers at Location 6.	141
Figure 5.15: The process parameters effect on amount of ESGs for different locations. The error bars represent one standard deviation resulting from three shock towers at same locations.	142
Figure 5.16: The defect band as in aluminum silicon alloys.....	149
Figure 5.17: The schematic of shot profile during filling cavity.	150
Figure 5.18: The filling and solidification through the cross section of casting during HPDC process.	151
Figure 5.19: Solid fraction rate is for a) die temperature =160 ⁰ C b) die temperature =240 ⁰ C. These curves were taken from simulation results.	153
Figure 5.20: Simulation of Mold filling top hat for Mode 1. Arrows shows locations of knit line begins.	155
Figure 5.21: Top hat casting with six selected locations representing the two flow directions incorporating knit lines.	156
Figure 5.22: Visual representation of the presence of pores using the results of X-ray tomography for Location 3.....	157

Figure 5.23: Visual representation of the presence of pores using the results of X-ray tomography for Location 6.....	157
Figure 5.24: An image using optical microscopy showing a cross-sectional sample 1 to sample 3 from left to right. Note that this Figure shows the micrograph in the plane X_Y, while the flow direction is in Z axis as shown in Figure 5.20.	158
Figure 5.25: The area fraction of porosity along the X- axis of sample 1 to 3. Arrows indicates the predicted knit line locations.	159
Figure 5.26: The area fraction of porosity along the X- axis of sample 3 to 6. Arrows indicates the predicted knit line locations.	160
Figure 5.27: Simulation of mold filling top hat for Mode 2. Arrows show where knit line begins.	163
Figure 5.28: Top hat casting with three selected locations from flow direction including knit line between left runner and middle runner.	164
Figure 5.29: The area fraction of porosity along the X- axis of sample 1 to 3. Arrows indicates the predicted knit line locations.	166
Figure 5.30: Simulation of mold filling top hat for Mode 3. Arrows show locations of knit line begins.	168
Figure 5.31: Top hat casting with three selected locations from flow direction including knit line between left runner and middle runner.	169
Figure 5.32: The area fraction of porosity along the X- axis of samples 1 to 3. Arrows indicate the prediction of knit line locations	170
Figure 5.33: Tomography image showing the internal pores in cross section of casting, indicating a gas pore and the shrinkage pores.....	171
Figure 6.1: Schematic diagram of MiniCaster machine.....	173
Figure 6.2: Configuration of the dies and adjustment of the thermocouples.	175
Figure 6.3: The position of thermocouples.	175
Figure 6.4: a) MiniCaster machine and b) the data acquisition system.	176
Figure 6.5: Wedge casting under applied pressure 175 bar.	176
Figure 6.6: Measured temperatures in the casting and die and predicted surface casting die temperatures.....	181
Figure 6.7: The predicted Heat flux and IHTC curves during solidification of magnesium alloys AM60 with applied pressure 150bar.....	182
Figure 6.8: The predicted heat flux with applied pressure 100, 125, 150 and 175bar. Arrows indicate different stages of heat flux curves.....	184
Figure 6.9: The predicted IHTC during solidification of magnesium alloys AM60 with applied pressure 100, 125, 150 and 175bar.	185
Figure 6.10: The dependency of cooling rate on the variation of pressure. Note that the cooling rate was measured by thermocouple which was located in the center.	186
Figure 6.11: The maximum IHTC values as a function of the applied pressure.....	187
Figure 6.12: Comparison of the experimental results and predicted values determined from Eq.16.	188
Figure 6.13: The typical microstructure of wedge cast from tip to bottom. a) tip b) middle c) bottom	190
Figure 6.14: Typical grain structure through the casting cross section. a) 175 bar, b) 125 bar. ...	192
Figure 6.15: Variation of grain size with respect to distance for different level of pressure.	192

List of Symbols

ΔG	Free energy
R	Radius
ΔT	Undercooling
C_0	Composition of alloy
$G.D$	Grain size
R	Cooling rate
f_s	Solid fraction
f_l	Liquid fraction
c	Specific heat
k	Thermal conductivity
L_f	latent heat of fusion
Ste	Ste Stefan number
$V1$	Slow stage of piston velocity
$V2$	Fast stage of piston velocity
IP	Intensification pressure
$IHTC$	Interfacial heat transfer coefficient
q	Heat flux
A	Area
σ_y	yield strength
ϵ_{avg}	Average indentation strain,
h_c	Plastic contact depth
h_d	Elastic deflection depth
P_M	Mean contact pressure
Ψ	Constraint factor
ϕ	Plasticity parameter
E^*	Modified young's modulus
ν	Poisson's ratio
K_{tg}	Global stress concentration factor
K_{tn}	Net stress concentration factor
S_{max}	Secant modulus
S_n	Secant modulus at the region far from the void
δ	ligament fraction
α	Thermal diffusivity
ρ	Density

θ	Dimensionless temperature
τ	Dimensionless time
ζ	Dimensionless distance
γ	Thermal diffusivity

Chapter 1

1 INTRODUCTION

World production of magnesium has been growing by around 3% per annum, mainly due to its very high strength to weight ratio, comparable to currently used metals in the industry [1, 2]. Magnesium shows high potential to substitute for conventional materials applications where low weight and high mechanical properties are required. The fastest growing magnesium alloy products are produced particularly for automotive components such as seat and door frames, engine cradles, cylinder head cover and instrument panel beams [3].

Many of the present magnesium components are produced by the high pressure die casting (HPDC) process due to its fast production rate, geometric accuracy and low cost [4]. Wider application of die cast magnesium alloy components is impeded by variations in the mechanical properties of die cast magnesium alloys, particularly in large, complex cast components typical in the automotive industry [5, 6]. The mechanical properties of HPDC depend fundamentally upon microstructural features, such as porosity, skin thickness, and bimodal distribution of grain size through the casting thickness [5, 7-9]. These microstructural features are affected by the filling and solidification process parameters [8, 10]. It is, therefore, important to understand the correlation between the process variables, microstructure and properties of the cast alloy.

The research presented here is part of a larger project conducted with a federal laboratory, CanmetMATERIALS, located in Hamilton, Ontario, Canada, with aim of fully understanding and ultimately predicting the process-structure-properties relationships for die cast magnesium alloy AM60 components. The first phase of the project dealt with understanding the influence of microstructural features on the resultant mechanical properties. Consequently, this project aims at obtaining a correlation between process parameters (filling and solidification) and the microstructure of die cast magnesium alloys. The specific sub-tasks of this project are:

- To precisely quantify cooling rate variation in the cross section of casting thickness and determine the relationship between cooling rate and local grain size.
- Prediction of local yield strength as a function of the variation of grain size based on the Hall-Petch equation.
- To quantitatively characterize the effect of process parameters on the formation of defects.
- Prediction of interfacial heat transfer coefficient during solidification of magnesium alloys.

The research presented here is separated into seven chapters. Chapter 2 introduces magnesium, magnesium alloys and their physical and mechanical properties. Further in this chapter, the process of high pressure die casting (HPDC) is discussed in detail along with the filling and solidification parameters. It further discusses the established theories and studies regarding the influence of microstructural features on the mechanical properties.

Chapter 3 describes the local mechanical properties determined using micro-indentation testing. The yield strength and flow stress values of die cast and gravity step-cast magnesium alloys are presented and discussed. Also, correlations established between grain size and local yield strength are discussed in Chapter 3.

Chapter 4 contains an analysis of the experimental and simulated results to establish a relationship between the cooling rate and its corresponding grain size. A new approach is described to estimate grain size distribution and skin thickness values in the cross section of casting. Chapter 4 describes the dependency of grain size on the variation of three factors: die temperature, filling time and heat transfer coefficient.

Chapter 5 presents a quantitative experimental study of the effects of process parameters on the formation of defects for different locations of HPDC magnesium alloy components. The amount of total porosity, shrinkage porosity, gas porosity and externally solidified grains (ESGs) are separately reported.

Chapter 6 describes the development of new casting process to simulate the HPDC process. This chapter presents the prediction of interfacial heat transfer coefficient between metal and die during the solidification of magnesium alloys. The effect of pressure on the interfacial heat transfer coefficient is discussed.

Finally, Chapter 7 summarizes the conclusions determined from this research project and discusses the scope for future work regarding the framework provided in this study.

Chapter 2

2 LITERATURE REVIEW

Generally, casting process and qualification production is characterized by process-structure-properties relationship. As shown in Figure 2.1, the microstructure of an alloy has strong influence on the resultant mechanical properties such as yield strength, ultimate tensile strength (UTS) and elongation. The yield strength is affected by grain structure and the amount of porosity controls the variation of elongation and UTS value. As shown in Figure 2.1, process contains three segments: Material selection, filling process and solidification process. Solidification process mostly has effect on the grain structure while the formation of porosity is influenced by filling process during die cast process.

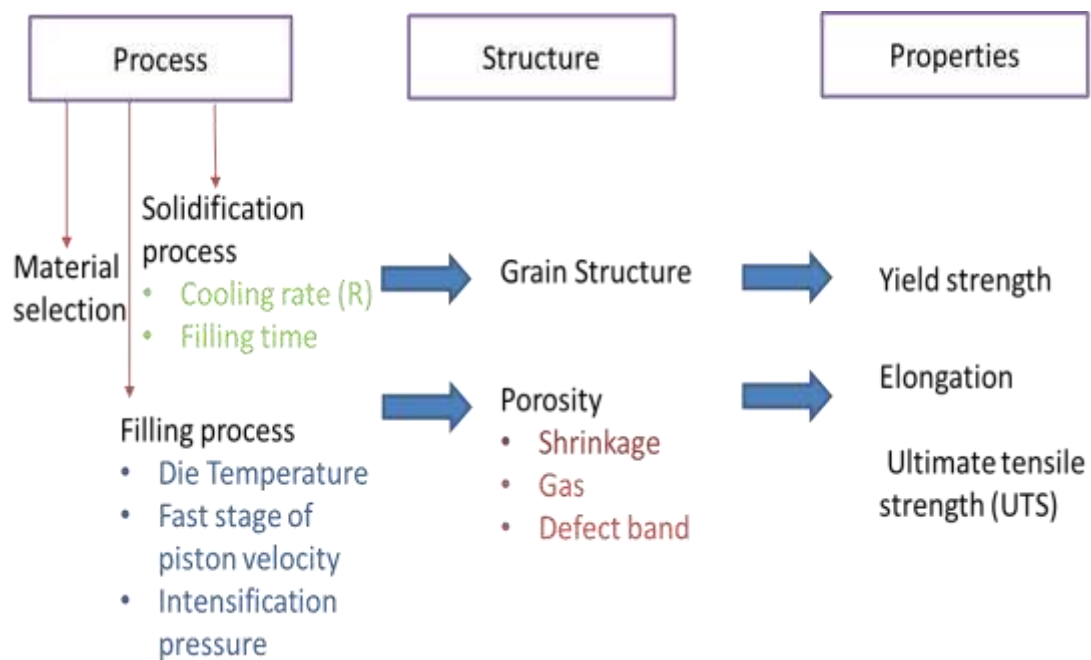


Figure 2.1: Process-structure-property relationship.

This chapter presents the general process-structure-properties relationship for die cast process. The microstructure of die cast magnesium alloys is discussed. The process of high pressure die cast process is described. Also, the role of interfacial heat transfer coefficient between liquid and solid during high pressure die casting process is discussed. It describes the formation of various defects in the microstructure of die cast such as: shrinkage

porosity, gas porosity and defect band. The effects of process parameters on the formation of these defects are discussed. Finally, the correlations between microstructure and mechanical properties of the HPDC components are described.

2.1 Materials Selection

2.1.1 Physical & Mechanical Properties of Magnesium Alloys

Magnesium is the lightest of all commonly used metals [1]. It is member of the periodic table group 2, having atomic number 12 and atomic weight of 24.31g/mol. Magnesium was first identified as a metal by Sir Humphrey Davey in the year 1808. Table 2.1 shows physical properties of pure magnesium.

Table 2.1: Physical properties of pure magnesium [11].

Physical properties	Density (g/cm³)	Melting Point (°C)	Specific Heat (Cal/g.°C)	Electrical Conductivity (%IACS)	Thermal Conductivity (W/m².°C)
Pure Magnesium	1.74	650	0.24	39	167

2.1.2 Magnesium Alloys

Pure magnesium is extremely reactive with a high affinity for oxygen at high temperatures; also it is relatively weak, and easy to deform. Pure magnesium has a tensile yield strength of 21 MPa, ultimate tensile strength of 90 MPa and an elongation to failure of approximately 2-6% [11]. Pure magnesium is rarely used in its unalloyed form for engineering applications. Alloying is used to improve the formability of magnesium for both wrought and cast products. The most common alloying elements are zinc and aluminum. Also, manganese, zirconium, silicon and rare earth metals are other alloying elements that have significant effect on the properties [1, 2, 11]. Table 2.2 shows the influence of alloying elements on the properties of magnesium alloys.

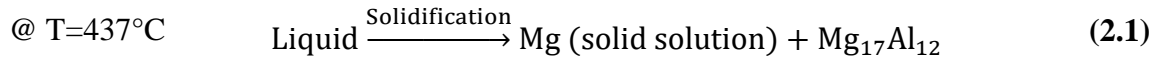
Table 2.2: The effect of alloying element on the resultant alloy [1, 11].

Alloying Elements	Significant Effects on the Properties
Aluminum (Al)	Increases tensile strength and hardness, forms precipitation of intermetallic phase ($Mg_{17}Al_{12}$), improves castability and increases corrosion resistance
Zinc (Zn)	Increases tensile strength and hardness, refine grain structure, improves castability, increases corrosion resistance
Manganese (Mn)	Increases corrosion resistance with reducing the effect of iron, increases yield strength
Silicon (Si)	Increases molten metal viscosity, improves creep resistance via forming Mg_2Si particles, reduces the castability and corrosion resistance
Rare Earth Metals	Reduces the freezing range, increases tensile strength and hardness

2.1.3 Magnesium-Aluminum Phase Diagram

The Mg-Al binary alloy system is the origin of some of the oldest and most commonly used casting magnesium alloys. The maximum solubility of Al in Mg ranges from about 2.1% at room temperature to 12.6% at the eutectic point (437°C). Figure 2.2 shows the magnesium-aluminum phase diagram. **Eq2.1** represents the eutectic reaction between primary magnesium (α -Mg) and the intermetallic phase β ($Mg_{17}Al_{12}$). The β -phase forms at a temperature of 437°C with the Al content at approximately 33wt.%. The β -phase is

formed during the cooling of the casting and preferentially precipitates at grain boundaries, which can be observed in final microstructure of Mg-Al alloys [11, 12].



Different eutectic morphology is observed in final microstructure of magnesium alloys when these alloys contain more than 2wt.% Al. It has been reported [12] that the aluminum content and cooling rate have significant impact on the eutectic morphology. The eutectic phase usually exhibits two morphologies: partially divorced and fully divorced. Partially divorced contains eutectic α -Mg phase within β -phase and fully divorced is characterized by the two eutectic phases being completely separated [12]. The formation and morphology of the eutectic phase play a major role in the size, shape and distribution of the intermetallic β -phase [2, 11-13].

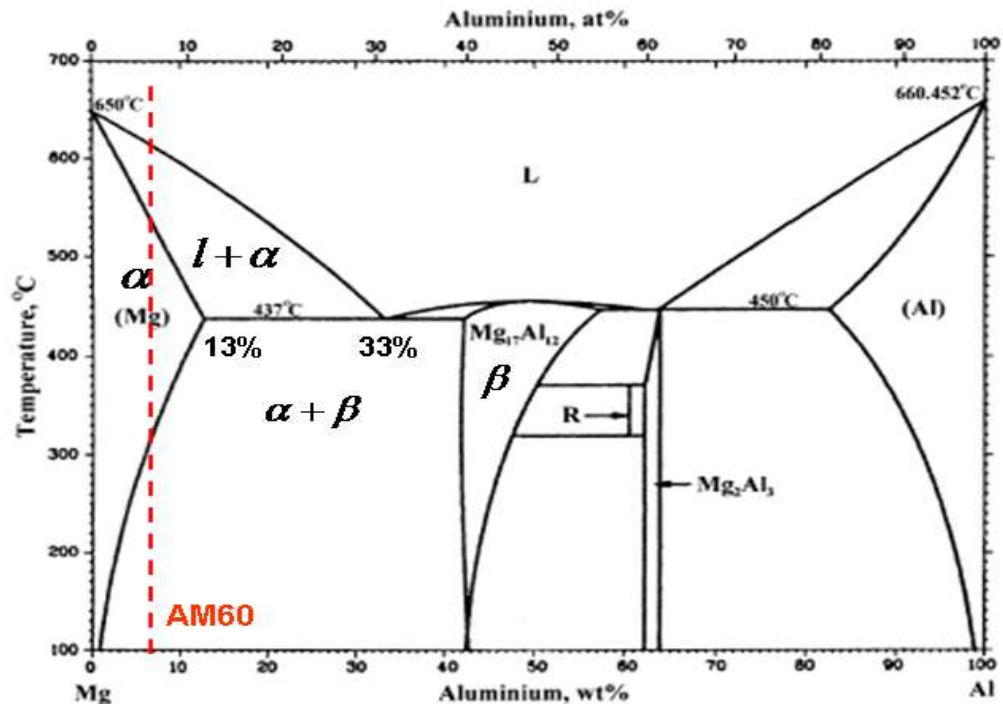


Figure 2.2: Magnesium-Aluminum phase diagram [11].

The intermetallic β -phase is very brittle and therefore it reduces the ductility but also improves the strength of the alloys [2, 11, 12]. The amount of β -phase depends on the cooling rate of the casting and the amount of aluminum [12, 13]. Most of the commercial magnesium aluminum alloys have aluminum content less than 10% such as AZ91, AM60, AS20, and AE44. Alloys of higher aluminum content have a greater ultimate tensile strength and yield strength. For example, AM60, a magnesium alloy with approximately 6wt.% Al, has a lower tensile strength than AZ91 (Table 2.3); however, it also has higher elongation to fracture. It means that AM60 alloy is generally able to absorb more energy prior of fracture as compared to AZ91. Table 2.3 shows the mechanical properties of different magnesium alloys with varying aluminum content [2, 11].

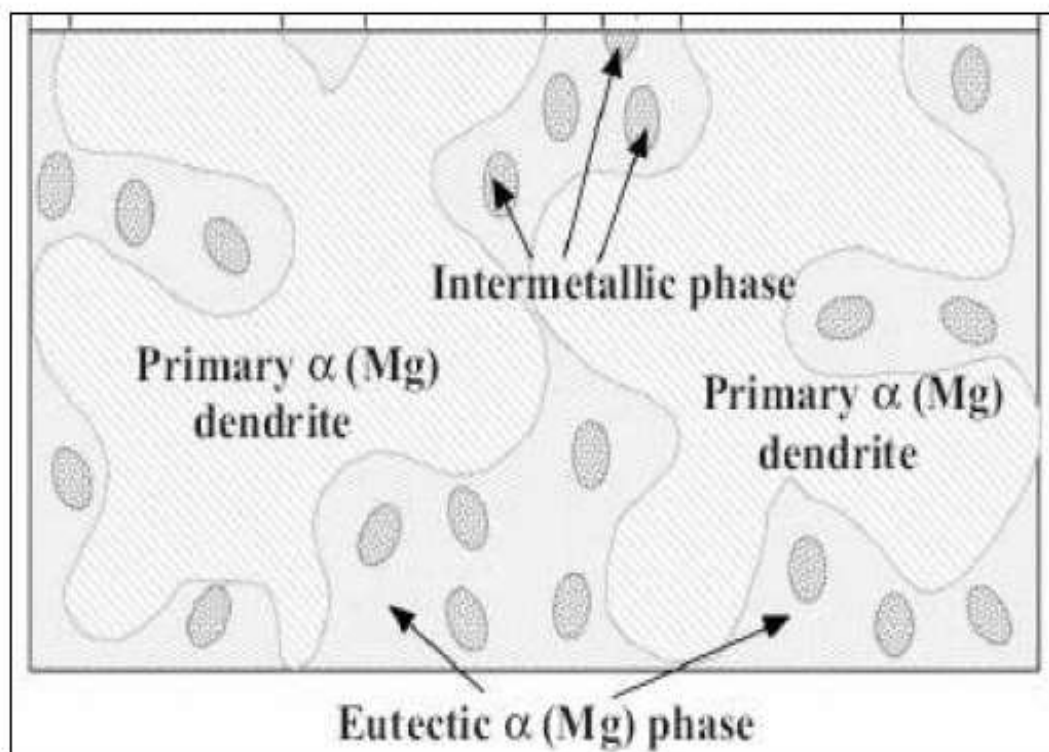


Figure 2.3: Schematic of eutectic microstructure of Mg-Al alloy.

Table 2.3: Aluminum content effects on the mechanical properties of magnesium alloys [2, 11].

Alloy	Al (%wt.)	Density (g/cm³)	Ultimate Tensile Strength (MPa)	Tensile Yield Strength (MPa)	Compressive Yield Strength (MPa)	Elongation to fracture (%)
Pure Mg	-----	1.745	90	21	-----	2-6
AZ91	8.3-9.7	1.81	240	160	165	3
AM60	5.5-6.5	1.80	225	130	130	8
AM50	4.4-4.5	1.77	210	125	110	10
AS20	1.7-2.5	1.78	190	90	90	12.6

2.2 Solidification of Alloys

The nucleation and the phase transformation control the solidification of alloys. Literature [14, 15] indicates that heterogeneous nucleation occurs during solidification of alloys under different casting methods. Figure 2.4 shows heterogeneous nucleation mechanism. In the case of casting process, the nucleus forms in contact with mold wall, therefore, the lower undercooling is required to reach certain nucleation rate. As a result the heterogeneous nucleation occurs. Figure 2.4 also shows the difference between homogeneous and heterogeneous nucleation in terms of interfacial energy. As shown in Figure 2.4 (b), the energy barrier for homogeneous nucleation is very much larger than for heterogeneous nucleation. The reduction in free energy barrier reduces interfacial energy in heterogeneous nucleation mechanism.

As shown 2.4 (c) and (d), the number of nuclei depends on the magnitude of free energy surface and variation of undercooling temperature. The heterogeneous nucleation begins at lower undercooling temperature as compared to the homogeneous nucleation.

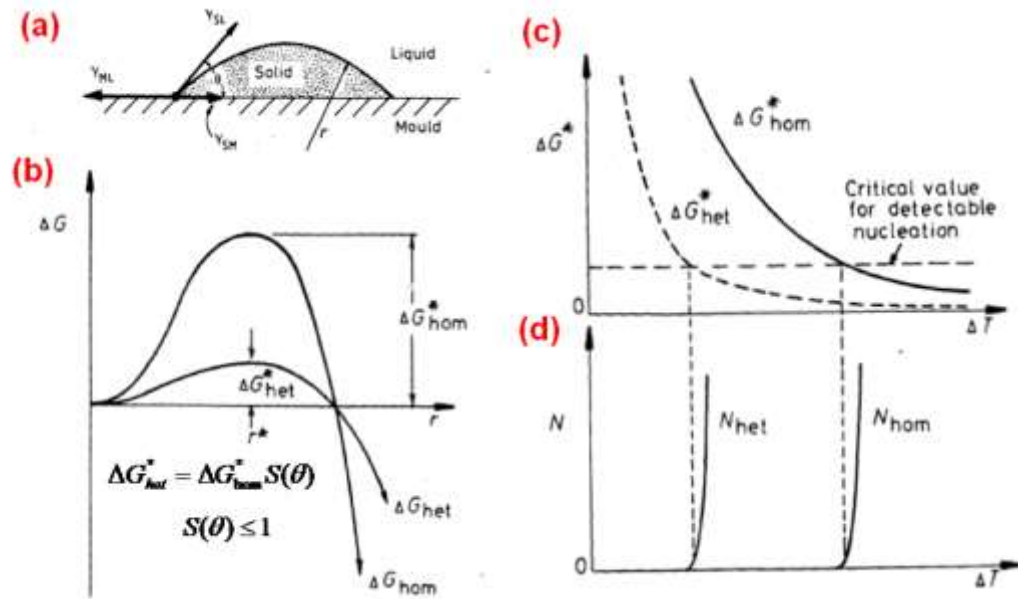


Figure 2.4: a) Heterogeneous nucleation of spherical cap on a flat mold wall. b) The excess free energy of solid clusters for homogeneous and heterogeneous nucleation. It should be noted that r^* is independent of the nucleation site. c) Difference of ΔG^* with undercooling (ΔT) for homogeneous and heterogeneous nucleation d) The corresponding nucleation rates assuming the same critical value of ΔG^* [15].

The fine grain structure of alloys can be produced by two major mechanisms [10, 16-18]. First is thermal undercooling near the mold walls which can encourage nucleation rate restricts the growth, therefore, the small equiaxed grains form in the final microstructure. Second is the presence of solute element in the constitutionally undercooled zone. The growth restriction factor (GRF) is utilized to quantify the effect of solutes in controlling grain growth in front of the solid-liquid interface under non-equilibrium solidification and is defined as:

$$GRF = C_0 m (K - 1) \quad (2.2)$$

where, C_0 , is proportional to the composition of alloy, slope of the liquidus line m as well as equilibrium partition (K). It was reported [15] that cooling rate depend on the rate of heat extraction in the casting.

Previous studies [10, 18, 19] show inverse relationship between the cooling rate and grain size. The dependence of grain size on the cooling rate can be described using an inverse power law relationship, given as:

$$D = kR^{-\alpha} \quad (2.3)$$

where D is grain size, R is the cooling rate ($^{\circ}\text{C/s}$) and k and α are constants. R is numerically defined as the negative of the rate of change of temperature, with respect to time during solidification [18, 19]. The numerical values of the cooling rate can be obtained by calculating the local cooling rate from the temperature-time data, using the following equation:

$$R = -\frac{T_{i+1}-T_i}{t_{i+1}-t_i} \quad (2.4)$$

2.2.1 Equilibrium Solidification

Equilibrium solidification depends on the complete diffusion in solid and liquid states [15, 20]. The composition of solid and liquid can be derived from the phase diagram, as shown in Figure 2.5. At temperature T^* , the composition of solid and liquid can be achieved from the following equation:

$$C_s f_s + C_L f_L = C_0 \quad (2.5)$$

where f_s and f_L are the weight fractions of solid and liquid. Since $f_s + f_L$ equal unity at given temperature, the solid fraction can be derived from above equation. Practically, the solidification process never occurs under equilibrium condition and the fraction of each phase in final microstructure cannot be derived from above equation.

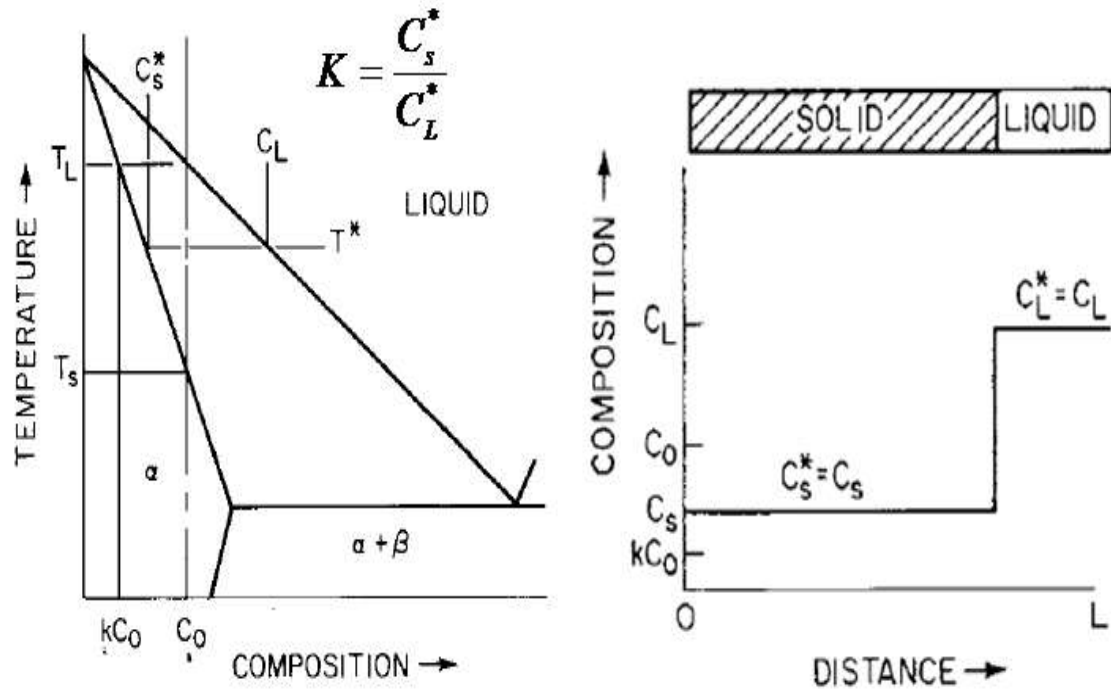


Figure 2.5: Equilibrium solidification and distribution of solute content [15].

2.2.2 Non-Equilibrium Solidification

In the non-equilibrium condition, it is assumed no diffusion in solid phase and complete mixing in the liquid phase. At temperature T_L , the first small solid forms with the composition KC_0 which does not change during solidification. As shown in Figure 2.6, the solute is rejected to the liquid phase during solidification and the liquid phase becomes progressively richer in solute. As a result, last portion of liquid phase contains higher solute content at later stages of solidification. The composition of solid and liquid phase can be calculated using the Gulliver-Scheil [20] equation:

$$C_s^* = KC_0(1 - f_s)^{(K-1)} \quad \& \quad C_L = C_0 f_L^{(K-1)} \quad (2.6)$$

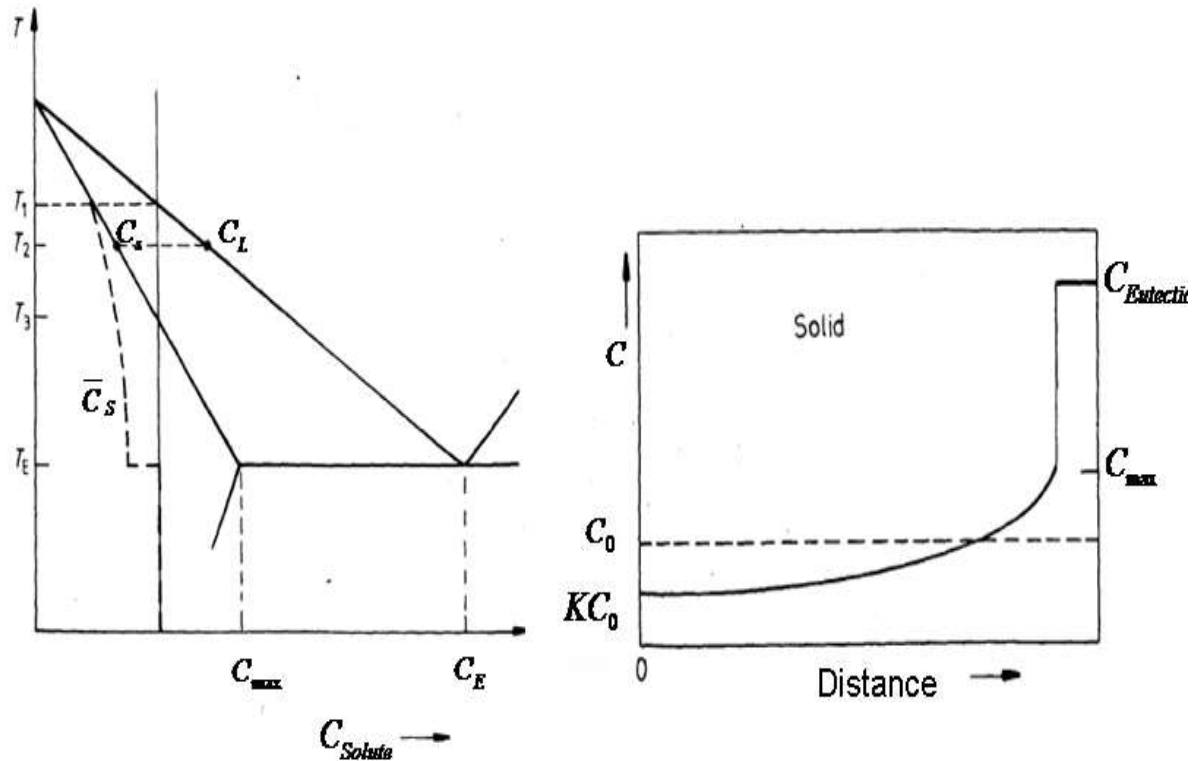


Figure 2.6: Non-equilibrium solidification once there is no diffusion in solid state and complete diffusion in liquid state [15].

The liquid and solid fraction also can be determined by the following equations [15, 20]:

$$f_L = \left[\frac{T_m - T_L}{T_m - T} \right]^{\frac{1}{1-K}} \quad \& \quad f_S = 1 - \left[\frac{T_m - T_L}{T_m - T} \right]^{\frac{1}{1-K}} \quad (2.7)$$

2.2.3 Phase Change Problem in Solidification

Transient heat transfer during solidification of alloys is generally referred to as "phase-change" or "moving-boundary" problems. There are more than two phases during solidification whose melting transformation occurs within a range rather than a specific temperature. The liquid phase and the solid phase have specific thermal and physical properties that change with temperature. Regarding phase change problem, an analytical of solution method was proposed by Stefan. This method is called "Stefan problem" [21-23]. Based on the Stefan problem, the boundary conditions at this interface are set for the solid

and the liquid regions in the casting, as indicated in Figure 2.7. Based on Stefan problem formulation, the energy balance at solid-liquid interface can be described by the following:

$$k \frac{\partial T_s(x_i, t)}{\partial x} - k \frac{\partial T_L(x_i, t)}{\partial x} = \rho L_f \frac{dx_i}{dt} \text{ at } x = S(t), t > 0 \quad (2.8)$$

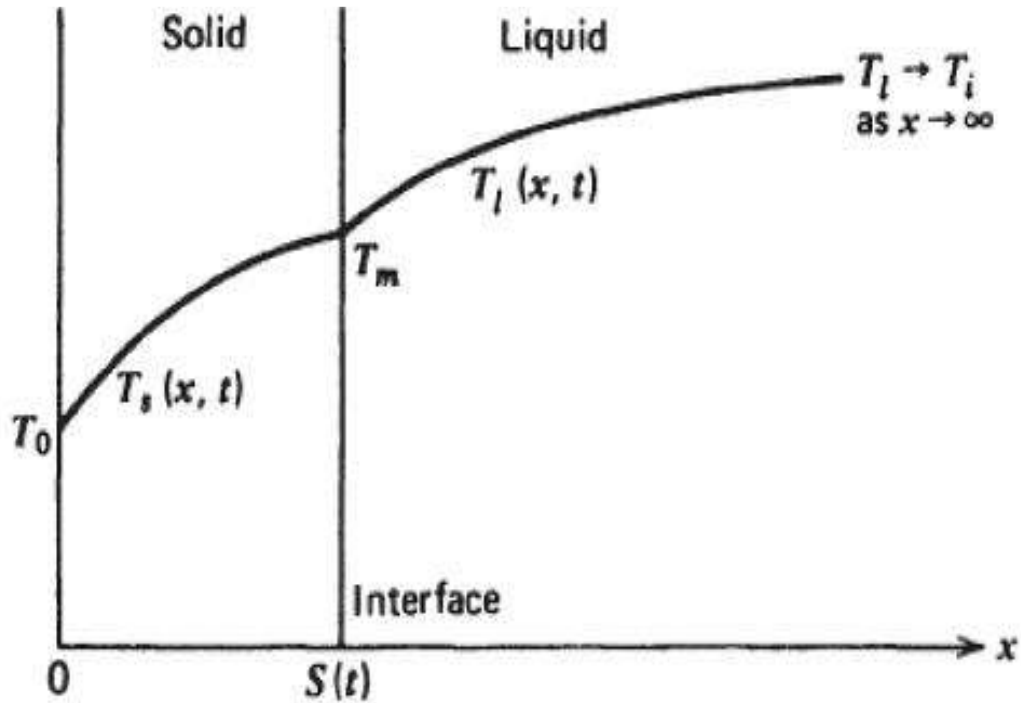


Figure 2.7: The general form of the one-dimensional solution to the Stefan problem [23].

The equation is represented in non-dimensional form in the following relations [23]:

$$\theta_s = \frac{T_s - T_0}{T_f - T_0}, \quad \theta_L = \frac{T_L - T_0}{T_f - T_0}, \quad \xi = \frac{x}{L}, \quad \psi = \frac{qL^2}{k(T_f - T_0)}, \quad \tau = Ste \frac{\alpha}{L_f^2} t,$$

The distribution of temperatures $T_S(x, t)$ and $T_L(x, t)$ are as:

$$\frac{\partial^2 \theta_s}{\partial \xi^2} + \psi = Ste \frac{\partial \theta_s}{\partial \tau}, \quad 0 \leq \xi \leq \xi_i \text{ Solid state} \quad (2.9)$$

$$\frac{\partial^2 \theta_L}{\partial \xi^2} + \psi = Ste \frac{\partial \theta_L}{\partial \tau}, \xi_i \leq \xi \leq 1 \quad \text{Liquid state} \quad (2.10)$$

where Ste is the Stefan number defined as:

$$Ste = \frac{c(T_f - T_0)}{L_f} \quad (2.11)$$

The Stefan number signifies the importance of sensible heat relative to the latent heat. Solving for the above heat equations and satisfying the required boundary conditions, the phase change temperature distribution with time can be calculated.

2.3 High Pressure Die Casting Process

There are three types of die cast methods: low-pressure die casting (LPDC), gravity die casting (GDC), and high pressure die casting (HPDC). Many of the present automobile components are produced through high pressure die casting (HPDC) process due to its fast production rate and its high accuracy and low cost as compared to other casting process. HPDC is a fully automatic, large volume, high productivity process for the production of complex, thin wall component. There are two kinds of high pressure die casting processes: hot chamber die casting and cold chamber die casting.

Figure 2.8 schematically shows the hot chamber die casting process. In this process, melting takes place in an enclosed steel crucible and then plunger directly injects this metal into the cavity of the die. Note that valve is able to control volume of molten metal into the gooseneck. The application of the hot chamber die casting process is limited to the metals which have low melting temperature. In order to produce die cast component with magnesium and aluminum alloys, the cold chamber die cast process is more appropriate [11].

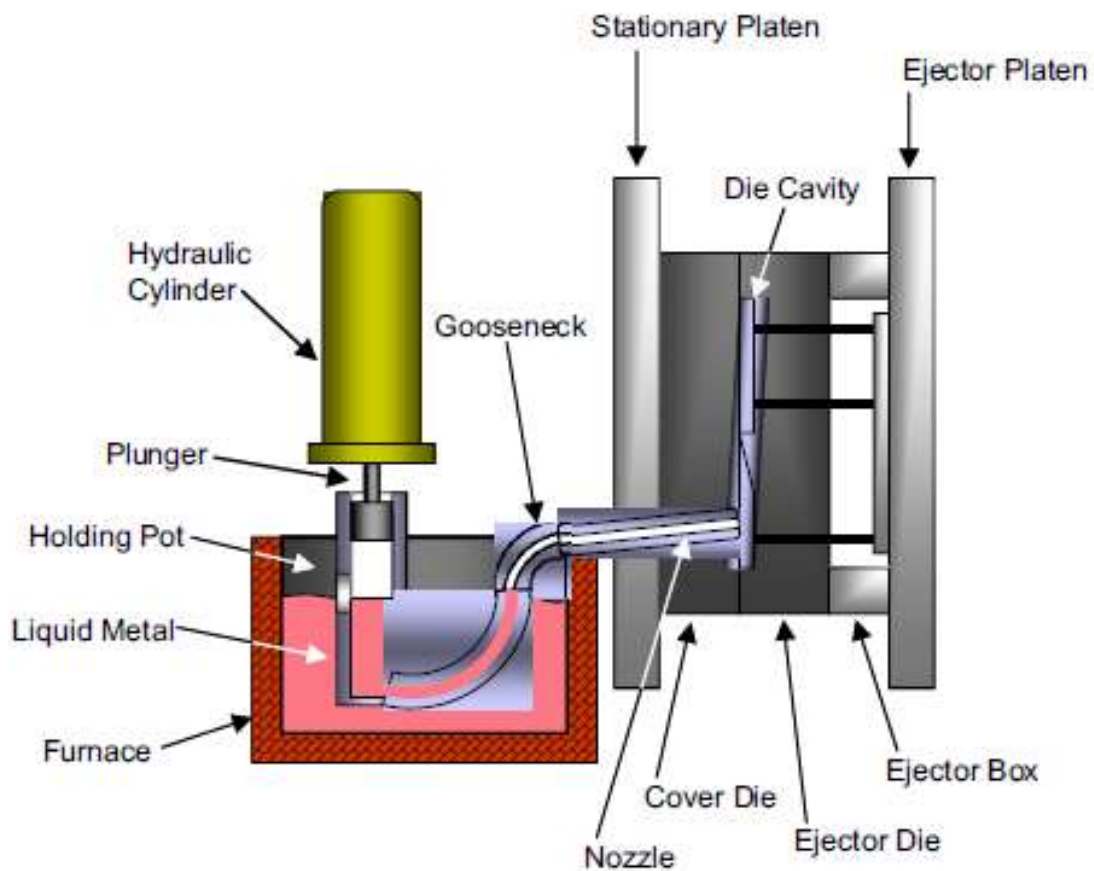


Figure 2.8: Schematics of hot chamber die casting [25].

In this study high pressure die cast process has been conducted by the cold machine die cast. Figure 2.9 schematically shows the cold chamber die casting process. The cold-chamber process requires ladling of the molten metal from the separate furnace into the shot sleeve which is colder than the metal, hence named cold-chamber. The mold cavity is filled rapidly by forcing the molten metal through a narrow gate using a hydraulic piston. The pouring temperature is ranging from 650°C to 730°C and the die temperature ranges 150°C-300°C. The molten metal can weigh up to 10 Kg for each shot and the time periods of each shot lasts less than 100 ms [4].

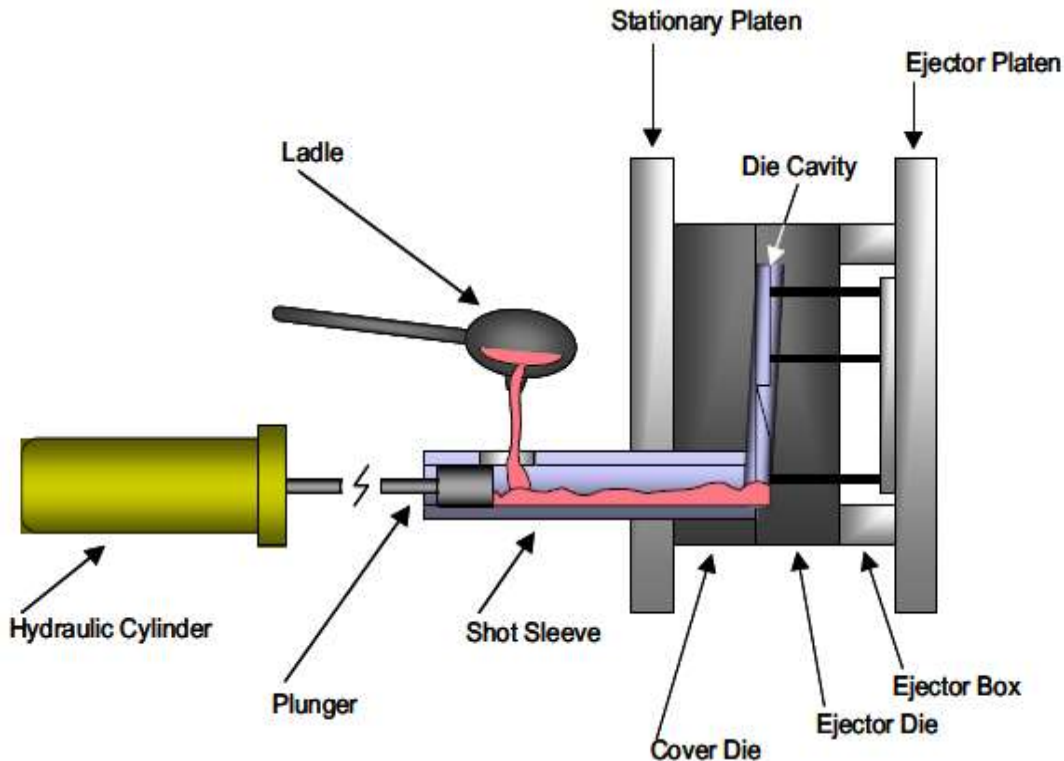


Figure 2.9: Schematics of cold chamber die casting [25].

Die cast mold consists of biscuit, runner, gate, overflows and vents. Biscuit is a part of the cast shot and is ejected from the die with the runner and casting. Runner controls the metal flow by accelerating and directing it to the right places inside the die. Overflows gather the oxidized front of the metal and function as heat storages near thin and/or distant parts of the casting. Vents lead gases out of the die cavity. The feeding metal is forced through the gate with a plunger, basically using the same route as during the filling phase [4, 26].

The three different stages of HPDC process are shown in Figure 2.10. First pouring of molten metal into the shot sleeve and then the slow stage of piston velocity is used. The purpose of slow stage of piston velocity (V_1) is to build up a wave that forces the air to the front and to prevent entrapment of air in the flow. If the slow stage of piston velocity exceeds an optimal value, it may cause a breaking wave, resulting in encapsulates air forms. Second rapid die filling is conducted using fast stage of velocity piston. The fast stage of piston velocity (V_2) aims to complete filling the cavity of die casting [27]. At the end of the second stage, the pressure slightly increases and the piston velocity drops before onset

of the last stage. Third, the intensification pressure is applied and the casting is then ejected. The purpose of intensification pressure (IP) is to compress any entrapped gas and transfer further material into the die cavity to feed the shrinkage of the casting during solidification [26, 27].

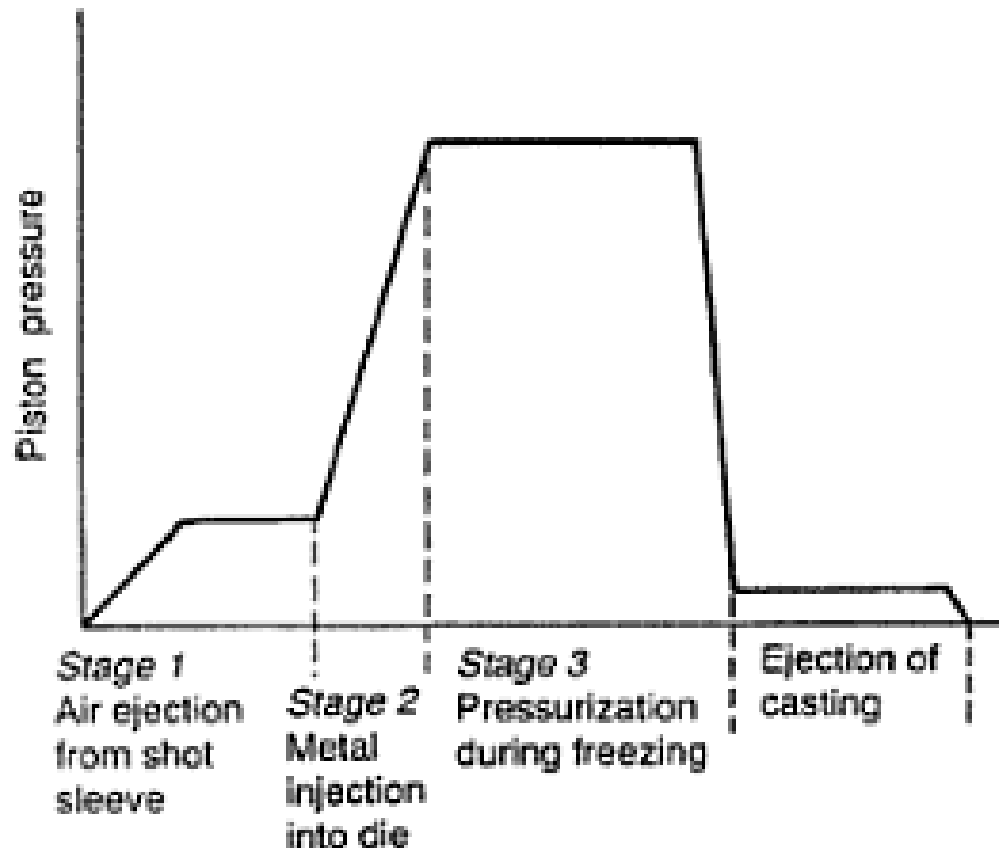


Figure 2.10: Three different stages of the HPDC. The pressure reaches the static point and intensification pressure is applied to maintain the pressure relatively constant in last stage [4].

HPDC components usually contain gas porosity due mainly to the entrapment of air or gas in the melt during the very high speed injection of the molten metal into the cavity. For this reason, it is suggested, the vacuum is utilized to improve the mechanical properties. A simple vacuum instantaneously evacuates all air from the cavities and feed channels. It was observed that the volume of gas porosity and the pore sizes in the castings were significantly reduced by using vacuum assistance during HPDC process. Recently, Li et al.

[28] reported that significantly improved mechanical properties of the magnesium alloy: 20% higher ultimate tensile strength, double elongation and treble low-cycle fatigue life, were achieved by vacuum-assist HPDC process.

In order to predict the local microstructure of die cast, the filling conditions and the local solidification process parameters should be determined. Due to extreme flow and high cooling rate in the HPDC process, the quantitative measurement of solidification parameters is practically very difficult. Hence, it is suggested that commercial software can be used to predict the filling condition and local solidification parameters in the HPDC process.

2.3.1 Simulation of Filling and Solidification during HPDC Process

Commercially available software is capable of simulating the HPDC operation with respect to the metal pressure, molten metal velocity and molten metal temperature while imposing some limitations in the simulation of HPDC for the sake of computational efficiency. In terms of modeling of HPDC process, there are three possible approaches to simulate the solidification phenomenon through the HPDC process. First approach, the solidification occurs when the filling of cavities is completed. In other words, the liquid enters the die cavity well above the melt temperature and cooling does not begin until filling ends. Second, the solidification occurs as soon as the melt touches the mold wall. Third, the cavity is filled with a semi-solid mush due to pre-solidification occurs once the liquid encounters with the shot sleeve wall during the filling process [29]. During the HPDC process, the second or third model have more chance to take place as compared to first model.

Most commercial software decouples the filling and the solidification cycles by assuming that the liquid enters the die cavity and solidification does not begin until filling ends. Therefore, the simulation of HPDC process has been conducted based on the first approach while this approach never occur in practice. However, commercial software enables users to simulate the filling and solidification of HPDC process before implementing experiment. Also, the commercial software gives users opportunity to identify the filling and

solidification condition for each location of components such as: knit line region, the last-to-fill region, the close-to-gate region, the last-to-solidify region.

Different kind of commercial such as: MAGMASoft and ProCAST™. MAGMASoft is adopted by many casting industries, due to MAGMASoft is capable of generating results regarding different casting features such as, the runner and gate effectiveness, velocity profiling and gas entrapment to an acceptable level of accuracy [30]. Since MAGMASoft decouples the filling and the solidification cycles, this software is unsuitable for analysis of heat transfer coefficient effects on the solidification [31]. Determination of heat transfer coefficient between molten metal and die surface is the most challenging issue in the numerical simulation of HPDC. ProCAST™ is capable of simulating the die cast operation with respect to the modeling of thermal heat transfer and fluid flow, including mold filling fully coupled. This commercial software is a finite-element program that solves thermal and fluid equations in casting systems. ProCAST™ is able to account turbulent flow in the casting. This feature is very useful for HPDC process, because this feature enable users to simulate the temperature and the solidification condition in shot sleeve.

2.3.2 Heat Transfer Coefficient in HPDC Process

The interfacial heat transfer coefficient (IHTC) at the metal-die interface plays a major role in the solidification rate and grain structure [32-40]. The IHTC defines the resistance to heat flow across the interface between the liquid and the mold wall surrounding it. The IHTC is quantified by the heat flux per unit area at the metal die interface, divided by the difference between the casting surface and the die surface temperature, as:

$$h = \frac{q}{A(T_{cs} - T_{ds})} \quad (2.12)$$

where h is IHTC and q is average heat flux at the metal-die interface; A is section area; T_{cs} and T_{ds} are the casting surface temperature and die surface temperature, respectively. Due to good contact between the mold and melt at the initial stage of solidification process, the heat transfer coefficient shows a high value in the initial stage of solidification and the nucleation occurs across the surface [4, 35], as shown in Figure 2.11. As solidification progresses, the casting contracts toward the center, the solid metal shrinks during cooling.

The air gap starts to expand because pressure becomes insufficient to maintain a conforming contact at the interface [36-39].

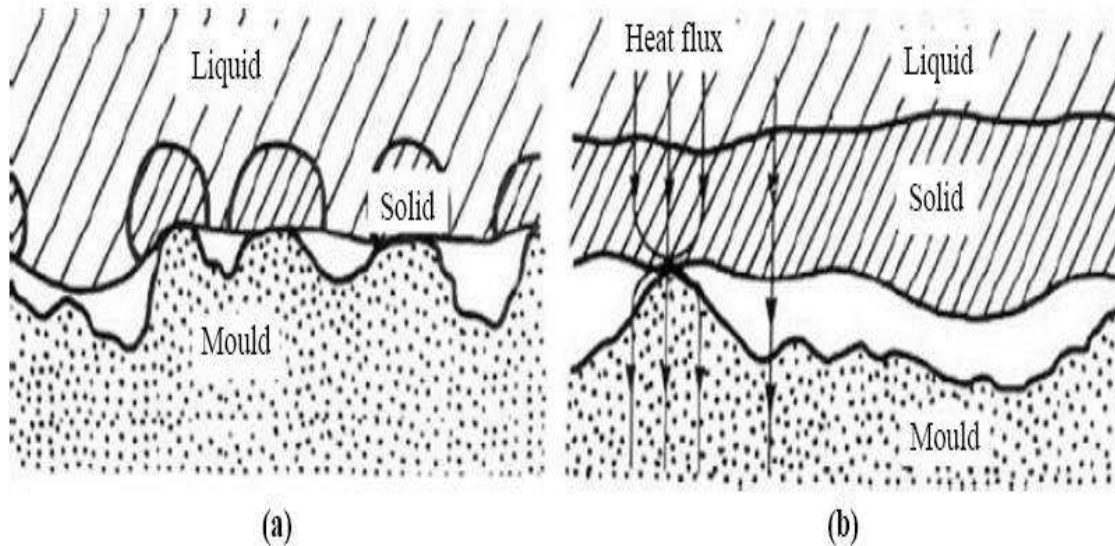


Figure 2.11: (a) The presence of micro gap on the mold wall at the initial stage of casting (b) as solidification progresses, the gap start to expand [4].

A lot of techniques have been attempted to determine IHTC for different metal-mold interfaces. Most previous [35, 37-39] works have focused on sand or permanent mold casting processes, and very few experiments [33, 36, 40] have been conducted about interfacial heat transfer coefficient during the solidification of the HPDC process. Determination of the interfacial heat transfer coefficient (IHTC) is performed with inverse heat transfer analysis. In the literature [36, 40] it was reported that the value of IHTC is affected by the different casting techniques, casting process parameters, casting geometry shapes, the applied pressure during squeeze casting and HPDC process, alloy characteristics and mold processing conditions. For aluminum- silicon alloys, it was [35] reported that the IHTC ranged 2,000 to 7,100 W/m^2K during solidification of the permanent mold casting processes. The heat transfer coefficient for HPDC or squeeze casting process can be expected to be much higher than that for other casting processes. Z. Sun et.al [32] reported that the IHTC was increased 7,195 to 10649 W/m^2K when pressure

changed from 30 to 90 MPa for magnesium alloys AM60 under solidification of squeeze casting.

In the HPDC process, there are some limitations in the measurement of temperature such as high solidification rate, arrangement of thermocouples, high pressure applied and thermocouple response time. Dour et al. [33] point out some requirements including the fast sensor response, proper location of the sensor, and proper way of applying the inverse method that should be used in order to accurately determine the IHTC during HPDC process. Gue et al. [40] determined the IHTC during the HPDC process using inverse method. They successfully predicted the variation of IHTC as a function of time for magnesium alloy AM50 as shown in Figure 2.12. They also studied the effects of different process parameters and casting thickness on the IHTC. They claimed that process parameters shows only effect on the IHTC peak value. It was observed [36] that a higher fast shot velocity leads in a higher IHTC value and the higher initial die surface temperature reduces the IHTC peak value.

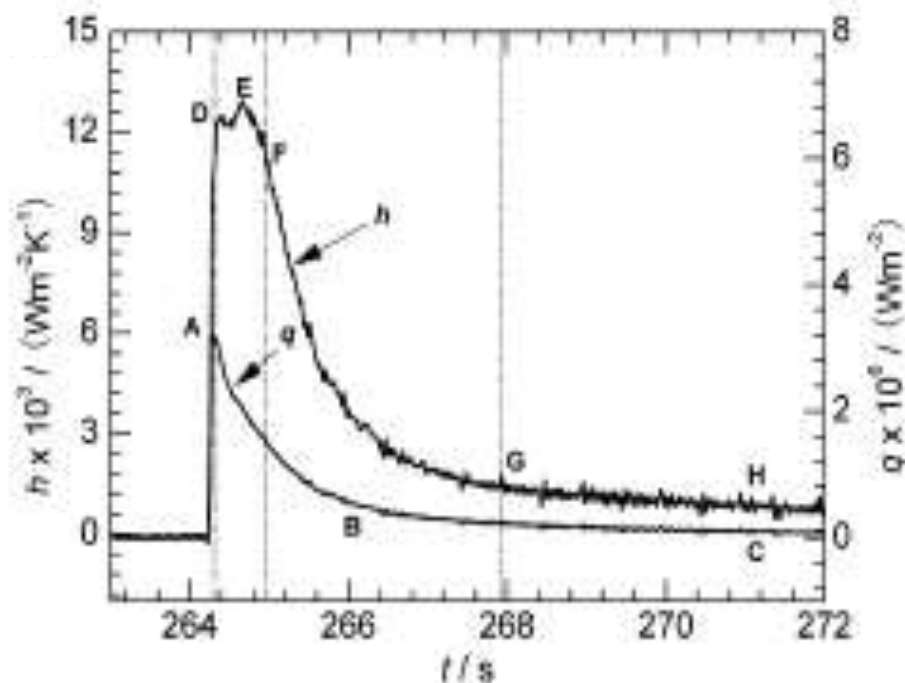


Figure 2.12: The IHTC (h) and heat flux (q) variation as a function of time [40].

Capital letters are from original reference and not used here.

As discussed, in previous works [32, 36, 40], the IHTC was determined using an inverse approach based on the temperature measurements inside the die. Figure 2.13 compares the direct and inverse heat conduction problem. In case of direct heat conduction problems, the determination of temperature distribution inside a heat conducting metal using appropriate boundary conditions while inverse problems are solved with the estimation of boundary conditions from knowledge of thermal history in the interior of the solid. Since an accurate determination of the thermal boundary condition may not be feasible in reality, inverse methods in heat conduction are frequently employed in the field of materials processing.

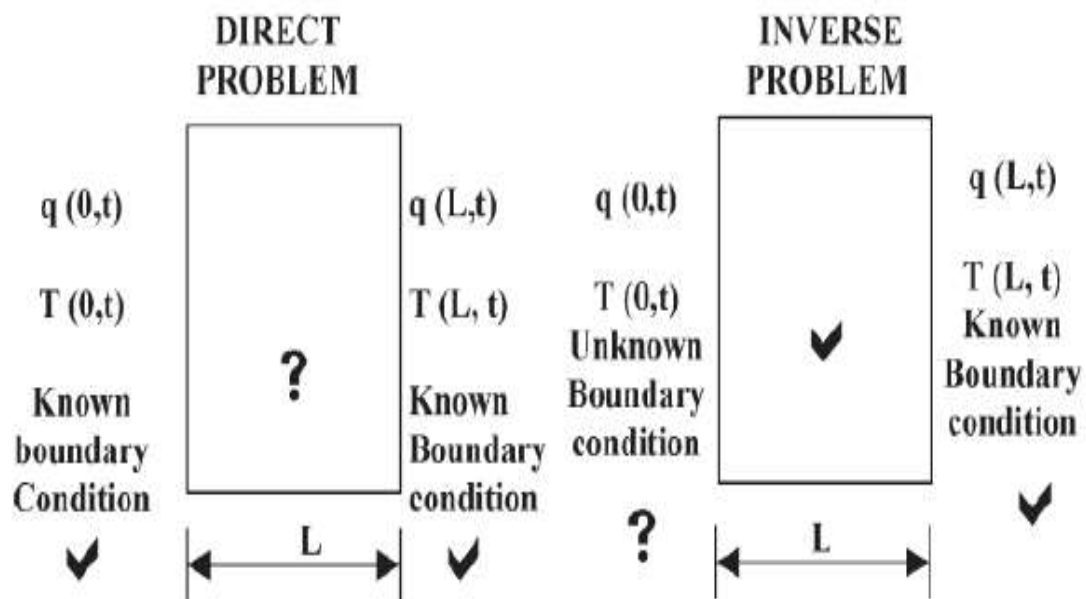


Figure 2.13: Comparison of direct and inverse heat conduction problems [42].

In case of metal castings, the inverse method of heat conduction is useful [41, 42] in the determination of heat flux or heat transfer coefficient at the metal/mold interface (Figure 2.13). In order to determine interfacial heat transfer with inverse method, the temperature history at one or more points should be supplied. An inverse model could be adopted using the temperature distribution data inside the die and the solidifying metal. The transient metal-die interface heat flux and temperature distribution can be estimated by the different techniques such as: control volume method, polynomial extrapolation method, boundary

element method a Laplace Transform and Beck's function [41, 42] specification with finite difference method. In previous works [32, 36, 40], the IHTC was determined through an inverse approach introduced by J.V. Beck [41]. This approach is based on minimizing the sum of squares function with respect to heat flux and the errors between calculated and measured data.

2.4 Microstructure of High Pressure Die Casting

The HPDC process is characterized by very high filling time and extreme cooling rates, with filling and significant initial solidification occurring over a time-scale of milliseconds, leading to non-equilibrium conditions and unique microstructures that are very different to those observed in other casting processes [4, 27]. The microstructure of die cast is typically comprised of fine grains near the walls, called the skin region and coarse grains in the center, referred to as the core region [5, 8, 12, 27]. The skin region is characterized by a finer grained microstructure and higher integrity, whereas the core region contains a coarser grained microstructure, a higher percentage of defects and externally solidified grains (ESGs) which depend on the thermal and flow properties in the shot chamber [12, 27]. Solidification during the die-casting process occurs on the die walls as soon as molten metal reaches the relatively cold mold walls and this leads to the formation of fine microstructure in the skin region. High cooling rates result in high nucleation rate in the melt, and as a result, forms refined microstructures. Figure 2.14 shows the difference between skin region and core region in grain structure. For the case of die cast magnesium alloy, Yang et al. [43] found that the average grain size was 6 and 16 μm in the skin region and core region respectively. H.I. Laukli [27] reported the grain size in the skin region varied from 5 to 10 μm while the grain size is in range of 11 to 20 μm in the core region. D. Yin reported that average grain size ranges from 5 to 9 μm in the skin region, and from 12 to 15 μm in the core region. The transition from the skin region to the core region can thus be determined by a grain size threshold value of 10 or 11 μm .

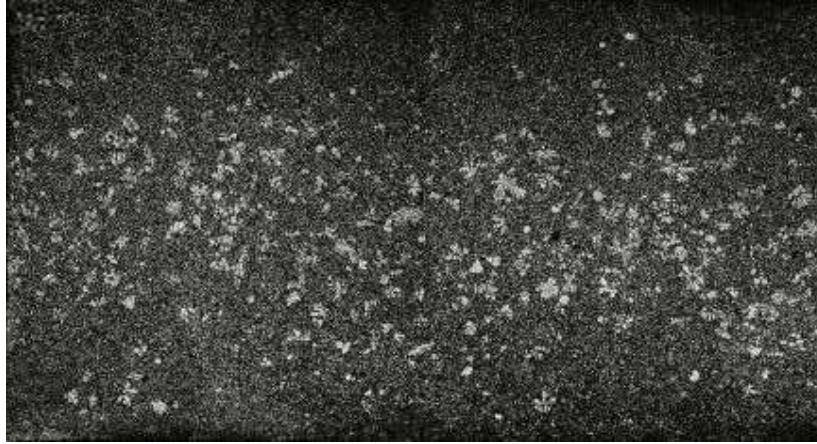


Figure 2.14: Typical grain structure in the cross section of casting for samples of die cast.

2.4.1 Different Kind of Defects in the Microstructure of HPDC

Several defects have been identified in HPDC magnesium alloys, including gas porosity, shrinkage, defect band and externally solidified crystals (ESGs). Literature [27, 44-46] confirms these defects have different origins. Table 2.4 summarizes typical defects of HPDC and their morphology and origins.

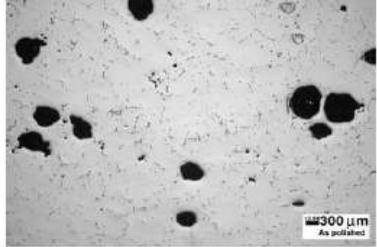
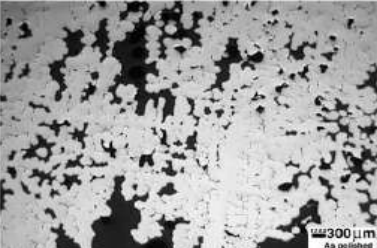
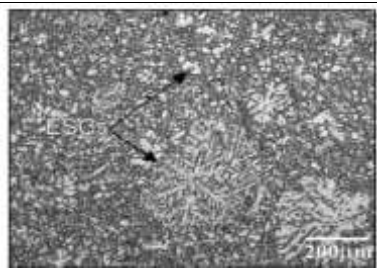
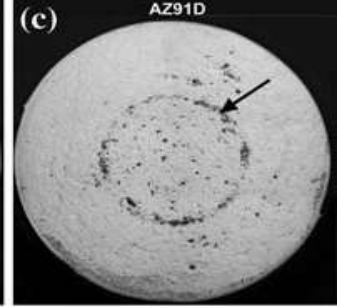
2.4.1.1 Shrinkage and Gas Porosity

Shrinkage porosity forms during solidification due to the volumetric contraction associated with the liquid to solid transformation. In terms of shrinkage source, the solidification of alloys causes a pressure drop in the melt and the shrinkage zone is fed by liquid metal which is restricted. Eventually, a pool of liquid gets surrounded by a shell of solid metal. This liquid then solidifies and the accompanying shrinkage becomes shrinkage porosity.

The most common defect in HPDC is gas porosity which has adverse effects on the ductility and toughness of components [45, 46]. The different mechanisms are recognized to explain the formation of gas porosity. Trapped air should be considered as the first and most likely source of gas porosity due to the very turbulent flow and the fast filling rate that is necessary during HPDC process. Gas porosity is typically formed at specific regions such as knit line and last region to solidify. There are typically areas of porosity, due to two molten metal flows meet [5, 45]. This region is called knit line. The last liquid

solidifying has a very high content of dissolved gas, which forms bubble creating pores in the casting [45]. A part of the gas porosity may also be due to dissolved hydrogen in the liquid of aluminum alloys. During solidification, hydrogen is rejected from solidifying metal into the liquid, and the solubility of hydrogen in the liquid exceeds the critical point, as a result, hydrogen bubbles can nucleate and grow [4].

Table 2.4: The origin and morphology of different defects in HPDC [4, 27, 44-47].

Type	Origin and Morphology	Microstructure
Gas porosity	The trapped air in the die cavity and dissolved gases in the liquid alloy Spherical shape	
Shrinkage	Lack of Liquid metal feeding the volume changes due to solidification crack-like morphologies	
ESGs	Pre solidification of alloys in the shot sleeve before injection Rosette shaped grains	
Defect Band	The mushy zone rheological properties, and the filling pattern of the casting with associated shearing of the mushy zone. Narrow band close to surface	

The average size of shrinkage pores is 10.5 μm and size of the gas pores ranges from 36.9 to 95.4 μm [47]. The 3D images which is obtained from the X-ray tomography investigation revealed that the area fraction of the internal porosities of AM60 die-cast specimens ranges from 0.8% to 6.5% [46, 47]. However, the mechanisms of formation of gas and shrinkage are distinctly different and independent. Gas pores are usually spherical in shape, due to the formation of bubbles and are distributed uniformly along the casting thickness whereas the shrinkage pores have crack-like morphologies [45, 46].

2.4.1.2 Externally Solidify Crystals (ESGs)

The externally solidify crystals are usually observed in the microstructure of die cast magnesium and aluminum alloys. This morphology of grains formed in the shot sleeve prior to injecting into the die cavity. In the time the metal spends in the shot sleeve, pre-solidification occurs due to the liquid contact cold wall of shot sleeve. When the plunger moves forward, a mixture of liquid and ESGs is then injected into the die so that filling occurs by semi-solid flow. The ESGs are significantly larger than the grains due to the slower solidification in the shot sleeve. As shown in Figure 2.14, the ESGs occupy significantly larger volume fractions at the center whilst the ESGs are more dilute when further away from the center.

It was reported that the fraction of ESGs from zero up to 20% for different locations of die cast component. H.I. Laukli [27] reported that the position near the gate includes significantly larger fractions of ESGs, whereas this microstructural feature is more dilute in the position further away from the gate. They point out the inhomogeneous distribution of ESGs is attributed to the shot sleeve filling, solidification conditions and the plunger movement. They also reported that the amount of ESGs increases with a decrease in the melt temperature.

2.4.1.3 Defect Band

Striking features commonly observed in HPDC microstructures are the defect bands, which appear as narrow regions of positive macrosegregation, porosity and cracks that are often parallel to the casting surface. Defect bands or segregation band have also been observed after partially solidified alloys are sheared in semi solid processes such as centrifugal

casting and thixocasting [27, 29]. Figure 2.15 shows typical examples of defect bands in die cast magnesium and aluminum alloys. The band in the magnesium alloy contains shrinkage pore and tears. The band might form in the aluminum alloys based on the segregation of the eutectic phase from the previously solidified layer in the skin region and ESGs in the center. In the case of aluminum alloys, it was observed the eutectic phase concentrated in the defect band region due to macrosegregation from enriched liquid.

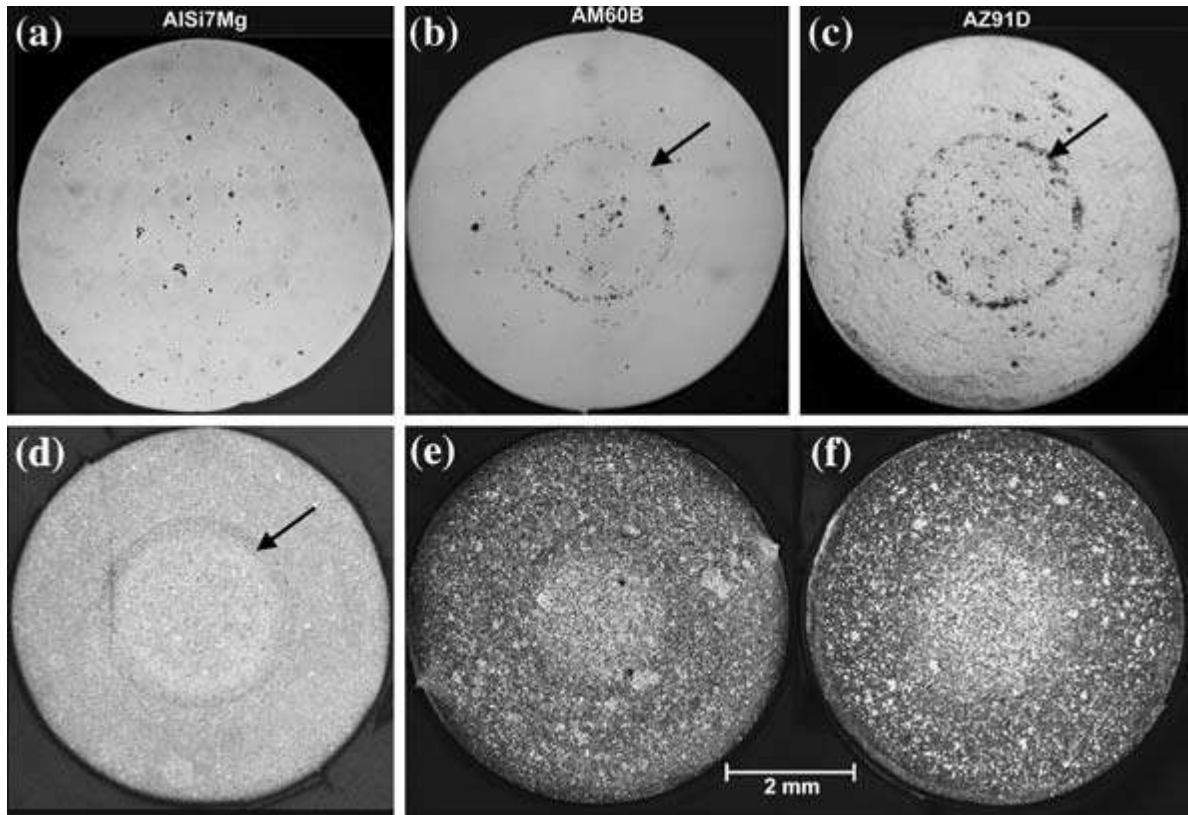


Figure 2.15: Typical defect band in the micrograph of AlSi7Mg, AM60, and AZ91. (a) through (c) are as-polished images and (d) through (f) are etched images revealing the ESGs (large white grains) and macrosegregation. Defect bands are indicated with arrows [26].

Several studies have been conducted to explain the mechanism of defect band formation. Dahle et al. [12, 26, 29] proposed a theoretical framework that defect bands form by a combination of a fraction solid gradient away from skin region and the presence of ESGs in the core region as a result of lift forces on the solid. They used the shear strength- fraction solid correlation to justify the formation of defect band. Figure 2.16 indicates the

dependency of shear strength on the solid fraction. As shown in Figure 2.16, the values of coherency and maximum packing solid fractions is affected by the dendrite size and morphology. When significant flow has to occur while partially solidified mush is present, the mush will deform, and the low-strength regions are the most likely to yield. The layers formed along the mold walls are relatively immobile and rigid. Therefore, shear bands occur between skin and core regions where the solid fraction is less than the maximum packing fraction.

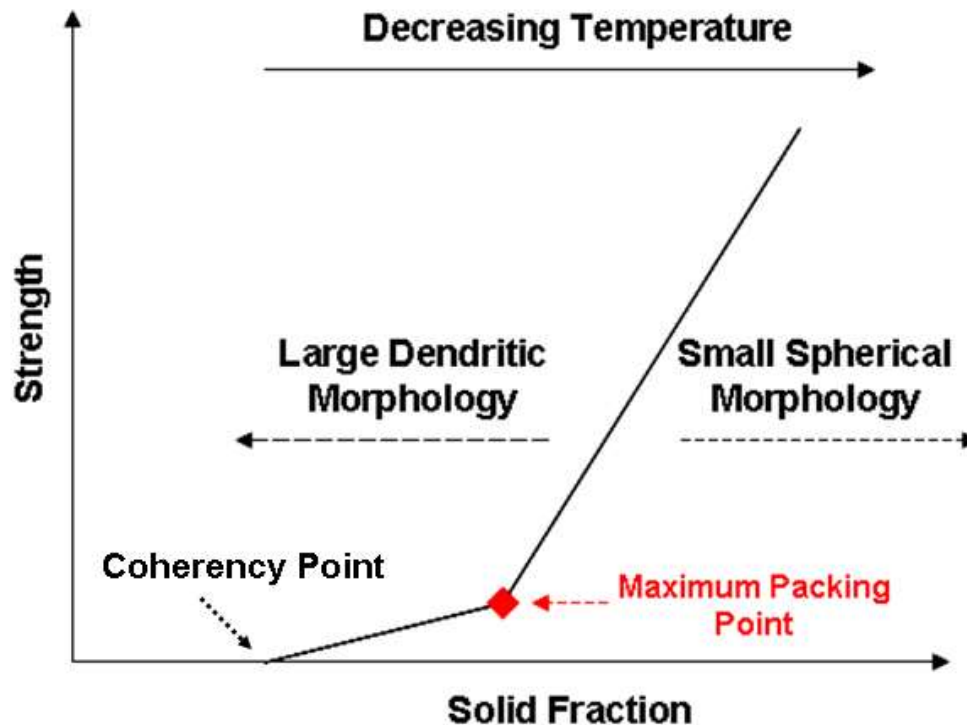


Figure 2.16: The material as a function of fraction solid, for the two extremes in crystal morphology; large dendritic crystals and small globular crystals [29].

Gourlay et al. [48] proposed a mechanism describing the deformation defect band as a result of local slip occurring in the dendrite network when the flow fluid past the stagnant skin region with higher level of solid fraction. This theory is based on the deformation of local slip into dendrite network in the region between skin and core region when the local applied stress is sufficient. They [48] also reported that formation of defect band occurred similar to HPDC without ESGs during gravity die casting for magnesium and aluminum alloys.

2.4.2 Effect of Process Parameters on the Defect in the HPDC Process

The defects show strong dependency on process parameters such as molten temperature, gate velocity, die temperature, intensification pressure, casting geometry, velocity first stage, and velocity second stage and venting gate area [46, 47, 49-51]. Table 2.5 summarizes past results regarding the process parameters effect on the different kinds of defects. Dargusch et al. [49] investigated the influence of section thickness and gate velocity on the microstructure. They pointed out that higher gate velocity leads to better surface finish but increases the amount of total porosity. Haunge et al. [50] reported that the increase in the consolidation pressure significantly reduces the total porosity if the shot sleeve rate is high. Tsoukalas et al. [51] investigated the effects of process parameters on the porosity distributions in an Al-Si-Cu alloy using the Taguchi approach. Lee et al. [46, 47] examined that the effects of gate velocity, intensification pressure, and melt temperature on the amount of total porosity, gas porosity, shrinkage porosity, and pore size distributions. They found the gas porosity is affected by intensification pressure, gate velocity and the melt temperature while these parameters have negligible effect on shrinkage porosity.

Several studies have been conducted to clarify the correlation between the process parameters and the defect band [27, 52]. Pitsaris et al. [46] reported that the defect band location has a strong dependency on the melt temperature, and the fast stage of piston. Rodrigo et al. reported that increasing the intensification pressure forces more material into the overflows make significant deformation, as a result, the defect band can form closed to overflow area. They also observed that the higher level of intensification pressure reduces the shrinkage and gas porosity in the defect band. Otarawanna et al. [26] observed that when sufficiently high intensification pressure and thick gate were used, shear banding occurred through the gate while low intensification pressure was combined with a thin gate, shear banding did not occur through the gate and feeding was less effective, resulting in a higher level of porosity in the HPDC component.

Table 2.5: Reported effects of the process parameters on different kinds of defects.

Author	Alloys	Contribution	Source
Dargusch et al.	AZ91	The effect of section thickness and gate velocity on the porosity level. There is an optimum gate velocity where castings of good surface finish are obtained.	[49]
Hunag et al	AM60	The effect of process parameter on total level of porosity (shrinkage and gas porosity).	[50]
Tsoukalas et al.	Al-Si-Cu	Using Taguchi method to optimize volumetric porosity level	[51]
Lee et al.	AM60	The effect of melt temperature, gate velocity and intensification pressure on the area fraction of gas porosity and shrinkage.	[46]
Pitsaris et al.	Al-Si	The location of defect band shows dependency on melt temperature and velocity second stage.	[52]

2.5 Structure-Property Relationships

2.5.1 Effects of Grain Size

A Grain is an individual crystal in polycrystalline metal or alloy. The average grain size plays a major role in mechanical properties of metals or alloys, including yield stress, hardness and strain to fracture. Yield strength or flow stress is directly depended on the grain size and this relation is known as the Hall-Petch equation [52, 53], given as:

$$\sigma = \sigma_0 + kd^{-1/2} \quad (2.13)$$

In above equation, K and σ_0 are known as the parameters of the Hall-Petch. Where σ_0 is the intercept stress and K is the Hall-Petch slope. Hall-Petch equation indicates that a smaller grain size leads to higher yield strength.

At least four different models have been suggested to justify the Hall-Petch relation. One of them and most commonly cited, is the dislocation pile-up model. It has been observed in Al-Mg alloys, that grain size affects the propagation of the Lüder's bands from applied stress in a tensile test and subsequently, the resistance to initiation of plastic flow in the material. The Lüder's bands can be attributed to the dislocation pile-up against grain boundaries [52, 53].

Many studies [55-59] on the effect of grain size on the as-cast mechanical properties of magnesium alloys have been conducted. Mann et al. [55] studied the Hall-Petch relationship in sand-cast magnesium alloyed with small amount of zirconium to provide grain refinement. In this investigation, both Hall-Petch parameters, σ_0 and K , were determined for tests performed under uniaxial tension and compression. Figure 2.17 shows the effect of grain size on the values of true stress for the uniaxial tests. The K value in compression was higher than in tension and a negative σ_0 was observed.

They also examined influence of plastic strain on the Hall-Petch slope, K . Figure 2.17 shows K as a function of plastic strain. They reported the K value increases approximately $200 \text{ MPa}\sqrt{\mu\text{m}}$ at a strain of 10^{-4} , reaches a maximum $540 \text{ MPa}\sqrt{\mu\text{m}}$ in compression and $470 \text{ MPa}\sqrt{\mu\text{m}}$ in tension at approximately 0.2% strain and then decreases. The values of K are lower than $200 \text{ MPa}\sqrt{\mu\text{m}}$ at strains <0.002 . This result is explained by the consideration of a "pre-yield micro strain" portion of the stress-strain curve, where only a few of the grains have yielded [55].

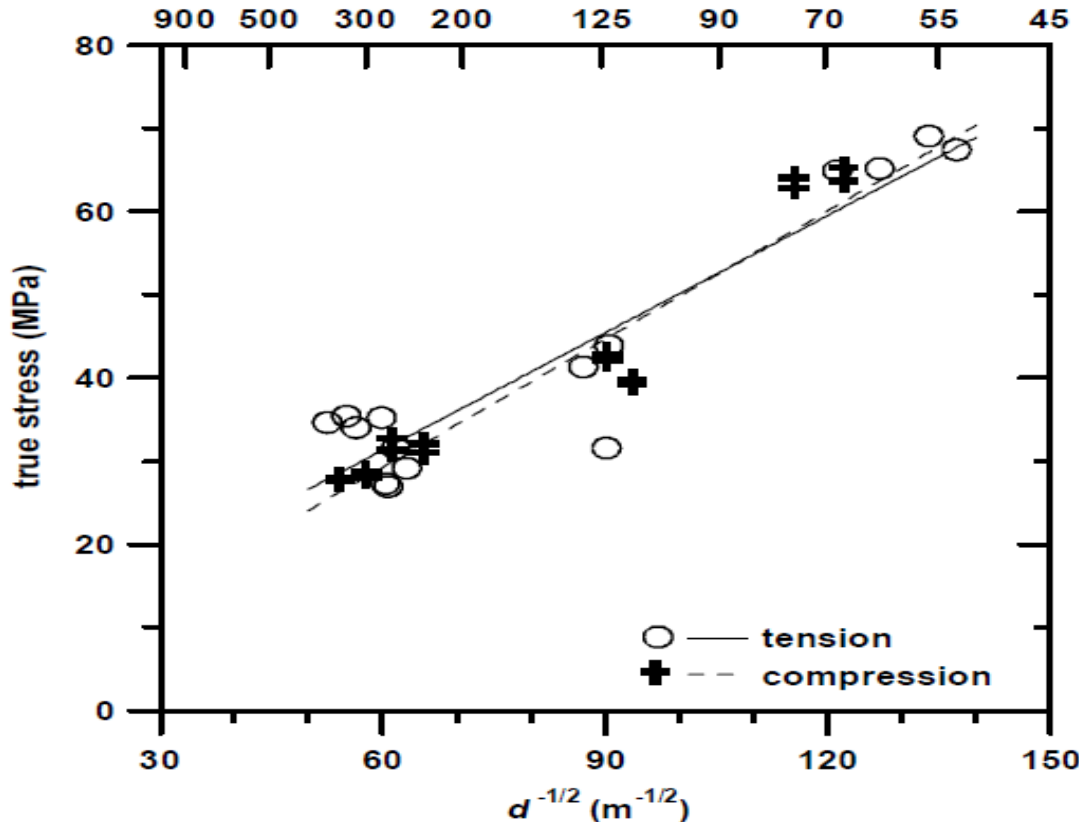


Figure 2.17: Hall-Petch relationship for sand-cast magnesium alloy [56].

The Hall-Petch equation has also been used to relate the measured hardness during spherical indentation to the grain size of metals. Further, J. Weiler [56] examined that the dependence of the yield stress of die-cast magnesium alloys on the grain size using spherical microindentation techniques. In this work, several samples were indented in both skin region and core region. Hall-Petch parameters, σ_0 and K were determined and compared with previous published results for pure magnesium and similar magnesium alloys, as shown in Figure 2.18. He reported the Hall-Petch slope, K , is $274 \text{ MPa}\sqrt{\mu\text{m}}$ and the intercept stress, σ_0 , is 10 MPa from the skin region. These values compare quite well with the Hall-Petch values observed by Hauser et. al. [57] who reported Hall-Petch parameters ($K = 220 \text{ MPa}\sqrt{\mu\text{m}}$, and $\sigma_0 = 12 \text{ MPa}$), for pure magnesium during uniaxial tensile testing. Andersson et al. [58] point out that both σ_0 and k then determined in tension are nominally greater than those values for pure magnesium [57].

Figure 2.18 also shows that the results of the core region do not follow the same Hall-Petch equation as the results in the skin region. These observations can be explained by the difference in microstructure between the skin and the core regions, which is discussed above.

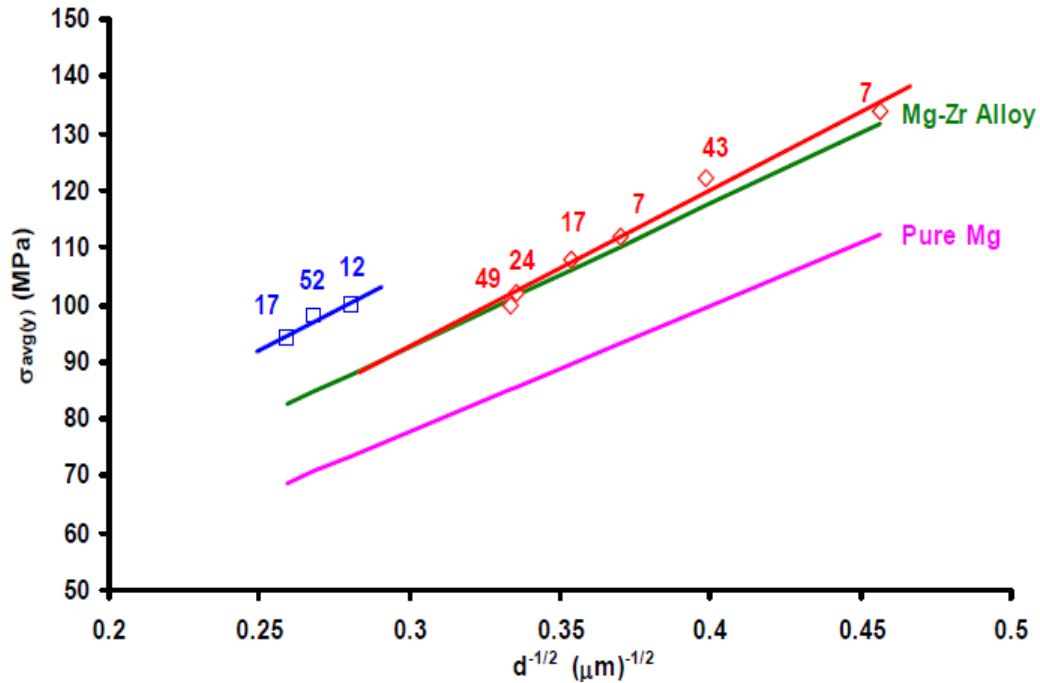


Figure 2.18: Average indentation yield strength as a function of grain size in comparison with published results on similar magnesium alloys [56].

Various investigations [8, 9, 12, 59, 60] have shown that the skin region has higher hardness and local yield strength as compared to the core region due to the finer microstructure and higher amount of dispersed intermetallic phase in the skin region. The strength mechanism of the die-cast specimens originated from solid solution, dispersion and grain boundary hardening mechanisms. It was reported [12] that the contribution of the grain boundary hardening mechanism in the die cast magnesium alloys is greater than that of the two other mechanisms. However, the difference in microstructure of the skin and core region results in the variation of the mechanical properties from the surface toward the interior region of the castings.

Some studies [43, 60] have also shown that the yield strength of die cast magnesium alloy is controlled by the skin region. The role of skin and core regions in the yielding behavior of HPDC Mg-Al have been characterized by Yang et al [43]. They pointed out that the core region of magnesium alloys appeared to yield first, whereas the skin remained elastic to much larger stresses. As a result, a strong mutual interaction occurs during transformation from elastic region to plastic region while the harder skin imposing elastic constrain on the softer core. In terms of predicting the yield strength of a HPDC alloy, the influence of skin thickness must be taken into account.

Skin thickness of magnesium die castings has been defined using the micro-hardness profile across the casting thickness, the location of the pore band through the casting thickness, porosity-free casting layer, the change in the grain size from the skin to the core region, the onset of ESGs and the areal percentage of eutectic phase [8, 9, 12, 59, 59-61].

Sequeira et al. [61] observed that the hardness decreases approximately 16% from the surface to the central region of cast tensile bars. Their observations are presented in Figure 2.19. Mao et al. defined the skin thickness based on the location of the 'defect band' through the thickness of the casting. Weiler et al. [9] showed that the skin thickness in different locations of an AM60B die-cast could be determined using the hardness profile, the areal percentage of eutectic composition, the average grain size, and the onset of large dendritic structures across the casting thickness. They also compared the skin thickness determined from those methods and they found those methods produce very consistent skin thickness values as shown in Figure 2.20.

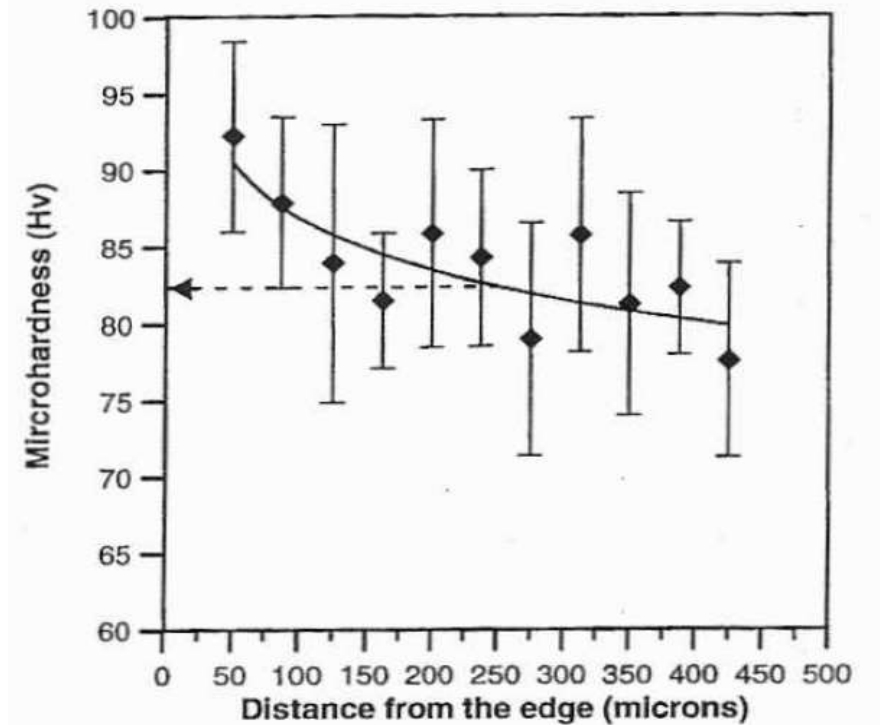


Figure 2.19: Variation of microhardness from skin to core for die-cast AZ91D [59].

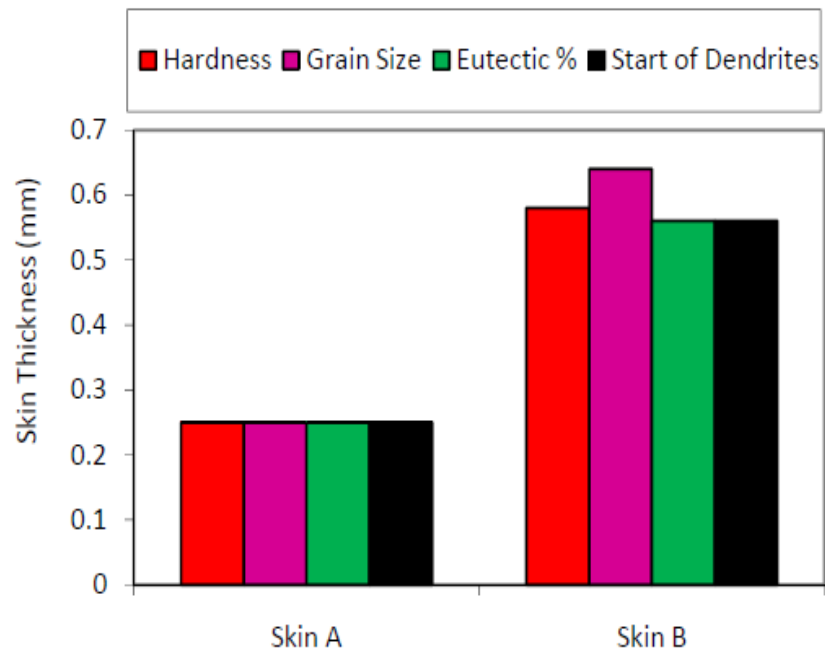


Figure 2.20: Determination of skin thickness using four methods: the hardness profile, the areal percentage of eutectic composition, the average grain size, and the onset of large dendritic structures across the casting thickness [9].

An approach was proposed [61] to model the microstructure as a composite of skin and core regions, based on their respective grain sizes. Thus, with a measure of the relative thickness of the skin and core regions, a modified Hall-Petch equation can be written as:

$$\sigma_y = \sum f_i (\sigma_0 + k d_i^{-1/2}) \quad (2.14)$$

where, f_i is the fraction of the thickness of the skin or core region. The modified Hall-Petch equation was used to characterize the role of the skin thickness on the overall yield strength. In the previous studies [45, 46, 61], the cross-section of a 3mm × 6mm tensile specimen were cut from instrument panel beams which is composed of approximately 67% fine-grained skin and 33% coarse-grained core. In comparison, a purpose-cast tensile specimen of the same dimensions would have a skin on all four sides, comprising 78% of the cross-sectional area.

2.5.1.1 Microindentation Testing

Microindentation testing techniques offer possibilities for evaluating the mechanical properties of different regions such as interface of composite material, welding heat affected zone, hard coating and other cases where the use of uniaxial tensile testing is impractical or impossible. The following sub-sections describe spherical indentation, expanding cavity model indentation, the indentation stress-strain relationship measurement underneath the spherical indentation and the calculation of the actual indentation contact radius.

2.5.1.2 Spherical Indentation

The term hardness refers to the measure of a material's resistance to deformation by surface indentation. The usual method to achieve a hardness value is to measure the depth of an indentation left by an indenter of a specific shape, with a specific force applied for a specific time. At first time, A. Brinell proposed the use of indenter of spherical shape as a technique to evaluate the hardness of materials [62]. According to the standard American Society for Testing and Materials (ASTM) [63], the Brinell hardness test method consists of indenting the test material with a 10 mm diameter hardened steel or carbide ball

subjected to a load of 4.9 kN. The diameter of the indentation left in the test after removal of the indenter is measured. The Brinell hardness value is calculated by dividing the load applied by the surface area of the indentation.

The mechanism of indentation of metals by blunt indenter commonly has been based on a slip-line field solution proposed by A. Wahlberg [62]. It was further improved upon by T.O. Mulhearn [64], who proposed that indentation occurs during loading by the radial compression of hemispherical shells centered at the point which the indenter first contacts the material (Figure 2.21).

Mulhearn [64] reported that the magnitude of the strain in the shells decreases progressively as the elastic-plastic boundary is approached and except for the regions close to the indenter tip, where the total strain is completely plastic. The differences in the deformation pattern with indenter geometry, for blunt indenters, are confined to the high-strain cap region closest to indenter (the shaded region Figure 2.21). Moderately large plastic deformations occur within this region [64. 65].

Samuels et al. [66] later also proposed circumferential extension of the plastically deformed shell occurs at the free surface during loading, but there is a corresponding downward deflection of the whole plastically deformed region. The downward deflection accounts for the displaced volume of the indentation and is accommodated by elastic deformation in the specimen as a whole.

F.M. Haggag [67] showed that the variation in hardness number is due to variation in the elastic recovery which occurs during unloading, producing an extruded lip, known as material pile-up in the free surface next to the indent. The volume of the material pile-up depends on the volume of the indentation affected by the degree of elastic recovery, which is in turn related to the strain-hardening characteristics of the indented material [68].

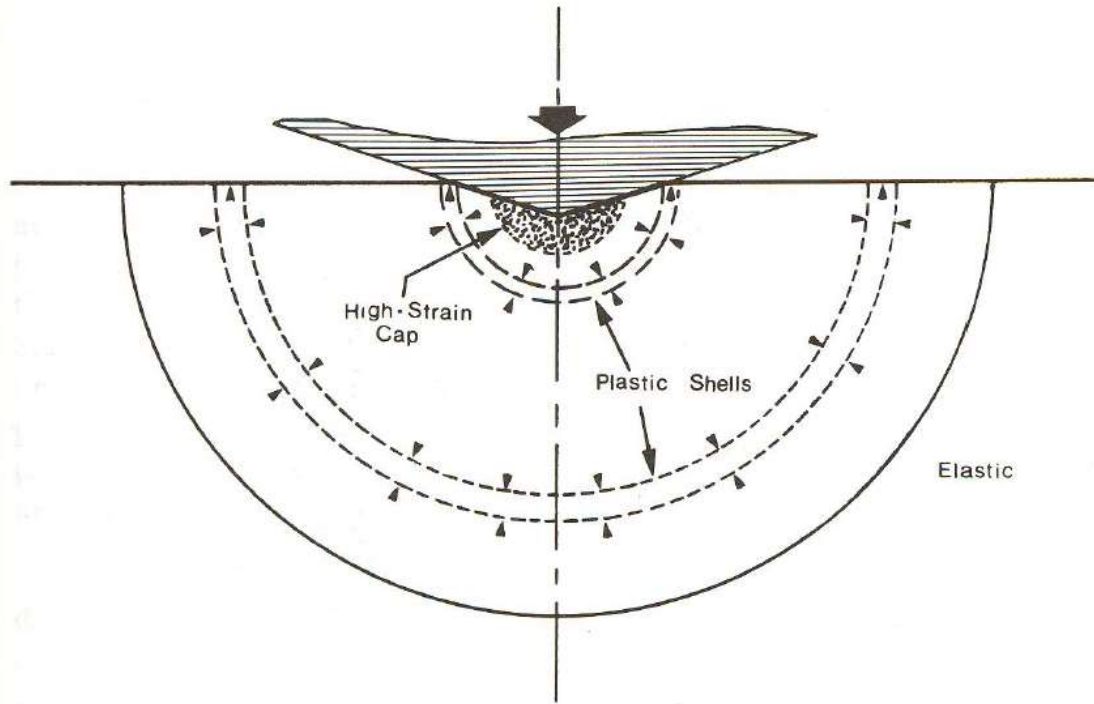


Figure 2.21: The compression mechanism of indentation proposed by Mulhearn. The circular continuous line represents the elastic-plastic boundary. The dashed lines indicate several hypothetical plastic shells, and the arrows represent the direction of straining of the shells [65].

2.5.1.3 Analysis of Indentation Load–Depth Curve

To derive the relationship between indentation stress and strain, the actual indentation contact radius should be considered. Tabor [69] showed that the average indentation strain, ϵ_{avg} , dependence on the ratio a/R , where R is the radius of spherical indentation and a is indentation contact radius (Figure 2.22). The real contact radius, a , between the indenter and the specimen determined the indentation load-depth curve, and is relative to the plastic contact depth, h_c , and the pile up or skin-in. The plastic contact depth, h_c , between the indenter and the specimen at a certain load is determined calculating the elastic deflection depth, h_d , from unloading curve [69], as:

$$h_c = h_{\text{max}} - h_d \quad (2.15)$$

where h_{max} is the maximum indentation depth, h_d is the elastic deflection depth. It should be noted that the effects of pileup or skin-in are not included.

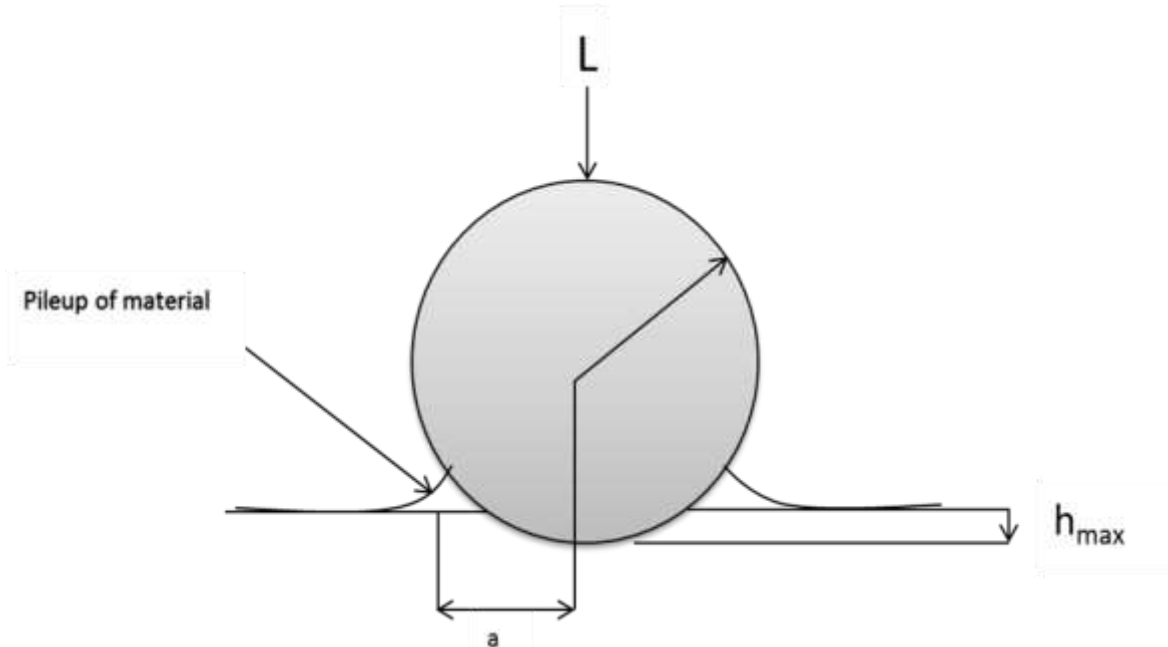


Figure 2.22: Schematic diagram of the indentation of a material by spherical indenter.

There are three different material response regimes of deformation during spherical indentation: elastic, elastic-plastic, and fully plastic. Figure 2.23 presents the typical indentation load with respect to indentation depth that corresponds to each deformation regime. In the elastic regime, elastic stress does not occur and elastic stress contours are observed beneath the indenter. In the fully plastic regime, an uncontained plastic zone is present beneath the indenter and in the elastic-plastic regime, contained plastic zone is observed beneath the indenter [70, 71].

The elastic deflection depth, h_d , in **Eq2.15**, can be obtained using the unloading curve which corresponds to elastic recovery during unloading. It is observed [71] the unloading curve reflects the elastic recovery when the indentation load is removed. For the case extreme of perfectly elastic response, there is no residual imprint after unloading, and h_c equals half of the maximum depth, h_{max} , for a rigid indenter. In the perfectly plastic response, there is essentially no elastic deflection and the effects of pileup or sink-in must be included.

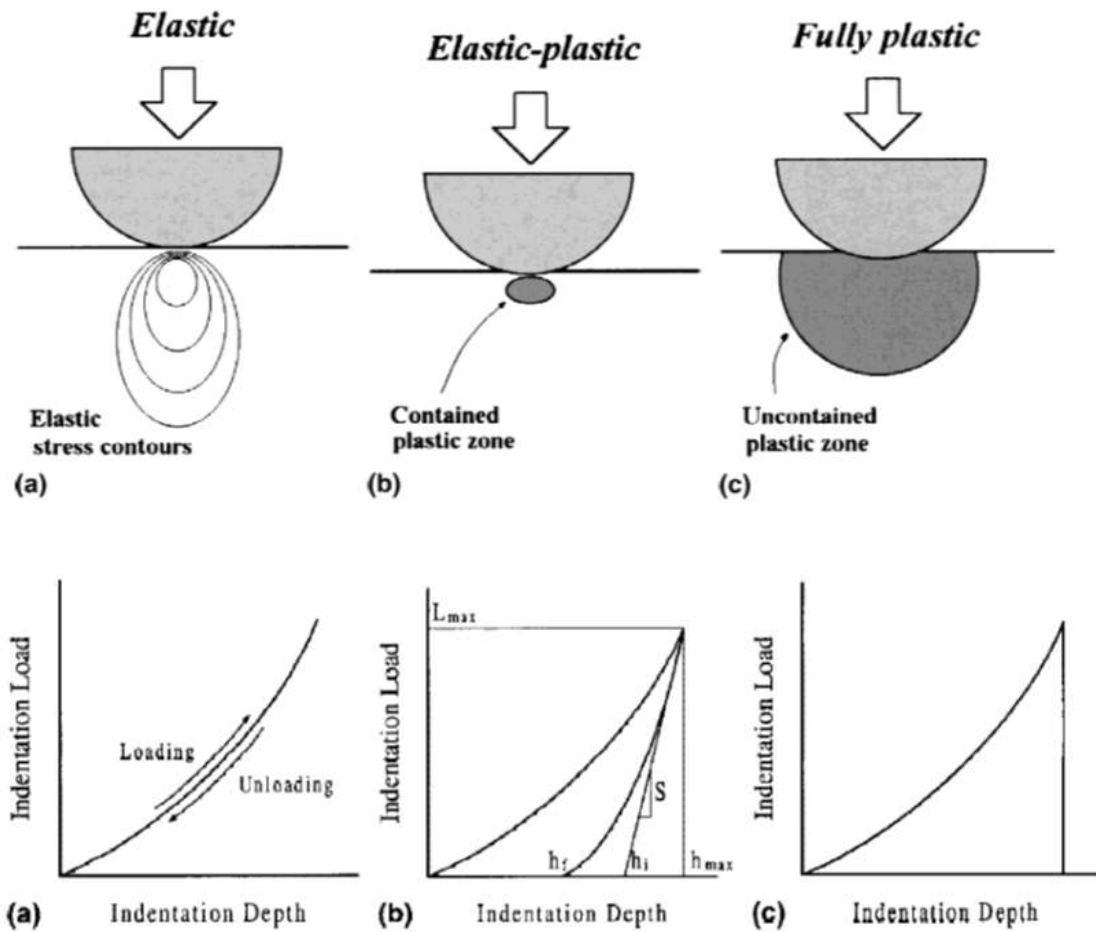


Figure 2.23: Schematic representation of plastic zone expansion during spherical indentation and indentation load-depth curves for a) elastic, b) plastic - elastic, c) fully plastic regimes [71].

In the elastic-plastic regime, due to considerable pileup or skin-in occurs during using of a spherical indenter, the actual elastic deflection depth, h_d , is difficult to measure. It is proposed [71] to use the indentation load-depth curve: h_d is calculated by analyzing the unloading curve, whose initial slope is the stiffness as shown in Figure 2.23(b).

By extrapolating this linear slope s to zero load, the intercept depth, h_i is determined [71, 72]. Value of elastic deflection depth, h_d is obtained, as shown in **Eq2.16**.

$$h_d = \omega (h_{\max} - h_i) \quad (2.16)$$

ω is a constant dependent on the indenter shape: for a flat punch indenter equals 1 and for a spherical indenter equals 0.75.

The pileup or sink-in behavior around indentation alters the real contact area. If pileup occurs, the real contact area will be larger than predicted, and will be smaller if sink-in occurs. It is well established that the effect of this pileup/sink-in is determined by the following dimensionless constant c for metals [71].

$$c = \left[\frac{a}{a^*} \right]^2 = \frac{5(2-n)}{2(n+4)} \quad (2.17)$$

a^* is the contact radius without considering the pileup or sink-in, and n is the work-hardening coefficient of material.

Using Figure 2.24, the value of a^* can be related to the indenter radius, R , and the plastic contact depth, h_c , which accounts for elastic recovery (**Eq2.15**) to formulate the following equation. [71].

$$a = \sqrt{c(2Rh_c - h_c^2)} \quad (2.18)$$

2.5.1.4 Average Indentation Stress and Strain

It is difficult for conventional hardness tests to find out quantitative information in terms of the mechanical properties to describe material deformation. The current indentation technique combined with numerical calculation is developed in order to quantitatively evaluate the mechanical properties. The local stress-strain behavior of a material can be obtained from load-depth curve, measured continuously during loading and unloading.

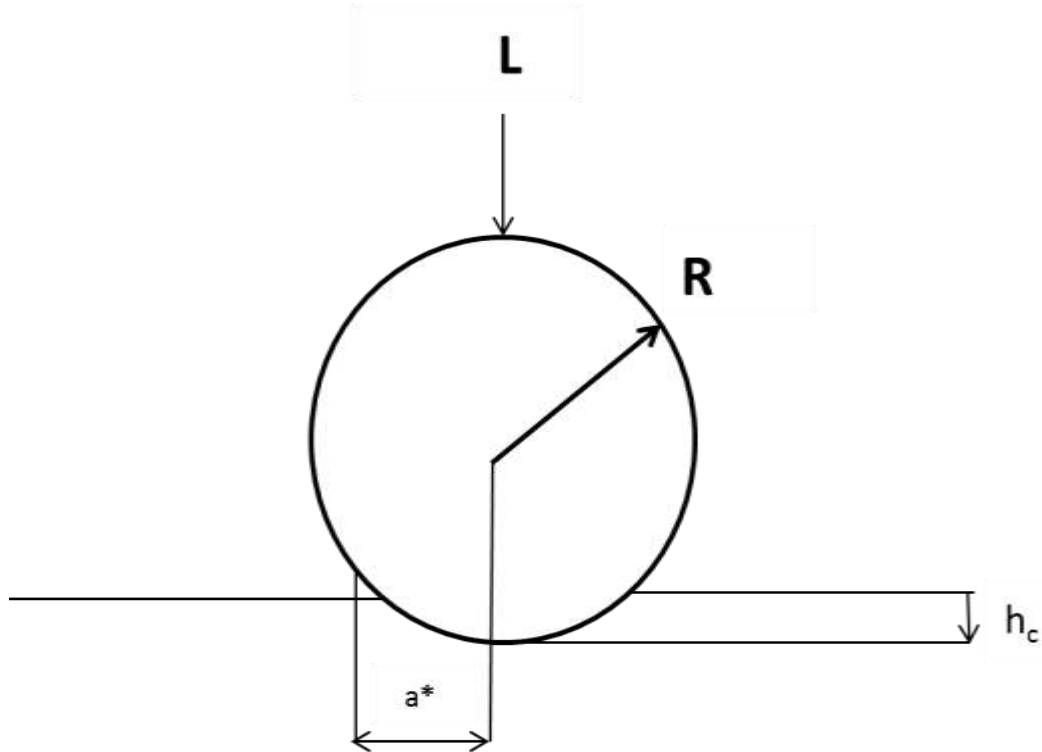


Figure 2.24: Calculating the contact radius without the consideration of the effect of pileup, a^* , at the given load, L .

As described in the previous sections, the radial compression of hemispherical shells around indentation constrained within an elastically deforming medium has been observed. With this in mind, it was presented the average plastic strain, ε_{avg} , in the hemispherical plastic zone around the indentation is function of the ratio of a/R .

During spherical indentation, the depth of the indentation is continuously increased, therefore, the ratio a/R changes. For the first time, Tabor correlated the average plastic strain, ε_{avg} , to the ratio a/R [68, 69]. He compared the hardness of many ductile materials and different value of a/R observed from spherical indentation testing, with the flow stress determined for the same materials, from uniaxial tensile testing to different levels of uniaxial strain. Finally, D. Tabor [69] proposed following equation:

$$\varepsilon_{avg} = 0.2 \frac{a}{R} \quad (2.19)$$

Tabor also used the following equation to determine the mean contact pressure, P_M , as:

$$P_M = \frac{L}{\pi a^2} \quad (2.20)$$

where L is the given indentation load and a is indentation contact radius.

The research efforts have been conducted to understand relationship between the mean contact pressure, P_M , during spherical indentation and the flow stress in uniaxial tension [69, 70]. The average flow stress, σ_{avg} , is correlated to the mean contact pressure, P_M , and a constraint factor, Ψ :

$$\sigma_{avg} = \frac{P_M}{\Psi} \quad (2.21)$$

Tabor found that Ψ equals three and therefore value of the mean contact pressure, P_M , is three times greater than flow stress was obtained from uniaxial tensile testing. The constraint factor, Ψ , depends on the plasticity of the deforming material and the shape of the indenter. It was also reported for a strain hardening material that the constraint factor is affected by work hardening properties. Johnson represented, Ψ as a function of plasticity parameter, ϕ , which depends on the yield stress, the modified young's modulus, E^* , and a/R [70].

$$\phi = \frac{a E^*}{R \sigma_y} \quad (2.22)$$

The modified young's modulus E^* is a function of the Poisson's ratio and young's modulus, given as:

$$E^* = \frac{E}{1-\nu^2} \quad (2.23)$$

2.5.2 Effect of Defects on the Mechanical Properties of Die Cast Ductile Metal

The presence of defects, such as shrinkage and gas porosity, can have a significant influence on the mechanical properties especially fracture behavior of material. The pores act as crack initiation sites causing premature failure. Several studies [73-78] have been conducted to understand the effect of porosity on the strength and ductility of an alloy. The size, distribution and area fraction of porosity strongly determines the elongation of magnesium [73-78]. The failure of die-cast magnesium and aluminum alloys can be

categorized based on the three different methods in terms of porosity measurement in the tensile samples [74, 75]. The first model is based on the correlation between the elongation measured in uniaxial tension and the bulk volumetric porosity in the tensile samples. A direct relationship is reported between the elongation and the ‘defect parameter’, which is defined as the ratio of bulk porosity to wall thickness for AM60 and AM50 magnesium alloys [79]. Gokhale et al. and C.D. Lee et al. [76] Observed that the variability in the elongation does not quantitatively correlate with the bulk volumetric porosity in the tensile samples of die cast AM60.

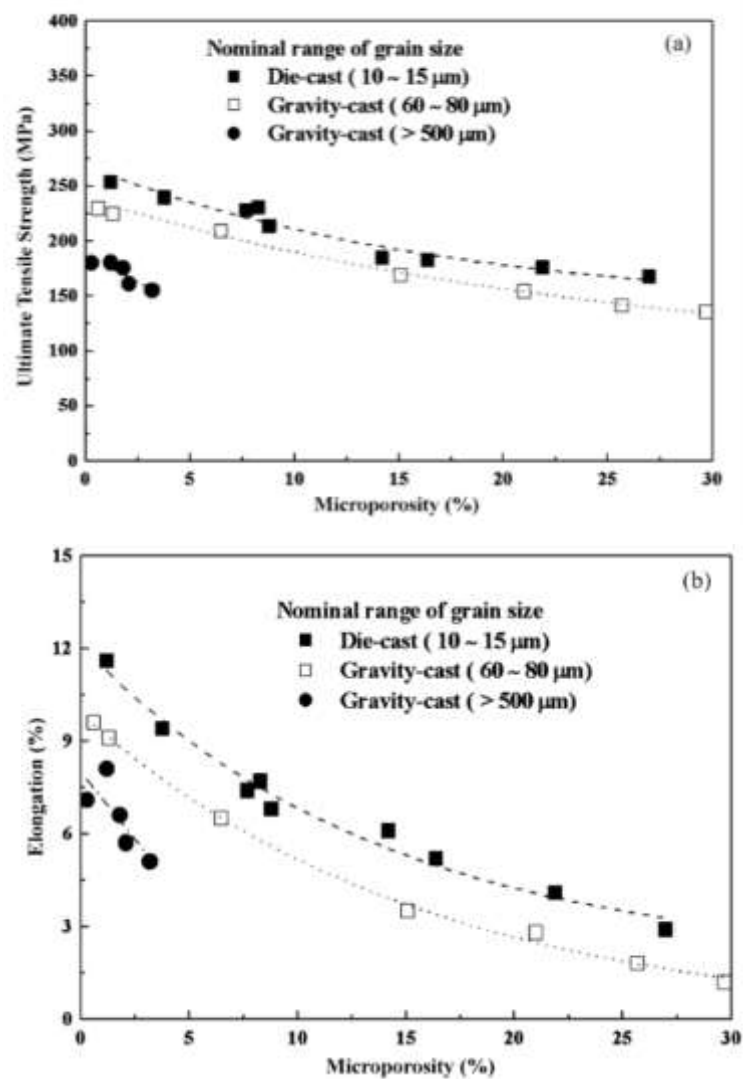


Figure 2.25: The influence of area fraction of porosity on the UTS (a) and elongation (b) for each nominal range of grain size [76].

The second model relates the measured area fraction of porosity of the post-test uniaxial tensile samples to the elongation. Gokhale et al. [79] clarified that variation in the elongation of magnesium alloy AM50 depends on the amount of porosity on the tensile fracture surface [78]. They measured the area fraction of porosity through quantitative fractography analyses using a scanning electron microscope (SEM). C.D. Lee et al. [76-78] studied the effect of fractography porosity on the tensile properties of the AM60 alloy and its dependence on the variation in grain size. In this investigation, the ultimate tensile strength (UTS) and elongation of as-cast AM60 alloy show a significant dependence on the variation of porosity with an inverse parabolic relationship. Figure 2.25 shows the dependency of the UTS (a) and the elongation (b) on the amount of porosity as observed by Lee. Figure 2.25 also indicates that their dependences on the porosity become sensitive to increase with increasing grain size.

The third model is related to the pre-existing porosity in the die cast magnesium and aluminum alloys. In this model, there is an assumption that the material which contains a microporosity is under local axial stress, F , (Figure 2.26). The load carrying capacity of a specimen is decreasing due to the presence of the pores within the sample. The stress distribution around the porosities is localized, and the magnitude of the stress is changing across the plane [74, 75].

The flow behavior of most metals can be quantified by the power law equation:

$$\sigma = K\varepsilon^n \quad (2.24)$$

where, σ and ε are the true stress and strain, K is a constant and n is the strain hardening exponent. By considering the force balance between the homogeneous plane A_h , and the plane containing pores, A_i , the relationship between ε_h as a function of ε_i can be obtained:

$$(\varepsilon_i)^n (1 - f) \exp(-\varepsilon_i) = (\varepsilon_h)^n \exp(-\varepsilon_h) \quad (2.25)$$

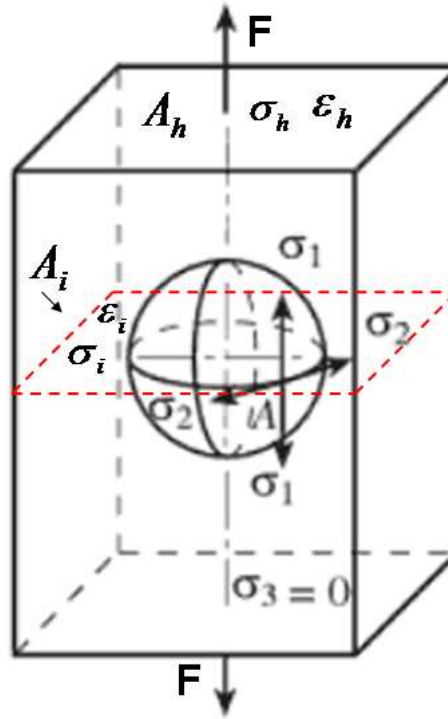


Figure 2.26: Material containing spherical void [45].

Eq2.25 is known as the constitutive model. According to the Considere's criterion and **Eq2.19**, the maximum stress of a sample free of imperfections is reached when the true strain at the instability point is equal to the strain hardening exponent. Therefore, the true tensile strength of the specimen (σ_f^*) can be determined by the power law equations at the instability point for both cross sections [81].

$$\sigma_f^* = K(\epsilon_h^*)^n \quad (2.26)$$

Above equation can be used to predict the tensile strength of the material from the values of n and f . This approach has been taken by different researchers to predict the elongation of the samples containing porosities [7, 76-78, 81]. Caceres et al. [81] verified systematically the area fraction effects on tensile properties, through a constitutive prediction with systematic experiments on aluminum alloys. They reported that the critical

strain in the region surrounding the void was 0.11. Their report confirmed that the elongation and ultimate tensile strength can be accurately characterized by the results of the critical strain model using the area fraction of defects.

Weiler et al [7, 9] show the elongation which can be predicted based on the observed porosity measurements from X-ray tomography before uniaxial tensile testing. C. D. Lee [76-78] reported that this model accurately predicts the tensile properties of magnesium alloys when the area fraction of porosity in the fracture surface is considered. Although, the conservative model can accurately predict the elongation as compared to other methods, there are some levels of uncertainty in this method. Noted that the model is only applicable for the pores located in the center of the specimen and the variation of stress concentration due to the proximity of the pore to the edge of the sample has not been taken into account. Weiler et al [74, 75] conducted an extensive research on the mechanical properties of the die cast magnesium alloys. They modified the constitutive model based on the location of pore and variation of stress concentration around pore.

The geometry of pores changes the distribution of the stress around the pores. The effect of the localized distribution of stress around the hole is defined by the stress concentration factor which is the ratio of the maximum stress to the nominal stress. The nominal stress can be defined with respect to the cross section far from the hole or it can be determined with respect to the cross section containing the hole. The stress concentration factor can be defined as the global stress concentration factor (K_{tg}) or net stress concentration factor (K_{tn}) which were derived by Wang et al for an infinite cylindrical geometry with radius b containing a spherical cavity with radius a . The stress concentration factor can be expressed by the following equations [82]:

$$K_{tg} = \frac{2.0714}{1 - 0.99563\left(\frac{a}{b}\right)^3 - 0.00437\left(\frac{a}{b}\right)^5} \quad (2.27)$$

$$K_m = \frac{2.0714}{1 - 0.99563\left(\frac{a}{b}\right)^3 - 0.00437\left(\frac{a}{b}\right)^5} \left[1 - \left(\frac{a}{b}\right)^2 \right] \quad (2.28)$$

Note that the stress concentration factors given in **Eqs2.27** and **2.28** are only applicable during elastic loading. Further, the plastic stress and strain concentration were characterized by secant modulus (S_{\max}) at the edge of the hole and secant modulus at the region far from the void (S_h) [83, 84]. The plastic strain concentration in the cross section containing the void (K_c) can be determined by the following expression [74]:

$$K_c = 1 + K_m^{elastic} - \frac{S_{\max}}{S_h} \quad (2.29)$$

where, $K_m^{elastic}$ is the elastic concentration factor in the cross section including defects. In order to determine the elastic concentration factor, above equation can be rewritten by considering the Considere's criterion and area fraction of the porosities [74].

$$K_c = 1 + 2.51.e^{-1.65f} - \frac{n^{n-1}}{(\varepsilon_h)^{n-1}} \quad (2.30)$$

Weiler et al. [75] demonstrated that the instability point occurred at the cross section containing imperfections. Due to the stress concentration around the void, the strain only reaches a fraction of the ideal magnitude at the net cross section, and the constitutive model can be modified to a new equation [75]:

$$n^n (1 - f) \exp(-n) = (K_c \cdot \varepsilon_h)^n \exp(K_c \cdot \varepsilon_h) \quad (2.31)$$

As the void is getting closer to the edge of the sample the elastic stress concentration factor is increasing rapidly. Therefore, the position of pore can affect the variation of elongation. Weiler et al. [75] proposed new method to predict elongation based on the position from

center. It has been considered the equivalent pore as the representative of the area fraction of porosities, and the distance of void from the edge of the sample is characterized by introduction of the ligament fraction (δ_L) [75].

$$\delta_L = \frac{d_t - r}{t} \quad (2.32)$$

where, d_t is the distance of the center of the equivalent pore to the edge of the sample, r is the radius of the equivalent pore and t is the thickness of the specimen. Finally, Weiler et al. found the relationship between the fracture strain and the area fraction of porosity using an appropriate finite element model, and the following equation is proposed to describe [75]:

$$\varepsilon_f = 0.016f^{-0.3} [0.18Ln(\delta_L) + 1.17] \quad (2.33)$$

Respectively the fracture stress can be predicted by the following expression [75]:

$$\sigma_f = 146f^{-0.1} [0.06Ln(\delta_L) + 1.05] \quad (2.34)$$

Chapter 3

3 PREDICTING THE FLOW STRESS OF AS-CAST MAGNESIUM ALLOYS

This chapter describes the characterization of three magnesium alloys, AM60, AZ91 and AE44, which were processed by high pressure die casting (HPDC) and gravity casting. Spherical microindentation was used to analyze the influence of microstructural features on the flow stress for both skin (finer grain sizes) and core (larger grain sizes and dendrites) regions of HPDC, as well as different regions of gravity step-cast plate for all three magnesium alloys. The dependence of flow stress of magnesium alloys on the grain size was investigated. The Hall-Petch slope and intercept stress were determined from indentation testing and then compared with the results obtained from uniaxial tensile testing and literature. The Hall-Petch equation was used for predicting the yield strength and the flow stress at several levels of plastic strains.

3.1 Experimental Procedure

This section describes the experimental techniques was used here. Spherical microindentation tests were performed on samples cut from gravity step-cast plate and high pressure die casting for three magnesium alloys. Indentation testing gives the local hardness of magnesium alloys that can be used to determine local yield strength. The metallographic analysis was then used to characterize microstructural features. The microstructural features were quantified using digital image analysis methods.

3.1.1 Alloys and Casting

The alloys examined in this work are AM60, AZ91 and AE44 which were processed by gravity step casting and HPDC. The nominal chemical compositions of those alloys are given in Table 3.1.

The step-shape plate castings were cast at CANMET – Materials Technology Laboratory in Ottawa, Canada, using a sand mold designed to promote directional solidification. A

simplified step-shape plate casting geometry was designed with 330 mm in length, 100 mm in width, and thicknesses of increasing steps, ranging from 4 mm to 40 mm from the feeding riser. These experiments were completed using a sand mold designed to produce a range of cooling rates and thermal gradients along the length of the casting. Temperature data was recorded during the casting process by thermocouples inserted in the mold. The thermocouples record the local temperature at intervals of 1.0 second. The melt temperature was maintained approximately at 730 °C and the casting was conducted at room temperature.

In order to study process-structure-mechanical property relationships, different criteria were considered to choose samples from different locations of step-cast plate. First, to choose a significant range of average grain size. Second to select a wide range of ultimate tensile strengths observed during uniaxial tensile testing. In a parallel study [85], the uniaxial tensile tests were performed on the samples which are extracted from different locations of step-cast plate. Third, to select the samples which were extracted from different locations via various local solidification rates. Based on these criteria, six samples were selected from three regions of the step- cast plates for three different magnesium alloys, as shown in Figure 3.1. The positions of each selected sample in the step-cast plates presents in the Table 3.2.

The HPDC plates were provided by Meridian Lightweight Technologies Inc and measured 165 mm in length, 100 mm in width, and 3mm in thickness as shown in Figure 3.2. The indentation testing was conducted on the skin region and core region for each die cast plate of different three magnesium alloys.

Table 3.1: Chemical composition (wt.%) of AZ91, AE44 and AM60 magnesium alloys.

Alloy	Mg	Al	Zn	Mn	Si	Cu	Fe	Ni	Be	Rare Earth
AZ91	90.3	8.7	0.77	0.23	0.006	0.002	0.002	0.002	0.001	-----
AE44	92.4	3.7	0.01	0.20	0.004	0.001	-----	0.001	0.001	3.8
AM60	93.6	6.1	-----	0.32	0.005	0.001	0.001	0.001	0.001	-----

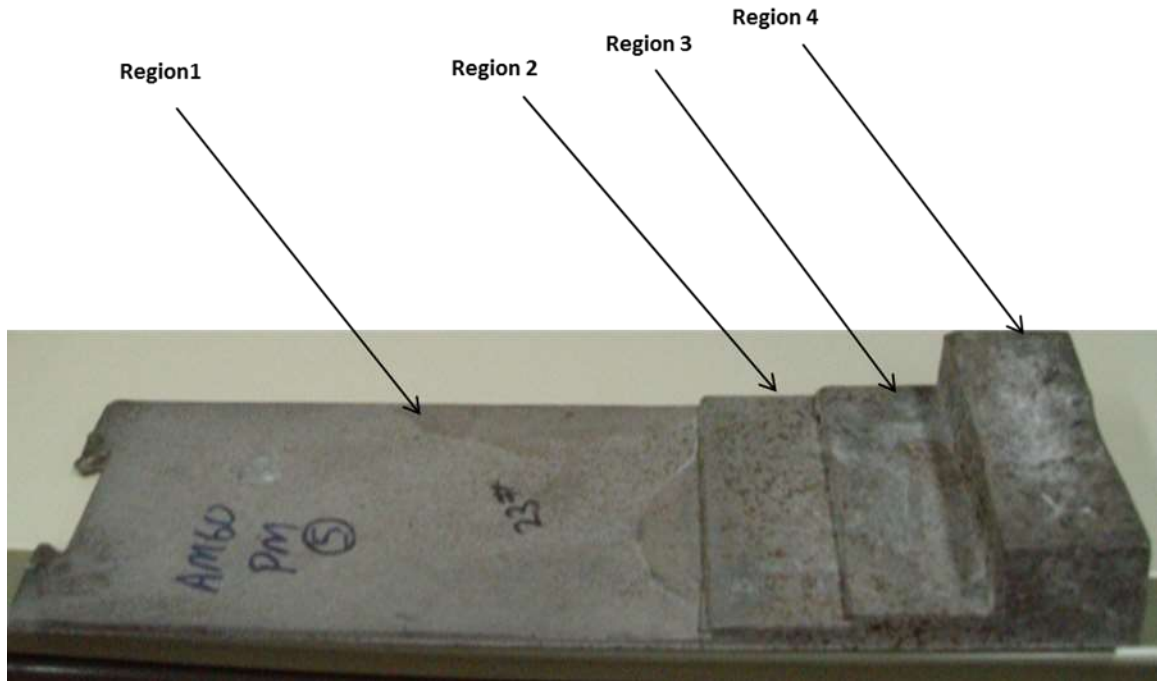


Figure 3.1: The different regions on step-cast plate.



Figure 3.2: High pressure die casting plate.

Table 3.2: The location of different selected samples s for magnesium alloys.

Alloy		AM60		AZ91		AE44	
Samples	Location (From left tip)	Area fraction β - phase (%)	Grain size (μm)	Area fraction β -phase (%)	Grain size (μm)	Area fraction β - phase (%)	Grain size (μm)
A	12mm(Reg1)	1.2	18.5	0.6	21.5	2.1	23
B	60mm(Reg1)	1.9	20	1.3	29.5	0.6	25
C	108mm(Reg1)	0.7	36	0.5	40	0.5	29
E	168mm(Reg1)	0.5	41	0.6	44	0.6	28
F	204mm(Reg1)	0.9	44	0.6	56	0.7	41
G	14mm(Reg3)	2.5	75	1	93.5	1.1	65
H	14mm(Reg4)	0.9	95	1.1	108.5	0.6	69
Skin		6.5	4.6	4.5	4.3	3.5	5.4
core		3.5	13.7	1.5	13.5	2	13

3.1.2 Microindentation Testing

In this work, spherical microindentation was employed to evaluate the local mechanical properties of magnesium alloys. A Micro materials (Wrexham, U.K.) NanoTest™ microindentation hardness tester (Figure 3.3) was used to perform indentation on the specimens. This instrument is computer controlled and load-unload indentation can be adjusted; therefore, it is capable of performing multiple load-unload indentation tests. The mechanism of NanoTest™ microindentation hardness tester for evaluating hardness is based on measuring the movement of stylus in contact with a surface. At the beginning, the maximum load is determined, and then the stylus starts to press into the surface with increasing from zero to maximum load. Once the pre-determined maximum is reached, it is reduced and the depth decreases due to elastic recovery of the deformed material. The indentation depth and load are monitored continuously during the movement of the stylus.

As described in Chapter 2, the indentation stress-strain curve can be plotted using the indentation depth and load.

At the heart of the NanoTest™ system is a pendulum to perform the indentation. A coil is mounted at the top of the pendulum (Figure 3.4). When an electric current passes through the coil which is attracted towards a permanent magnet and producing motion of the indenter towards into the samples. The displacement of the indenter is measured by means of a parallel plate capacitor. One plate of the capacitor is attached to the indenter holder. There is the capacitance bridge unit close to the measuring capacitor. When the indenter moves the capacitance changes and is measured by the capacitance bridge.

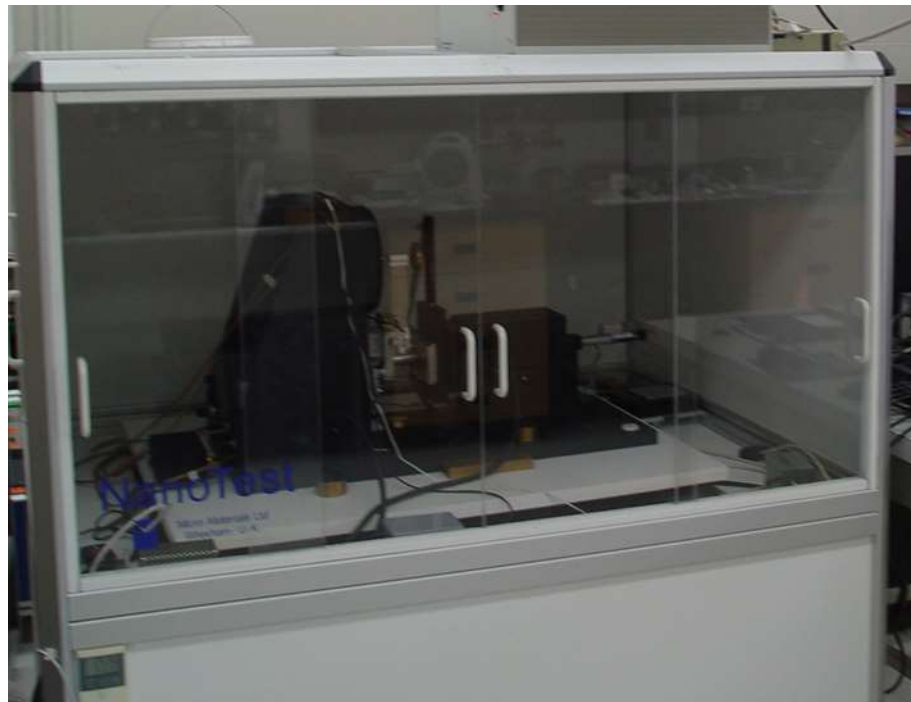


Figure 3.3: The Micro materials NanoTest™ microindentation hardness testing apparatus in which the spherical indentation was performed.

As shown in Figure 3.5, a high-carbon steel sphere of 0.795 mm radius was used as the indenter. Eight partial cycles were performed during each test. The maximum indentation load achieved during each test was 18000mN. The indentation was performed with a loading, and unloading rate of 200mN/s. Three indentations were made on each sample.

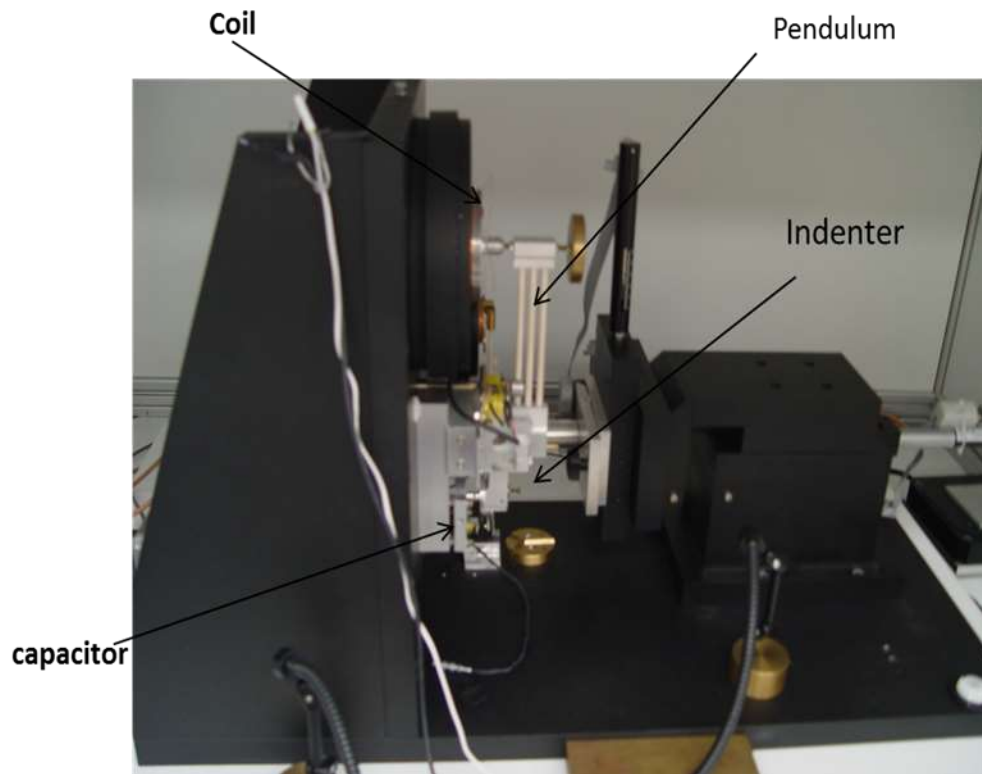


Figure 3.4: The NanoTest™ pendulum assembly showing the operation of the indenter.



Figure 3.5: The spherical indenter.

3.1.3 Metallography

Samples for microstructure analysis were prepared using conventional metallographic techniques, however magnesium and its alloys are the most difficult metallic specimens to prepare for microstructural examination. It should be considered following points:

1_ Magnesium and its alloys are typically soft and it may occur during cutting if pressures are excessive.

2_ Magnesium and its alloys are attacked by water. Therefore, polishing and cleaning operations should avoid or minimize the use of water.

3_ Microstructure of magnesium contains primary or α phase and secondary or precipitate phase. Primary or α phase is low in hardness and, on other hand, the precipitate phase is higher in hardness. This makes it difficult to eliminate scratches and lead to relief problem. Therefore, polishing times are kept suitable to avoid relief.

The 320-1200 grit SiC papers are used in grinding steps, and then the polishing procedure is performed in two steps. The specimens were polished by the automatic polisher. The solution mixture of water and 1 μm Al_2O_3 were used in the first step, and 0.05 μm was used in the second step. The applied force and the polishing speed can be controlled during use of the automatic polisher. The force was applied 15 N and a polishing speed of 20 rpm.

The grain structure was revealed by selectively etching in 1% Nital, 10% HF and Glycol for AM60, AZ91 and AE44 magnesium alloys, respectively. Table 3.3 shows etchants used and their composition. The specimens exposed to etchants solution from 3 to 5 seconds. Also, the 10% hydrofluoric acid is used to reveal the β -phase Magnesium alloys AM60 and AE44. The image analysis software-Clemex was employed to measure grain size and area fraction of β -Phase. The average grain sizes were determined by taking an average for five individual fields of measurement on each specimen, at a magnification of 200X. Each field of measurement in the grain size analysis sampled a range of 600-1200 and 200-500 grains for HPDC and step-cast, respectively.

Table 3.3: Etchants were applied for three different kinds of magnesium alloys.

Alloys	Etchant Used	Composition
AM60	1% Nital	Ethanol 99%, Nitric acid 1%
AZ91	10% HF	10 mL HF, 90 mL Water
AE44	Glycol	1 mL HNO ₃ , 24 mL Water, 75 mL Ethylene glycol

3.2 Experimental Results

The following section presents the results of this chapter. The results of experimental procedure were divided into two sections: Microstructural features and Indentation results.

3.2.1 Microstructural Result

Figure 3.6 shows the typical optical microstructure of AE44 magnesium alloys observed for several locations of step-cast plate. The base microstructure of as-cast magnesium-aluminum alloy is comprised of primary α -Mg grains or dendrites surrounded by intermetallic phase. The eutectic phase, between primary magnesium α -Mg and intermetallic phase, is formed from the last-to-solidify liquid. There are intermetallic phase and divorce eutectic at grain boundaries as a massive compound. As shown in Figure 3.6, in the case of step-casting, the grain morphology is shown to change from region 1 to region 4, as the cooling rate decreases. On moving away from the cooling end, the grains coarsen and elongate, giving a rise to dendritic structures. This is consistent with the theory [15] of increase in the rate of grain coarsening with the reduction in cooling rate, due to lack of nucleation and consequently increased growth of the existing grains as shown in Table 3.2.

In HPDC, as can be seen in Figure 3.7 (a), the skin region contains refined grains, while in the core region (Figure 3.7 (b)), significantly larger grains, externally solidified crystals and porosity are observed. The grain size has a significant variation in the core region, while it is relatively uniform in the skin region. As a result, the average grain size varies

gradually from skin region to core region. It has been reported [9, 44,45] that the transition region from skin to core can be determined by a grain size threshold value of 10 to 11 μm .

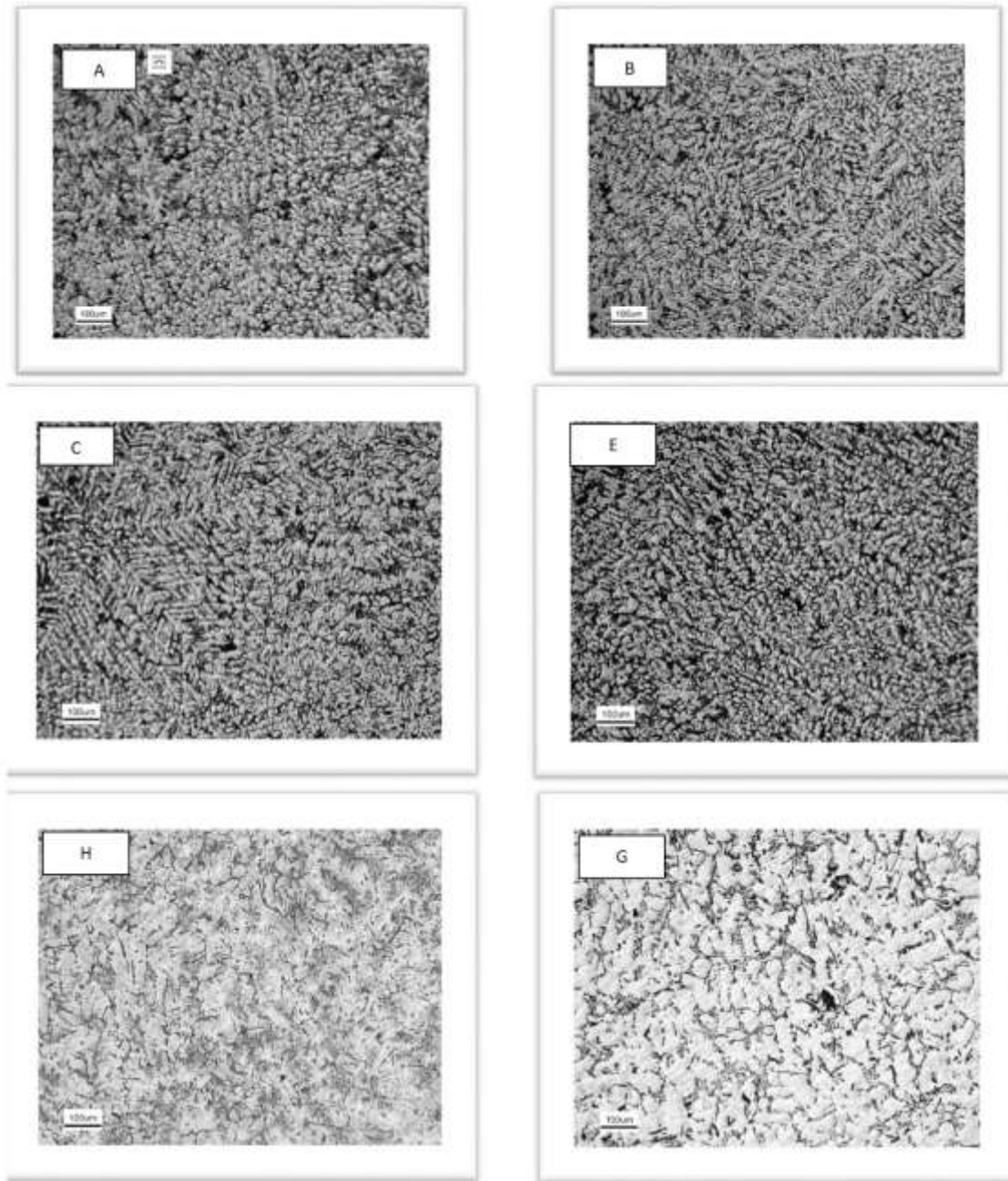


Figure 3.6: Typical microstructures of AE44 alloy for different locations of the step-cast plate.

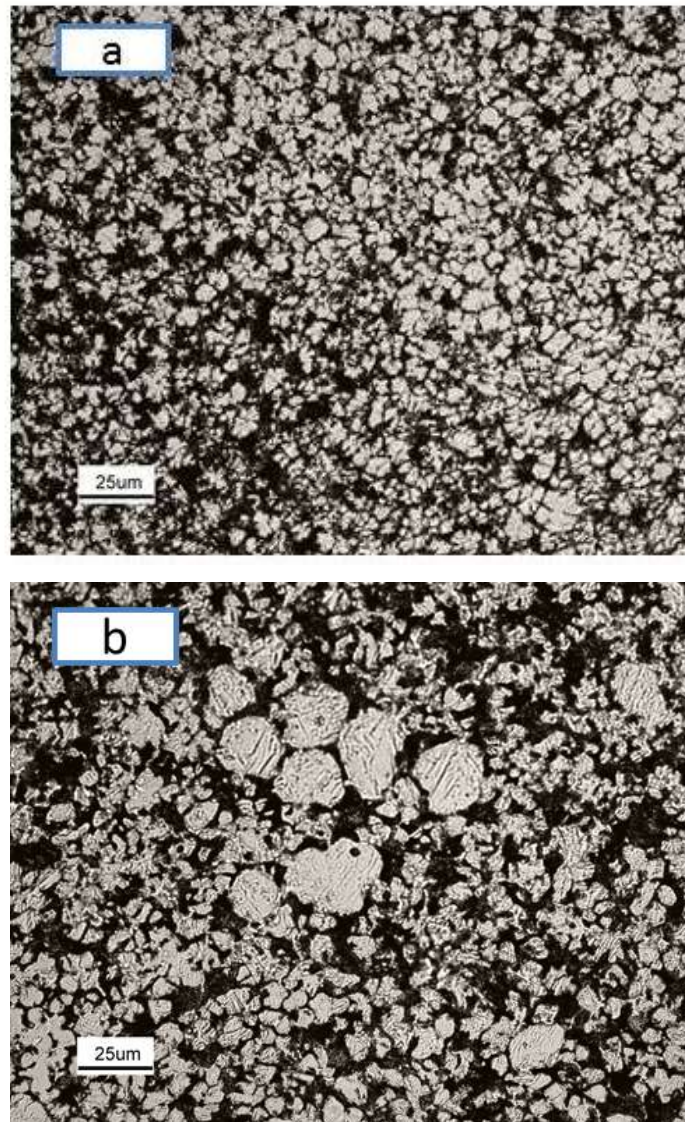


Figure 3.7: Typical microstructures of HPDC a) skin b) core for AE44. In the skin region, the area fraction of β phase is approximately 3.5% and core region contains less than 2%.

3.2.2 Indentation Results

The spherical microindentation technique was used to measure local flow stress for each specimen. Each sample chosen for spherical indentation testing was first cut from post-tensile test coupons. Figure 3.8 shows residual indentations that are left on the surface of magnesium alloy AE44 after indentation process. Figure 3.9 shows the load-depth curves of indentation tests performed on the skin and core region of HPDC and sample A cut from step-cast of magnesium alloy AE44. The skin region is shown to have comparatively higher indentation hardness than the HPDC core region and sample of step-casting. Similar results are observed for the other two magnesium alloys examined in this study.

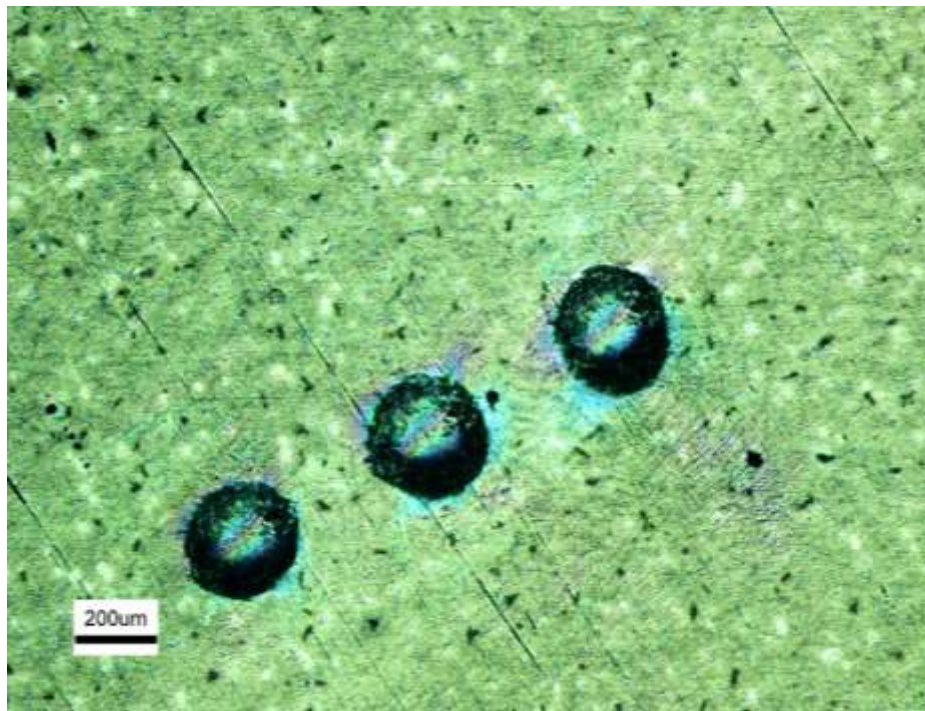


Figure 3.8: Three indentations on the surface of location.

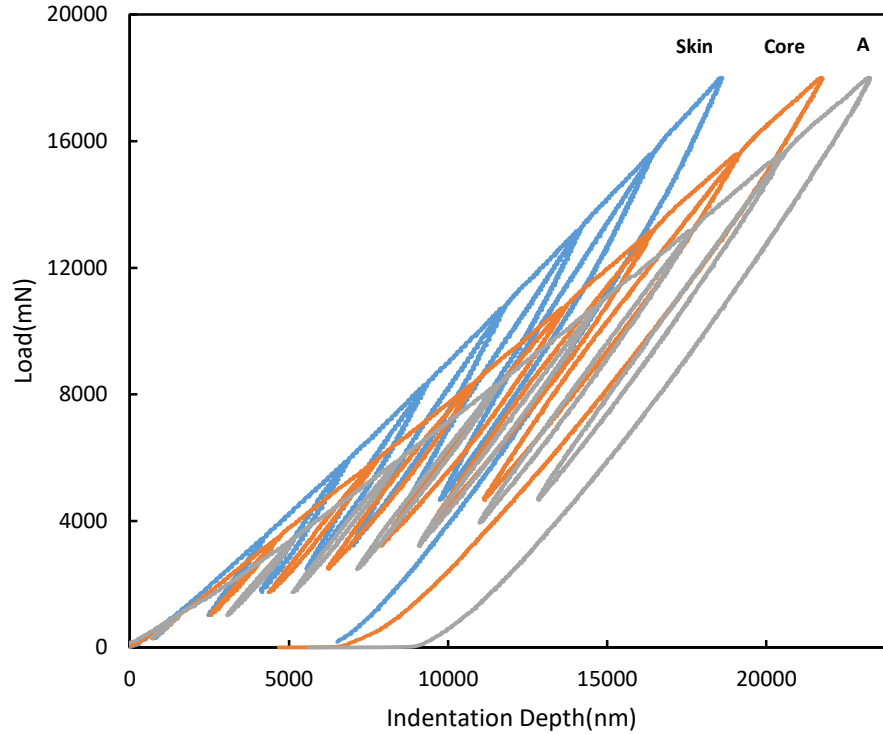


Figure 3.9: The typical indentation load-depth curves for HPDC skin region, core region and step-cast sample A for AE44.

As discussed in Chapter 2, the average indentation stress was obtained from indentation depth and load curve. The average indentation stress, σ_{avg} , is correlated to the mean contact pressure underneath the spherical indenter, P_M , which is the ratio between the indentation load, and the projected indentation area. ψ is the constraint factor which depends upon the work hardening properties of the material and the shape of the indentation [69].

$$\sigma_{avg} = \frac{P_M}{\psi} \quad (3.1)$$

It is proposed that the effects of work-hardening can be accounted for using a plasticity factor, ϕ which is determined by the mode of material response depended upon yield stress, σ_y , modified Young's modulus, $E^*(E^* = E/(1-\nu^2))$, ν is Poisson's ratio), and the ratio of the contact radius to the radius of spherical indenter (a/R).

$$\Phi = \frac{a E^*}{R \sigma_y} \quad (3.2)$$

There are three typical regimes of material deformation during spherical indentation: elastic deformation, elastic-plastic deformation and fully plastic deformation. Figure 3.10 shows correlation between constraint factor and plasticity parameter. The following equation presents the relationship between the constraint factor and plasticity parameter for the three regimes mentioned during spherical indentation testing [70, 71].

$\Psi=1.3$	$\phi < 2$	Elastic	
$\Psi=1.3+0.0037\phi$	$2 < \phi < 100$	Elastic-plastic	(3.3)
$\Psi=1.65$	$\phi > 100$	Plastic	

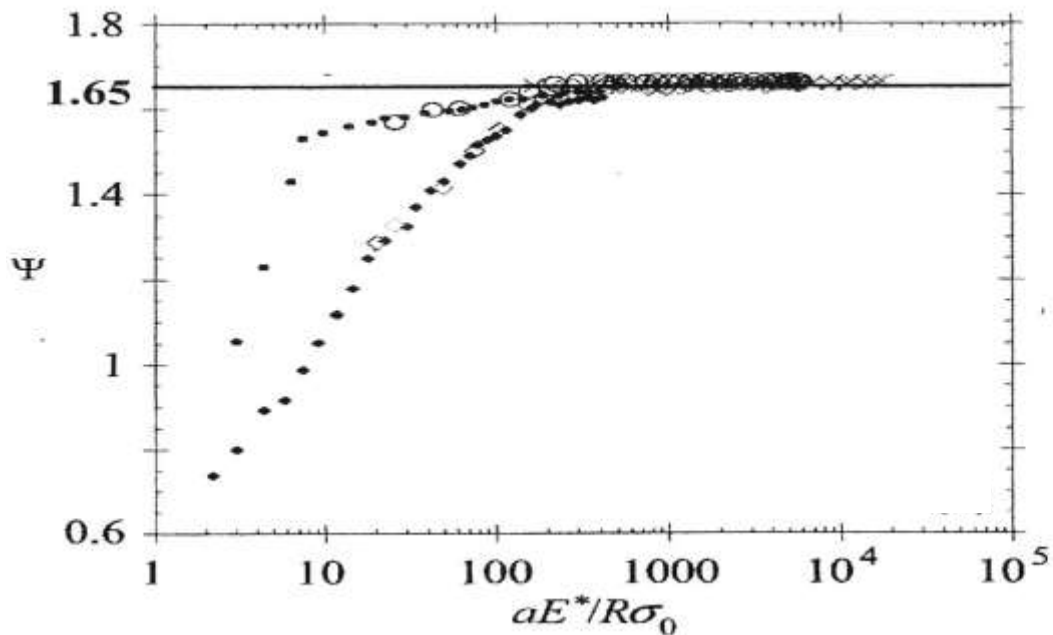


Figure 3.10: The constraint factor Ψ , as function of ϕ in the plastic regime in elastic-plastic regime [70].

In the present study, the plasticity parameter, ϕ , was found to be within the elastic-plastic transition zone (Figure 3.11) for three different magnesium alloys. These results can be used to acquire the constraint factor for the calculation of indentation stress.

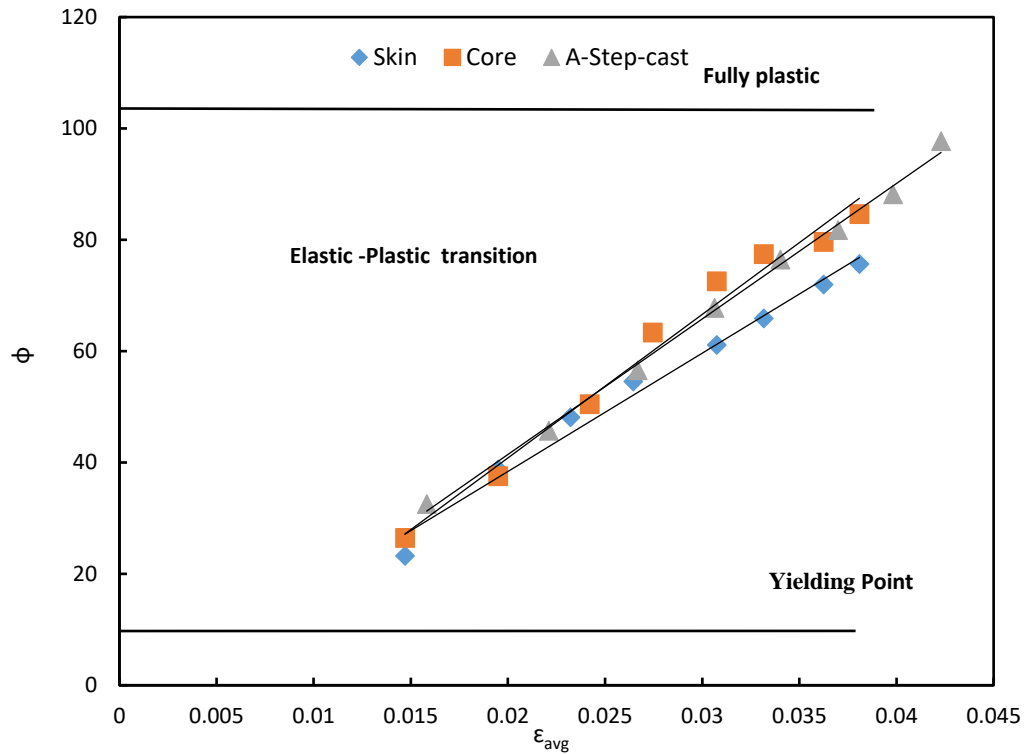


Figure 3.11: The plasticity parameter, Φ , with respect to average plastic strain for AE44. All tests preform in this study were in elastic-plastic zone.

The average indentation stress, σ_{avg} , was obtained from the indentation load-depth curve (Figure 3.9) using Eq3.1 through Eq3.3. The indentation stress-strain curves in Figure 3.12 shows that there is a distinct difference, both in the magnitude of indentation stresses and the strain-hardening trend, between samples of the HPDC skin region and samples of step-cast for all magnesium alloys.

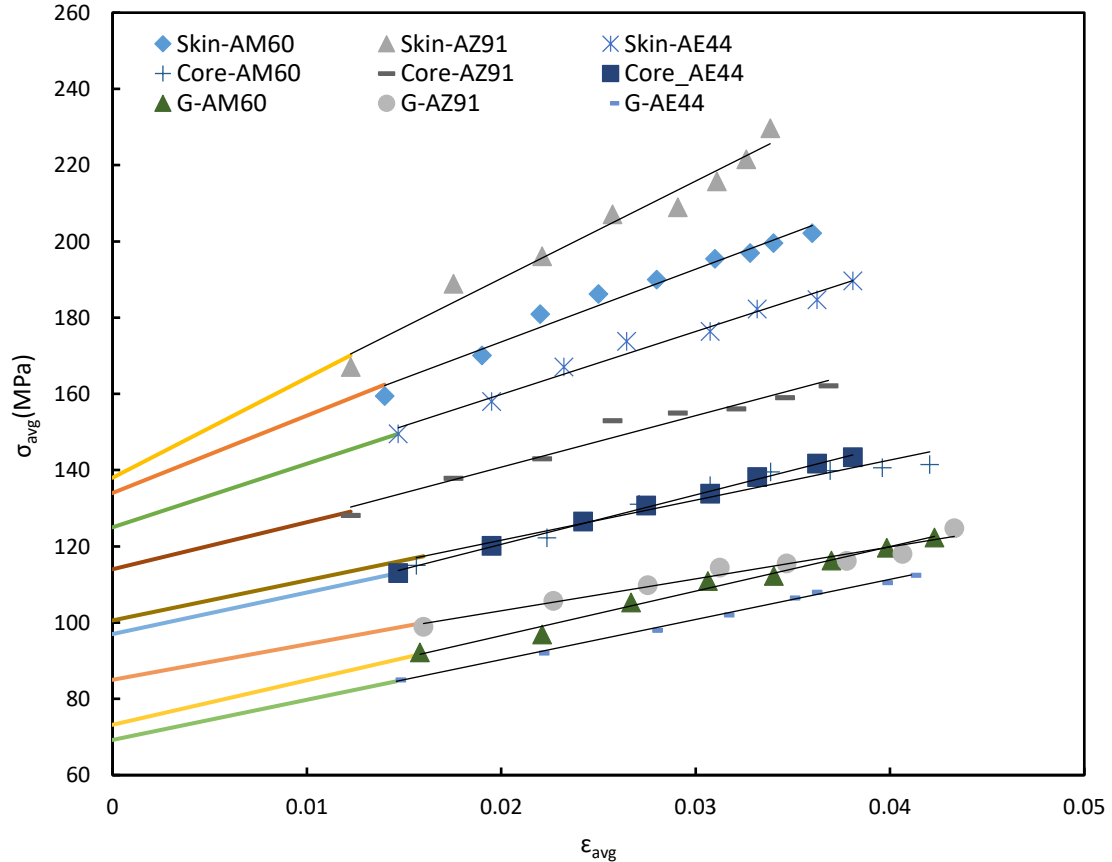


Figure 3.12: The average indentation stress, σ_{avg} , with respect to average plastic strain, ϵ_{avg} , for the samples indented in the HPDC skin region, core region and sample G from gravity step-cast. Constitutive linear extrapolations are shown to obtain the indentation yield strength.

The indentation yield point, σ_y , at a plastic strain of zero, can be approximated by linear extrapolation of the σ_{avg} , versus ϵ_{avg} , plot as shown in Figure 3.12. The average indentation stress curves were linearly extrapolated to $\epsilon_{avg}=0$ (zero plastic strain), representing an initial yield stress. The indentation yield stress and tensile yield stress for each examined sample are presented in Figure 3.13 through 3.15 showing the dependency of yield stress upon grain size. It should be noted the tensile yield stress was taken from reference [85].

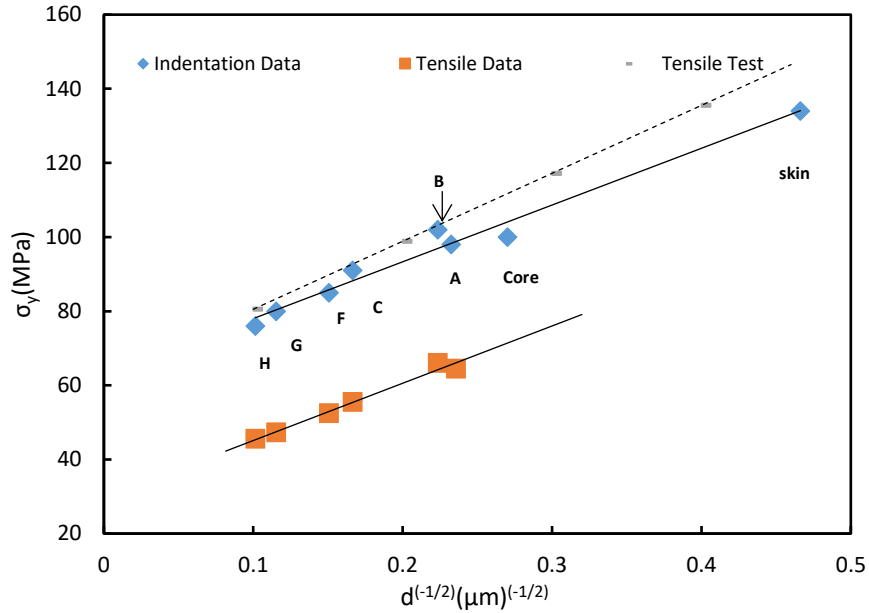


Figure 3.13: The yield strength, σ_y , with respect to average grain size, $d^{-1/2}$, for the samples indented in the skin region, core region and step-cast sample G from step-cast for AM60. The indentation result of the skin and core regions for HPDC AM60 have been presented in Reference [85].

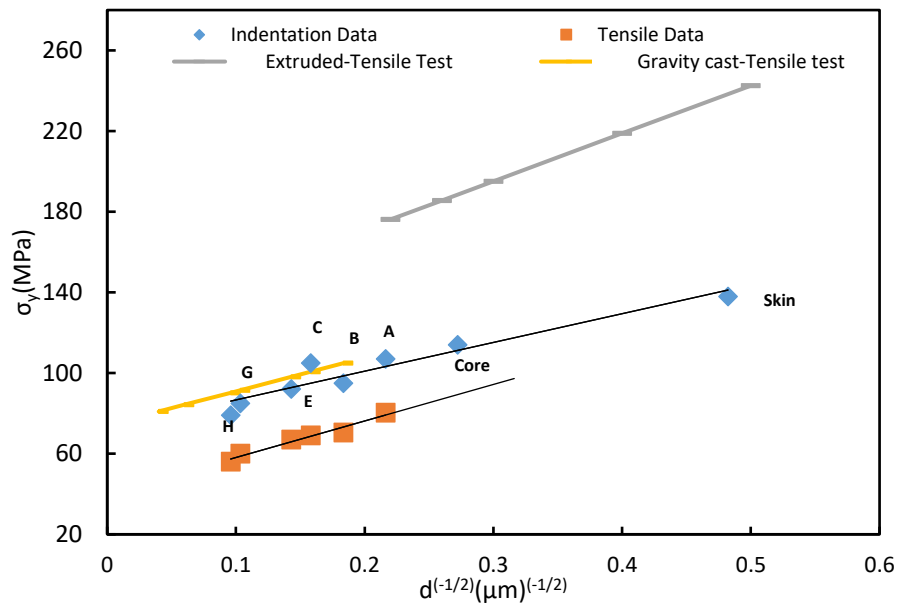


Figure 3.14: The yield strength, σ_y , with respect to average grain size, $d^{-1/2}$, for the samples indented in the skin region, core region and step-cast sample G from step-cast for AZ91.

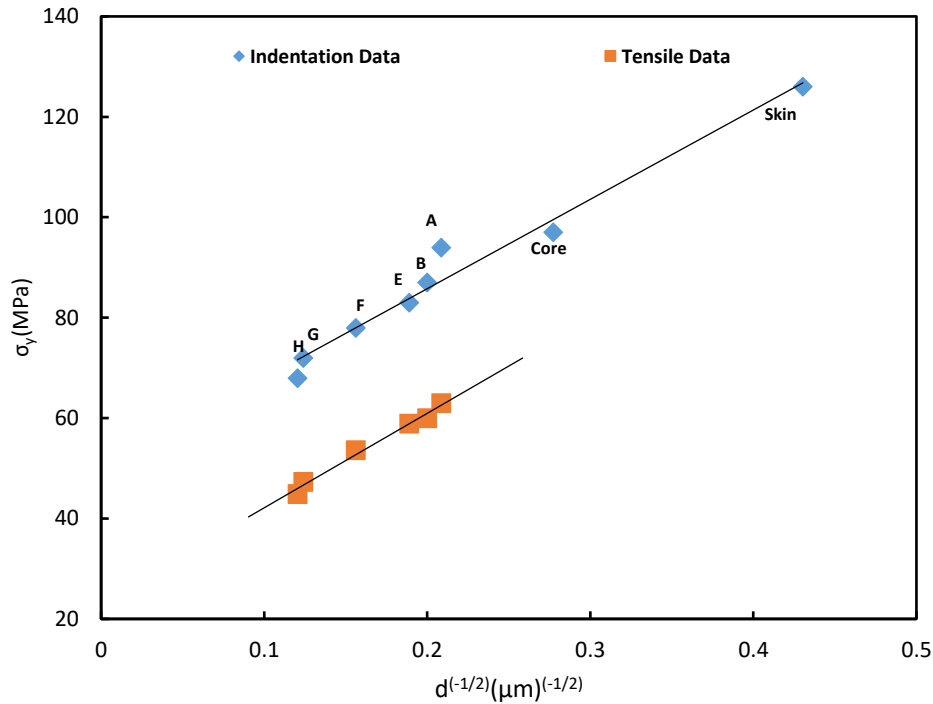


Figure 3.15: The yield strength, σ_y , with respect to average grain size, $d^{-1/2}$, for the samples indented in the skin region, core region and step-cast sample G from step-cast for AE44.

3.3 Discussion

3.3.1 Microstructure-dependent local mechanical properties

There is an obvious difference in indentation response between samples of HPDC (skin and core regions) and step-casting for three types of magnesium alloys as shown in Figure 3.9 and Figure 3.12. This result can be explained by the variation in microstructural features of these samples, such as grain size, intermetallic phase and porosity. The average measured grain size in the skin and core regions varies from 5 to 17 μm while that of step-cast samples is in the range of 19 to 108 μm (Table 3.2). This is one of the reasons that result in the decrease of local mechanical properties in the samples of step-cast as compared to those of HPDC. It is also noted that the local yield strength values show an increase with the decrease in grain size, for all three step-cast magnesium alloys. This observation

indicates the local yield strength of magnesium alloys have a strong dependency on grain size distributions which are closely related to the cooling rate.

Similar effect can be noticed in HPDC samples. The indentation stress-strain curves in Figure 3.12 indicate that there is a significant variation, in the magnitude of indentation yield strength from samples of the skin region to that of the core region. This can be attributed to the variation in the microstructure between the regions. The microstructural difference in the skin and core region can lead to notable changes in local mechanical properties. As illustrated in Figure 3.7, it is clear that the microstructure of the core region is much coarser than that of the skin region. Solidification during the die-casting process occurs on the die walls as soon as molten metal reaches the relatively cold mold walls and this leads to the formation of fine microstructure in the skin region. High cooling rates result in high nucleation rate in the melt, and as a result, refined microstructures are formed. With finer microstructure, the skin region shows higher flow stress as compared with the core region.

Concerning the influence of microstructure on yield strength, the effect of the intermetallic phase should also be taken into account. Similar to the influence of grain size, the increase in intermetallic phase results in an increase of yield strength. It has been reported that the β -phase contributes to higher yield strength when the aluminum content is over 10wt% [12]. In the case of HPDC, typically, there is a higher aluminum content in the skin region as compared to the core region. The formation of pre-solidified α -grains (externally solidified grains), as dendrites in the core region, contains very low aluminum concentrations during the die-casting process. The remaining liquid, higher in aluminum content, solidifies mainly in the skin region. This leads to the increased intermetallic phase concentrations in the skin region, because the volume fraction of intermetallic phase increases with increasing Al content. Figure 3.16 shows the intermetallic phase in the skin region and core region for AM60. In this investigation, it was found that by using image analysis from optical micrographs, the skin region contained a higher concentration of intermetallic phase (β -phase $Mg_{17}Al_{12}$ in AM60 and AZ91 and $Al_{11}Re_3$ in AE44) than the core region as shown in Table 3.2. An increased presence of intermetallic phase in the skin region is in accordance with literature [12, 13, 27].

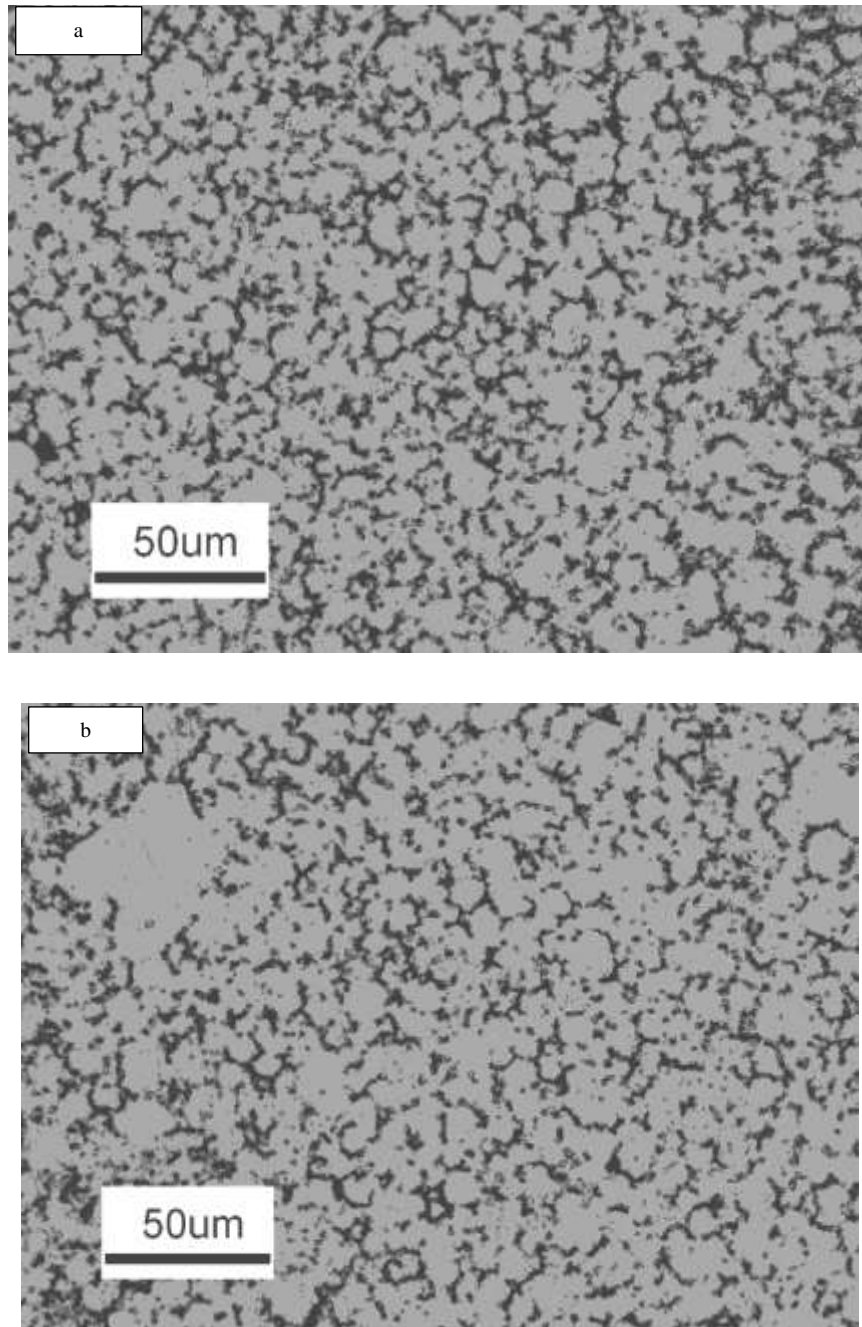


Figure 3.16: The intermetallic phase in the HPDC; a) skin region and b) core region.

In an AM50 magnesium die-casting alloy, Mg grains observed in the core region contains aluminum concentrations as low as 2 wt%, while α -Mg grains in the skin region possesses relatively higher aluminum [12]. The increased presence of the β -phase in the skin region implies higher hardness and yield strength. Therefore the difference in the indentation results, as shown in Figure 3.9 and Figure 3.12, can be attributed to the higher concentration

of the intermetallic phases in the skin region and significant variation in the grain size of the samples. Since those microstructural features are affected by cooling rate, this finding discloses the influence of solidification parameters on local mechanical properties.

3.3.2 Prediction of local mechanical properties using Hall-Petch relationship

Figure 3.13 through Figure 3.15 exhibit the dependence of indentation yield strength on the variation of grain size for three different magnesium alloys according to the Hall-Petch equation. Eight samples have been chosen from the HPDC skin region, core region and step-casting. The different types of casting processes lead to a variation in grain size distribution which influences the local yield strength represented by a single Hall-Petch equation. This finding suggests, in magnesium alloys, that the Hall-Petch equation works for a wide range of grain sizes regardless of the type of casting used.

The comparison shown in Table 3.4, demonstrates the magnitude of intercept stress, σ_0 , via microindentation testing is higher than that obtained from tensile testing for the three sand-cast magnesium alloys while the Hall-Petch slope, k , obtained from microindentation testing are in good agreement with the tensile testing results. With this testing technique, the spherical indenter samples approximately 20-50 grains in the indented region. The literature [86] generally agrees that the Hall-Petch slope k , indicates the strength share due to the resistance to dislocation motion caused by the grain boundaries while the intercept stress parameter comprises the contributions of solutes and particles to the increase of strength. The variation in intercept stress determined by tensile and microindentation testing and suspect that the explanation may be related to surface imperfections in the sand-castings that lead to the premature onset of plasticity.

Table 3.4: The Hall-Petch slop values are determined from microindentation testing and uniaxial tensile testing.

Alloys	Microindentation Testing		Uniaxial Tensile Testing	
	Friction stress σ_0 (MPa)	Hall-Petch slope K (MPa $\sqrt{\mu m}$)	Friction stress σ_0 (MPa)	Hall-Petch slope K (MPa $\sqrt{\mu m}$)
AM60	61.2	152.9	39.5	153.3
AZ91	73	142.2	48.2	134
AE44	50.1	178	21	175

Figure 3.13 through Figure 3.15 also represent previously published results of similar alloys as AM60 and AZ91. In more detail, the Hall-Petch parameters effects were investigated, intercept stress, σ_0 , and the Hall-Petch slope, k , with the use of microindentation and compared them with literature. Both Hall-Petch parameters of AM60 are comparable to the results reported by Lee [77], as shown in Figure 3.13. The Hall-Petch slope, k , is 152.9 MPa- $\sqrt{\mu m}$ and the intercept stress, σ_0 , is 62.1MPa which are close to the published data of as-cast AM60 magnesium alloy ($k= 183.3$ MPa- $\sqrt{\mu m}$ and $\sigma_0= 62.2$ MPa).

In AZ91 alloy, both Hall-Petch parameters ($k= 142.2$ MPa- $\sqrt{\mu m}$ and $\sigma_0= 73$ MPa), determined from indentation, correlate well with the observed tensile results [87] of conventional as-cast AZ91 alloy ($k= 167.2$ MPa- $\sqrt{\mu m}$ and $\sigma_0= 74.2$ MPa) as shown in Figure 3.14. The results found in this experiment indicate that the Hall-Petch parameters deviate considerably from extruded AZ91 alloy ($k= 237$ MPa- $\sqrt{\mu m}$, and $\sigma_0= 124$ MPa). There are several possible explanations for this variation. First, the range of grain size has not always been very wide, that is why the effect of grain refinement on mechanical properties is not clear. Second, the observed results of extruded material [88] might have been affected by the preferred orientation created by the equal channel angular extrusion process [88, 89].

A relationship between flow stress and grain size is also proposed in the literature [53] :

$$\sigma(\varepsilon) = \sigma_0(\varepsilon) + k(\varepsilon) d^{-1/2} \quad (3.4)$$

where, $\sigma(\varepsilon)$ is the flow stress at a given strain, k is the Hall-Petch slope, and d is the average grain size, and σ_0 is the intercept stress. Two main models [86, 88] have been proposed to justify the Hall-Petch equation, the dislocation pile-up model and the work hardening (dislocation density) model. According to the pile-up dislocation model, the Hall-Petch slope is theoretically constant, whereas the work hardening model predicts dependence of the Hall-Petch slope, $k(\varepsilon)$, on plastic strain. It is implied that grain size has a strong contribution to increasing work hardening due to the additional limitation on dislocation motion caused by grain boundaries. The work hardening model was developed by Ashby [90] and considers that this dislocation density is necessary to accommodate the strain incompatibility in small grains with different crystallographic orientation. The modified model also predicts the strain-dependence of the Hall-Petch slope $k(\varepsilon)$. In previous experiments [60], the Hall-Petch slope, decreases with increasing plastic strain which is not consistent with the expectation of the work hardening model.

The correlation between the flow stress and the grain size has been investigated for a number of metals and alloys and good agreement with **Eq3.4** has been found. Figure 3.17 through Figure 3.19 show the average stress, σ_{avg} , plotted as a function of average grain size, directly derived from the indentation stress-strain curves, for different levels of plastic strains during microindentation testing for all three magnesium alloys. There exists a linear relationship between the average grain size and the average indentation stress for different levels of plastic strains. It is suggested that the Hall-Petch relationship applies at different levels of plastic strains. This finding confirms that the dependency of indentation flow stress upon local grain size is in accordance with **Eq3.4**.

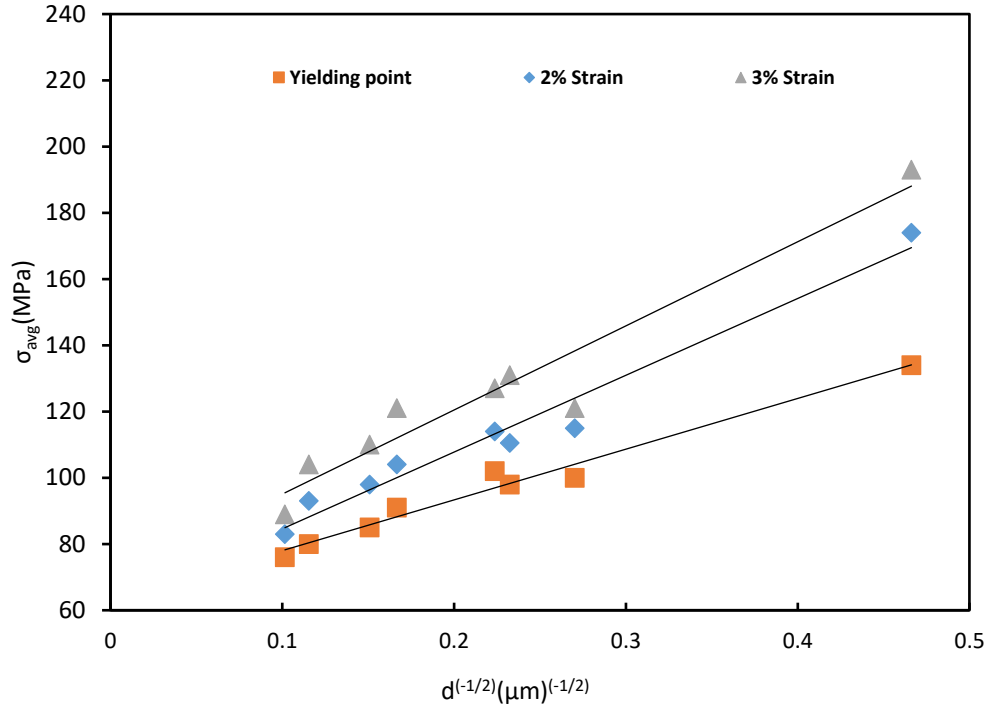


Figure 3.17: The average indentation stress, σ_{avg} , with respect to average grain size, $d^{-1/2}$ for different levels of plastic strain for AM60.

The $k(\epsilon)$, derived from the Hall-Petch equation (Figure 3.17 through Figure 3.19) for different levels of plastic strains, is shown in Figure 3.20 as a function of $\epsilon^{1/2}$ for the plastic strain range studied in this investigation. The Hall-Petch slope shows a linear dependency on the plastic strain. This observation is consistent with the theory of the work hardening model, which establishes that $k(\epsilon)$ increases with plastic strain. However, it has been reported [91] that the $k(\epsilon)$ decreased with increasing strain at high plastic strain range for AZ31 and A5754 magnesium-aluminum alloys. The present study does not focus on high plastic strain.

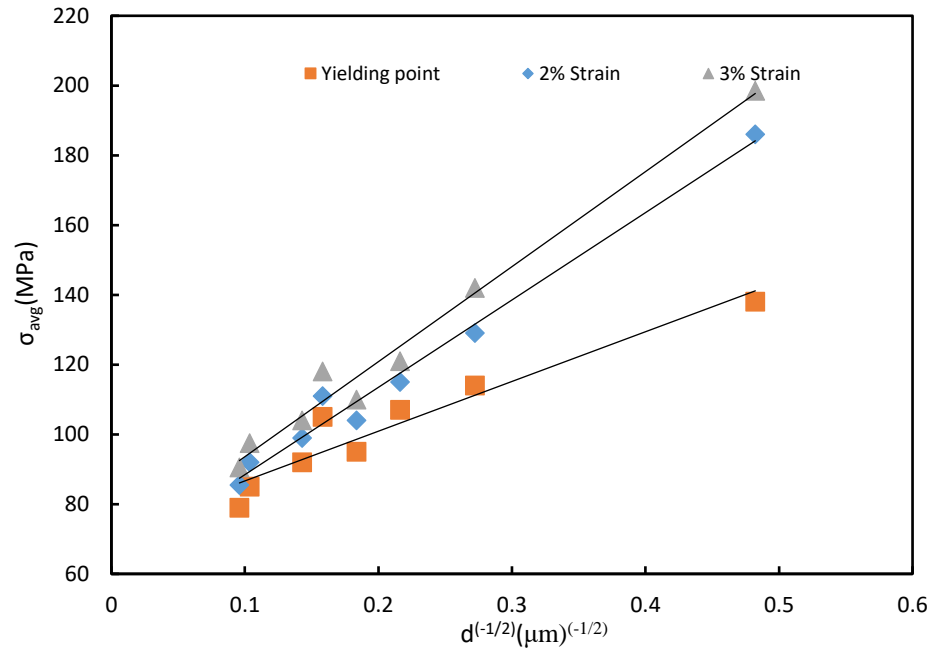


Figure 3.18: The average indentation stress, σ_{avg} , with respect to average grain size, $d^{-1/2}$ for different levels of plastic strain for AZ91.

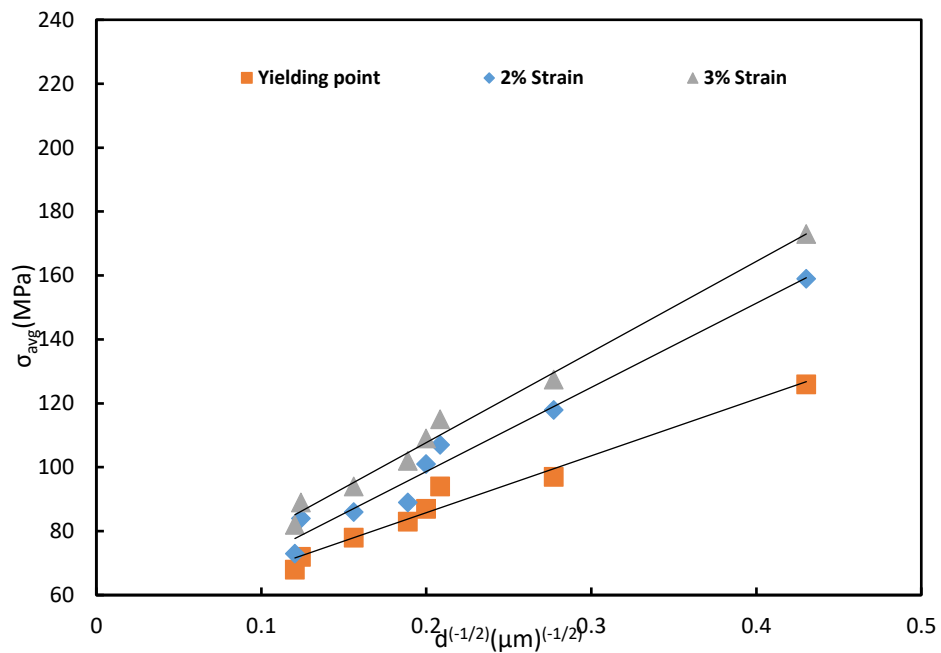


Figure 3.19: The average indentation stress, σ_{avg} , with respect to average grain size, $d^{-1/2}$ for different levels of plastic strain for AE44.

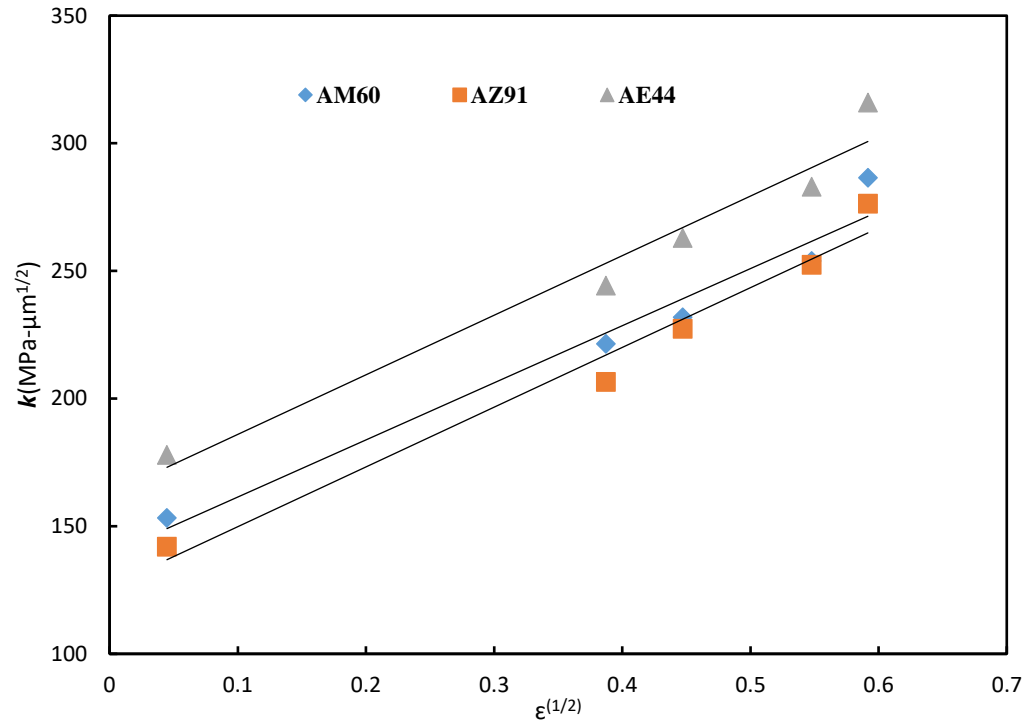


Figure 3.20: Hall-Petch slope as a function of $\epsilon^{1/2}$, encountered during indentation testing of wear process.

Chapter 4

4 PREDICTION OF THE EFFECTS OF COOLING RATES ON THE MICROSTRUCTURE AND STRENGTH OF HPDC AM60

As discussed in Chapter 2, there are two well-differentiated regions in the microstructure of HPDC: the skin region and the core (interior) region. The skin region is characterized by a fine grained microstructure and higher integrity whereas the core region contains a coarser grained microstructure, a higher percentage of defects and externally solidified grains (ESGs). In the case of HPDC, yield strength strongly depends on the grain size and the skin thickness. The distinction between the skin and core regions in the mechanical and microstructural properties is attributed to the variation of cooling rate from the wall mold to the center. The cooling rate is controlled by interfacial heat transfer coefficient between die and metal during solidification. The objective of this chapter is to predict grain size, skin thickness and the heat transfer coefficient at the metal–die interface during the high pressure die casting (HPDC) process the magnesium alloy AM60.

Multiple runs of the commercial casting simulation package, ProCAST™, were used to model the mold filling and solidification events employing a range of IHTC values. The simulation results were used to estimate the center line cooling rate at various locations through the casting. The center line cooling curve, together with the die temperature and the thermodynamic properties of the alloy were then used as inputs to compute the solution to the Stefan problem of a moving phase boundary, thereby providing the through-thickness cooling curves at each chosen location of the casting. Finally, the local cooling rate was used to calculate the resulting grain size and skin thickness via established relationships. The effects of die temperature, filling time and heat transfer coefficient (HTC) on the grain structure in skin region and core region are quantitatively characterized. The grain size distribution from surface to center was estimated from the relationship between grain size and the predicted cooling rate. Finally, the locally varying yield strength was predicted using a modified Hall-Petch equation.

4.1 Experimental Procedure

In this section, the experimental techniques are described. Two automobile components were produced by high pressure die casting process. Several samples were cut from different locations of these components. Metallographic analysis was then used to characterize microstructural features of these samples. The average grain size and area fraction of ESGs were quantified using image analysis methods. The local mechanical properties of those components were determined from the results of uniaxial tensile tests.

4.1.1 Alloys and Casting

The alloy examined in this work is AM60 which was processed by gravity step casting and HPDC. The nominal chemical compositions of those alloys are given in Table 3.1. Section 3.1.1 describes the process of gravity step casting which was conducted in this study.

Two casting components (shock tower and top hat) were produced by CanmetMATERIALS in Hamilton, Ontario, Canada on a 1200t Buehler dual -platen die-caster with vacuum capability. Both tools were designed to be evacuated during filling to reduce the level of gas porosity. The shock tower was fed by four runners making three distinct knit lines; on the other hand, eight runners are used in top hat tool leaving seven knit lines.

Table 4.1: The reference process parameters were used in this study.

Process parameter	Slow shot speed of piston (m/s)	Fast shot speed of piston (m/s)	Intensification pressure (bar)	Die temperature (°C)	Melt temperature (°C)	Vacuum (mbar)
Shock tower	0.6 ± 0.05	5 ± 0.2	450 ± 15	160 ± 2	700 ± 10	<30
Top hat	0.8 ± 0.05	4.5 ± 0.2	550 ± 0.2	160 ± 2	700 ± 10	<30

Coupons used in the characterization of casting microstructure were obtained from six different locations in shock tower and five locations in top hat castings. The locations are noted for shock tower and top hat in Figure 4.1 and Figure 4.2 respectively. The local solidification conditions for each of these locations were identified from ProCAST™ software simulations of the filling and solidification processes. The shock tower and top hat were produced using process parameters as shown in Table 4.1. Three castings for each set of process parameters were chosen and examined. To obtain a quasi-steady-state temperature in the shot sleeve and die, 10 shots were made before producing the investigated casting.

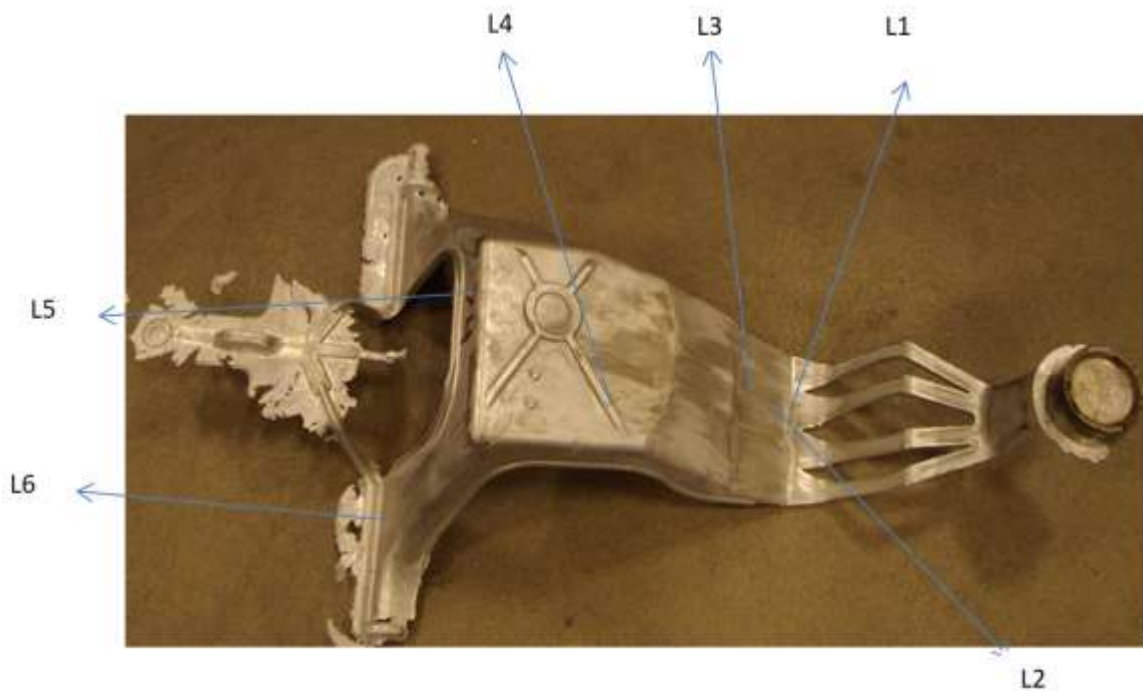


Figure 4.1: The shock tower and the six selected Locations.

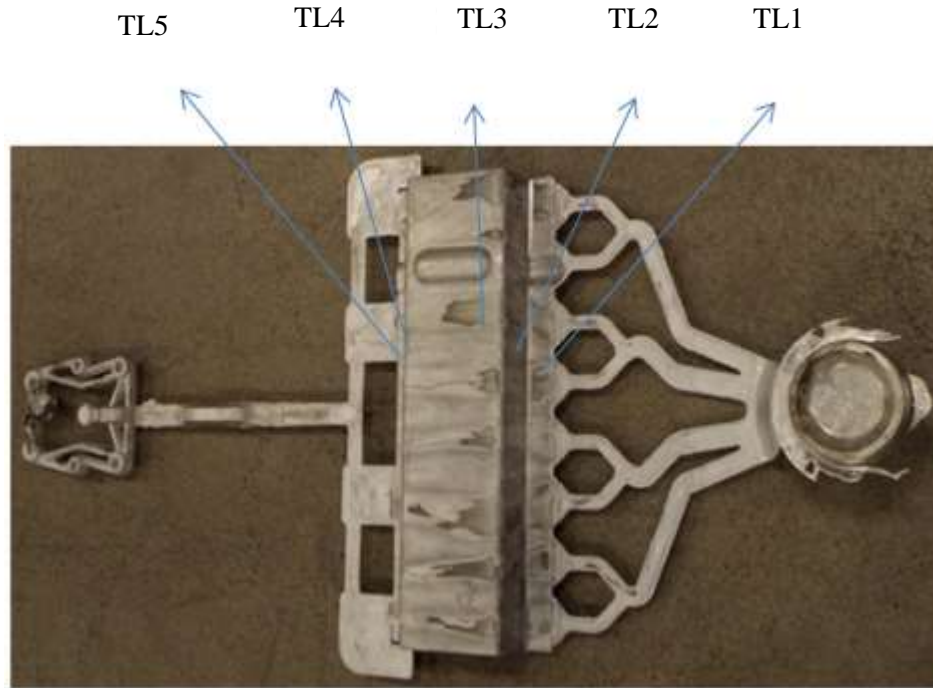


Figure 4.2: Top hat casting and five selected locations.

4.1.2 Computation of Cooling Rate

In the case of the stepped-casting, temperature data was recorded during the casting process by seven thermocouples embedded in different locations of the mold, and subsequently the cooling rate of each sample was computed directly. The solidification and filling process of the instrument panel has been simulated using commercial software package MAGMASoft at Meridian Lightweight Technologies Inc [5, 31]. From the MAGMASoft simulation, the centerline temperature-time history for a series of locations was obtained from the onset of filling through to the point when the simulation was completed. The samples were chosen based on the difference in the local solidification conditions, grain size and predicted centerline cooling rate as shown in Table 4.2. In the case of instrument panel, the grain size and simulations results have been published in the reference.

Table 4.2: The different samples were selected from the instrument panel. These results has been published in the Reference [45].

Sample	Solidification condition	Grain size(μm)		Predicted cooling rate in the core region ($^{\circ}\text{C/s}$)
		Skin	Core	
1	Knit line	4.5	13	222
2	Last to fill	5.3	13.3	162
3	Last to fill	6	14.9	105
4	A position of casting	5.8	13.4	146
5	close to gate	6.2	13.3	186
6	A position of casting	5.8	14.2	187
7	A position of casting	7.2	13.3	58
8	A position of casting	4.6	12.6	182
9	Last to fill	5.8	14.3	140
10	Last to fill	7	13.4	210
11	Last to solidify	7.7	15.7	83
12	Last to fill	7.5	12.6	59
13	Knit line	7.5	13	134
14	A position of casting	6	13.8	55
15	A position of casting	4.1	13.4	122
16	Close to gate	6.2	14.5	175

4.1.3 Grain Size Measurement by Image Analysis Software

In the Section 3.1.3, the method of metallography of magnesium alloys was described in this study. The grain size measurement was performed using image analysis software Clemex. In this study the grain diameter (G.D) is considered as grain size measurement. The grain size variation has been examined both in transverse and longitudinal directions. The binary operation in image analysis software enable user to detect the interest area. The grains are detected using binary feature of image analysis software.

Due to presence of big dendrite grains in the microstructure of HPDC, the area fraction of grains was measured and then the diameter of grain is calculated. Figure 4.3 shows the measurement of average grain size distribution through the cross section of casting. The local average grain size in each cube can be measured as shown in Figure 4.3.

In order to measure area fraction of ESGs in the cross section of casting, the image montages have been made by 8 contiguous fields. Figure 4.4 also shows the measurement of area fraction of ESGs in the microstructure of HPDC using image analysis software.

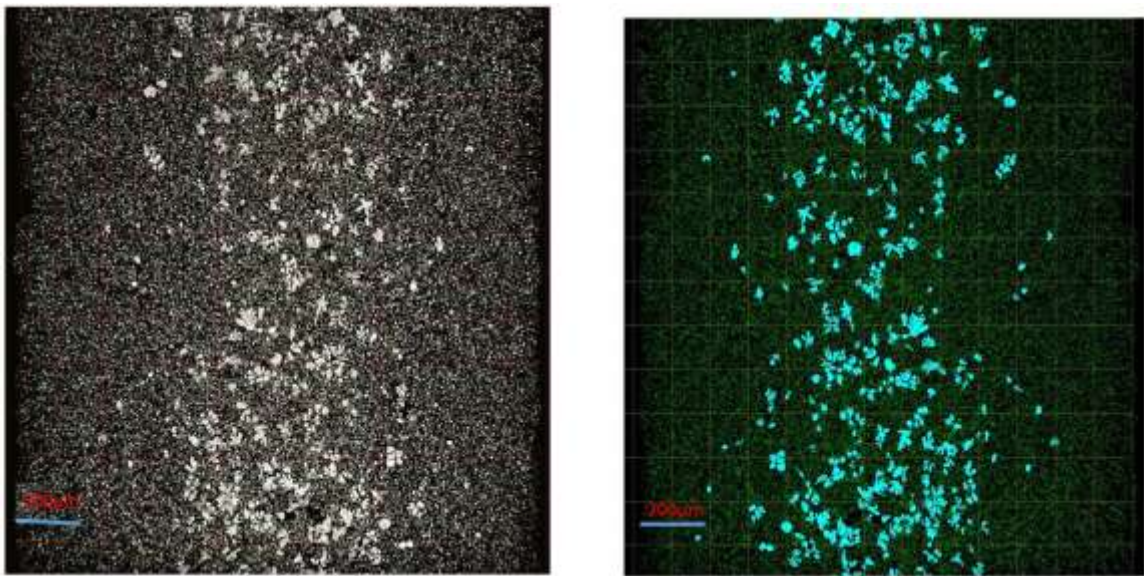


Figure 4.3: The measurement of variation of average grain size in the cross section of casting using image analysis software.



Figure 4.4: The measurement of area fraction on ESGs in the cross section of casting using image analysis software Clemex.

4.1.4 Uniaxial Tensile Testing

Tensile testing was performed on an Instron servo hydraulic load frame with 250kN load cell at a constant strain rate of 0.05s^{-1} . The strain was measured continuously using an extensometer with a gauge length of 25 mm. The tensile specimens were machined to the dimensions specified in ASTM B557M.

The stress-strain curve can be determined from results of uniaxial tensile tests. The yield strength, unlimited tensile strength and elongation value were determined from tensile strain-stress curve according to ASTM B557M. Twelve tensile specimens were cut from the top hat, as shown in Figure 4.5. In order to examine the local filling and solidification condition effects on the tensile properties, tensile coupons were extracted from different locations from gate to overflow, as indicated in Figure 4.5.



Figure 4.5: Locations of 12 tensile specimens were cut from a die-cast Top hat from gate to overflow.

4.2 Modeling of Solidification of Magnesium Alloys in the HPDC

Due to extreme flow and high cooling rate in the HPDC process, the quantitative measurement of cooling rate is practically very difficult. Hence, it is suggested that commercial code software can be used to predict the cooling rate in the HPDC process. In this study, the commercial code software ProCAST™, was used to simulate the filling and solidification of magnesium alloys in the high pressure die cast. The temperature distribution across the thickness at these locations in the component is then determined by solving the one-dimensional Stefan problem for a moving phase boundary. The local cooling rates are calculated with respect to distance from the mold wall of the casting.

4.2.1 Simulation of High Pressure Die Cast Process

ProCAST™ is a finite-element program that solves thermal and fluid equations in casting systems. Thus, ProCAST™ enables user to the implement the simulation of HPDC process

based on second and third model. In this study, the mesh is generated by ProCAST™ automatically in 2D and 3D. Three-node linear trilateral elements were used, and different mesh density for the casting and the die was used in an effort to reduce execution times. In order to conduct the mesh convergence study, the central solidification time was determined from four different mesh size ranges and simulation results were then compared at these mesh size ranges. The element sizes were then utilized for the mesh ranged from 0.2–0.5mm for the casting, and from 7.0–14.0mm for the die sections and cooling channels.

Table 4.3: The values of thermo-physical variables were used [52].

Thermo-physical Variables	T_l (°C)	T_s (°C)	α (m ² /s)	k (W/m °C)	ρ (kg/m ³)	c (kJ/kg °C)	L_f (kg/J)
Values	615	565	0.044	Variable from solid to liquid phase 101.8-704	Variable from solid to liquid phase 1810-1620	Variable from solid to liquid phase 1-1.17	37000

4.2.1.1 Initial Conditions

The material properties of magnesium alloys were utilized from the software database. Figure 4.6 shows how to set up the material properties of AM60 before the implementation of simulation. The thermo-physical properties used for the purpose of this simulation are presented in Table4.3. The density, thermal conductivity and specific heat were input as a function of temperature as shown in Figure 4.6 (b). It should be noted that the initial die temperature was assigned as a part of initial conditions. The Initial die temperature varies from 160 °C to 240 °C for different sets of process parameters.

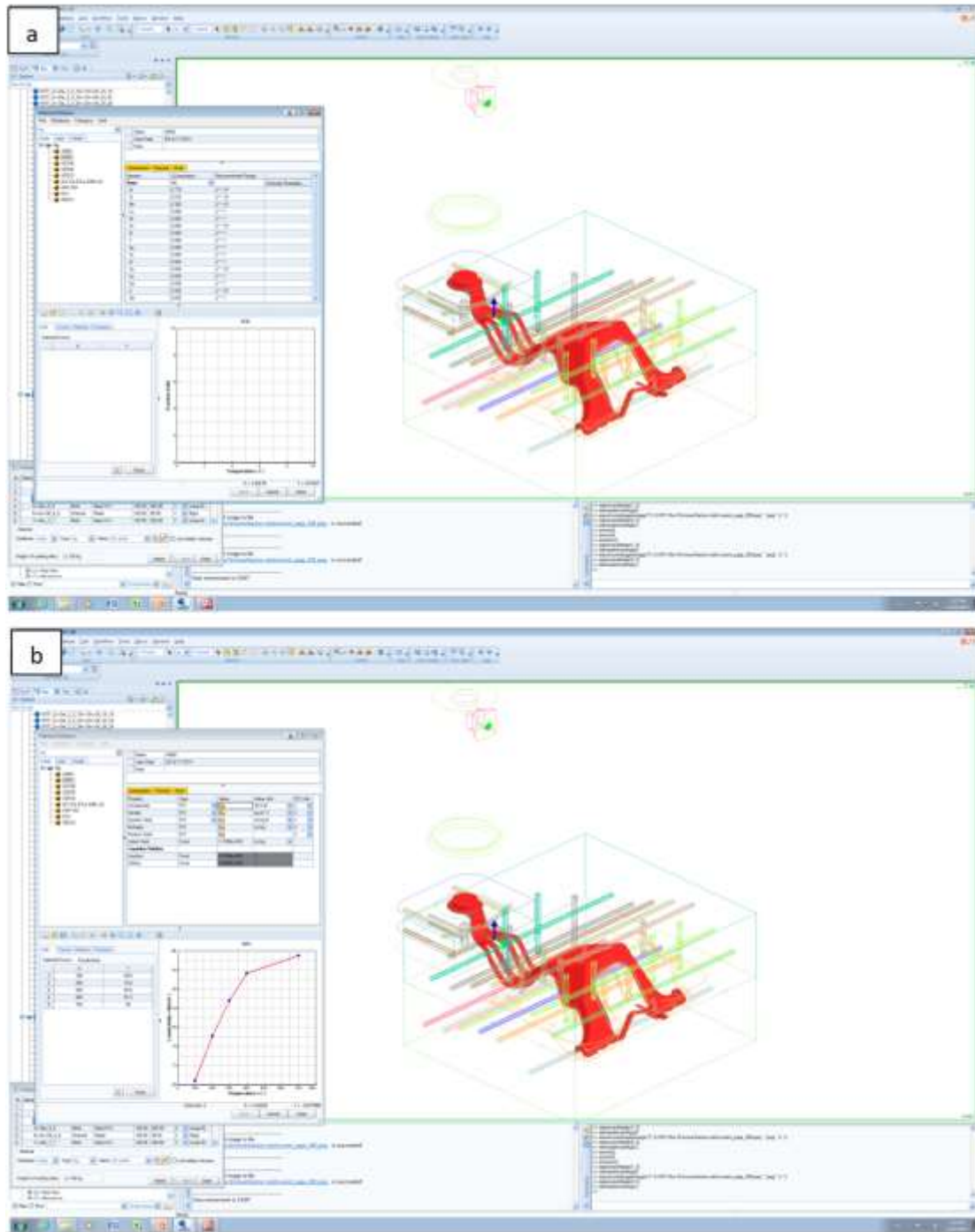


Figure 4.6: how to set up the alloy (a) and thermo-physical properties of alloys (b).

4.2.1.2 Boundary Conditions

In order to implement the simulation process, the variation of IHTC, initial die temperature and filling time varied in each set of the simulation for shock tower. The other values were kept the same as a reference operation condition as presented in Table 4.1.

In this study, the maximum IHTC value is defined as interfacial heat transfer coefficient between liquid metal/die for shock tower and top hat. It should be noted that the IHTC is a function of temperature during the simulation process. The heat transfer coefficient linearly decreases when temperature drops from liquid phase to solid phase as shown in Figure 4.7. The heat transfer coefficient for solid phase is $1200 \text{ Wm}^{-2} \text{ K}^{-1}$ and assumed constant for all sets. For all sets, the heat transfer coefficient values for liquid metal/runner and metal/shot sleeve are assigned $8000 \text{ Wm}^{-2} \text{ K}^{-1}$ and $10000 \text{ Wm}^{-2} \text{ K}^{-1}$, respectively. Also, constant value of $1000 \text{ Wm}^{-2} \text{ K}^{-1}$ was employed for die/die and piston/die surfaces as heat transfer coefficient for both components.

Figure 4.8 shows the determination of piston velocity as a part of boundary condition. The piston velocity has been assigned as a function of time. Two different stages were defined: slow stage of piston velocity and fast stage of piston velocity. The amount of fast stage varies from 3 m/s to 5 m/s and the amount of slow stage varies from 0.6 m/s to 1 m/s for different set of process parameters.

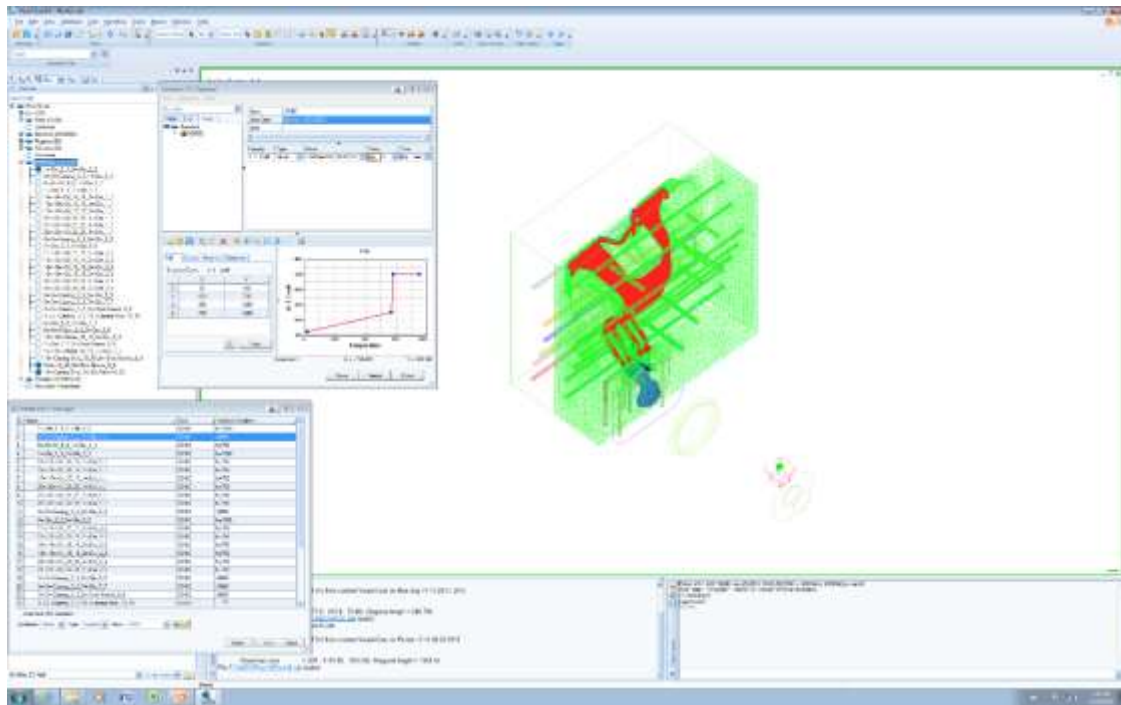


Figure 4.7: The determination of interfacial heat transfer coefficient in the ProCAST™.

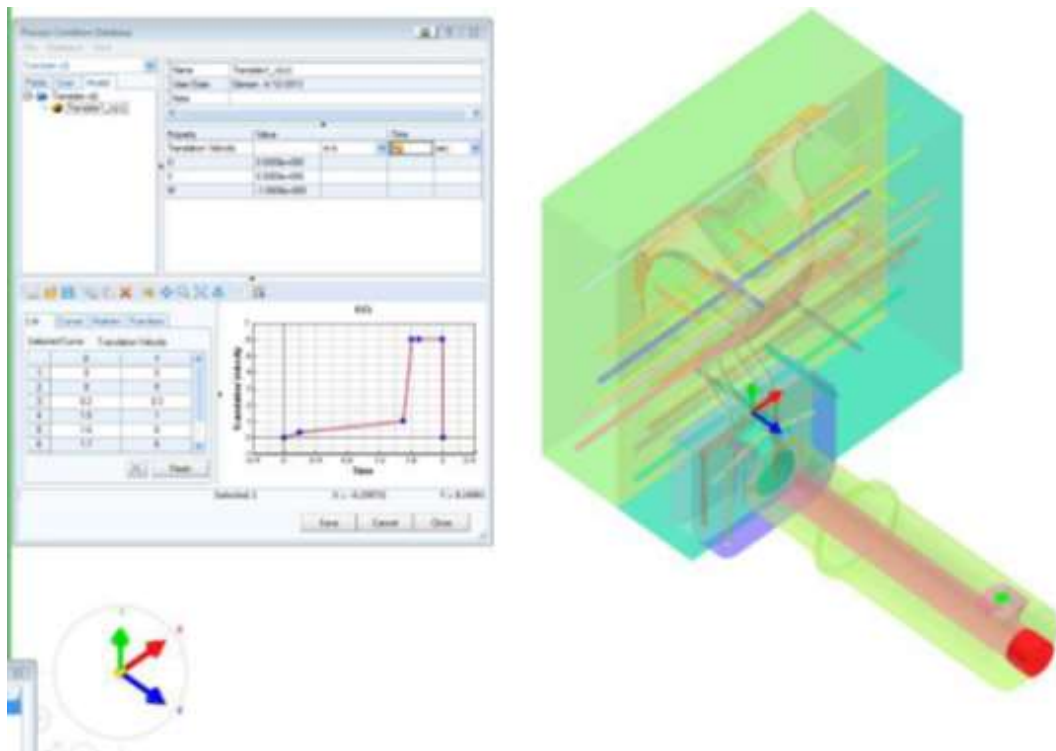


Figure 4.8: The determination of piston velocity as a function of time.

4.2.2 Predicting of Temperature-Time Distribution

In order to predict cooling rate through the thickness of casting, a model including the “phase-change” solution during solidification phenomenon is required. Typically, Stefan Problem [21-23] model has been suggested to solve phase-change problems, particularly, when the freezing boundary is not stationary. In this study the following assumptions were made to implement Stefan problem:

- A) Since the solidification rapidly occurs in the HPDC, this could be assumed as a purely transient conduction problem with negligible convection.
- B) The heat transfer from the liquid towards the mold walls is assumed to be in one dimension.
- C) The initial temperature of the liquid (T_L) at center equals the melt temperature and decreases with time.

In order to utilize the Stefan solution, the die surface temperature and temperature- time distribution at the center of the casting has been obtained by ProCAST™. The cooling rate at center should be the lowest value, therefore, the temperature-time distribution was extracted from a node that indicated highest value of solidification time across section of casting thickness. To prevent increasing in computation time, ProCAST™ was not used to predict the variation of cooling rate through the cross section of casting. The accurate prediction of cooling rate through the cross section of casting requires more elements and subsequently the computation time would be increased.

In the classical Stefan problem, the boundary conditions at this interface are set for the solid and the liquid regions in the casting, as indicated in Figure4.8. According to the Stefan problem formulation, the interface energy balance at interface solid-liquid can be described as following:

$$k \frac{\partial T_s(x_i, t)}{\partial x} - k \frac{\partial T_L(x_i, t)}{\partial x} = \rho L_f \frac{dx_i}{dt} \quad \text{at } x = S(t), t > 0 \quad (4.1)$$

The equation is represented in a one dimensional form in the following relations:

$$\theta_s = \frac{T_s - T_0}{T_f - T_0}, \quad \theta_L = \frac{T_L - T_0}{T_f - T_0}, \quad \xi = \frac{x}{L}, \quad \psi = \frac{qL^2}{k(T_f - T_0)}, \quad \tau = Ste \frac{\alpha}{L_f^2} t,$$

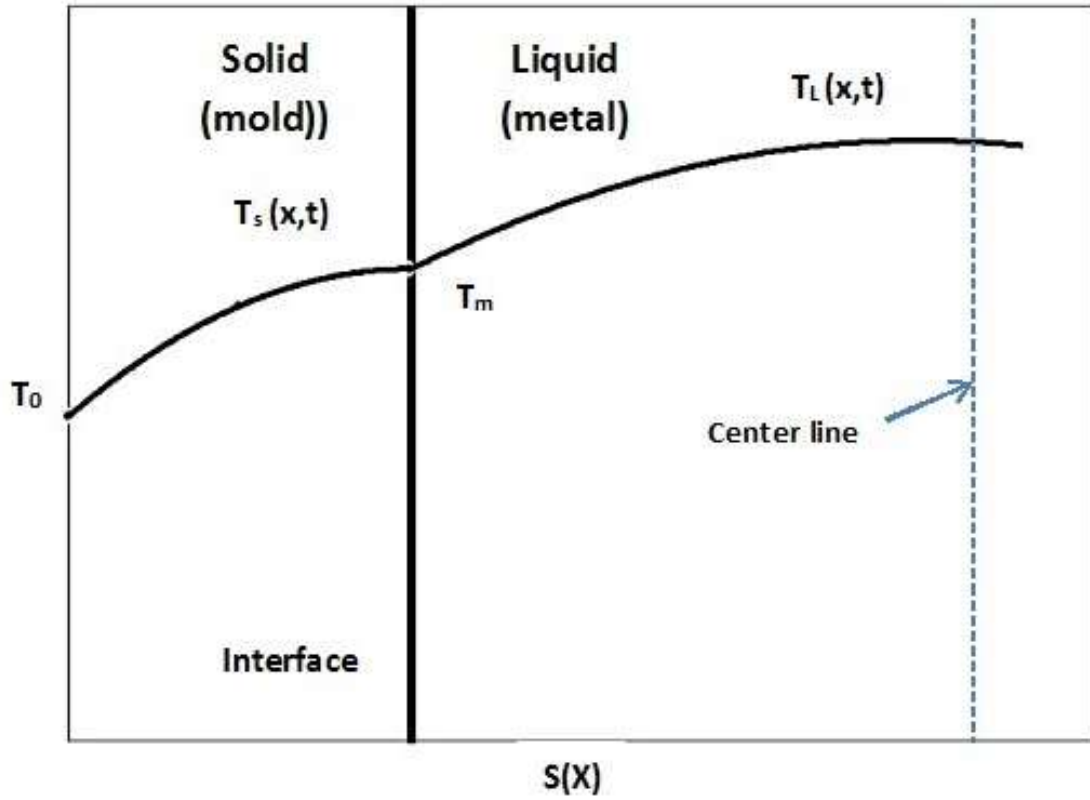


Figure 4.9: Schematic view for the solidification through the thickness of casting based on the modified heat transfer approach.

The distribution of temperatures $T_s(x, t)$ and $T_L(x, t)$, are as:

$$\frac{\partial^2 \theta_s}{\partial \xi^2} + \psi = Ste \frac{\partial \theta_s}{\partial \tau}, \quad 0 \leq \xi \leq \xi_i \quad \text{Solid state} \quad (4.2)$$

$$\frac{\partial^2 \theta_L}{\partial \xi^2} + \psi = Ste \frac{\partial \theta_L}{\partial \tau}, \quad \xi_i \leq \xi \leq 1 \quad \text{Liquid state} \quad (4.3)$$

Where Ste is the Stefan number defined as:

$$Ste = \frac{c(T_f - T_0)}{L_f} \quad (4.4)$$

Interface energy equation can be rewritten based on the “Stefan problem” the one dimensional, as:

$$\frac{\partial \theta_s(\xi_i, \tau)}{\partial \xi} - \frac{\partial \theta_L(\xi_i, \tau)}{\partial \xi} = \frac{d\xi_i}{d\tau} \quad (4.5)$$

The quasi-steady is extensively applied in calculating the exact analytical solution for a variety of phase change problems [92]. In practice the quasi steady-state approximation is justified for Stefan number, $Ste < 0.1$ as very small Ste number would mean a very high latent heat of fusion value [23]. The Stefan number can be calculated by substituting the thermal variables (Table 4.3) in **Eq4.4** and in this case it was calculated as 0.06. In this model the Stefan number is assumed to be small compared to unity and thus the right hand side, which is the transient part of the one-dimensional heat equation, Eq. (4.2) and Eq. (4.3) can be neglected. Thus, substituting $Ste = 0$ in **Eqs4.2** and **4.3**, as:

$$\frac{\partial^2 \theta_s}{\partial \xi^2} + \psi = 0 \quad (4.6)$$

$$\frac{\partial^2 \theta_L}{\partial \xi^2} + \psi = 0 \quad (4.7)$$

Boundary Conditions are [17]:

1. $\theta_s(0, \tau) = 0$
2. $\theta_s(\xi_i, \tau) = 1$
3. $\theta_L(\xi_i, \tau) = 1$

$$4. \quad \frac{\partial \theta_L(1, \tau)}{\partial \xi} = 0$$

In this approach, Interface energy (**Eq4.5**) is unchanged and thus temperature distribution and interface motion are time dependent. Integrating **Eq4.6** and **Eq4.7** and applying the boundary conditions, give the solution to the temperature distribution in the solid and liquid phases.

$$\theta_s(\xi_i, \tau) = -\frac{\psi}{2} \xi^2 + \left(1 + \frac{\psi}{2} \xi_i^2\right) \frac{\xi}{\xi_i}, 0 \leq \xi \leq \xi_i \quad (4.8)$$

$$\theta_L(\xi_i, \tau) = -\frac{\psi}{2} (\xi_i^2 - \xi^2) - \psi(\xi_i - \xi) + 1, \xi_i \leq \xi \leq 1 \quad (4.9)$$

The interface solution can be determined by substituting **Eq4.8** and **Eq4.9** in **Eq4.5**;

$$\frac{1}{\xi} + \frac{\psi}{2} \xi_i - \psi = \frac{d\xi_i}{d\tau} \quad (4.10)$$

Integrating **Eq4.10** gives;

$$\int_0^\tau d\tau = \int_0^{\xi_i} \frac{\xi_i d\xi_i}{\left(\frac{\psi}{2}\right) \xi_i^2 - \psi \xi_i + 1} \quad (4.11)$$

As discussed, the problem is simplified to the case of the high pressure die cast where solidification occurs with negligible volumetric heat generation. Thus this would be the limiting case where $\psi = 0$. Implementing this condition in **Eq4.11**, as,

$$\xi_i^0 = \sqrt{2\tau} \quad (4.12)$$

where, $\xi_i^0 = 0$, the solution becomes the following form:

$$\theta_s(\xi_i, \tau) = \frac{\xi}{\xi_i}, 0 \leq \xi \leq \xi_i \quad (4.13)$$

On further substitution,

$$\theta_s = \frac{T_s - T_0}{T_f - T_0} = \frac{\xi}{\xi_i}, 0 \leq \xi \leq \xi_i \quad (4.14)$$

$$T_s = \left(\frac{\xi}{\xi_i} \right) (T_f - T_0) + T_0, 0 \leq \xi \leq \xi_i \quad (4.15)$$

And the temperature distribution of the liquid phase becomes,

$$\theta_L(\xi_i, \tau) = 1, \xi_i \leq \xi \leq 1 \quad (4.16)$$

$$T_L = [(T_f - T_0)] + T_0, \xi \leq \xi_i \leq 1 \quad (4.17)$$

$$T_L = T_f, \xi \leq \xi_i \leq 1$$

Using this exact analytical solution, the temperature distribution through the thickness of the casting can be computed.

4.3 Results

4.3.1 Cooling Rate- Grain Size Correlation

The grain size is strongly correlated to the cooling rate as shown in Figure 4.10. The dependence of grain size on the cooling rate can be described using an inverse power law relationship, given as:

$$d = 75.6R^{-0.326} \quad (4.18)$$

where R is cooling rate ($^{\circ}\text{C/s}$). Seven samples were selected from step-cast and sixteen samples from different locations of complex die cast component. In the case of HPDC, the average grain size in the core region was taken into account as indicated in Table 4.2 and central cooling rate was obtained from commercial software.

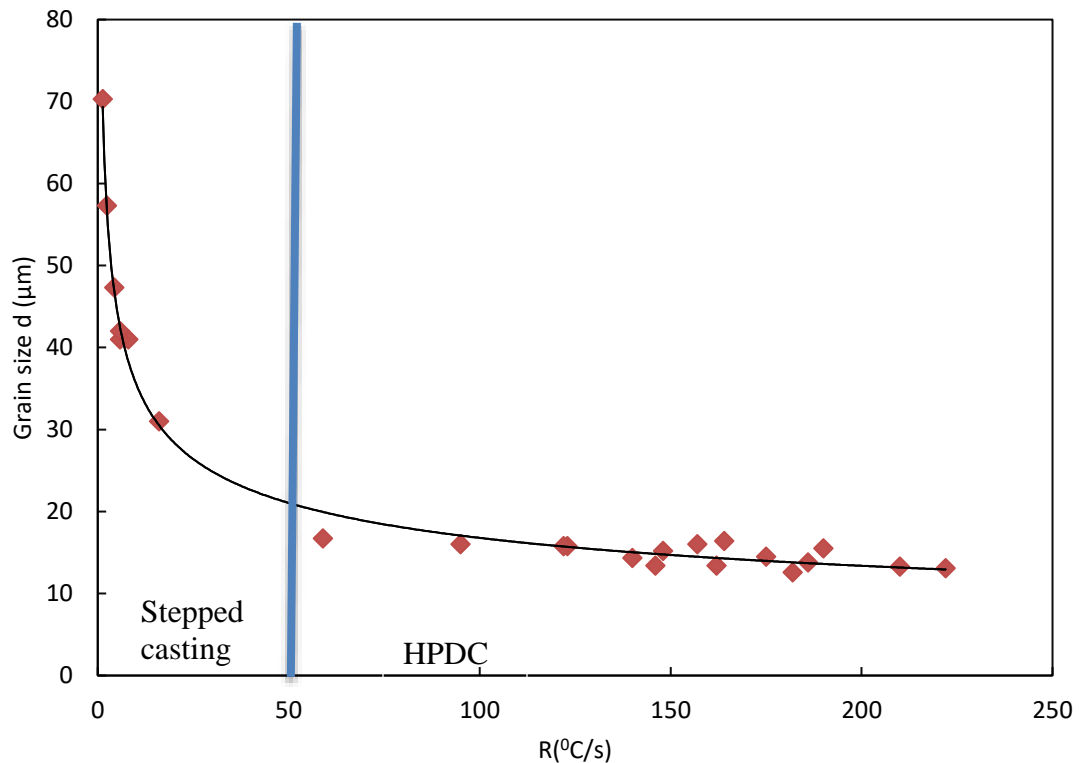


Figure 4.10: Grain size as a function of cooling rate.

Figure 4.11 shows the variation of microstructure across the thickness of the die-casting samples. As shown in Figure 4.11, the grain size increases from skin region to the core region due to the high variation in cooling rate near the mold wall. For the case of AM60, Yang et al. [43] found that the average grain size was 6 and 16 μm in the skin region and core region respectively. H.I. Laukl et al. [27] reported the grain size in the skin region varied from 5 to 10 μm while the grain size is in range of 11 to 20 μm in the core region. The data presented in Ref. [45] gives specific results for the instrument panel, average grain sizes range from 5 to 9 μm in the skin region, and from 12 to 15 μm in the core region. The transition from the skin region to the core region can thus be determined by a grain size threshold value of 10 or 11 μm . The value of critical cooling rate was calculated using **Eq.4.18** for the transition region with average grain size between 10 to 11 μm .

$$R_{10}=490 \text{ (}^{\circ}\text{C/s)} \quad R_{11}=375 \text{ (}^{\circ}\text{C/s)}$$

R10 and R11 are cooling rates which will result in the average grain sizes of 10 or 11 μm . In this study the average grain size below 10 μm will be defined as the average grain size of skin region (D_s) and higher 11 μm as average grain size of core region (D_c).

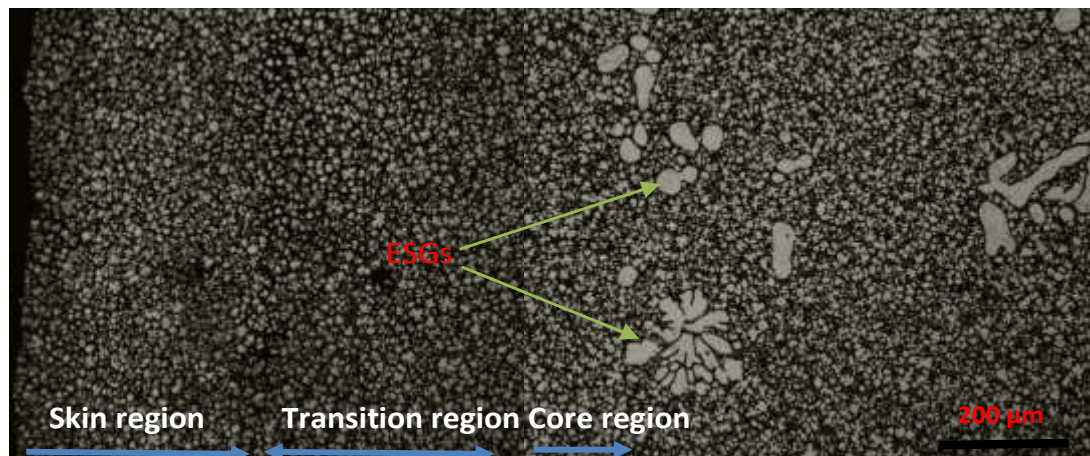


Figure 4.11: The prediction of grain size along the thickness of the casting for Sample 1. This also shows variation grain structure through the casting cross section.

4.3.2 Microstructure of HPDC

Figure 4.12 presents the optical micrograph of etched microstructure of each locations of shock tower. In the Location1 and Location 2, ESGs occur occupy significantly larger fractions of the volume. In both locations, the grain structure at the center consists of coarse grains surrounded by small grains and near the surface, fewer coarse grains are observed in these positions. In the other locations, the skin region completely contains refined grains, while in the core region, some ESGs can be observed. Table 4.4 shows average grain size and area fraction of ESGs for six locations of shock tower. The ESGs are characterized by the dendrites and fragmented dendrites with the size ranging from 15 to 80 μm and an average of 43 μm . Thus, the presence of ESGs in the microstructure obviously leads to increase the average grain size.

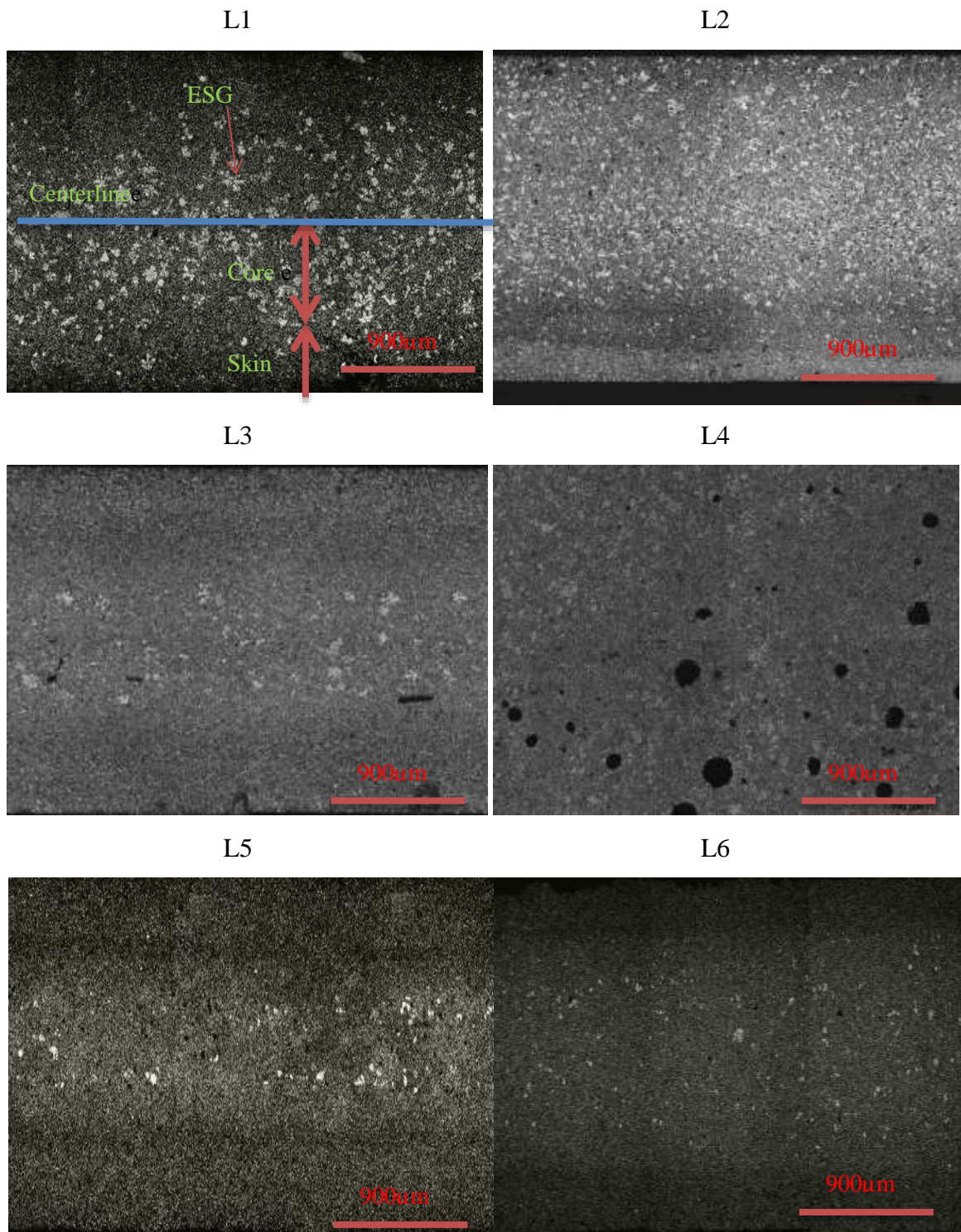


Figure 4.12: The typical microstructure of six locations.

Table 4.4: The characteristic of six location for shock tower which have been performed under the reference process parameter.

Location	Thickness (mm)	Average grain size in the skin region(μm)	Average grain size in the core region(μm)	Area fraction of ESG (%)
1	3	9.8	22.3	26.4
2	3.2	8.5	17.8	19.4
3	3.8	8.1	15	5.7
4	6.3	7.3	20	6.2
5	3.1	7.7	13.7	1.3
6	3.2	7.5	13.1	<1

4.3.3 Simulation and Modeling Results

As shown in Figure 4.13 and 4.14, the filling and solidification process in different times were simulated by commercial software ProCAST™ for shock tower and top hat. In this model, fluid flow simulation starts in the sleeve and comprises the moving boundary of the plungers as indicated in Table 4.1.

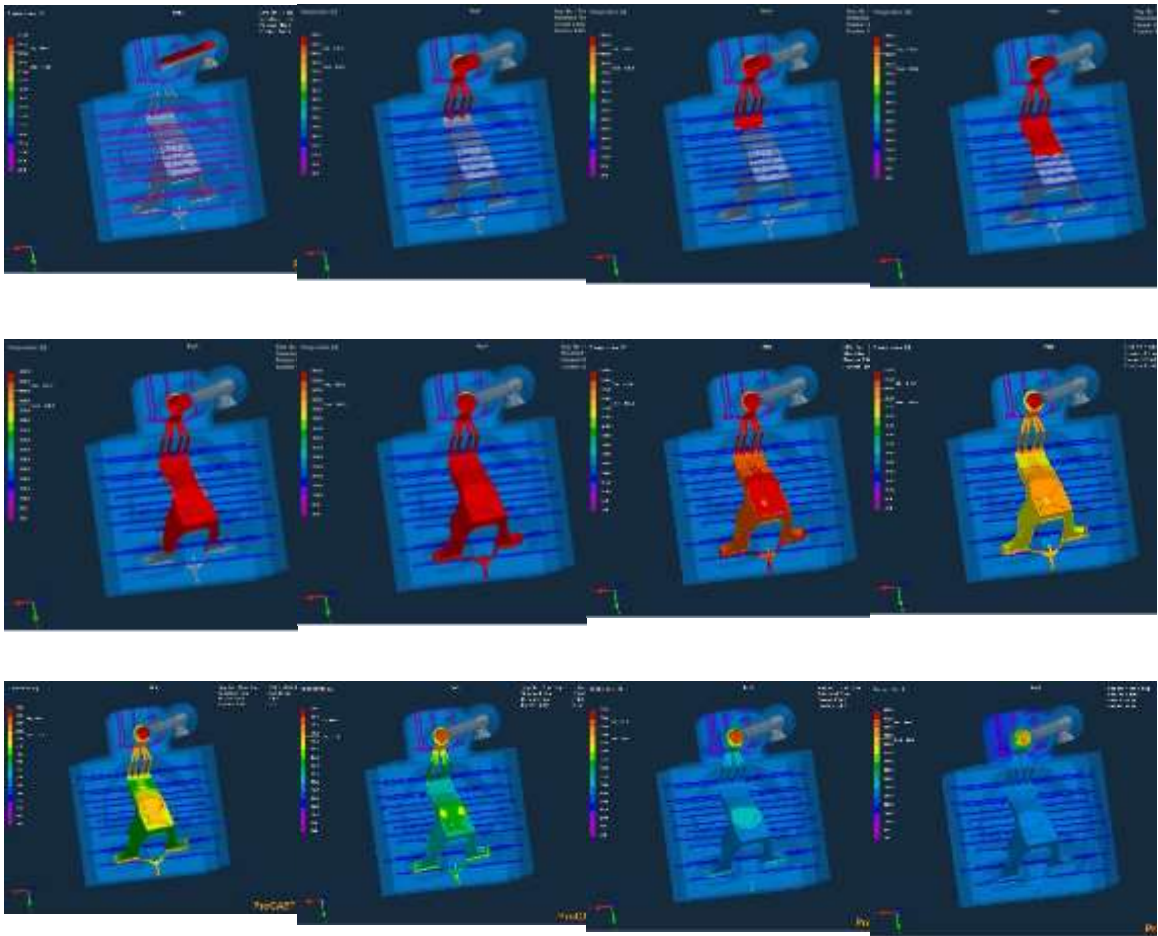


Figure 4.13: Sequence and solidification of shock tower was simulated by ProCAST™.

The filling time in HPDC process is depending mostly on second stage piston velocity as shown in Figure 4.15. After filling into cavities the casting changes from liquid state to solid state with the decrease of the temperature. During the FE simulation of the die filling process, the flow direction, the velocity, the pressure within the melt and the temperature, are calculated for each filled area of the casting at any time. From the simulation results, the temperature-time relationship for dies and casting part can be obtained when the simulation was completed.

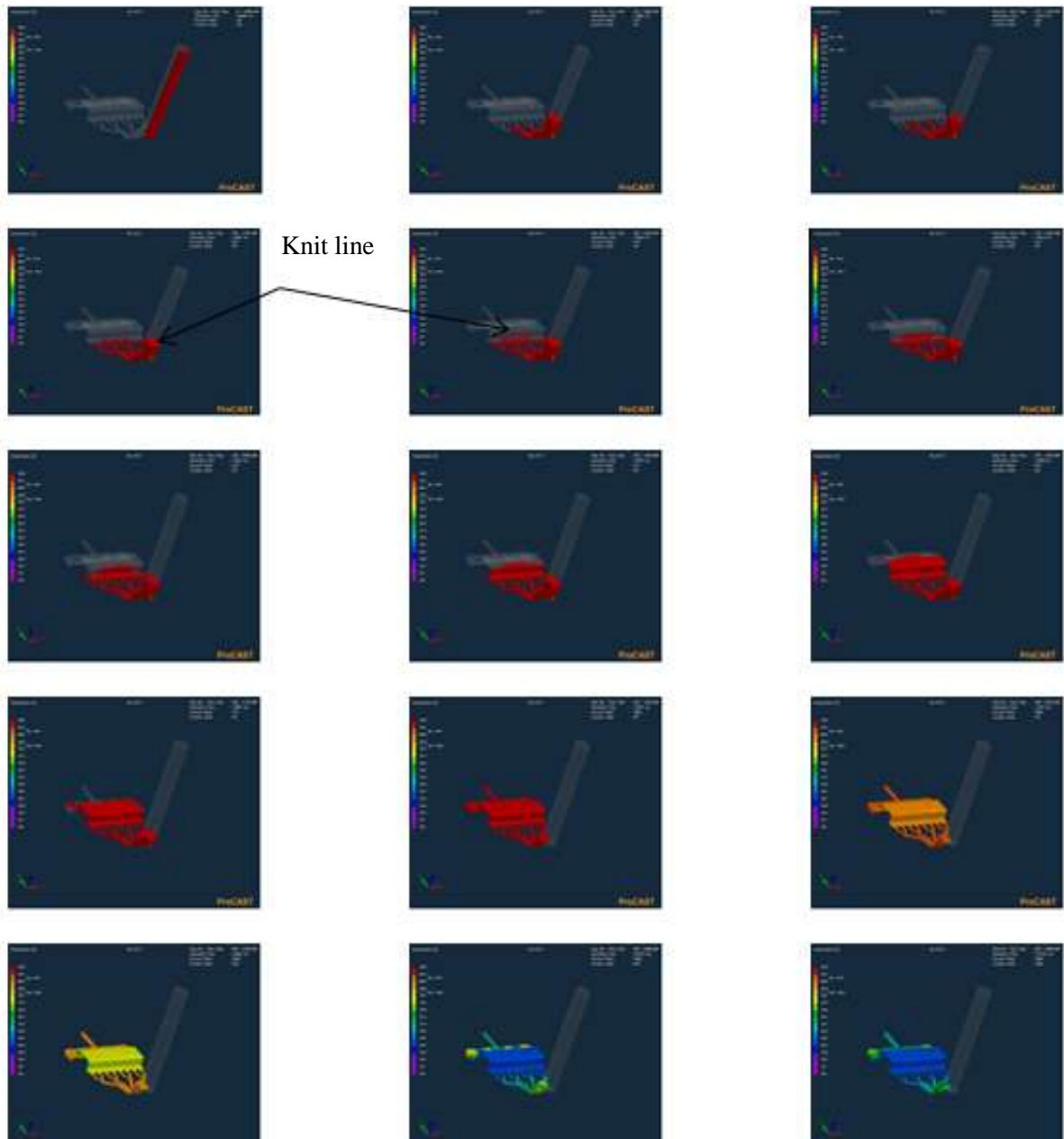


Figure 4.14: Filling sequence and solidification of top hat was simulated by ProCAST™.

As indicated in Figure 4.16, the die temperature is increased as soon as metal molten contacts with mold die. In this study, the chosen value of temperature can be assumed as die surface temperature. The die surface temperature values determined from simulation are in good agreement with the analytical method and experimental results in the literature

[33, 40]. The range of die surface temperature for different process parameters is from 230(°C) to 405(°C).

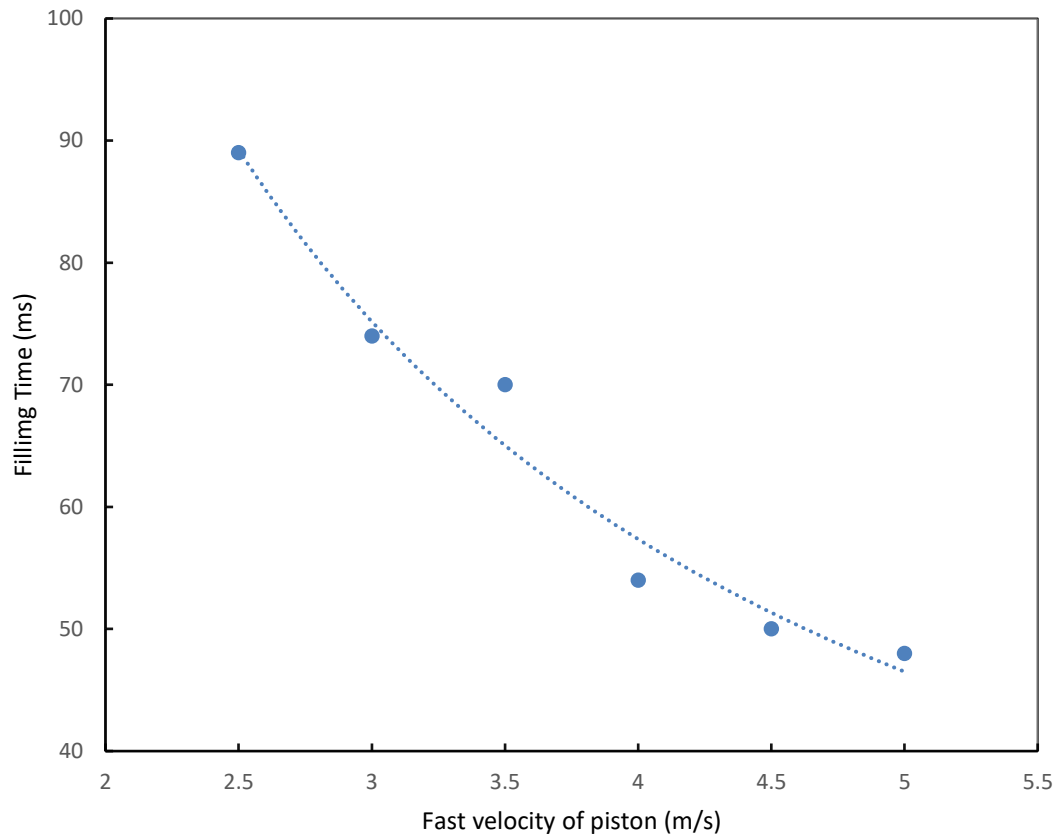


Figure 4.15: Dependency of the filling time on the variation of fast velocity of piston at a fixed value of IHTC.

Figure 4.17 presents the temperature distribution across the thickness of casting which is determined using the centerline temperature, T_L , with respect to time increment. In this study the liquid temperature is considered based on the variable approach. It means that the liquid phase temperature is subjected to variations with time corresponding to the values obtained from T_L -time data.

Figure 4.17 shows how the cooling rate is calculated at 0.4 mm from the mold wall for samples under T_L . This shows different cooling rates, R1, R2, R3, etc., calculated at different time increments at the same distance from mold wall, x, and finally an average cooling rate is obtained at that point.

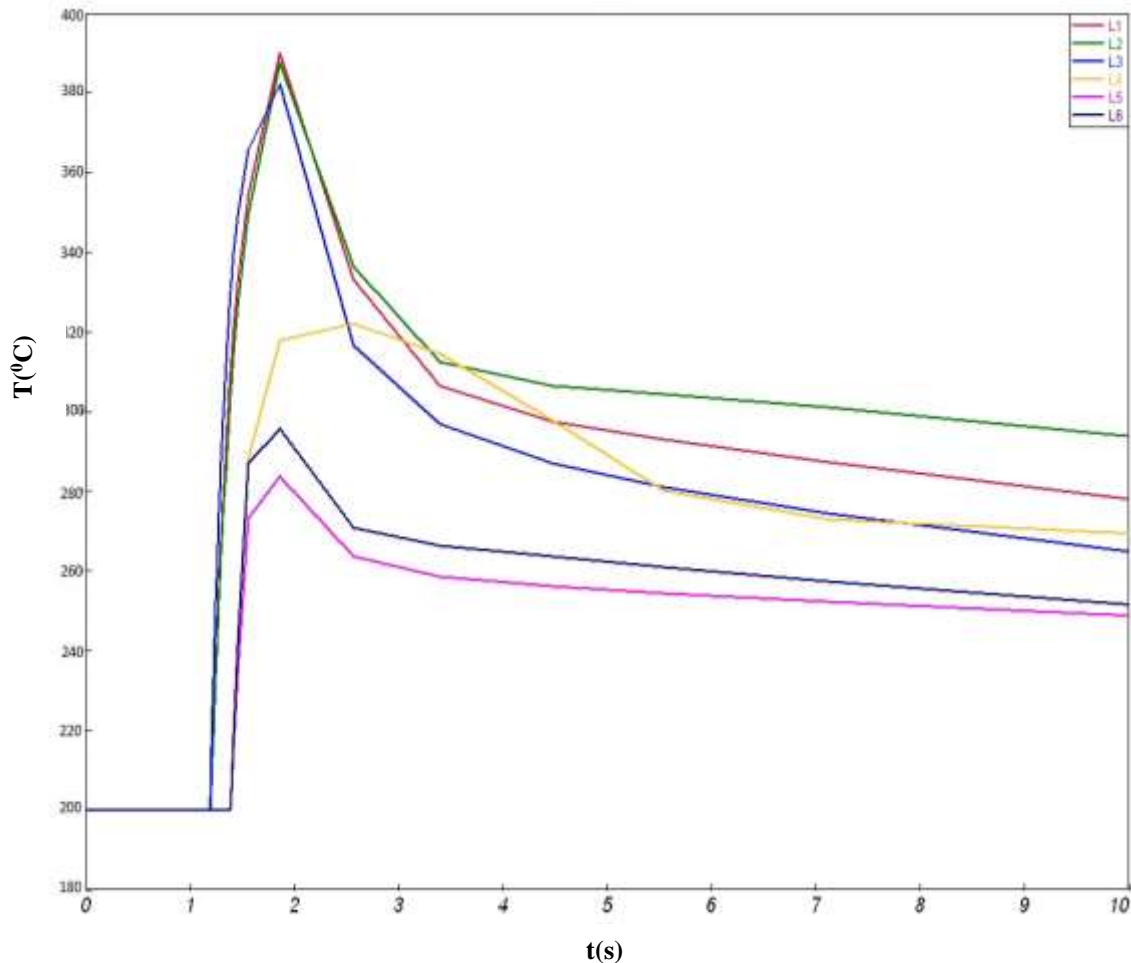


Figure 4.16: Predicted die surface temperatures in selected locations at IHTC =15000 $\text{Wm}^{-2} \text{K}^{-1}$, die temperature =200°C and fast stage velocity=4m/s. This curve was directly obtained from simulation result.

In order to examine the effect of IHTC, the simulation was unable to run for IHTC values higher than $15000 \text{ Wm}^{-2} \text{K}^{-1}$ due to the incomplete filling cavity. Figure 4.16 demonstrates the dependence of D_s and D_c on the variation of IHTC. It is apparent that the D_s and D_c generally decrease as the IHTC increases.

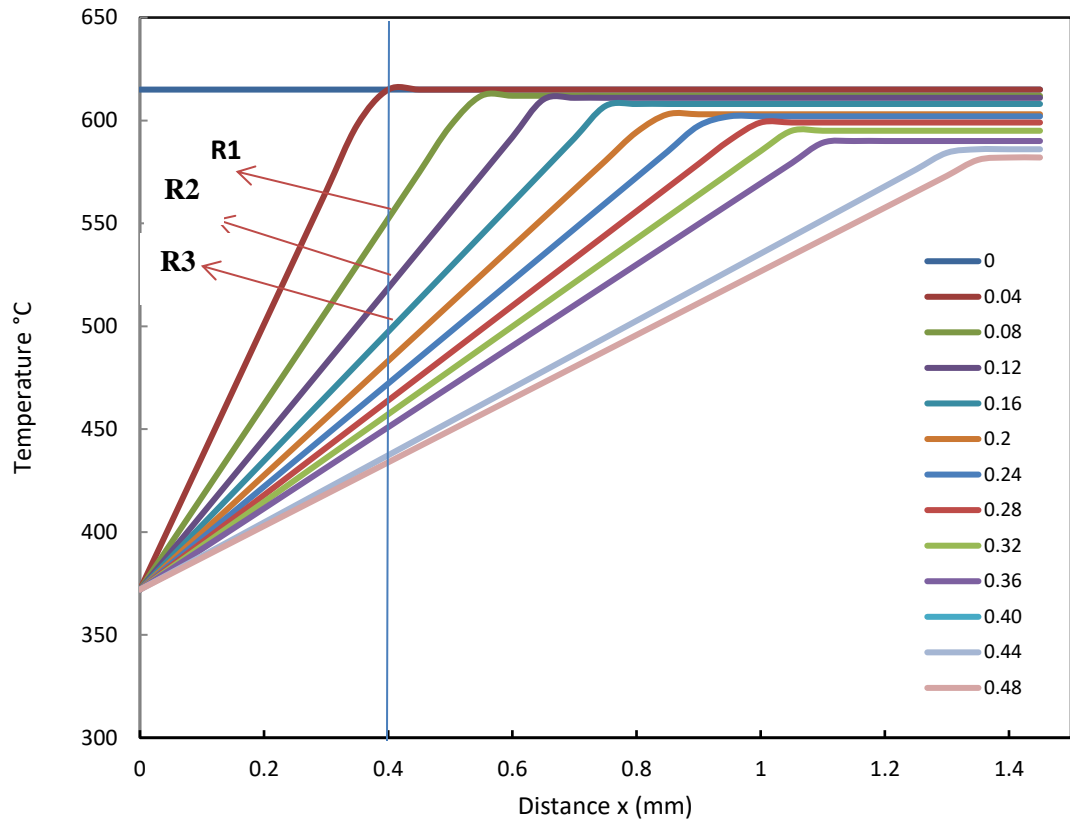


Figure 4.17: Temperature distribution along the die wall to center with time for Location 1 of shock tower.

Figure 4.19 and Figure 4.20 present the variation of D_s and D_c on the die temperature and filling time, respectively. The D_s is decreased with reduction in the initial die temperature and filling time. As shown in Figure 4.19 and Figure 4.20, the dependency of D_s on the initial die temperature and filling time is more sensitive than D_c .

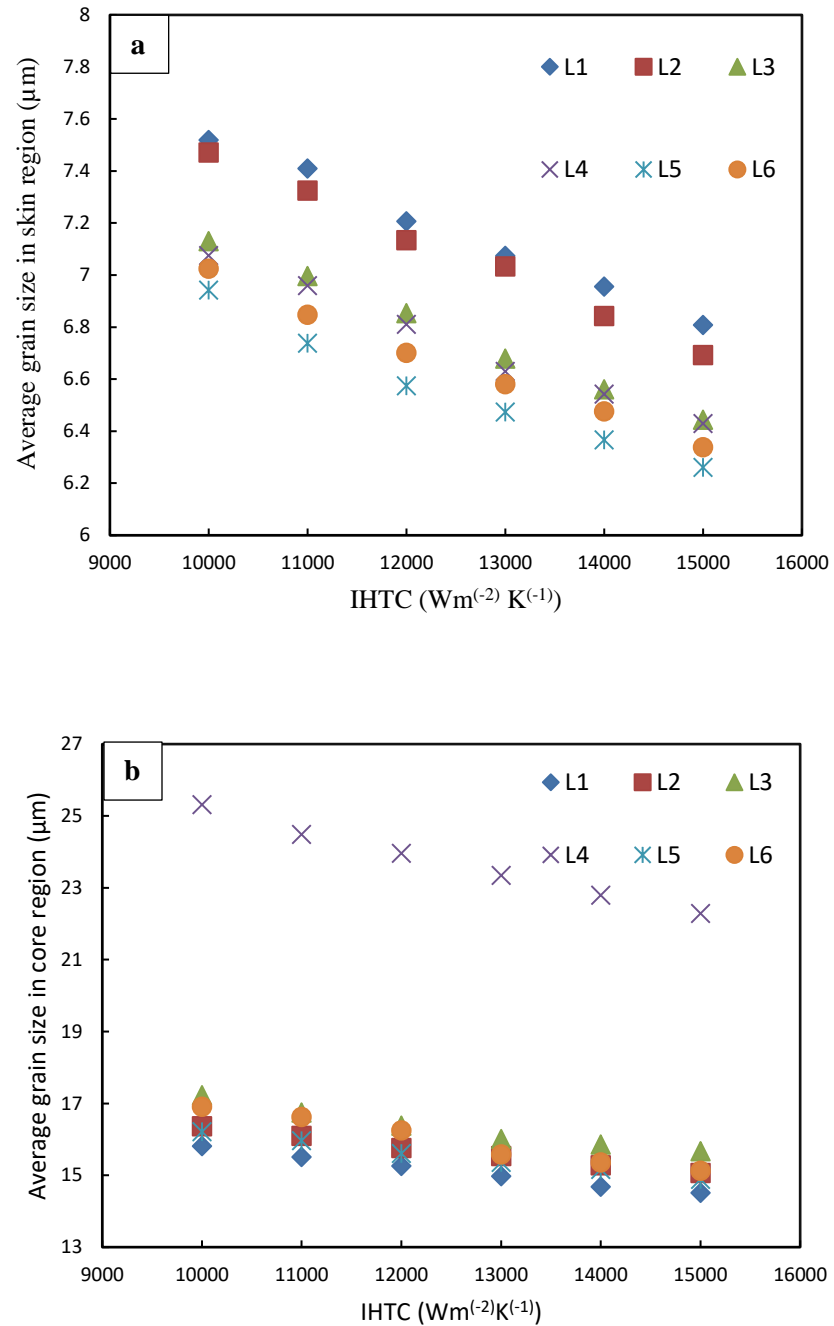


Figure 4.18: Relationship between cooling rate and IHTC at different locations for a) skin b) core.

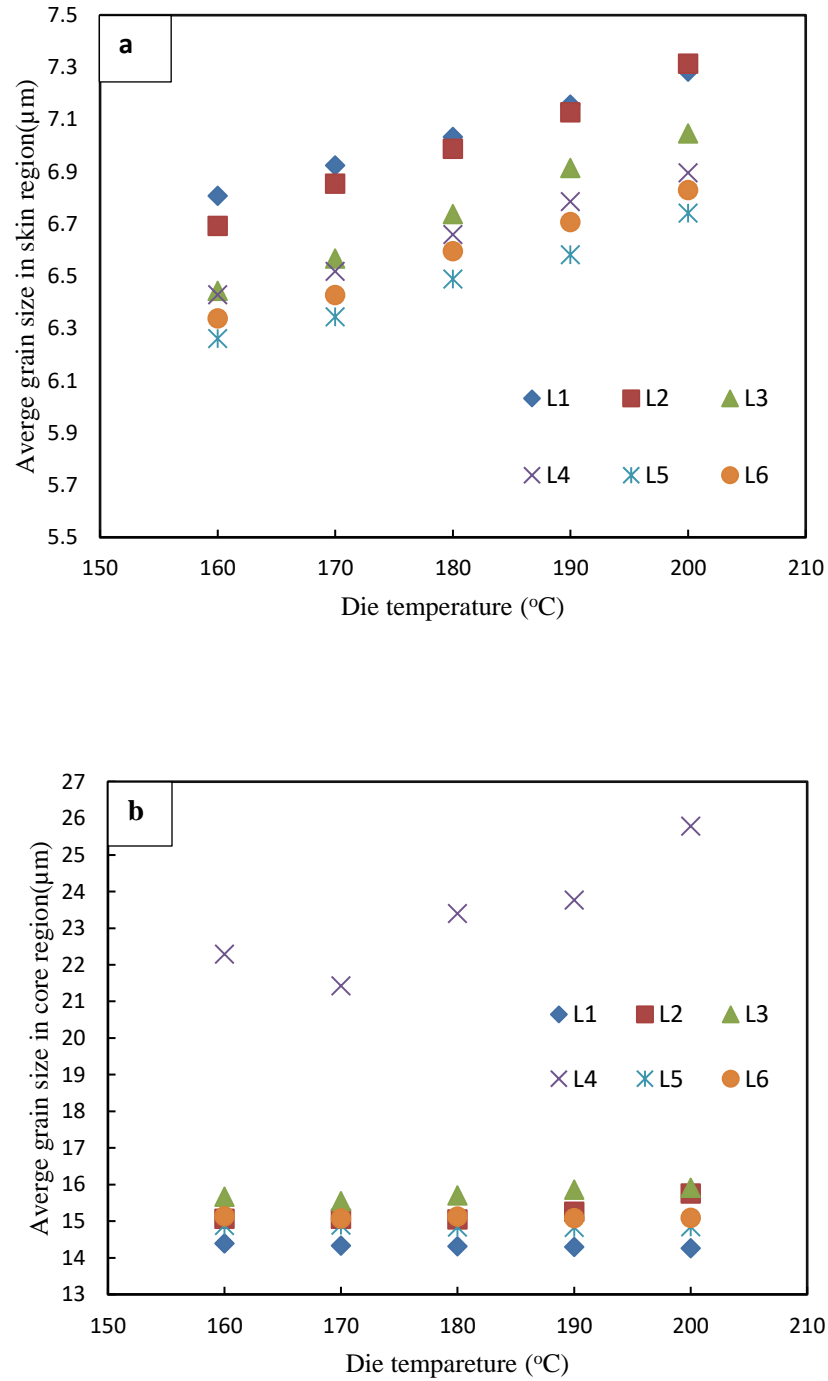


Figure 4.19: Dependency of average grain size on the variation of die temperature at a) skin region b) core region.

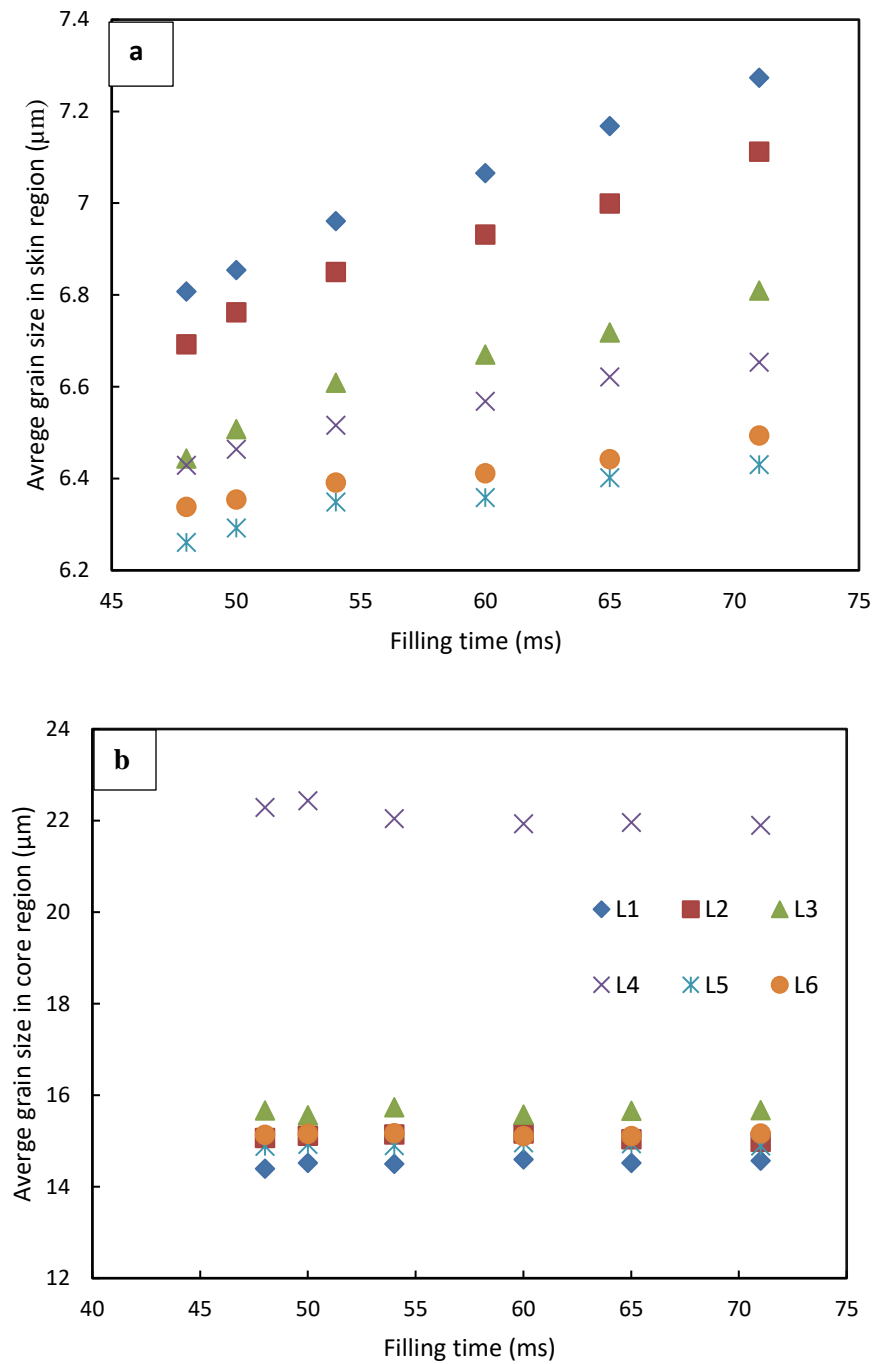


Figure 4.20: Dependency of average grain size on the variation of filling time at a) skin region b) core region.

4.4 Discussion

4.4.1 Effect of Process Parameters on the Grain Size Distribution

As shown in Figure 4.16 there is a significant variation in the die surface temperature values at different locations, determined from the simulation method while the IHTC value and the initial die temperature were constant for all locations. The die surface temperature value at locations near the gate is higher as compared to die surface temperature at the other locations. This is because there is a higher contact time duration between flow and die in locations closed to gate (for example L1 and L2) as compared to other locations (for example L5 and L6). Therefore, the more heat is extracted from liquid to die in locations close to gate, and the local die surface temperature is expected to be higher than in other locations. In addition, the die surface temperature in Location 5 shows the lowest value even less than the value in Location 6. This is due to the fact that there is less amount of flow touches the die in Location 5 that location in comparison with Location 6 that the flow movement continue from the position of Location 6 to fill over flow, as shown in Figure 4.13. Thus, higher contact time duration between dies and flow in the Location 6 lead to increase die surface temperature as compared to Location 5.

The dependency of D_s on the filling time for different locations confirms the impact of contact time duration between die and flow on the grain structure. As shown in Figure 4.20, the filling time has more influence on the D_s in locations which are near the gate as compared to other locations. The decrease in filling time makes reduction in the time duration of flow movement in the locations near to gate in comparison with the farther locations. Actually, the reduction in filling time reduces the die surface temperature. As a result, the lower die surface temperature increases the local cooling rate closed to the die, consequently D_s is reduced. To study the impact of filling time on D_s , the local molten temperature should be taken into account. The lower filling time keeps the liquid phase temperature at higher level during the filling process; therefore, more heat in the liquid phase can be preserved. As a result, a higher cooling rate is induced, especially in the skin region. Guo, et al. [40] confirmed that a higher fast shot velocity may lead to a higher metal temperature during the filling process; therefore, more liquid phase can be preserved. The effect of the filling time on the grain size distribution can be categorized in two

contributions. The first is the original contribution through which the heat is retained in the flow and second is the additional contribution to the time duration between dies and flow. Actually, the second contribution of filling time increases the values of D_s in the locations close to gate more than the locations farther away.

The variation of die surface temperature at different locations can be explained by the local flow direction during die filling. Z.W. Chen [94] pointed out that the die surface temperature value in the direct impingement situation was higher than the indirect impingement situation. It has been attributed to the molten metal hit directly the die, the more heat is transferred to the die at the end of the die filling stage. The flow pattern direction of the molten metal injected into the cavity from the gate is parallel to die in Locations 1 to 4, but flow direction is changed in Location 5 and 6 as shown in Figure 4.13. Hence, the local die surface temperature in the position of direct impingement flow (Location 1 to Location 4) is expected to be higher than that in the position of indirect impingement flow (Location 5 and 6). The way that the liquid flows to come into contact with the die wall during die filling plays a significant role on the die surface temperature.

As shown in Figure 4.19, the value of D_s is increased as the initial die temperature is increased. This is due to the linear inverse relationship between the initial die temperature and the die surface temperature. However, the IHTC values and die temperature have more influence than on D_s as compared to the filling time, as shown Figure 4.18 (a), Figure 4.19(a) and Figure 4.20(a). In addition, it can be seen in Figure 4.18(b), Figure 4.19(b) and Figure 4.20(b), that the dependence of D_c on die temperature and filling time variation relatively insensitive as compared with the effect of IHTC on D_c . These findings reveal that the IHTC has significant contribution in the grain structure through cross section of casting as compared to other factors.

As shown in Figure 4.18, Location 1 and 2 show higher value of D_s as compared to other locations, even Location 4 which has highest thickness. Additionally, the same trend was observed for different process parameter at fixed value of IHTC as indicated in Figure 4.19 and Figure 4.20. This is because there is a significant variation in the die surface temperature at different locations, as shown in Figure 4.16. This observation confirms that

the D_s is more sensitive to local die surface temperature than the thickness of location in the complex die cast component. As indicated in Figure 4.18, 4.19 and 4.20, Location 4 has highest value of D_c and the lowest value of D_c is in Location 1 when the same process parameter is applied at a fixed value of IHTC. This difference is attributed to the fact that there exists variation in thickness of locations as presented in Table 4.4. In addition, the same trend can be observed for other locations that the D_c is increased with increasing the thickness. This is because the heat transfer coefficient was decreased due to the formation of air gap during solidification through the cross section of casting which agrees with the literature. Therefore, the above discussion points out that the dependence of the D_s on thickness variation is relatively insensitive as compared with D_c .

4.4.2 Prediction of Grain Size

Figure 4.21 to 4.26 present comparison of experimental result and the predicted value using Stefan approach in grain size through the cross section of casting thickness. The error bars represent one standard deviation resulting from three shock towers. However, the Stefan approach underestimates the grain size value in the core region for all locations. In addition, the predicted grain size values in the skin region for Location 1 and 2 indicate a deviation of approximately 10 % while the estimated value of grain size in the skin region for other locations shows less than error percentage of %2. This can be attributed to the presence of ESGs within the skin or core region, due to incipient solidification in the shot sleeve. As shown in Figure 4.21 to 4.26, the prediction of grain size distribution from Stefan approach compare quite well with measured grain size with excluding ESGs. When the metal is injected into the cavity, the contact between metal and the wall of shot sleeve and plunger, generate a large fraction of ESGs. As shown in Figure 4.12 the position near the gate (Location 1 and Location 2) include significantly larger fractions of ESGs whereas this microstructural feature are more dilute in the position farther away from the gate. This observation in the position of ESGs is consistent with previous investigation [27, 29] on the complex die cast magnesium alloys. It was reported [27] that the positions of ESGs depend on the condition of shot sleeve, die temperature and initial melt temperature. The ESGs occupy significantly larger volume fractions (Figure 4.12) at the center whilst the ESGs are more dilute when farther away from the center. This can be explained by this

morphology of grains formed in the shot sleeve prior to inserting the die cavity and the migration of them to the center as a result of lift forces acted on the solid. As a result, the underestimation of grain size in core region by Stefan model can be justified to the formation of large grains during the filling of cavities. However, the Stefan approach enables us to predict grain size distribution across section of casting thickness by excluding ESGs with accuracy.

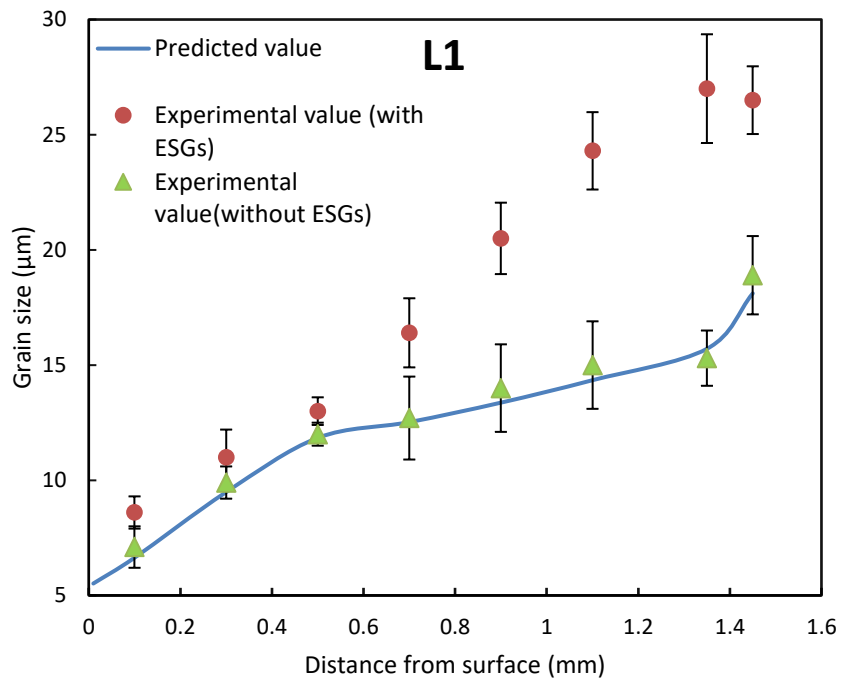


Figure 4.21: Comparison of the experimental results and predicted values using the modified model in term of grain size from surface to center for Location 1.

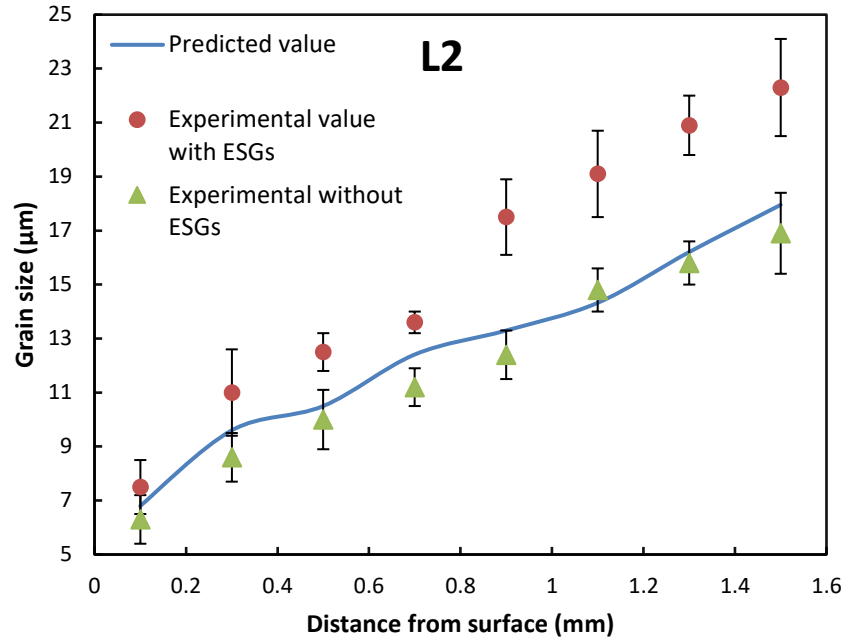


Figure 4.22: Comparison of the experimental results and predicted values using the modified model in term of grain size from surface to center for Location 2.

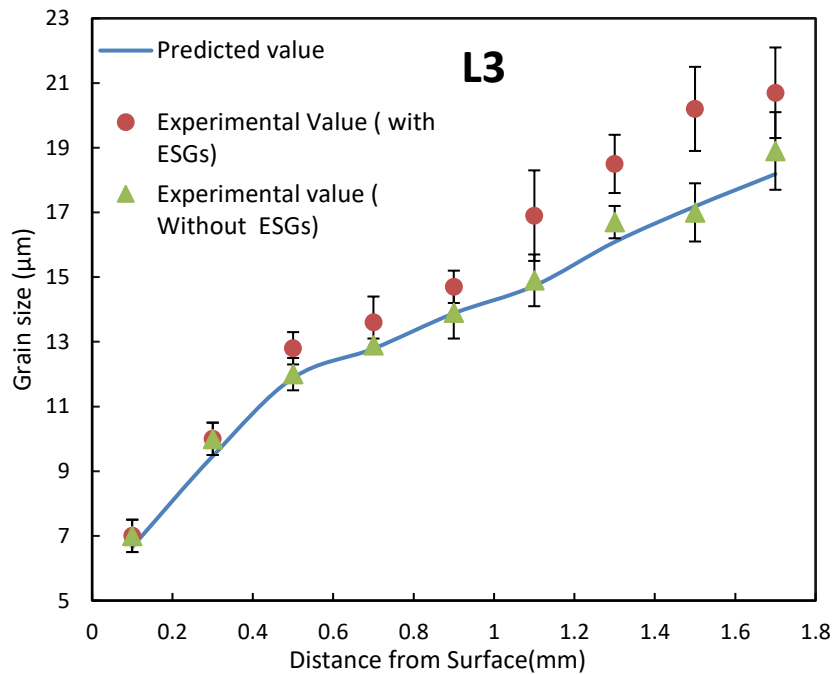


Figure 4.23: Comparison of the experimental results and predicted values using the modified model in term of grain size from surface to center for Location 3.

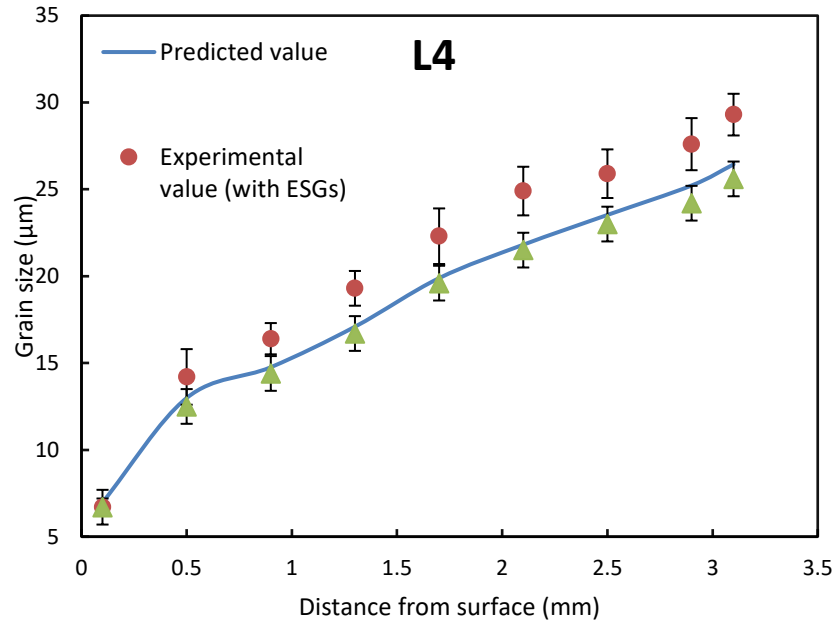


Figure 4.24: Comparison of the experimental results and predicted values using the modified model in term of grain size from surface to center for Location 4.

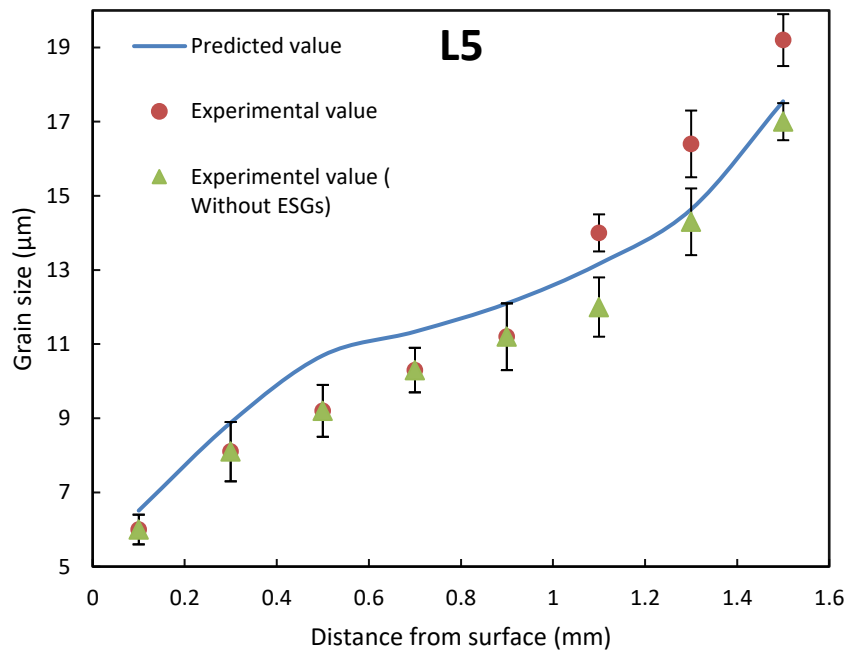


Figure 4.25: Comparison of the experimental results and predicted values using the modified model in term of grain size from surface to center for Location 5.

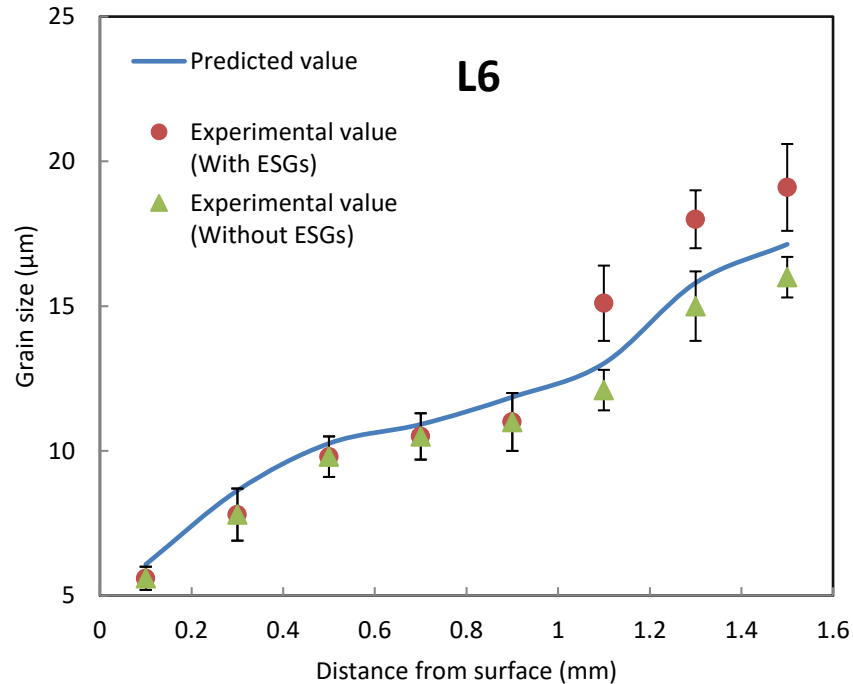


Figure 4.26: Comparison of the experimental results and predicted values using the modified model in term of grain size from surface to center for Location 6.

As shown in Figure 4.21 and 4.22, the skin region of Location1 and Location 2 includes significant fraction of ESGs. It means that the degree of differentiation between the skin and core region is very low in Location 1 and 2. Few previous investigations [12, 27] reported the same observed microstructure of skin region in some locations of die cast component. It was reported that [27] the inhomogeneous distribution of ESGs is affected by the thickness of casting, die temperature, the local geometry of die, flow rate and local solid fraction.

4.4.3 Prediction of Interfacial Heat Transfer Coefficient

As discussed in Chapter 2, determination of heat transfer coefficient between molten metal and die surface is the most challenging issue in the numerical simulation of HPDC. In this study, the simple method is suggested to predict IHTC value especially in complex geometry.

Figures 4.27 to 4.32 indicate the measured grain size through the cross section of casting for each location in comparison with the prediction of grain size using the Stefan model with different values of IHTC. It should be noted that the prediction of results was determined under reference process parameter condition. As discussed, the origin of ESGs is related to the solidification conditions present in the shot sleeve, therefore, the size effect of ESG is removed in the measurements of grain size which are presented in Figures 4.27 to 4.32. In Location 1 to Location 4, the prediction of grain size with IHTC value of $13000 \text{ Wm}^{-2} \text{ K}^{-1}$ is in very good agreement with experimental value whereas in the Location 5 and 6, the deviation of the predicted grain size using IHTC value of $14000 \text{ Wm}^{-2} \text{ K}^{-1}$ from experimental results is lowest as compared to other IHTC values. This comparison enables us to estimate the best value of IHTC for each location in the complex die cast component without performing any tests. In order to make validation, the estimated value of IHTC has been compared with the data in the previous investigation. The IHTC values are listed in Table 4.5 for the casting process with applied pressure. There is significant fluctuation in the IHTC value which has been reported in the previous report [33-40]. The literature confirms that the IHTC is affected by alloys composition, pressure, casting processing condition, initial die temperature, superheat, geometry of mould and die materials. Gue et al [40] estimated the IHTC value in a range from 10820 to 14,780 $\text{Wm}^{-2} \text{ K}^{-1}$ for different thickness of step-shape casting of magnesium alloy AM50 which was produce by HPDC is in good agreement with the result in this investigation despite there is difference on the thickness and process parameter. They also pointed out [40] that the IHTC value in range $1000 \text{ Wm}^{-2} \text{ K}^{-1}$ to $4000 \text{ Wm}^{-2} \text{ K}^{-1}$ can be increased by the fast shot velocity and the pressure.

The fluctuation of the estimated IHTC value for various locations can be explained by difference on the die surface temperature of each location and local flow direction. Literature [33] confirms that there is an inverse relationship between IHTC values and die

surface temperature in HPDC process. As mentioned, the die surface temperature of Location 1 to Location 4 is higher than Location 5 and 6, as result, the IHTC value in location 5 and 6 is expected to be higher in comparison with Location 1 to Location 4. Despite of the effect of the die surface temperature, the IHTC were influenced by the local flow direction. The heat transfer from the flow to the die is higher in the direct impingement positions (Location 1 to Location 4) than in the indirect impingement zone (Location 5 to 6). When the flow changes its direction, more heat is preserved in the liquid phase at the end of the die filling stage and then extracts more heat from liquid to the wall cavity. In other words, there exists higher super heat in the locations that the flow pattern is changed as compared to other locations that flow direction is unchanged. This finding suggests that the local flow direction as well as local die surface temperature plays a major role in IHTC value.

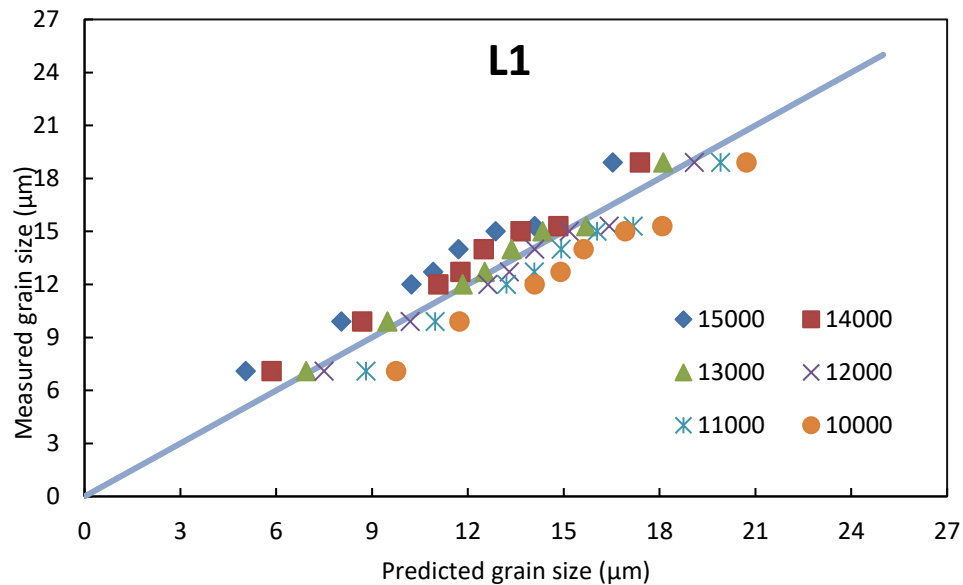


Figure 4.27: Comparison of the measured grain size and predicted values using the modified model for different IHTC value from surface to center for Location 1.

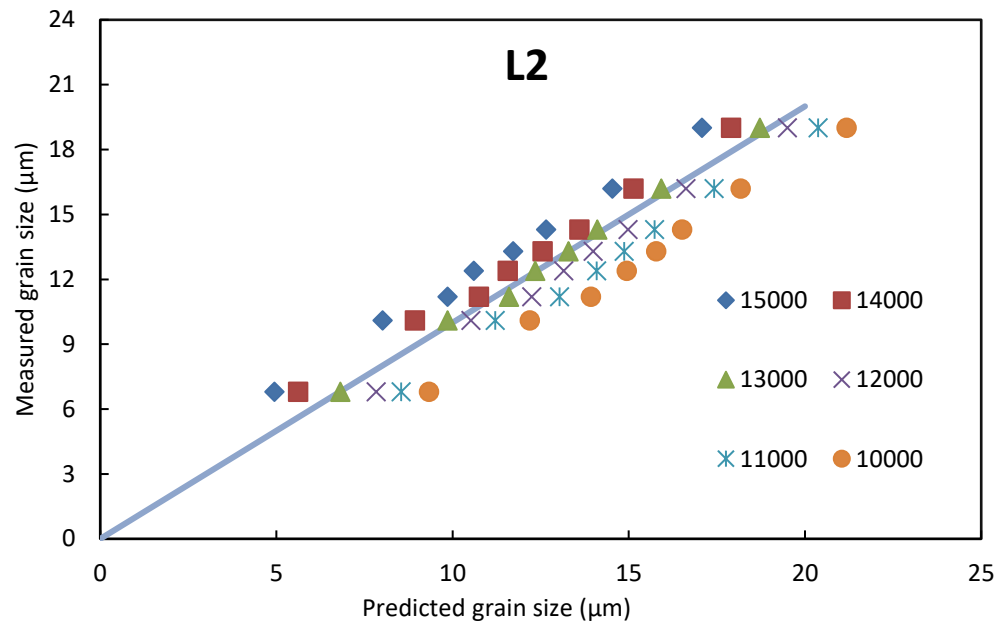


Figure 4.28: Comparison of the measured grain size and predicted values using the modified model for different IHTC value from surface to center for Location 2.

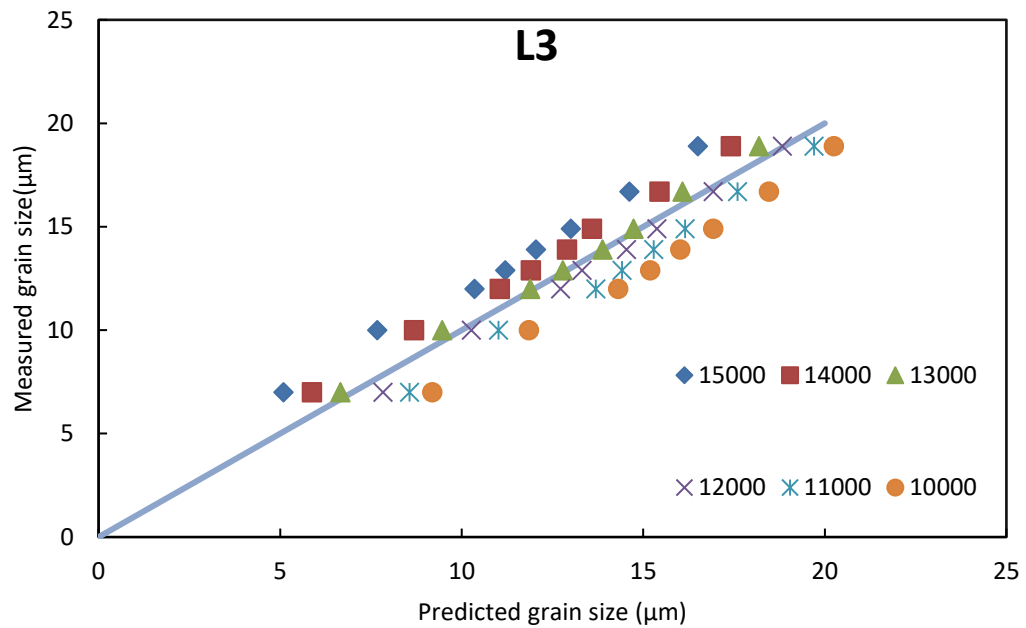


Figure 4.29: Comparison of the measured grain size and predicted values using the modified model for different IHTC value from surface to center for Location 3.

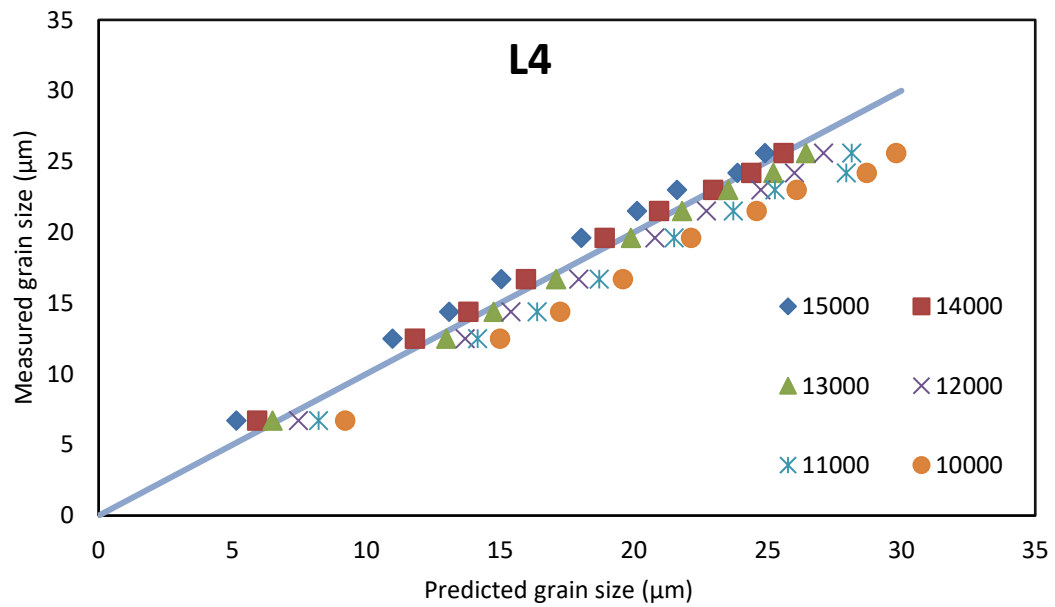


Figure 4.30: Comparison of the measured grain size and predicted values using the modified model for different IHTC value from surface to center for Location 4.

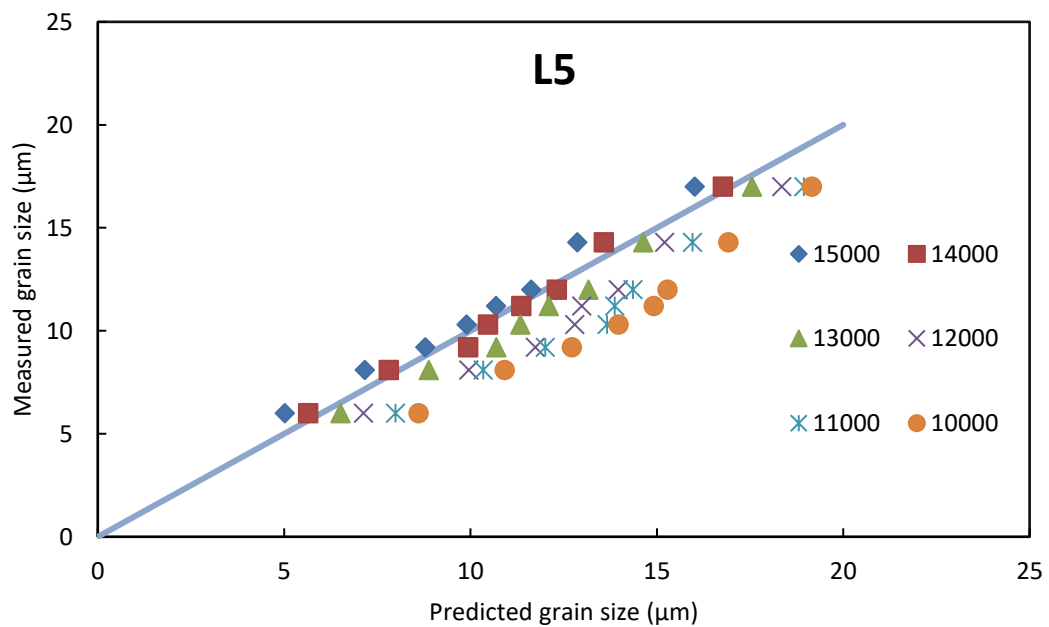


Figure 4.31: Comparison of the measured grain size and predicted values using the modified model for different IHTC value from surface to center for Location 5.

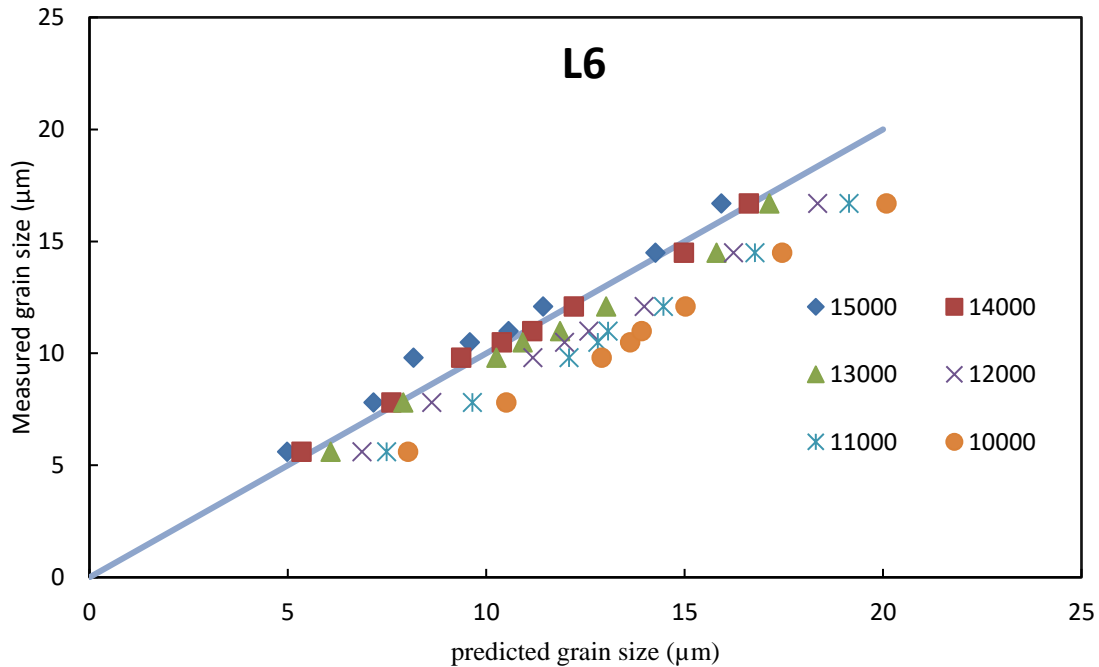


Figure 4.32: Comparison of the measured grain size and predicted values using the modified model for different IHTC value from surface to center for Location 6. Table 4.5: IHTC value for casting process in the literature that the pressure is applied.

Reference	Process casting	Alloy	Features	IHTC (W/m ² K)
[40]	HPDC	AM50	Effect of the thickness, pressure, fast stage velocity of piston are examined	10820 to 14,780
[40]	HPDC	ADC12	Effect of intensification pressure, fast stage velocity of piston and initial die temperature	16,450 to 20,760
[37]	HPDC	AZ91	Effect of pressure cavity, slow and fast stage velocity pressure are investigated	8500 to 9000
[32]	Squeeze casting	AM60	Pressure range: 30 to 90 MPa Effect of thickness is examined	7195 to 10649

4.4.4 Determination of Skin Thickness

Various investigations [9, 60, 93] have shown that the skin region has higher hardness and local yield strength as compared to the core region due to the finer microstructure and higher amount of dispersed intermetallic phase in the skin region. Some studies [5, 8] have also shown that the yield strength of die cast magnesium alloy is controlled by the skin region. Therefore, in order to predict mechanical properties, it is critical to determine the skin thickness or area fraction of that region [60, 93]. As discussed in Chapter 2, the distinction between the skin and core regions is attributed to the variation of cooling rate from the wall mold to the center. However, those investigations lack systematic studies regarding the effect of the local cooling rate on skin thickness. Weiler et al. [9] showed varying skin thickness measurements applicable to the different local solidification conditions in the complex AM60 HPDC, but the influence of cooling rate on the formation of skin thickness was not quantified.

This section focuses on the determination of skin thickness based on the variation of cooling rate versus the distance from the mold surface. As discussed in section 4.3.1, R_{10} and R_{11} are cooling rate values corresponding to the average grain size of 10 and 11 μm . As shown in Figure 4.17, the cooling rate for each point across thickness of die casting sample can be determined. In order to determine skin thickness, the intersection between the threshold cooling rate value and the cooling curves obtained from the one-dimensional Stefan solution would give the skin thickness values at a distance from the mold wall of the casting, as shown in Figure 4.33. The skin thickness is calculated using the mentioned method for two conditions: 1) R_{10} and 2) R_{11} . Figure 4.32 shows the calculated thickness value of five samples which were cut from top hat.

In previous studies [9, 57-60, 93], the skin thickness was defined by some criteria such as the size of the grains, hardness profile, the concentration of intermetallic phase, location of ESGs and the position of porosity or defect band. The advantage of the method developed in this study as compared with previous research is that the skin thickness was directly defined based on the variation in the cooling rate from surface to center. Additionally, the skin thickness was successfully determined without performing any tests.

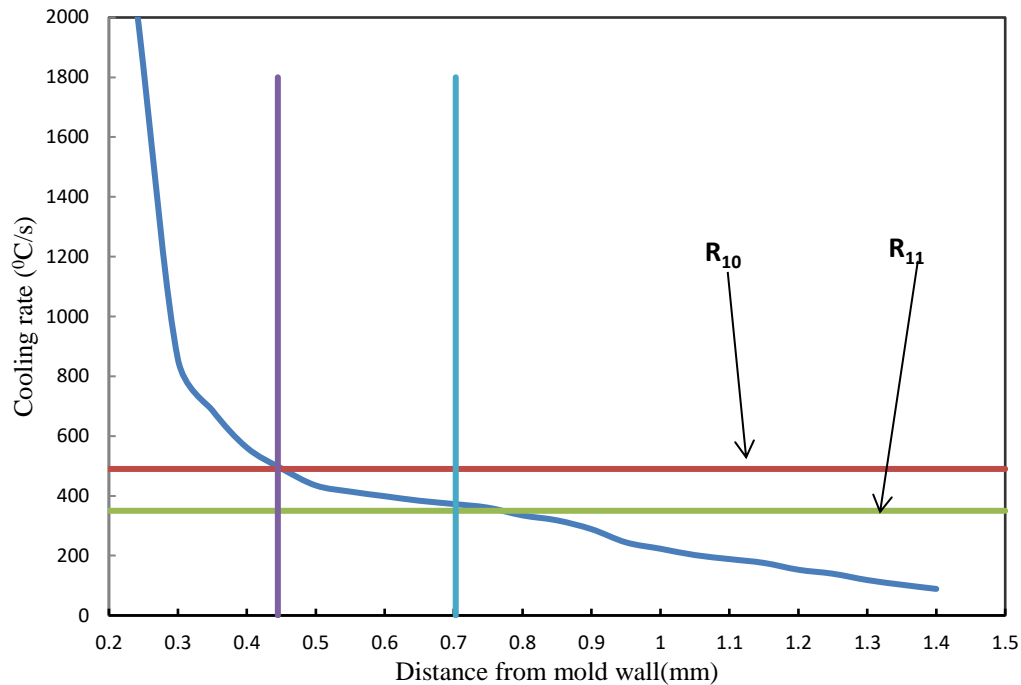


Figure 4.33: Cooling rate variation from mold wall to casting centerline. As shown in Figure 4.17, the cooling rate for each point a cross thickness of die casting sample can be determined.

Figure 4.34 shows the measured skin thickness for each location in comparison with the prediction of skin thickness using the modified model with different values of IHTC. This comparison enables us to estimate the best value of IHTC in the die cast component without performing any tests. The prediction of skin thickness with IHTC value of $12000 \text{ Wm}^{-2} \text{ K}^{-1}$ is very good with experimental value as compared to other the IHTC values. As shown in Figure 4.34, the predicted skin thickness values are increased with increasing in IHTC value for all locations. This can be attributed to the higher IHTC value leading to increases average cooling rate near to the surface. As a result, the region including fine grains is expanded.

As discussed, the transition from the skin region to the core region can be determined by the average cooling rate threshold values of 375 (R_{10}) to 490 (R_{11})°C/s. Power law regression analysis was carried out in order to quantify the relationship between cooling rate and skin thickness from R_{10} to R_{11} . Figure 4.35 illustrates the thickness of skin as a

function of cooling rate. This finding also confirms that the role of cooling rate on the development of the relative differentiation between the skin and core. In other words, this method gives us opportunity to predict an appropriate range of cooling rate that skin can be formed.

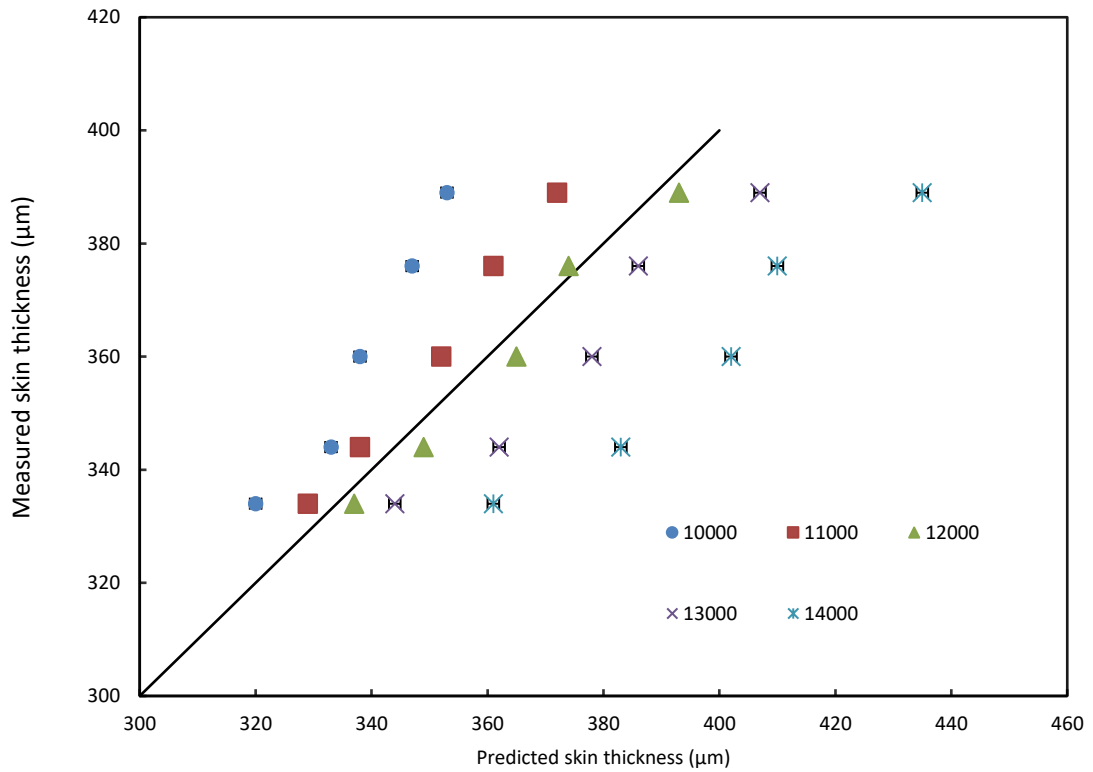


Figure 4.34: Accuracy of predicted skin thickness with different IHTC value.

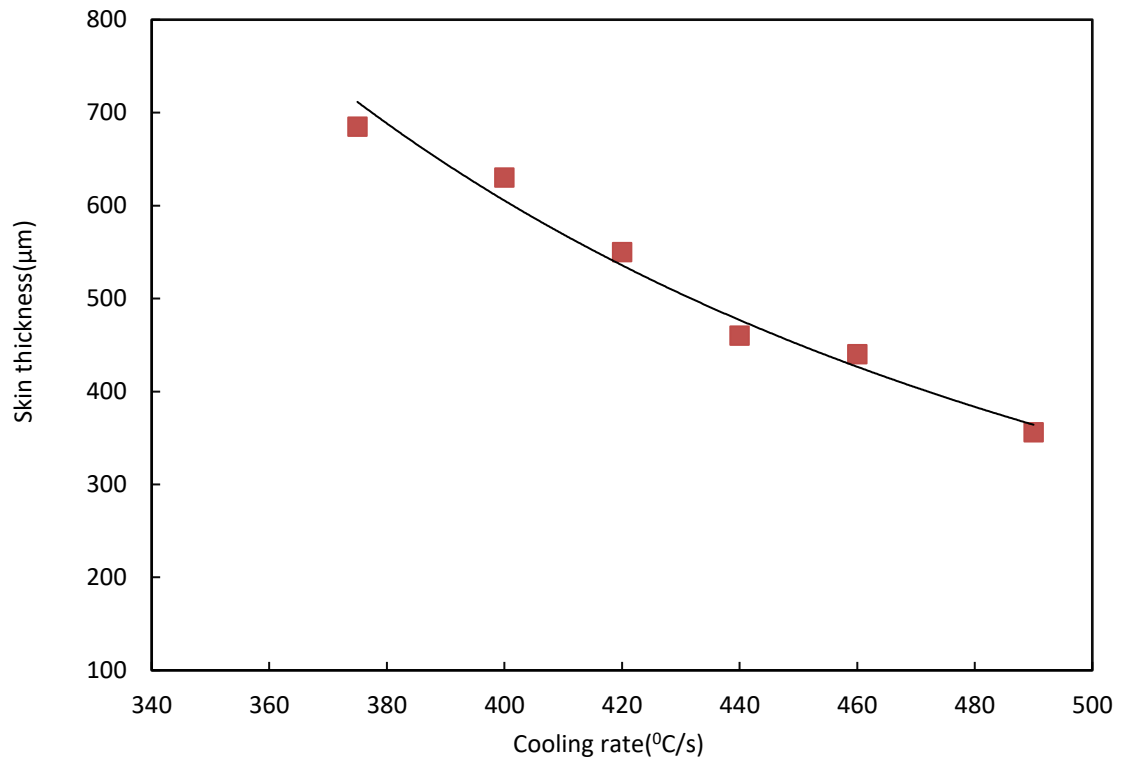


Figure 4.35: Skin thickness as a function of cooling rate. The cooling rate should be higher than 375 °C/s that skin can be formed.

4.4.5 Prediction of Yield Strength for Different Locations

An approach is proposed [5] to model the microstructure as a composite of skin and core regions, based on their respective grain sizes. Thus, with a measure of the relative thickness of the skin and core regions, a modified Hall-Petch equation can be written as:

$$\sigma_y = \sum f_i (\sigma_0 + k d^{1/2}) \quad (4.19)$$

where, f_i is the fraction of the thickness of the skin or core region. To quantitatively determine the effects of grain size on the yield strength, the modified Hall-Petch equation was applied. In Section 3.4, microindentation testing was used to determine the Hall-Petch equation for average grain sizes from 4.8-95 μm and found $k = 152.9 \text{ MPa}\cdot\mu\text{m}^{-1/2}$, and $\sigma_0 = 62.1 \text{ MPa}$. Substituting Hall-Petch parameters into the **Eq.4.11**, gives.

$$\sigma_y = \sum f_t (62.1 + 152.9d^{-\frac{1}{2}}) \quad (4.20)$$

The data measured in this study, average grain sizes range from 5 to 9 μm in the skin region, and from 12 to 17 μm in the core region. It should be noted that the average grain size for core region without ESGs ranges from 9 to 11 μm and the sizes of ESGs are from 38 to 40 μm . Thus, the area fractions of three different regions were measured to be used in the modified Hall-Petch equation. Figure 4.36 compares the yield strength obtained by experiments (Section 4.1.4) and prediction using modified and conventional Hall-Petch equations.

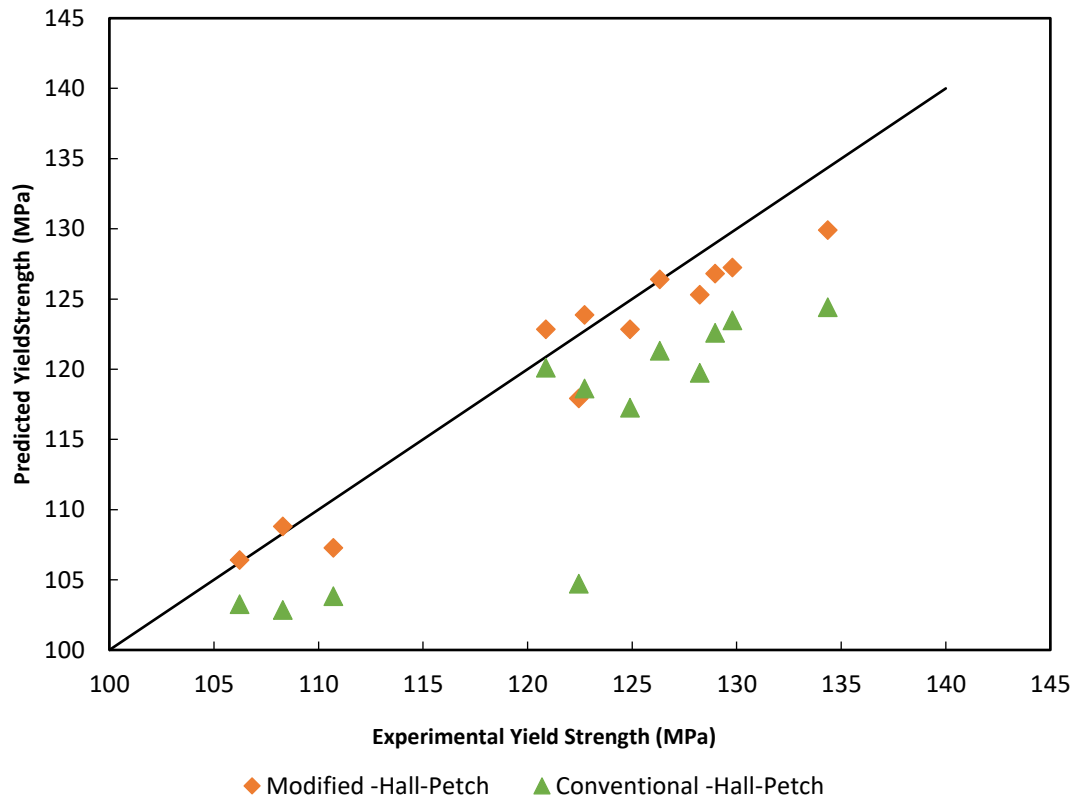


Figure 4.36: Accuracy of predicted yield strengths of specimens cut from a Top-Hat die casting.

The errors for the predictions are 1.9% and 7% for the modified and conventional Hall-Petch equation, respectively. This finding confirms that the yield strength predicted by the modified Hall-Petch is in very good agreement with the experimental results, better than the predictions of the conventional Hall-Petch equation. This can be explained as that the modified Hall-Petch equation takes into account the difference in grain size across the thickness of the die-casting samples. The smaller deviation using the modified Hall-Petch equation confirms the contribution of skin layer on the overall yield strength.

4.4.6 Prediction of Elongation

As discussed in Section, 2.6.3 C. Caceres [81] proposed the failure model which is able to predict the effect of internal porosity on the elongation. This model is well suited to microstructures of HPDC that contain pre-existing pores. Under the assumption that the material containing internal porosity f , exists in axial local equilibrium under tensile loading, the conventional equation for stress distribution can be expressed in terms of load carrying area as the following equation:

$$(\varepsilon_i)^n (1 - f) \exp(-\varepsilon_i) = (\varepsilon_h)^n \exp(-\varepsilon_h) \quad (4.21)$$

Where n is the strain-hardening coefficient of the material and ε_i is the critical strain in the region surrounding the spherical pore and ε_h is fracture strain. Recently this model was modified by Weiler et al. [74, 75] who suggested a modified form of failure model which contains the strain concentration factor which considers the location parameter for the distribution of porosity. This modified failure model for HPDC alloys is given as:

$$\varepsilon_f = 0.016f^{-0.3} [0.18Ln(\delta_L) + 1.17] \quad (4.22)$$

δ_L can be determined by following equation:

$$\delta_L = \frac{d_i - r}{t} \quad (4.23)$$

where, d_i is the distance from the center of the equivalent pore to the edge of the sample; r is the radius of the equivalent pore and t is the thickness of the specimen. This model is

able to clarify the role of porosity location on the fracture strain. In this study, the modified failure model was used to estimate the range of tensile elongation for corresponding area fraction of porosity.

This model requires the inputs of the area fraction and the location of the porosity. Due to the skin region of HPDC magnesium alloys is typically free from porosity, we assume a minimum tensile elongation when the pore is located adjacent to the skin, while a maximum tensile elongation occurs for pores located at the central point of the specimen. The thickness of the skin region then can be used as a minimum distance from a possible pore location to the specimen surface, substituting for the parameter expression: $(d-r)$ in **Eq4.14**. The skin thickness has been used from the results of section 4.4.4.

In this section, three different terms were used to evaluate amount of porosity: bulk porosity, fractographic porosity and shrinkage porosity. The bulk porosity was obtained by measuring the area fraction of porosity into the surface which is close to the fracture surface. The fractographic porosity was expressed as the area ratio of porosity to the entire area of a fracture surface. The area of porosity on fracture surface was measured by scanning electron microscope (SEM) according to the quantitative fractographic technique. Figure 4.37 shows the typical as-polished microstructures and fracture surface for a sample of the Top hat casting.

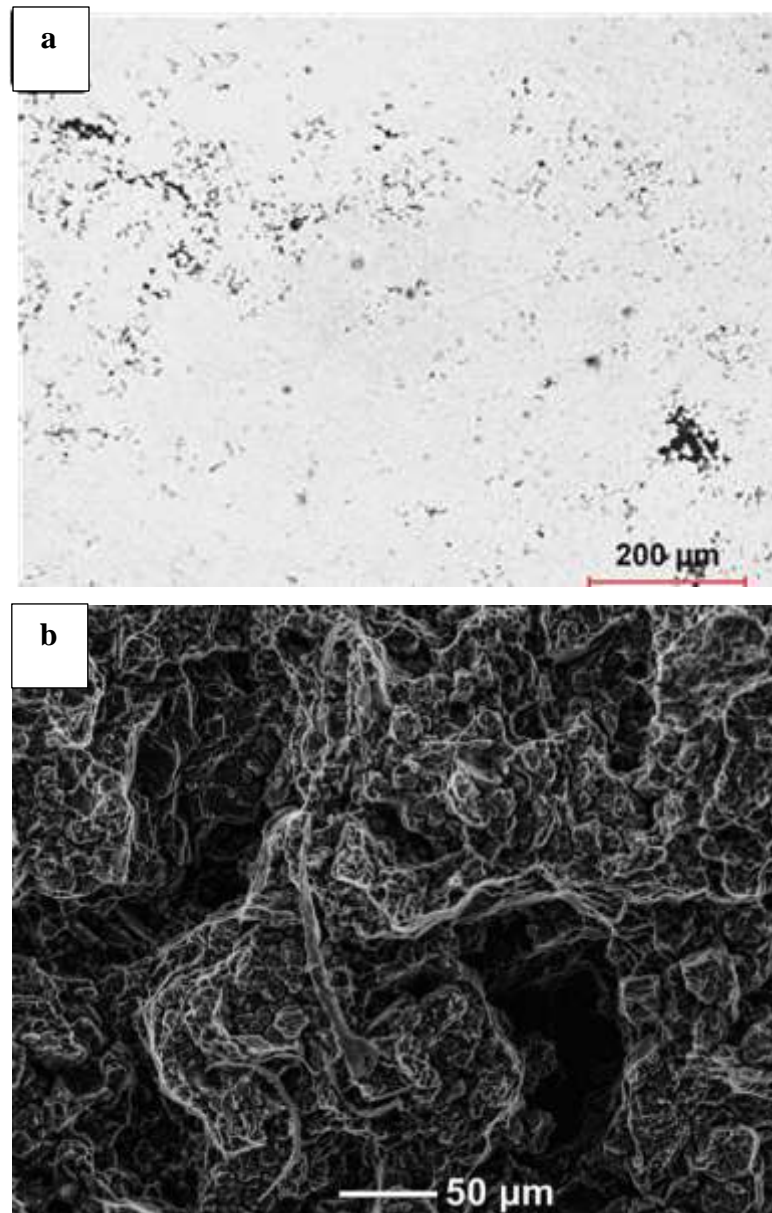


Figure 4.37: a) The presence of porosity and shrinkage into the surface which is close to the fracture surface. b) SEM image of a fracture surface of the HPDC AM60 alloy.

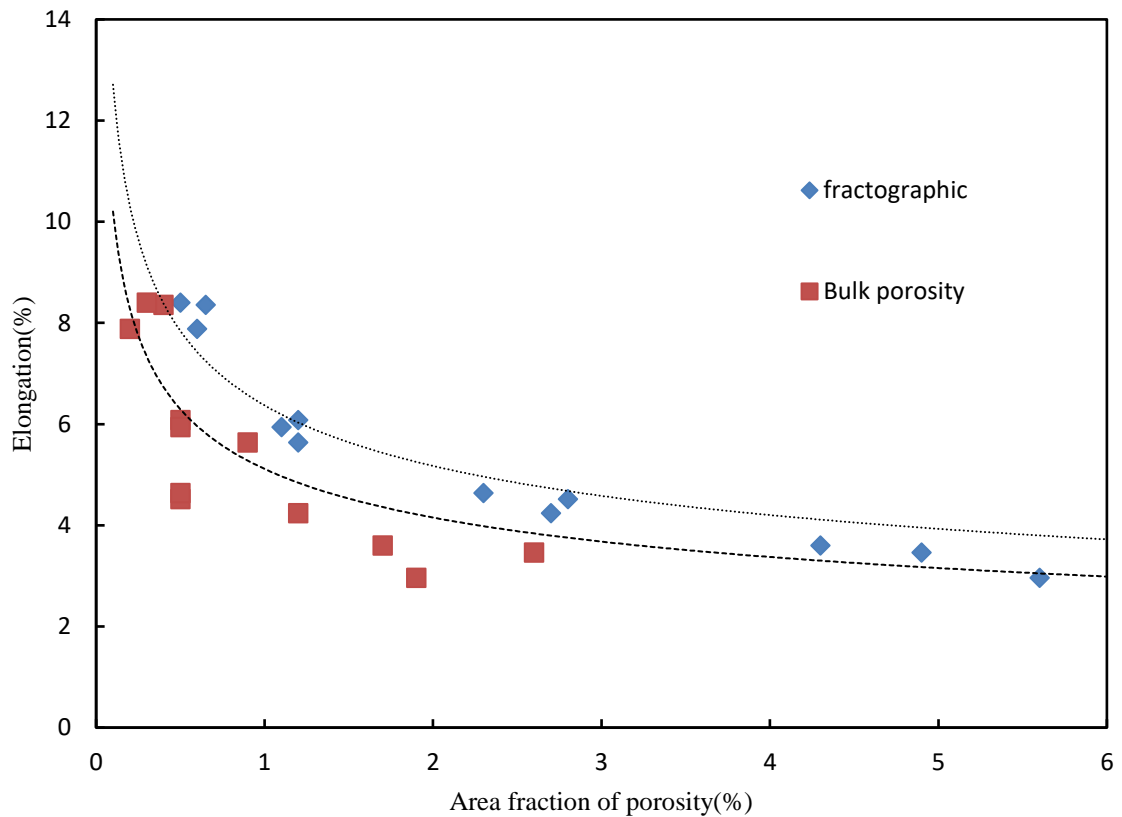


Figure 4.38: Predicted tensile elongations as a function of area fraction of porosity using the modified analytical model compared with experimental tensile elongations.

The predicted values of tensile elongation (lower bound or upper bound) using the modified models are presented in Figure 4.38, in comparison with the experimental results. The area fraction of porosity was measured with three methods for each sample: bulk porosity and fractographic porosity. In the case of fractographic porosity, the tensile elongations generally fit well with the prediction while the shrinkage porosity shows considerable variation with the predicted range. This is attributed to the simulation which neglects the gas porosity in the measurement of area fraction of porosity. In the case of bulk porosity, the average error percentage is 7.1% as compared to the predicted range. Figure 4.38 also exhibits there is a slight difference between the predicted elongation versus fractography and the tensile elongation. It should be noted that the area fraction of porosity used in the Ghosh model or the modified model is based on the porosity measurement of pre-facture. Thus,

the mentioned variation might be attributed to the growth of internal defects during tensile testing, especially in higher elongation values. However, the tensile elongation versus fractography predicted by the modified failure model is in very good agreement with experimental results. This model gives researcher a possibility to estimate the local elongation across a die-cast component with the knowledge of local area fraction of porosity and skin thickness.

Chapter 5

5 QUANTITATIVE EXPERIMENTAL STUDY OF DEFECTS INDUCED BY PROCESS PARAMETERS IN THE HIGH-PRESSURE DIE CAST PROCESS

In this chapter, a quantitative experimental study of the effects of process parameters on the formation of defects during solidification of high pressure die cast magnesium alloy components is presented. As discussed in Chapter 2, the variations in mechanical properties have been found to depend upon casting defects such as gas and shrinkage porosity, defect band and externally solidified grains (ESGs). These defects adversely affect the mechanical properties of die cast magnesium alloys such as ductility and ultimate tensile strength [9, 60, 93, 95]. As discussed in Chapter 2, the amount of defects shows a dependency on the process parameters such as melt temperature, gate velocity, die temperature, intensification pressure, casting geometry, slow stage of piston velocity, fast stage of piston velocity and venting gate area [4, 27, 44-47]. Since various defects are formed by different mechanisms, their dependencies on the process parameters are not the same. Furthermore, most of the previous studies [44-47] focused on simple geometries which ignored the contribution of local filling and solidification on the formation of defects. The formation of defects in large, complex castings is influenced by location in the casting, due to different molten metal flow characteristics and location in the casting such as knit line, last-to-fill, last-to-solidify and close-to-gate.

In this work, the amount of defects in magnesium alloy components was quantitatively characterized. Multiple runs of the commercial casting simulation packages, ProCAST™ and MAGMASoft, are used to model the mold filling and solidification events. Several locations in the component including knit lines, last-to-fill and last-to-solidify are identified as the critical regions that have a high concentration of defects. The area fraction of total porosity, shrinkage porosity, gas porosity and externally solidified grains (ESGs) are measured by metallographic methods and x-ray tomography. In this chapter, the process of die cast component production was carried out by experiment and simulation method to focus on three central aims. First, effect of process parameters on the formation of defects

have been quantified. Second, a new mechanism for prediction of defect band position in the complex geometry has been suggested. Third, impact of knit line conditions on the formation of defects have been investigated.

5.1 Experimental Procedure

In this chapter, two experiments have been conducted. First, defect formation was quantitatively evaluated for a shock tower casting which was produced with different process parameters. In the second experiment, the gating design in the top hat casting was modified and effect of the modifications on knit lines and the formation of defects was assessed.

5.1.1 Shock Tower

The casting experiments were conducted at CanmetMATERIALS laboratory in Hamilton, Canada. The magnesium alloy AM60 castings were produced using a 1200 tons, Buhler Carat 105, cold chamber die cast machine. The nominal chemical composition of the alloy is given in Table 3.1.

Figure 5.1 shows the geometry of shock tower and the locations of biscuit, runners, gates, vents, and overflows. The die tool was designed to be evacuated during filling to reduce the of gas porosity. To obtain a quasi-steady-state temperature in the shot sleeve and die, 10 shots were made before producing the investigated casting in this experiment.

Coupons used in the characterization of casting microstructure were obtained from six different locations in shock tower. Six samples of 2mm×1mm×3mm were extracted from different locations as shown Figure 5.1. The local solidification condition for each location was identified by simulating the filling and solidification processes. The shock tower has been produced by different sets of process parameters as indicated in Table 5.1. In this segment, the effects of slow stage of piston, fast stage of piston, intensification pressure and die temperature on the variation of defects were investigated. Other process parameters such as: melt temperature, vent area, die and plunger lubrication were kept the same during HPDC process. Three castings for each set of process parameters were chosen for

evaluation. The slow and fast shot velocities and intensification pressure values were extracted from the recorded shot profile as shown in Figure 5.2.

Table 5.1: The different Sets of process parameters.

Process parameters	Slow shot speed (m/s)	Fast shot speed (m/s)	Intensification pressure (bar)	Die temperature (°C)
A	0.9	5	600	160
B	0.7	5	600	160
C	0.9	3	600	160
D	0.9	5	400	160
E	0.9	5	600	240

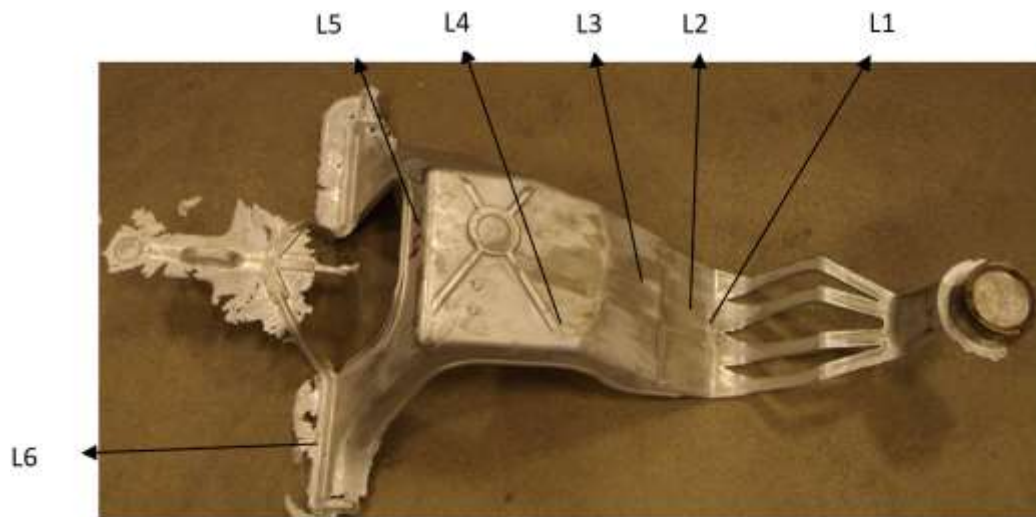


Figure 5.1: The shock tower casting with gates and overflow. Selected locations for the characterization are marked from L1 to L6.



Figure 5.2: The shot profile of one casting from HPDC

5.1.2 Production of Top Hat

There are two regions where knit lines might occur during filling of cavity in HPDC process. The first region exists close to gate where the runners are designed to meet together. Second region is far from gates and closer to overflow. Top hat contains four runners and eight gates, therefore, will be very suitable for the evaluation of knit line formation in both regions. To develop knit lines at different regions three different ingate (Figure 5.3) modes are designed as follows:

Mode (1): All Four runners are utilized to fill the casting; in this case knit lines will develop closer to ingates

Mode (2): One runner in the middle is blocked; in this case a mix of knit lines will form.

Mode (3): Two runners in the middle are blocked, as a result, the knit lines will form far from overflows.

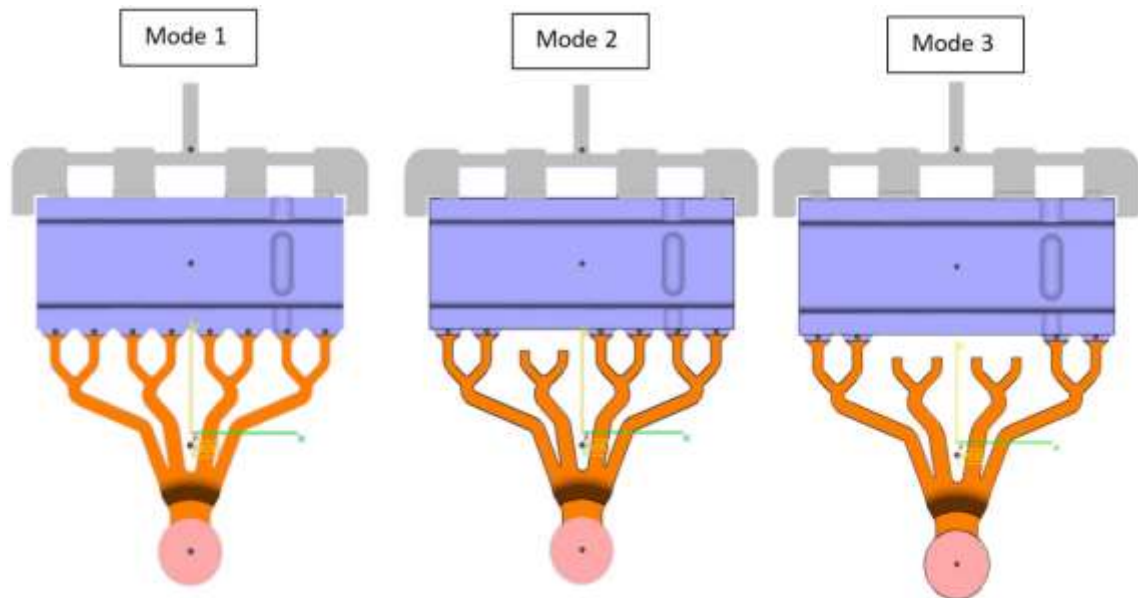


Figure 5.3: Three different gate configurations to study knit line formation and impact.

5.1.3 Defect Analysis

In this chapter, evaluation of different of defects were quantitatively conducted by two methods: Optical microscopic analysis and X-ray tomography analysis. Optical microscopic and image analysis were employed to measure total porosity including, shrinkage porosity, gas porosity, defect band and ESGs. The distribution and area fraction of porosity were characterized by X-ray tomography analysis in the segment of knit line study.

5.1.3.1 Optical Microscopic Analysis

The Sample preparation for microstructural examination was as follows:

- wet grinding with progressively finer grades of sandpapers from 180 to 1200
- polishing with slurries of 1 μm , and finally 0.5 μm diameter alumina in water and ethanol on an automatic polisher with a applied force of 10 N at a polishing speed of 15-20 rpm

- After polishing, the specimen was thoroughly washed with ethanol and ultrasonically cleaned.
- Optical microscope and CLEMEX image analysis software were used to measure the area fraction of porosity.

Data on the total area fraction of gas porosity, shrinkage porosity and ESGs were determined by taking an average for 15 individual frames on each specimen, at a magnification of 100x. In this study, gas porosity has been separated from shrinkage porosity based on their shape difference. The gas porosity is assumed to have round shape in 2D image while shrinkage porosity appears like a thin long crack. Figure 5.4 shows a flowchart algorithm for the separation procedure of gas and shrinkage pores. First, the image is converted into its binary image by thresholding as shown in Figure 5.5(b). Second, the gas porosities with a diameter larger than 20 μm are separated from the field of view as shown in Figure 5.5(c). Third, the separation of small gas porosity from shrinkage porosity was accomplished using the differences in roundness factor. The following equation is the basic definition of roundness factor in image analyses software.

$$\text{RoundnessFactor} = \frac{4 \times \text{Area}}{\pi \times L^2} \quad (5.1)$$

where L is the largest diameter, and the roundness is equal to 1 for a perfect circular object. In this study, the roundness factor of gas porosity is considered from 0.5 to 1. Thus, the shrinkage porosity is separated from gas porosity as shown in Figure 5.5 (d). Finally, the total area fraction of porosity is calculated by adding area fraction of small gas pores to area fraction of big ones.

In order to measure area fraction of defect bands, the images from 12 contiguous fields were montaged as shown in Figure 5.6. The montaged image is converted into its binary image by thresholding (Figure 5.6 (b)) and separating defect band from shrinkage and gas porosity (Figure 5.6 (C)). Finally, the area fraction of defect band is measured using image analysis software. It should be noted that in the samples containing defect band, the area fraction of gas porosity and shrinkage is measured separately using the above mentioned

method. In this study, the total area fraction of porosity contains area fraction of gas, shrinkage and defect band.

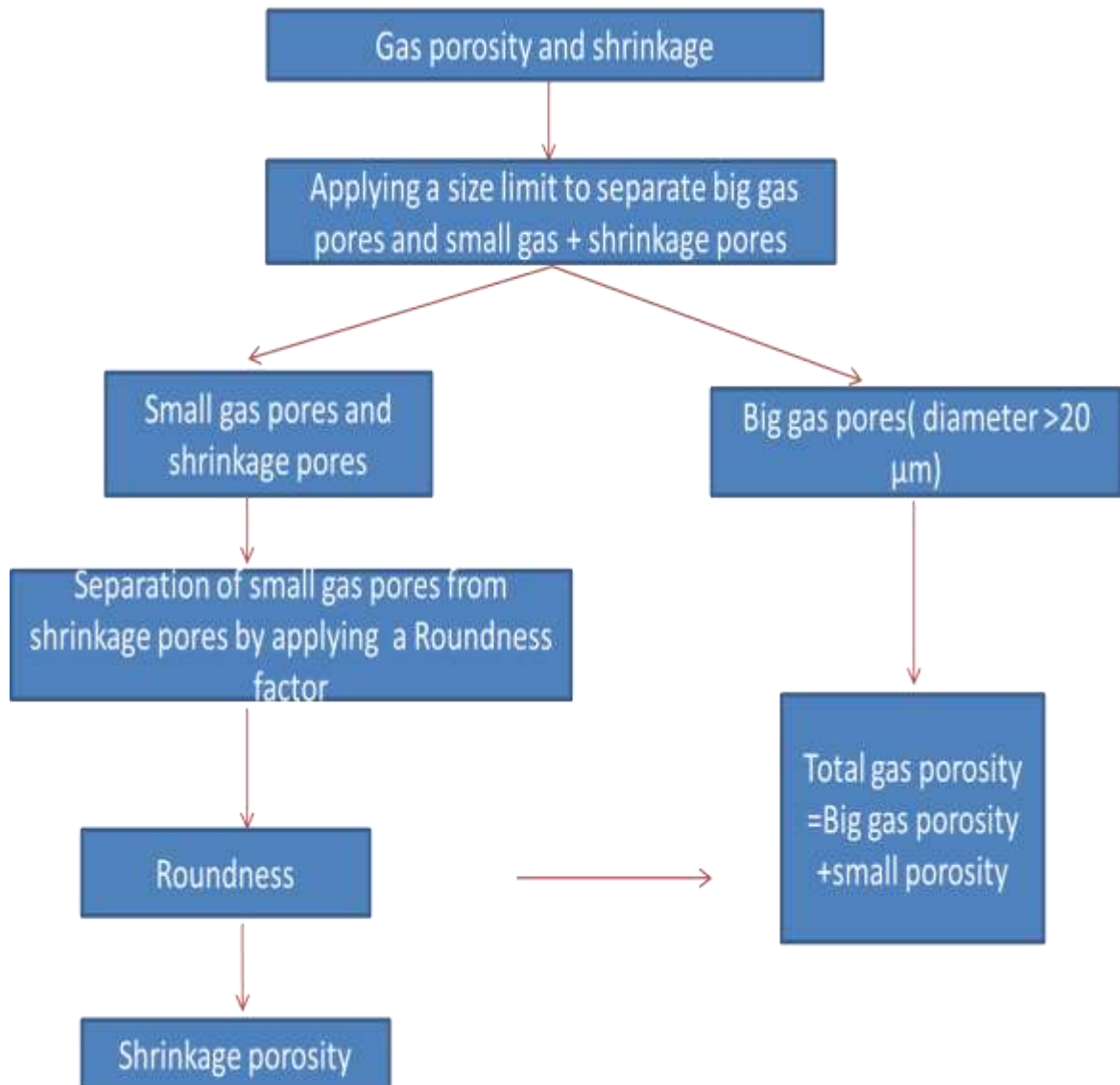


Figure 5.4: Flowchart algorithm for the separation procedures of gas and shrinkage pore.

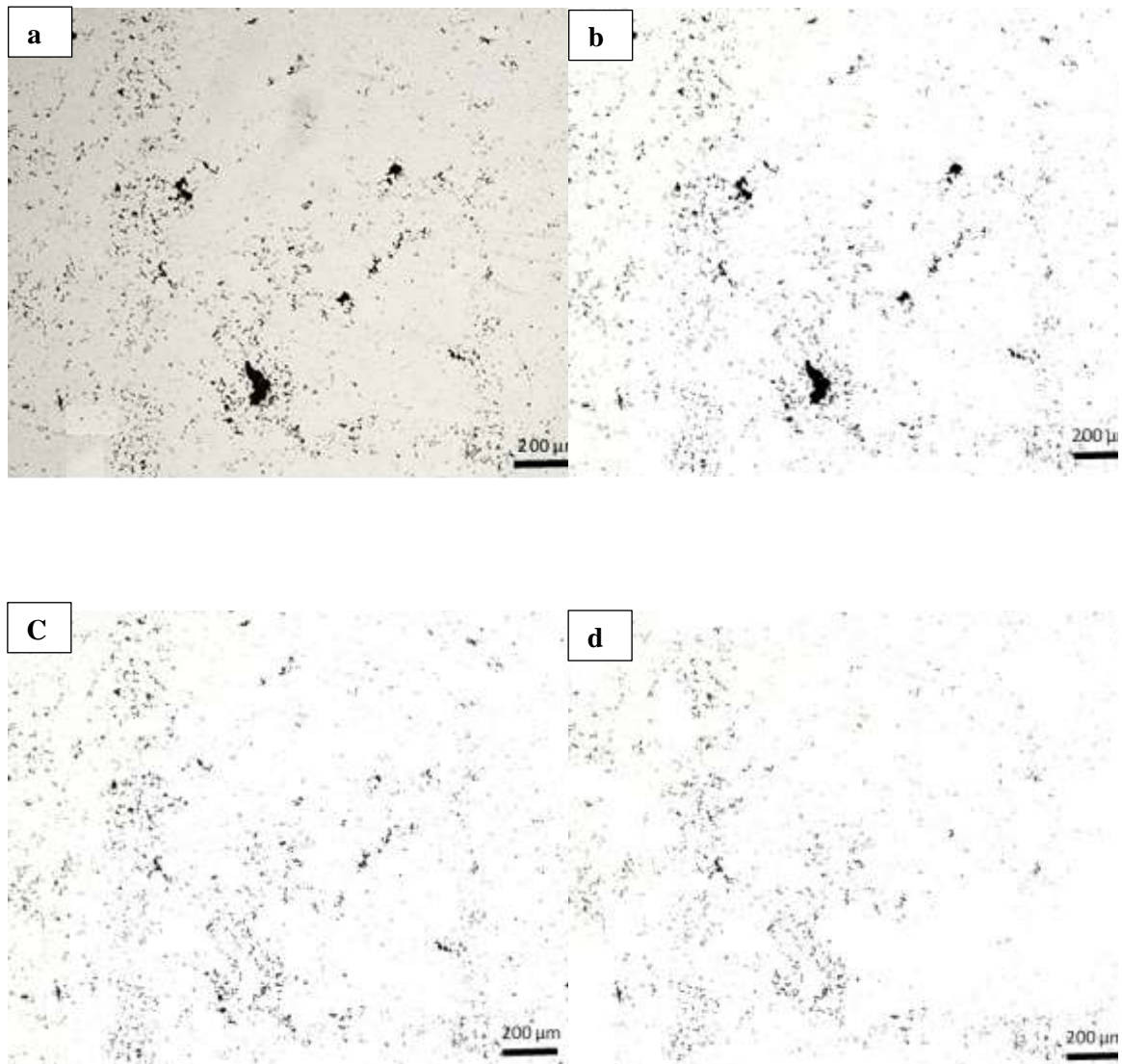


Figure 5.5: Separation of gas porosity from shrinkage a) Gray scale of typical micro structure magnesium alloy AM60 including gas porosity b) Binary image of the gray scale image. c) Small gas pores and shrinkage porosity. d) Shrinkage porosity.

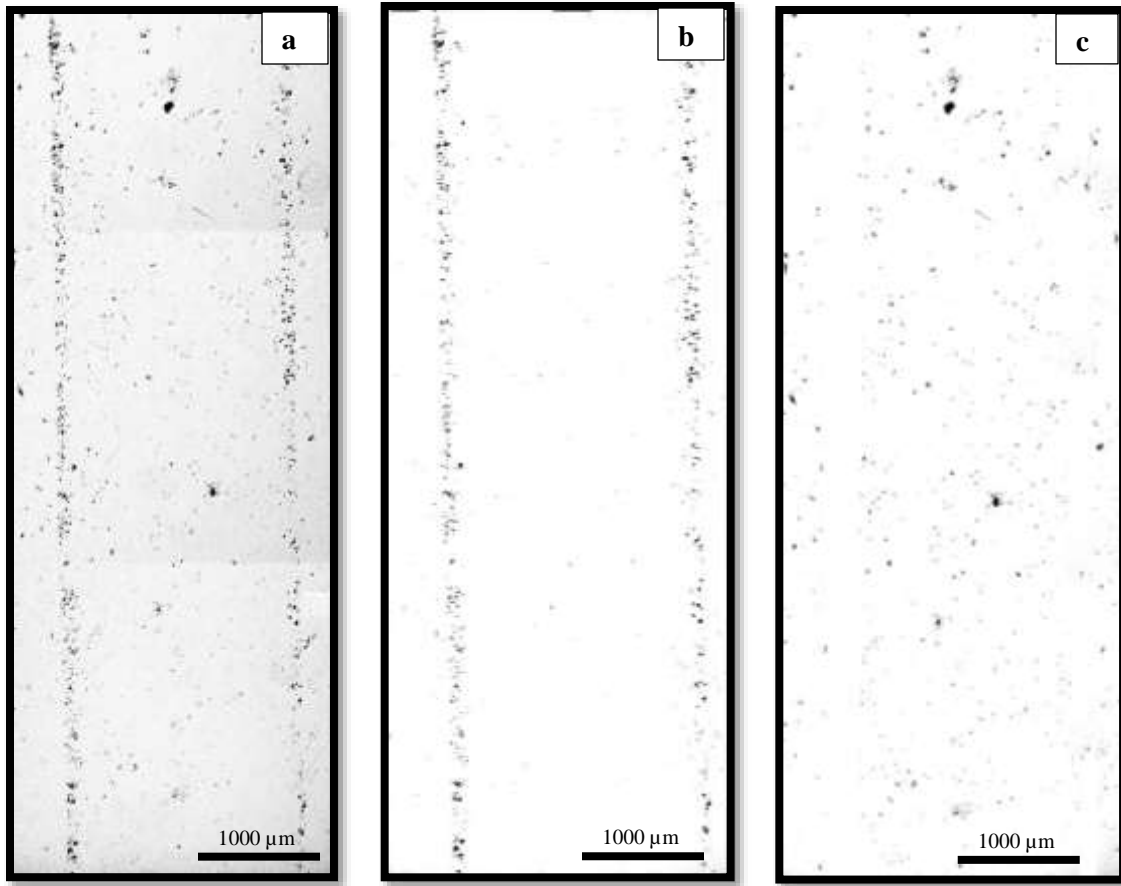


Figure 5.6: Separation of defect band from gas and shrinkage porosity a) gray scale of 12 montaged picture of microstructure from Location 6 b) defect band c) shrinkage and gas porosity.

5.1.3.2 X-ray Tomography Analysis

X-ray tomography scan was conducted using a Skyscan 1172 CT scanner at McMaster automotive resource centre (MARC). The X-ray tomography was performed on samples of 10mm x 6mm x 3mm dimension cut from different locations of top hat. During the scan the sample is rotated through 360° with a rotation step of 0.3° in resulting 1200 two-dimensional projections. The X-ray tomography scans were performed at a voltage of 80 keV, with the pixel size of 4.94μm. A three-dimensional image was generated from a series of 1200 two-dimensional projection images using the analysis software CTAn.

5.2 Simulation and Modeling

In this work the commercial software ProCAST™ was employed to simulate the filling and solidification conditions of each location such as: knit line region, last-to-fill region, close-to-gate region and last-to-solidify region. In this study, the initial conditions, boundary conditions and mesh size for implementing the simulation of shock tower were the same as described in the Section 4.2.1.

In order to study knit line effects, mold-filling and solidification simulation was performed to identify the knit line locations in the different modes. These simulations were performed in MeridianTechnologies Inc. using MAGMASOFT, a commercially available software package.

5.3 Effect of Process Parameters on the Formation of Defects

Figure 5.7 presents a typical polished section of each selected location in shock tower. Filling and solidification simulation was performed using ProCAST™ to characterize the general solidification conditions for shock tower as shown in Figure 5.8. The local solidification conditions for each of the sampling locations were identified such as knit line region, last-to-solidify region, and last-to-fill region. Figure 5.9 to Figure 5.14 show the variation in area fraction of total porosity, shrinkage porosity, gas porosity and defect band for each location. This data enable investigating the effects of process parameters on different kinds of porosity.

As shown in Figure 5.8, Sample 1 is located inside a knit line region where two molten metal flows meet. Practically, the knit line might occur in Location 2 or 3. Simulation results indicate that Location 4 and Location 6 are last-to-solidify region and last-to-fill region, respectively. Last-to-solidify regions are generally the thicker parts of the casting such as Location 4. As shown in Figure 5.7, large gas porosity was found in Location 4. The total area fraction of porosity in Location 4 is much higher than other locations as shown in Figure 5.7. The diameter of some gas porosities exceeds 500 μ m in Location 4. The formation of large gas pores is due to the fact that molten metal remains in the liquid

state for longer periods of time in last-to-solidify regions and solidification occurs without sufficient molten metal.

Mold filling simulations indicate that the flow does not continue after Location 5 because there is no overflow in front of this location. This induces accumulation of gas porosity in Location 5. The last-to-fill is typically furthest away from the gate and last to receive molten flow such as Location 6. As shown in Figure 5.7, the defect band was observed just in Locations 5 and 6. No defect band was observed in Locations 1 through 4 for all sets of process parameters.

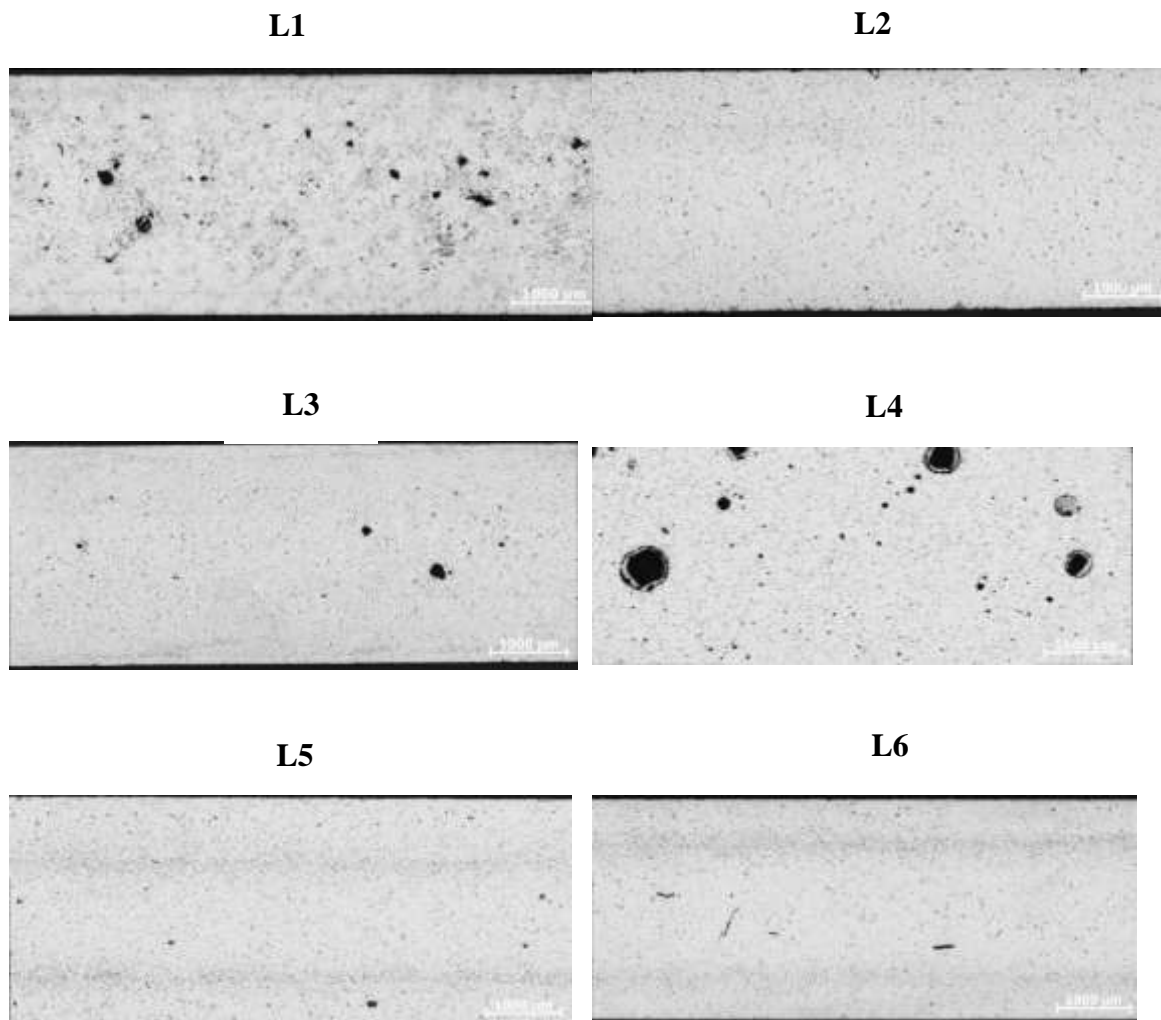


Figure 5.7: The montage of micrograph covering the thickness of sample cut from locations 1 to 6.

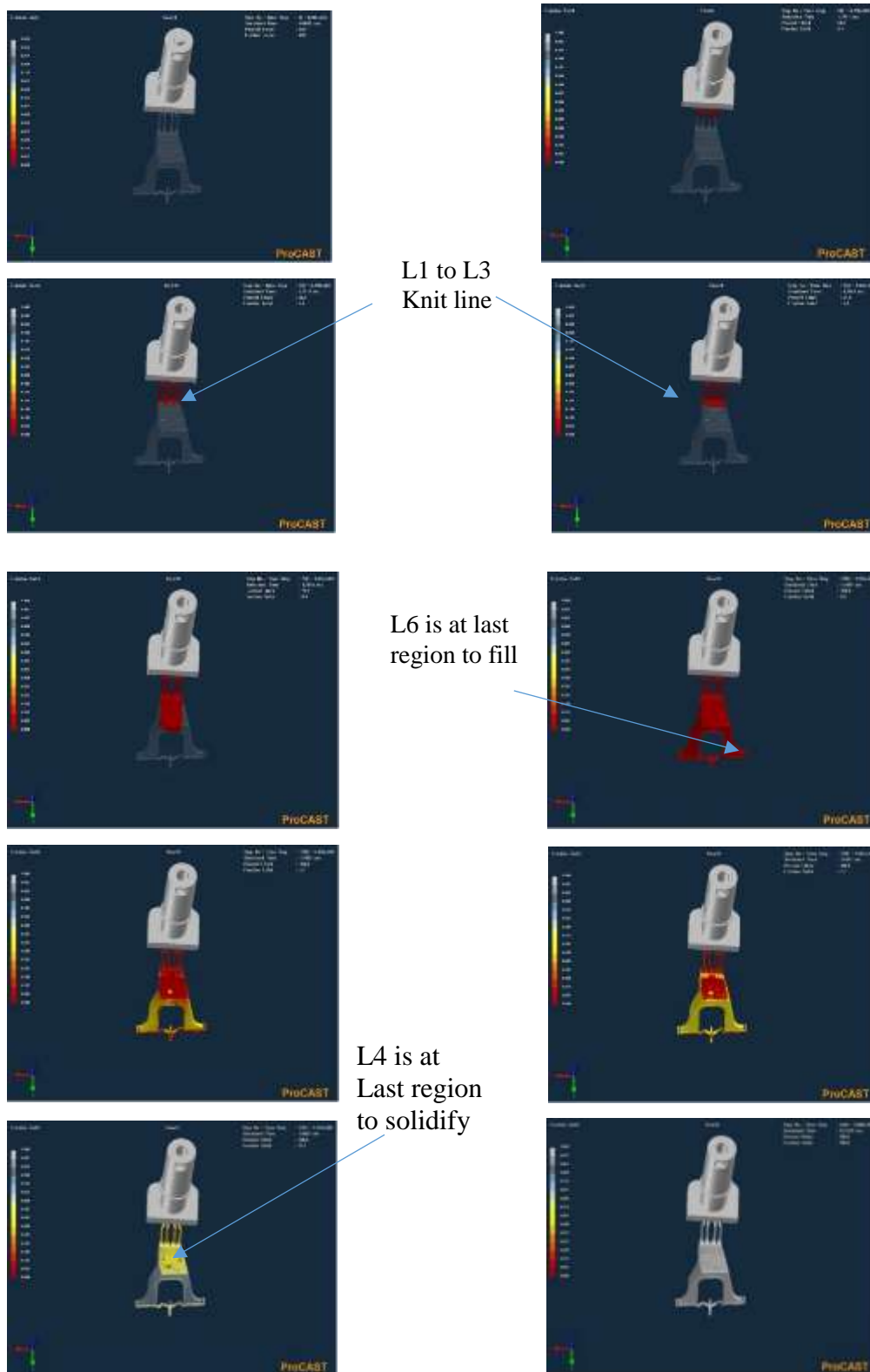


Figure 5.8: Filling sequence and solidification conditions predicted in Pro-cast. Arrows show the location of knit lines.

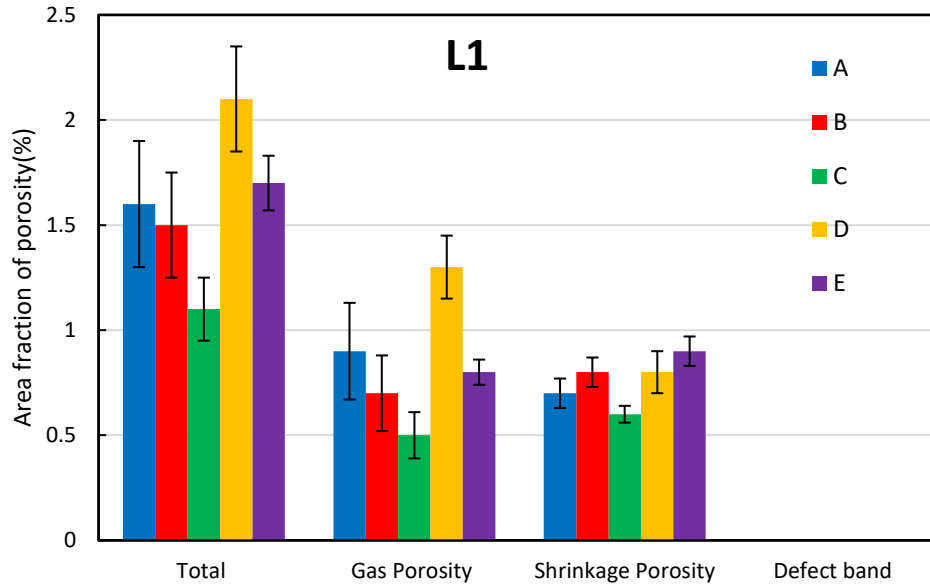


Figure 5.9: The effect of different Sets of process parameters on the amount of various porosities at Location 1. The error bars represent one standard deviation resulting from three shock towers at Location 1.

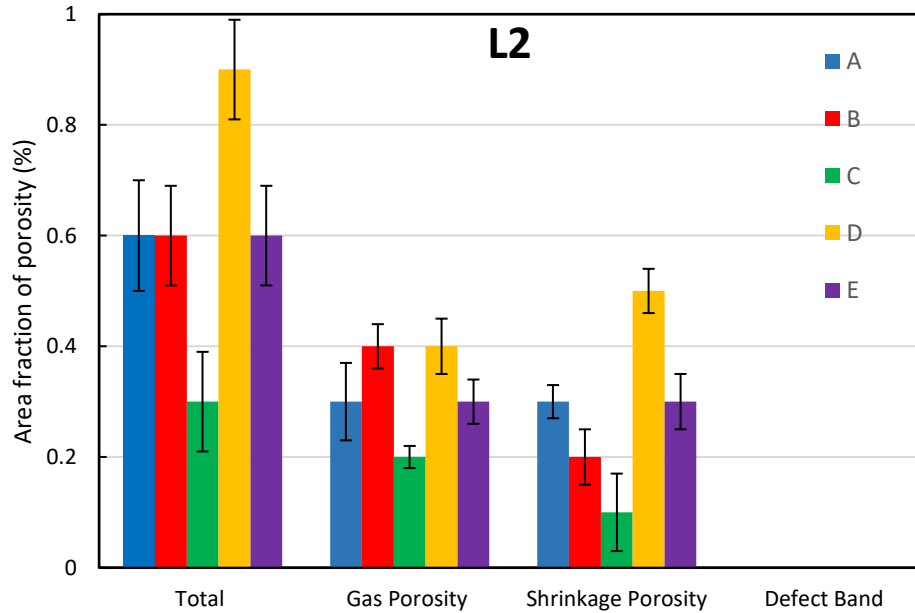


Figure 5.10: The effect of different Sets of process parameters on the amount of various porosities at Location 2. The error bars represent one standard deviation resulting from three shock towers at Location 2.

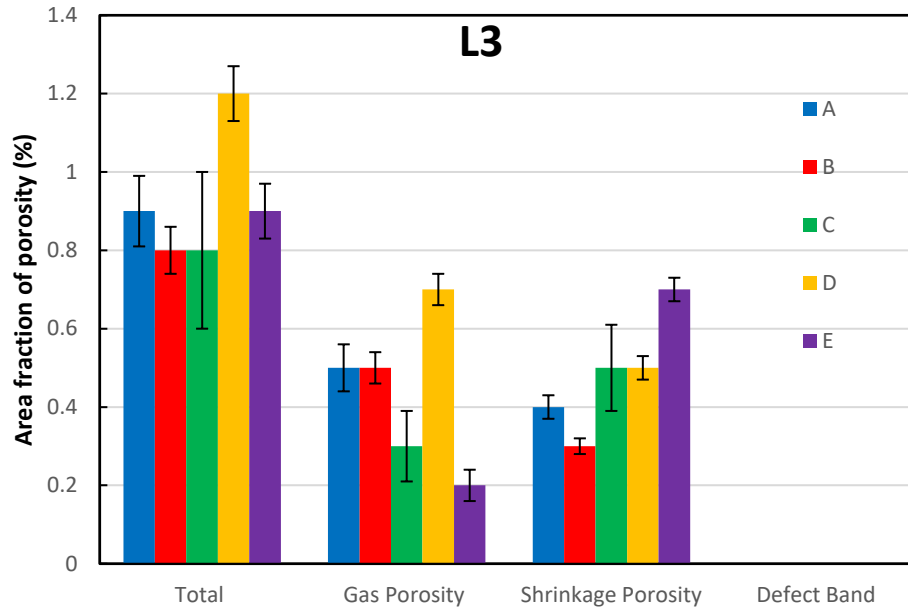


Figure 5.11: The effect of different Sets of process parameters on the amount of various porosities at Location 3. The error bars represent one standard deviation resulting from three shock towers at Location 3.

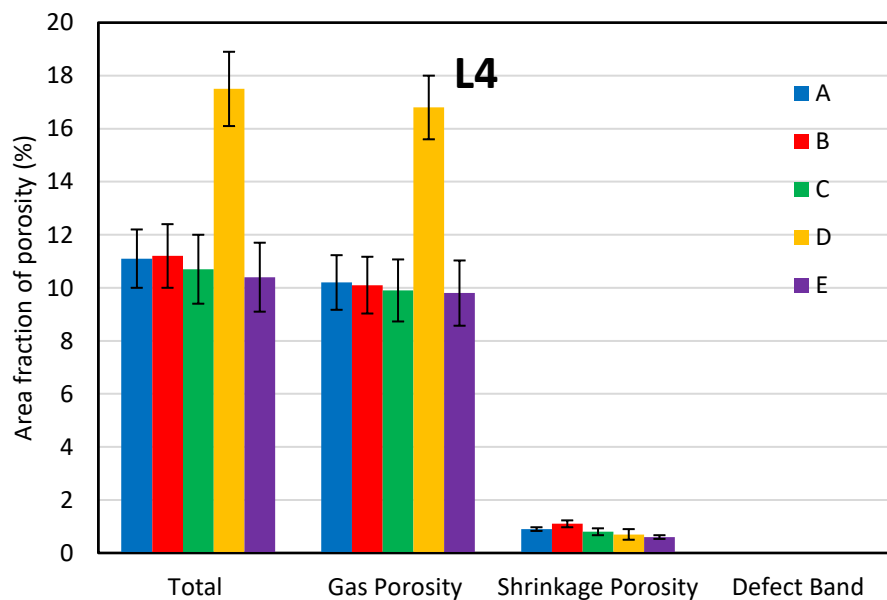


Figure 5.12: The effect of different Sets of process parameters on the amount of various porosities at Location 4. The error bars represent one standard deviation resulting from three shock towers at Location 4.

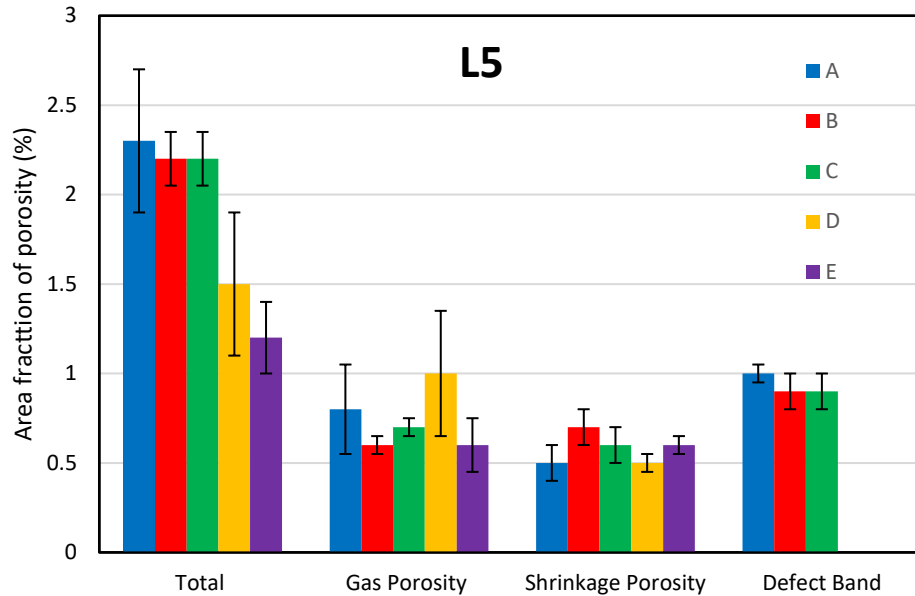


Figure 5.13: The effect of different Sets of process parameters on the amount of various porosities at Location 5. The error bars represent one standard deviation resulting from three shock towers at Location 5.

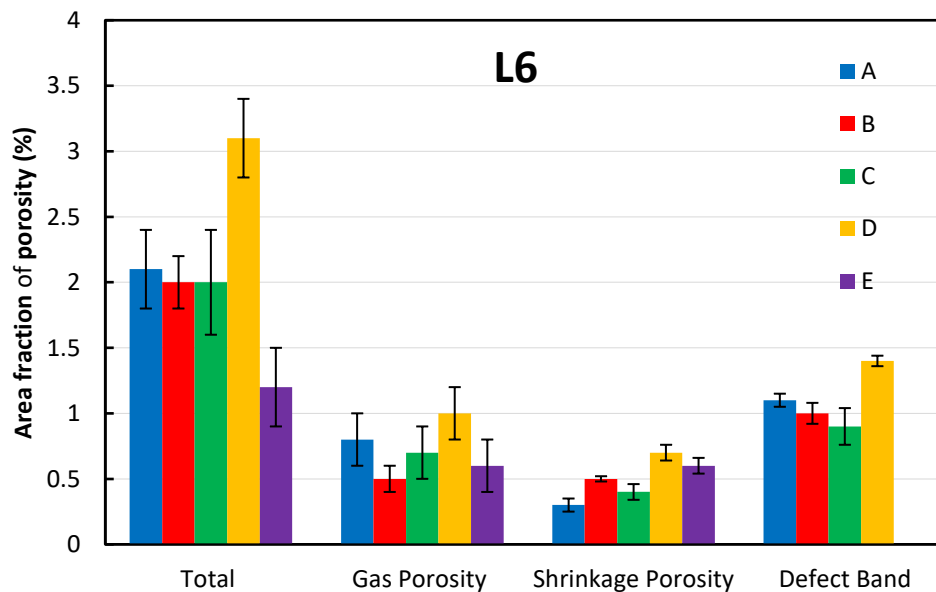


Figure 5.14: The effect of different Sets of process parameters on the amount of various porosities at Location 6. The error bars represent one standard deviation resulting from three shock towers at Location 6.

In Chapter 4, Figure 4.12 presents the optical micrograph of the etched microstructure of each location. Figure 5.8 shows the ESGs variation for various locations with different sets. As shown in Figure 4.12, locations near the gate (Location 1 and Location 2) include significantly larger fractions of ESGs, whereas this microstructural feature is more dilute in the position farther away from the gate. In both locations, the grain structure at the center consists of coarse grains surrounded by small grains and near the surface, fewer coarse grains were observed in these positions. In other locations, the entire skin region contains refined grains while in the core region, some ESGs can be observed.

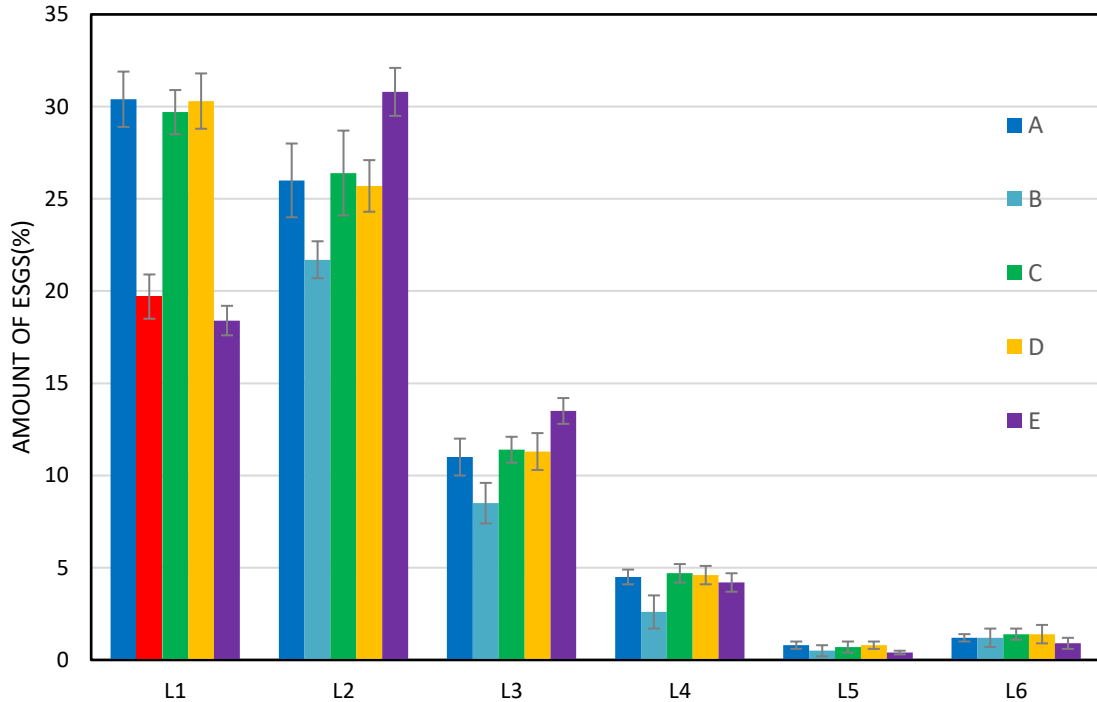


Figure 5.15: The process parameters effect on amount of ESGs for different locations. The error bars represent one standard deviation resulting from three shock towers at same locations.

In order to study the influence of the slow stage of piston velocity on the amount of porosity, the shock tower has been produced with Set A and Set B including the same values of all process parameters except the slow stage of piston velocity. As shown in

Figure 5.9 through Figure 5.14, there is no relationship between the amount of the different classes of porosity and the slow stage piston velocity. In order to investigate the influence of fast stage of velocity, Set A and Set C were applied using the same process parameters except the fast stage of piston velocity. The fast stage of piston velocity has an effect on the variation of area fraction of gas porosity.

Intensification pressure effects, can be seen in the comparison of Set A and Set D. As shown in Figure 5.9 to Figure 5.14, intensification pressure influences on the total area fraction of porosity, shrinkage porosity, gas porosity and defect band. The influence of die temperature on the amount of porosity can be characterized by making comparison between results of Set A and results of Set E. As shown in Figure 5.13 and Figure 5.14, the die temperature shows significant effect on the total area fraction of defect for Locations 5 and 6 while die temperature has negligible effect on the area fraction of total amount of porosity, shrinkage porosity and gas porosity for other locations as shown Figure 5.9 to Figure 5.12.

As shown in Figure 5.15, the area fraction of ESGs shows a significant reduction from locations near the gate to the farther locations regardless of which set of process parameters was applied. As shown in Figure 5.15, while the amount of ESGs is not affected by the intensification pressure, it is dependent on the slow and fast stage of piston velocity and die temperature for locations near the gate.

5.3.1 Slow Stage of Piston Velocity Effects

As discussed, there is no significant difference between the application of Set A and Set B in the amount of total porosity, shrinkage porosity, and gas porosity. Therefore, these porosities do not show any dependency on the slow stage of piston velocity. The primary purpose of the slow stage of piston velocity (V_1) is to build up a wave that forces the air to the front and to prevent entrapment of air during the flow. If the slow stage of piston velocity exceeds an optimal value, it may cause a breaking wave, resulting in the entrapment of air. For this reason, we avoid using considerable variation between Set A and Set B in the slow stage of piston velocity level. However, the area fractions of porosity were not affected by the slow stage of piston velocity while a significant reduction in the

area fraction of ESGs is found by increasing the slow stage of piston velocity for locations near the gate. This is due to the reduction in the contact time between the liquid metal and shot sleeve wall.

5.3.2 Fast Stage of Piston Velocity Effects

The fast stage of piston velocity (V_2) aims to complete filling the cavity of die casting. Since cavity was completely filled in the range from 3 m/s to 5 m/s, the appropriate value of fast stage of piston velocity is 3 m/s. A comparison of the results between Set A and Set C indicates that the reduction in the fast stage of piston velocity leads to a reduction in the total area fraction of porosity for all locations. As shown in Figure 5.9 to Figure 5.14, the amount of gas porosity in Set C is lower than the percentage of gas porosity in Set A for all of locations. As discussed in Chapter 2, the reduction of turbulent flow caused by a lower level of the fast stage of piston velocity and higher turbulent flow during filling cavity leads to more air in the liquid melt.

The fast stage of piston velocity has more influence on the amount of gas porosity in locations close to the gate as compared with the other locations. Higher fast stage of piston velocity increases the average percentage of gas porosity by approximately 45% in Location 1 whereas it has a smaller effect in increasing the gas porosity to approximately 12% in location 6. In fact, the average percentage of gas porosity is raised by knit line condition occurring in locations near the gate as shown in Figure 5.8. These locations are expected to have higher amount of porosity, due to entrapped gas and oxide inclusion when two liquid fronts meet. This finding shows that the area fraction of gas porosity in locations at knit line region is more sensitive to fast stage of piston velocity than the area fraction of porosity in other locations. Figure 5.9 to Figure 5.12, indicate that the percentage of total porosity and gas porosity in Location 1 is much higher than Location 2 and 3 when the same process parameters were used. This suggests that the knit line probably occurred at Location 1 for all sets of process parameters.

The fast stage of piston velocity does not show the same impact on shrinkage porosity for all locations. In locations 1, 2 and 4, the amount of shrinkage is increased with increasing in the fast stage of piston velocity while the percentage of shrinkage is decreased in other

locations with an increase in the fast stage of piston velocity. These differences mean that fast stage of piston velocity results in various formations of shrinkage in different locations of the cast. More studies are necessary to understand the reasons for these differences.

5.3.3 Intensification Pressure Effects

As discussed in Chapter 2, the purpose of intensification pressure (IP) is to compress any entrapped gas and transfer further material into the die cavity to feed the shrinkage of the casting during solidification. As shown in Figure 5.9 to Figure 5.14, the intensification pressure has small effect on the amount of shrinkage porosity as compared with the gas porosity. The area fraction of gas porosity is remarkably decreased by higher level of intensification pressure. The application of intensification pressure has more influence on the reduction of gas porosity level in Location 4 as compared to other locations. This is because there is a very large pore formed in the last-to-solidify region and higher level of intensification pressure reduces the size and number of gas pores. The average size of gas porosity is decreased from 312 μm to 195 μm when the intensification pressure is increased from 400 bar to 600 bar.

The effect of intensification pressure on the total area fraction of porosity alters from location to location. As shown in Figure 5.9 to 5.14, a higher level of intensification pressure reduces the total area fraction of porosity for all the locations except location 5. This is attributed to the disappearance of a defect band in Location 5 when Set D is used, resulting in the reduction of the total area fraction of porosity.

In addition, the defect band is observed for Set A, B and C at locations 5 and 6, when the higher level of intensification pressure was applied. This can be explained by higher local deformation occurring in those locations when higher intensification pressure is applied. There is a narrow region of lower fraction solid between skin and core region, and that the deformation is concentrated in this region, which could then form defect band. Since the cavity is filled before applying intensification pressure, the skin region forms before applying intensification pressure. Therefore, there is a significant gradient of solid fraction between skin region and core region before applying intensification pressure. The defect band probably forms in the last stage of solidification, whereas solid fraction is very high

and the applied local pressure is sufficient. Regarding defect band formation, some researchers [12, 29] believed that there is a direct relationship between defect band and ESGs. In this study, it has been observed that defect band forms in the locations with the lowest amount of ESGs, as a result, there is no relationship between ESGs and defect band. The same observation has been reported by H.I. Laukli [27] who reported defect band might form in locations with few or no ESG.

As shown in Figure 5.13 and 5.14 defect band has a considerable share to increase the total area fraction of porosity in Locations 5 and 6. Previous researchers [46, 49] generally believe that the application of intensification pressure in the HPDC process lead to reduces the total amount of porosity. Most of the studies focused only on the simple geometry that ignores the local effect of intensification pressure on the defect band formation. In this study, it was found that the application of higher intensification pressure lead to the significant reduction in the amount of gas porosity, but increasing the intensification pressure also might increase the total area fraction of porosity via defect band formation in some locations of complex geometry component.

5.3.4 Die Temperature Effects

As shown in Figure 5.9 to 5.14, the effect of die temperature variation on the total area fraction of porosity is more sensitive to locations 5 and 6 as compared to other locations. This data appears to indicate a trend of decreasing the total amount of porosity with increasing die temperature for Locations 5 and 6. It is due to the defect band which disappears when the die temperature is increased from 160 to 240 °C. Additionally, the defect band was observed in location 6 for all Sets except Set E, where a higher level of die temperature was used, presumably reducing the solid fraction in the casting at the time of Intensification Pressure application. These observations are consistent with the findings of H.I. Laukli [28] who observed that defect bands disappeared with increasing the die temperature.

As shown in Figure 5.15, the position of ESGs is more sensitive to die temperature as compared to other process parameters. The area fraction of ESGs in Location 2 is much higher than the area fraction of ESGs in Location 1 when Set E was applied. Additionally,

area fraction of ESGs shows that the highest value in Location 2 and the lowest value in Location 1 occur in Set E compared to the other sets (ie. Set A to Set E). This variation can be explained by increasing in the fluidity of liquid metal, whereas the die temperature increases during filling cavity, because less solidification occurs near the die wall. As a result, more ESGs transfer further from the locations near the gate to other locations.

It was observed that at Location 1 to Location 4, the total area fraction of porosity via Set C is significantly less than the total area fraction of porosity in the same locations with other Sets. Also, the percentage of total area fraction of porosity in Locations 5 and 6 using Set E is smaller as compared with applying other Sets. As discussed, variation in the effect of process parameters on the amount of shrinkage porosity, gas porosity and defect band were found from location to location. These findings confirm that the local solidification and filling conditions, similar to process parameters, play a major role in the formation of different kinds of defects.

5.4 Prediction of Defect Band Location in the Complex Geometry

As discussed, the formation of defect band is affected by die temperature and intensification pressure. Additionally, the defect band was observed only in location 5 and 6 of shock tower while die temperature is similar for all the locations. This observation is consistent with finding of H.B. Anaraki [96] who reported that formation of defect band occurs for different locations in the complex geometry. Two main theories in the literature [27, 29] have been proposed to justify the formation of defect band in the HPDC process. First, Dahle et al. [29] proposed a theoretical framework that defect bands form by a combination of a fraction solid gradient away from skin region and the presence of ESGs in the core region as a result of lift forces on the solid. They point out that there exist a narrow region of lower fraction solid between skin and core region, and that deformation will be concentrated in this region, which could then form defect band. They believed that the deformation of defect band is linked to the presence of ESGs in the core region while this study found that the formation of defect band occurs in the absence of ESGs. Similar observation was reported by Rodrigo et al. [97] who point out that the formation of defect

bands occurs irrespective of presence of ESGs. Thus, this theory does not sufficiently explain the formation defect band without ESGs during HPDC process.

Second, Gourlay et al. [98] proposed a mechanism describing the deformation defect band as a result of local slip occurring in the dendrite network when the flow fluid pass the stagnant skin region with higher level solid fraction. This theory is based on the deformation of local slip into dendrite network in the region between skin and core region when the local applied stress is sufficient. They also reported that formation of defect band occurred similar HPDC without ESGs during gravity die casting for magnesium and aluminum alloys. There are some levels of uncertainties points in this investigation: First, the gradient solid fraction from skin region to core region is not sufficient for occurring shear deformation, because, there is no significant variation in cooling rate between skin region and core region in the gravity die cast. Second, the existence of region with lower solid fraction between skin and core region is necessary to deform defect band while this region does not form in the fully liquid alloy as feedstock material was used in the gravity die cast. Third, the additional force or higher shear rates during filling is necessary to the formation of defect band while additional force or higher filling condition is not applied in the gravity die cast. Meylan et al. [99] reported that the local sufficient deformation plays major role in the formation of defect during solidification. Although the band might form without external pressure in the gravity die cast, due to the segregation eutectic (Al+Si) from ESGs under solidification of Al-Si if the semi solid in filling cavity is applied, but, in the case of magnesium alloys defect band essentially forms based on the local shear stress. It should be noted that nature of band in the HPDC process is completely different in the magnesium alloys and aluminum alloys. The band in the magnesium alloy contains shrinkage pore and tears while the band might form in the aluminum alloys based on the segregation eutectic phase from earlier solidifying layer in the skin region and ESGs in the center. As shown in Figure 5.16, the defect bands contain a greater fraction Al–Si eutectic than the surroundings. However both above mechanisms are not applicable to predict the location of defect band in the complex geometry of die cast component. Additionally, both approaches do not completely explain the role of local die temperature and intensification pressure on the formation of defect band.

In this study a new mechanism is proposed that enables researchers and designers to predict the location of defect band in the complex geometry component of die cast magnesium alloy. Before a mechanism for the formation of banded defects in HPDC process is proposed, the flow and solidification behavior in the cross section of thickness casting during filling cavity must first be considered.

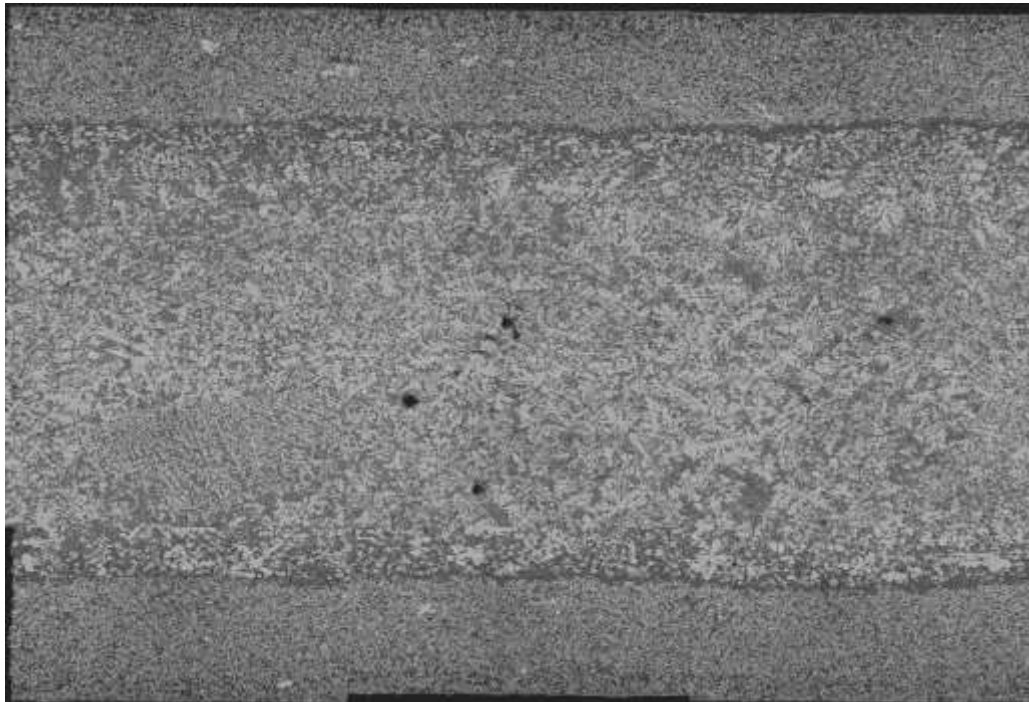


Figure 5.16: The defect band as in aluminum silicon alloys.

As shown in 5.17 Figure, the cavity is filled in three stages: a) slow stage of piston velocity b) molten metal is then injected into the cavity by applying fast stage of piston velocity c) maximum pressure (intensification pressure) is then applied. As shown in Figure 5.17, there is an interval time between maximum value of fast stage velocity of piston and intensification pressure.

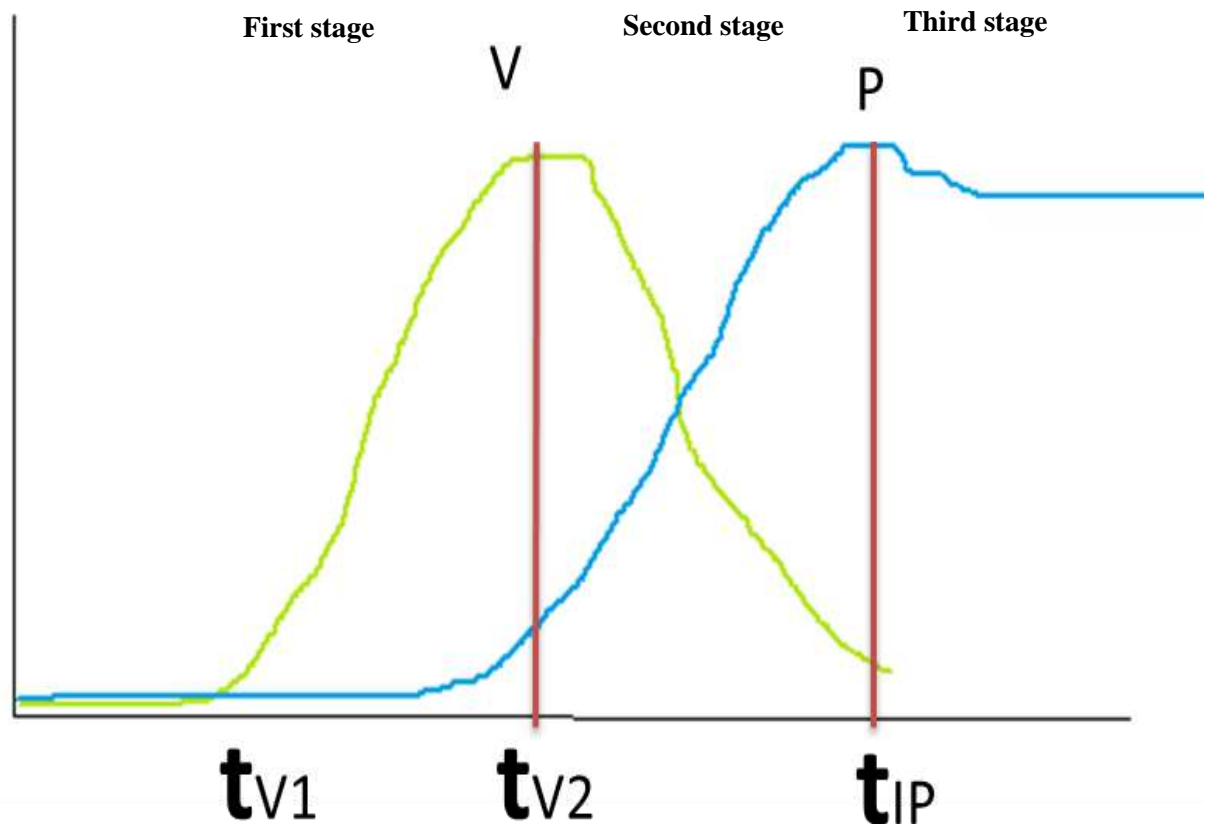


Figure 5.17: The schematic of shot profile during filling cavity.

Figure 5.18 schematically shows the filling and solidification through the cross section of casting during HPDC process. As shown in Figure 5.18, the skin region with higher level of solid fraction rapidly forms as soon as molten metal contacts the mold. Therefore, the solid fraction distribution can then be split into two regions through the cross section of casting thickness; first, the immobile region comprise higher level of solid fraction close to wall mold and the second is the mobile region which might contain some ESGs.

In the pressurization stage, the considerable resistance of immobile region (skin layer) is expected to local stress induced by intensification pressure while the core region easily moves forward. As a result, local shear deformation can occur in the narrow region between the skin and core region as shown in Figure 5.18. However, defect band forms under two certain conditions during HPDC process:

First, there is sufficient significant variation of solid fraction between skin region and core region through second stage to third stage:

$$f_s(\text{skin}) \gg f_s(\text{core}) \text{ at } t_{v2} < t < t_{IP}$$

Second is the sufficient external force that is able to create localization of deformation between skin and core region.

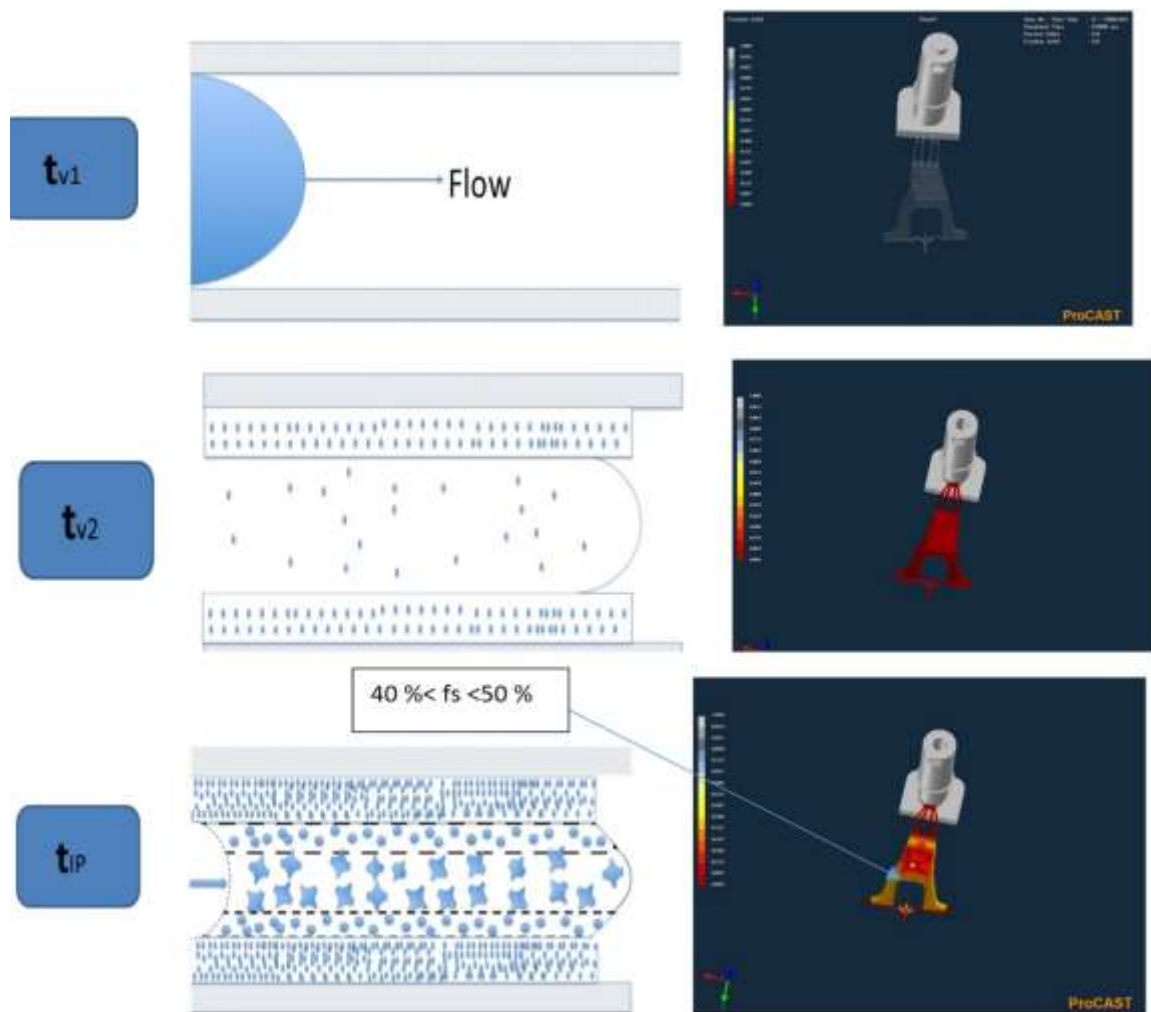


Figure 5.18: The filling and solidification through the cross section of casting during HPDC process.

The above mechanism can justify the formation of defect band in the location 5 and 6 based on the local filling and solidification conditions of those locations. Figure 5.19 shows the variation of solid fraction as a function time for all the locations when the die temperature is 160°C and 240°C . As shown in Figure 5.19, the solid fraction rate for die temperature $=160^{\circ}\text{C}$ is much higher than the die temperature $=240^{\circ}\text{C}$. For the die temperature $=160^{\circ}\text{C}$, the solid fraction rate three times higher than the die temperature $=240^{\circ}\text{C}$ when solid fraction increases from zero to 50%.

As mentioned, the defect band was observed only in L5 and 6 of shock tower while die temperature is consistent for all the locations. The solid fraction rate is much higher than in locations 5 and 6 as compared to other locations. It is due to the fact that the die surface temperature at locations 5 and 6 is lower as compared to die surface temperature at the other locations as shown in Figure 4.16. As discussed in Chapter4, this is because there is a lower contact time duration between flow and die in locations close to overflow (for example L5 and L6) as compared to other locations (L1 through L4). Therefore, less heat is extracted from liquid to die in locations close to the overflow during filling cavity and the local die surface temperature is expected to be lower than the one in other locations. Lower die surface temperature increase solid fraction rate during filling cavity. However, in L5 and 6, higher solid fraction rate leads to form sufficient solid crystal in the skin region before applying intensification pressure when the die temperature is 160°C . This indicates that the formation of defect band is affected by the local die surface temperature, not initial die temperature. However, in the complex geometry of die cast magnesium alloy, defect band forms in locations whereas there is enough solid fraction before pressurization stage and sufficient intensification pressure is able to create local stress deformation.

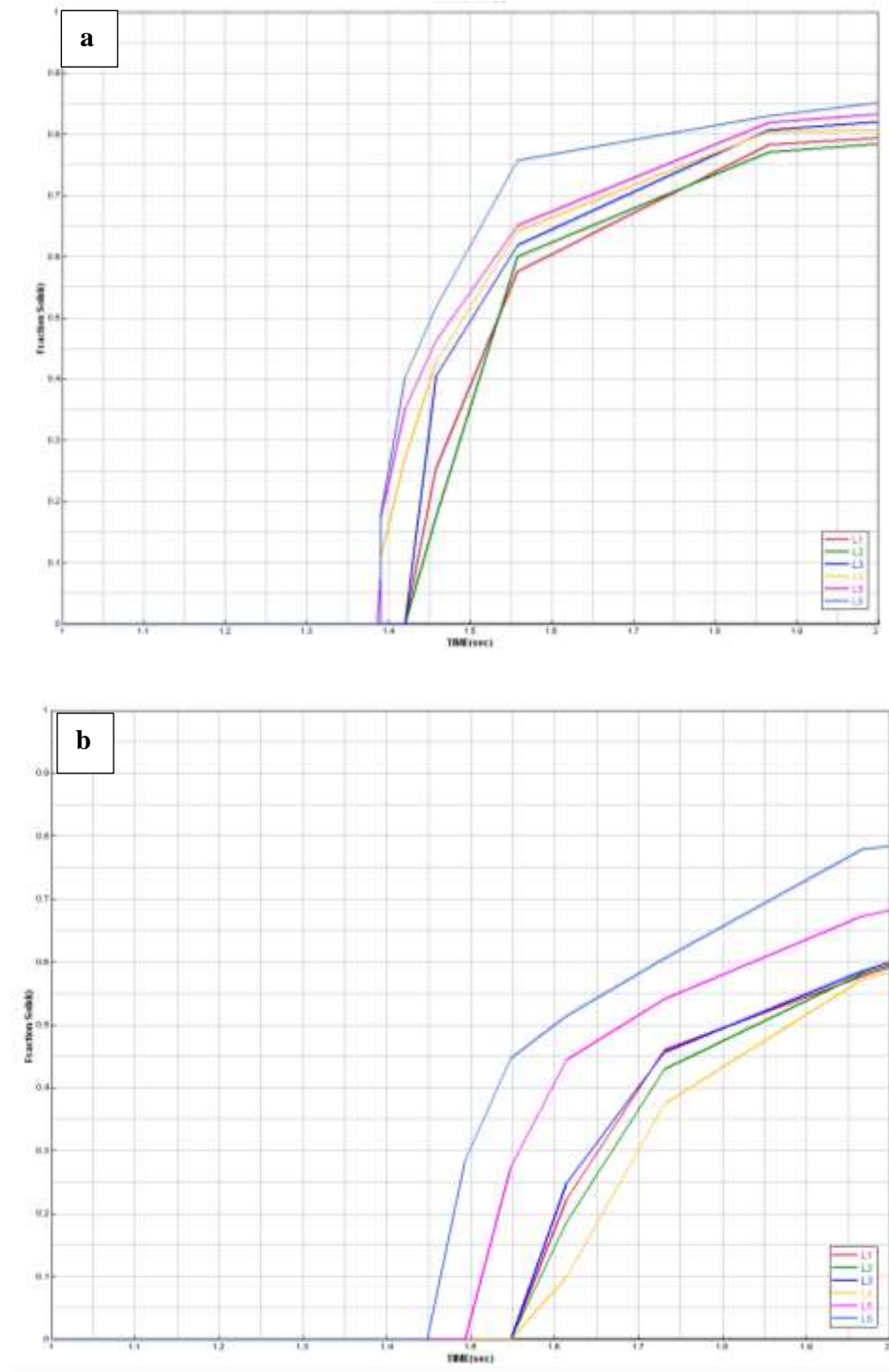


Figure 5.19: Solid fraction rate is for a) die temperature =160^o C b) die temperature =240^o C. These curves were taken from simulation results.

5.5 Investigation of Knit Line Impacts on the Formation of Porosity

Commercial code software MAGMASoft was used to identify the locations of knit line conditions in the top hat die cast component for three different designed Modes. Figure 5.20 shows the filling conditions in the different selected time stages for the Mode 1. The top hat is fed by four runners making it a casting with seven distinct knit lines in the case of Mode 1. As shown in Figure 5.20, the flow reaches the middle gates earlier than corner gates. Three knit lines condition begins among middle gates when flows do not reach corner gates. Actually, three knit lines in the middle happen sooner than the four knit lines observed in the edges.

As shown Figure 5.21, the knit line in the middle does not end up overflow while other knit line reaches the overflow. Based on the simulation results, six samples of 10mm×6mm×3mm were extracted from different locations as shown Figure 5.21. Three locations were selected from knit line whereas flow direction (B) reaches overflow and three locations were chosen from knit line direction (A) which does not end up overflow.

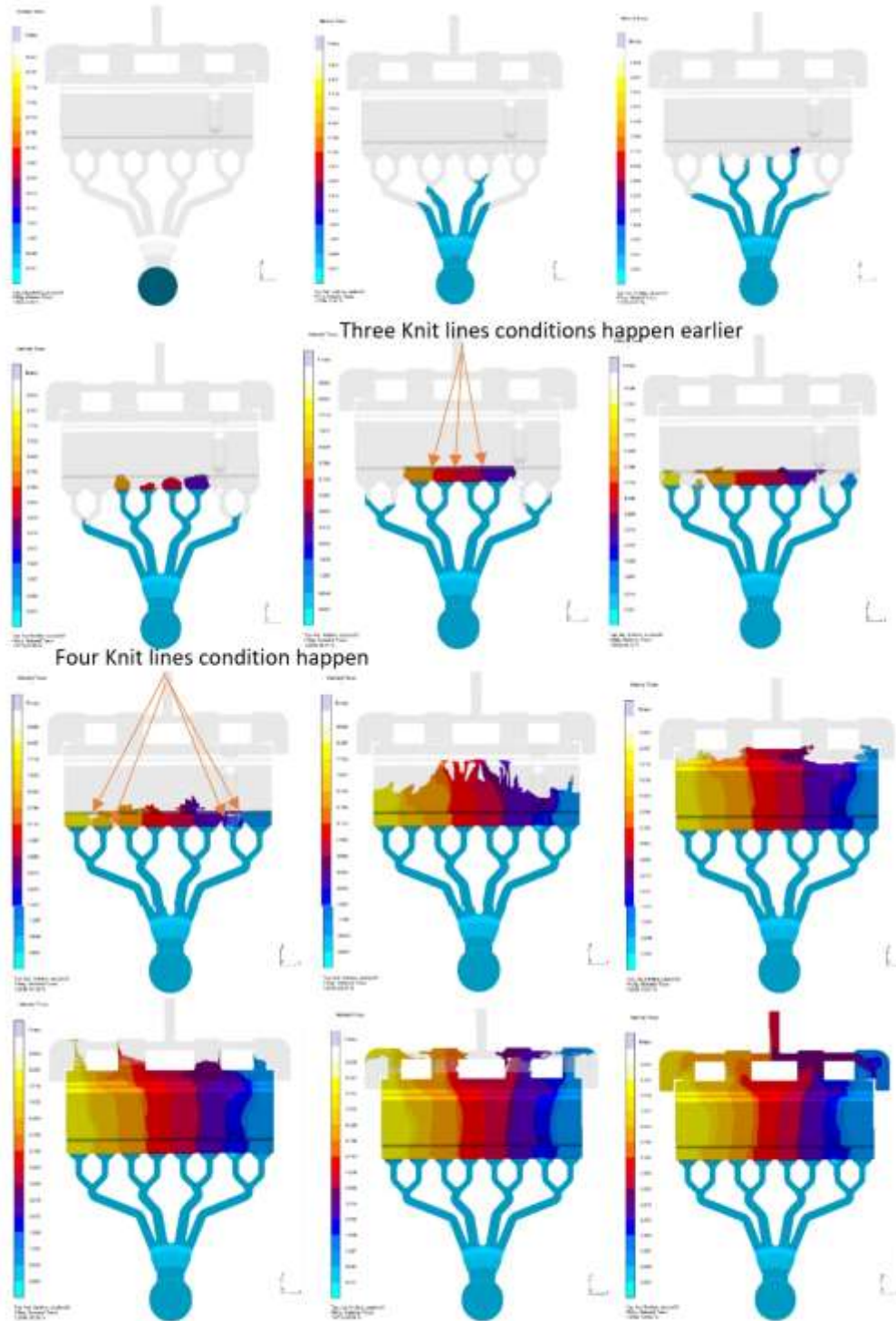


Figure 5.20: Simulation of Mold filling top hat for Mode 1. Arrows shows locations of knit line begins.

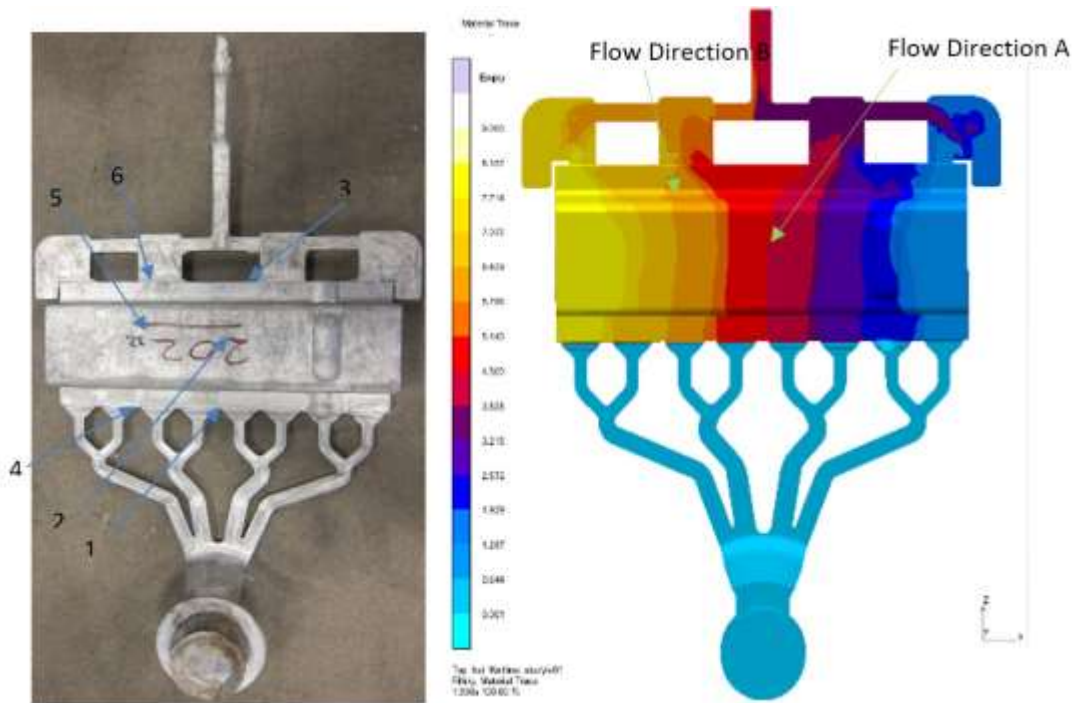


Figure 5.21: Top hat casting with six selected locations representing the two flow directions incorporating knit lines.

In this section, the porosity distributions are quantitatively characterized using the X-ray tomography. Since the entire thickness can be scanned at reasonable resolution using the X-ray tomography equipment, X-ray tomography is a suitable method for the characterization of porosity in the cross section of casting thickness. Figures 5.22 and 5.23 show visual representation of the presence of porosity using the results of X-ray tomography for location 3 and location 6, respectively. In order to effectively reduce the error produced in the reconstruction process, porosities smaller than four voxels in area and eight voxels in volume were removed. Figure 5.22 presents that the majority of the pores, and in particular the larger pores, are located in the core region, while skin region is relatively pore-free. Similar results were observed for other locations. Figure 5.24 presents that the typical optical micrograph for cross sectional samples 1, 2 and 3. These images were made using 20 contiguous fields which were montaged. Figure 5.24 reveals the distribution porosity through the cross section of casting thickness.

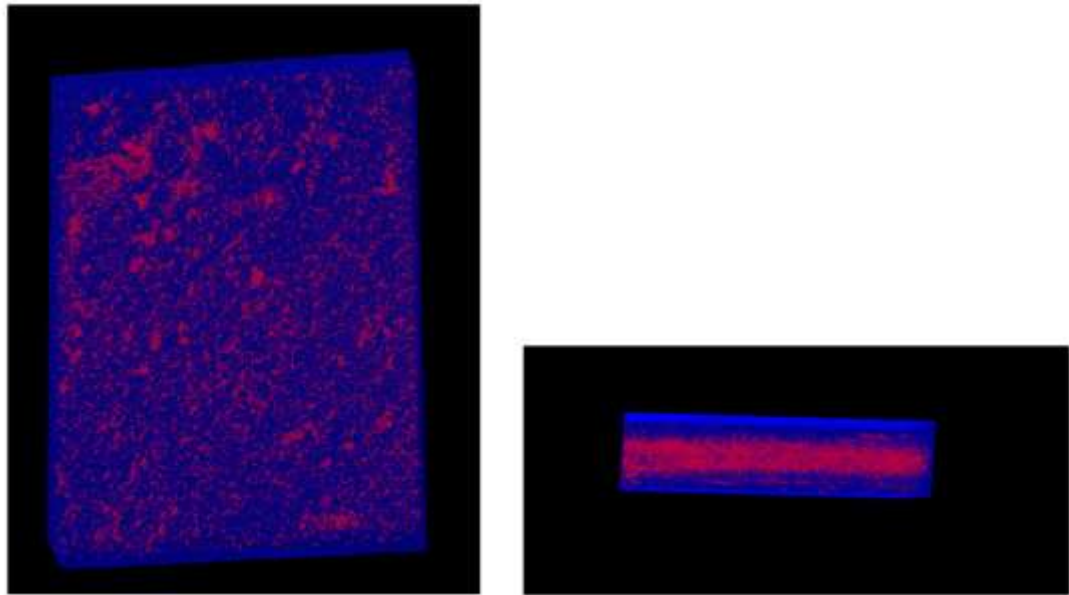


Figure 5.22: Visual representation of the presence of pores using the results of X-ray tomography for Location 3.

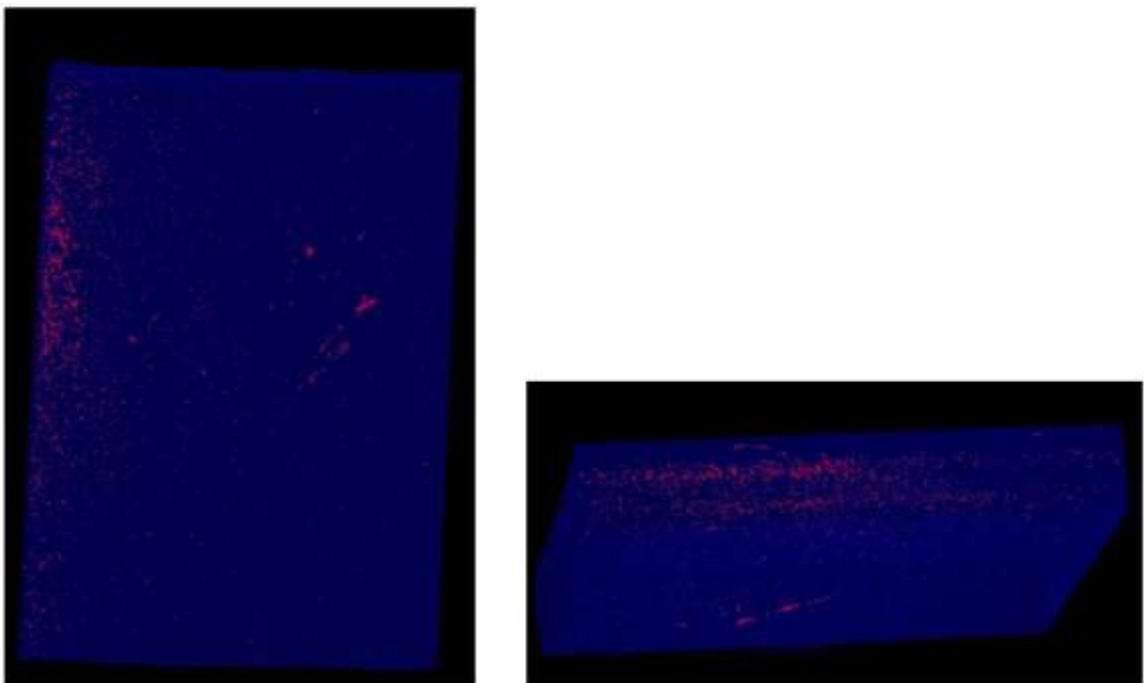


Figure 5.23: Visual representation of the presence of pores using the results of X-ray tomography for Location 6.

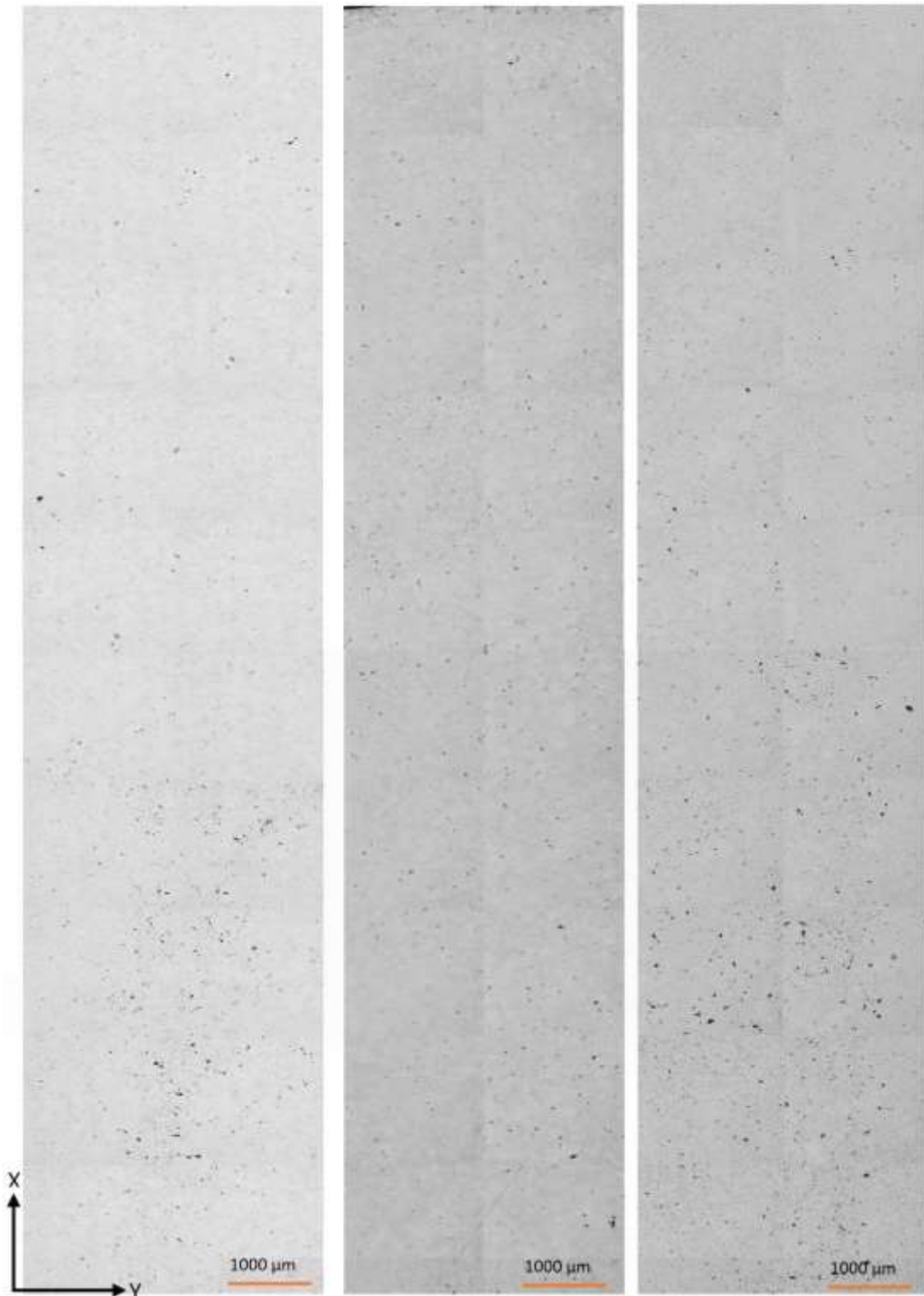


Figure 5.24: An image using optical microscopy showing a cross-sectional sample 1 to sample 3 from left to right. Note that this Figure shows the micrograph in the plane X_Y, while the flow direction is in Z axis as shown in Figure 5.20.

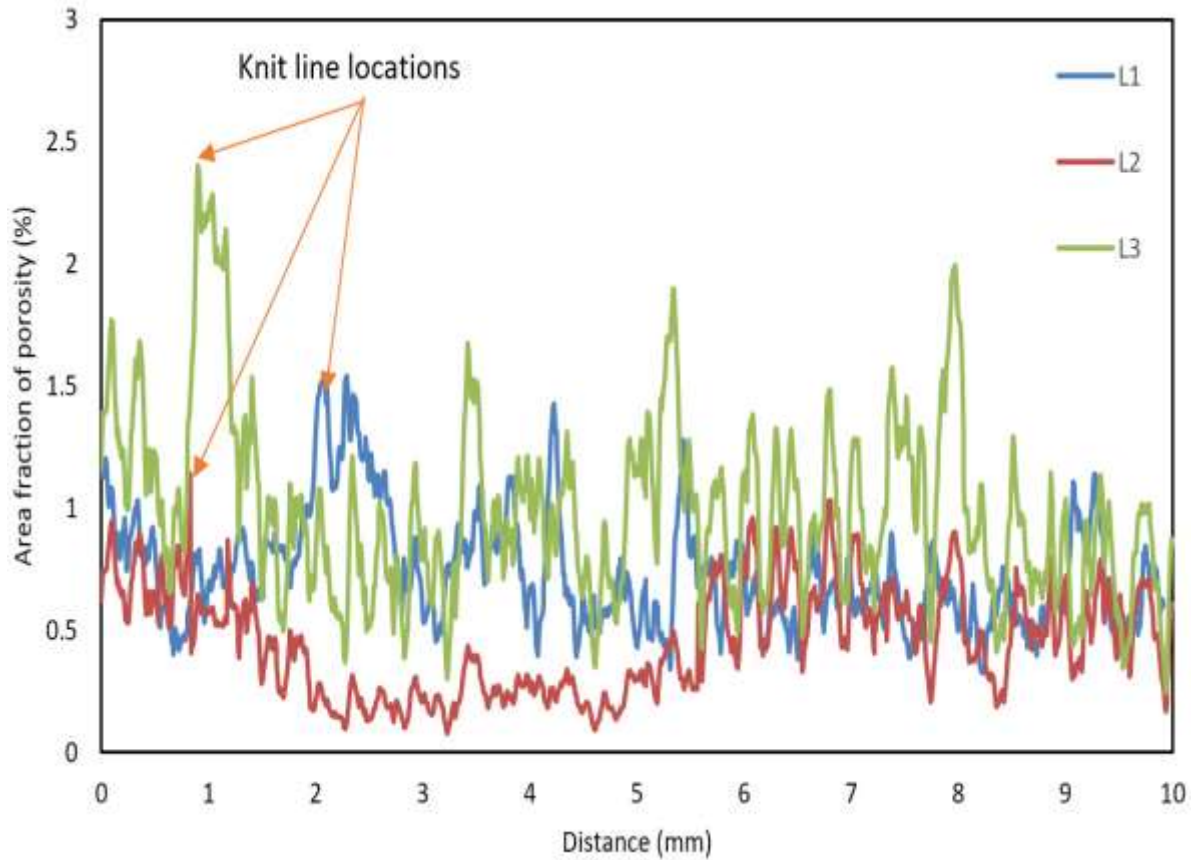


Figure 5.25: The area fraction of porosity along the X- axis of sample 1 to 3. Arrows indicates the predicted knit line locations.

The area fraction of porosity was plotted as a function length using thresholded 1200 two-dimensional projection images. Figure 5.25 and Figure 5.26 show the profile of the area fraction of porosity in the direction parallel to the X- axis for locations 1 to 3 and locations 4 to 6, respectively.

The profile of the area fraction of porosity enables researcher to identify the locations of knit line. The knit line probably happened in the location where shows maximum area fraction of porosity. As shown in Figures 5.25 and 5.26, arrows indicate the prediction of knit line locations. For example, knit line occurred at a distance of approximately 1 mm and 2.5 mm from zero point along X direction for locations 1 and 4, respectively.

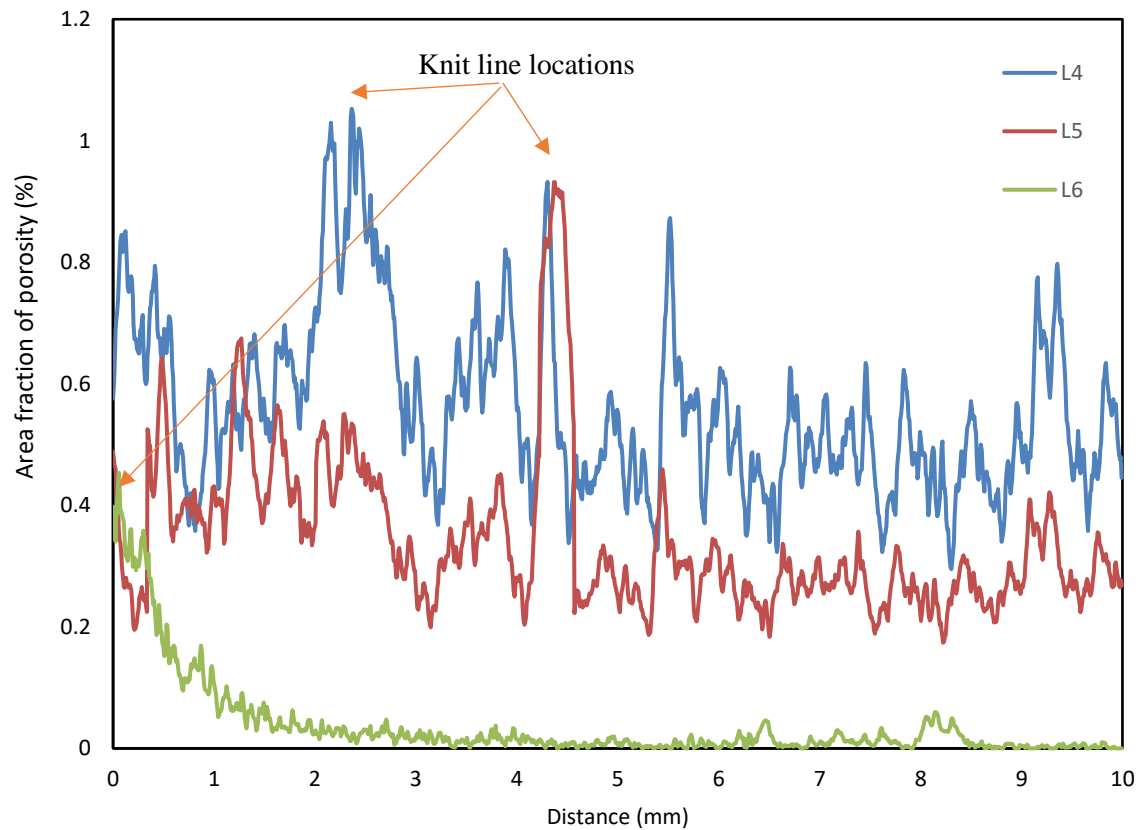


Figure 5.26: The area fraction of porosity along the X- axis of sample 3 to 6. Arrows indicates the predicted knit line locations.

Table 5.2 shows maximum area fraction of porosity, minimum area fraction of porosity, volumetric porosity determined from x-ray tomography and area fraction of porosity from optical metallography results. As indicated in Table 5.2, the volumetric porosity trend among different locations is in accordance with the area fraction of porosity trend measured from optical microscopy.

Table 5.2: Quantitative data on the porosity presents in each location using X-ray tomography and optical microscope.

	Maximum area fraction of porosity (%)	Minimum area fraction of porosity (%)	Volumetric porosity (%)	Area fraction of porosity from optical micrograph (%)
Location 1	1.47	0.96	0.94	1.19
Location 2	1.43	0.4	0.86	1.13
Location 3	2.83	.24	1.24	1.8
Location 4	1.04	0.34	0.95	0.84
Location 5	0.91	0.19	0.54	0.45
Location 6	0.42	0	0.32	0.28

As indicated in Figure 5.25, locations 1 and 3 show remarkably higher area fraction of porosity profile as compared to location 2. The maximum or minimum area fraction of porosity is in location 2 much lower than maximum or minimum area fraction of porosity in locations 1 and 3. As shown in Figure 5.26 and Table 5.2, area fraction of porosity decreases from gate to overflow in the direction flow which ends up overflow.

The area fraction of porosity profile for locations close to gate or overflow in flow direction A is much higher than the similar locations in flow direction B. In direction A, the maximum area fraction of porosity in location close to overflow is almost five times greater than that of location close to overflow in direction B. This variation can be attributed to the porosity remains in the liquid before solidification when flow does not ends up overflow. This indicates knit line locations and overflow locations play major role in the formation of porosity in the die cast components. This finding suggests that die cast components should be designed in the way that knit line patterns reach overflow during filling cavity.

Figure 5.27 shows the filling simulation conditions in the different selected time stages for Mode 2. The top hat is fed by three runners making it a casting with 5 distinct knit lines in the case of Mode 2, as shown in Figure 5.28. As indicated in Figure 5.27, the knit line among middle gates earlier than knit line occurs among corner gates. There is a considerable delay to start knit line condition between left runner and middle runner. In addition, the position of four knit lines start near gates while last knit line starts far from gates, as shown in Figure 5.27. This leads to make delay in filling the locations close to gates between left runner and middle runner, as a result, probably entraps more gas in those locations. Also, this leads to increase large gas porosity in those locations.

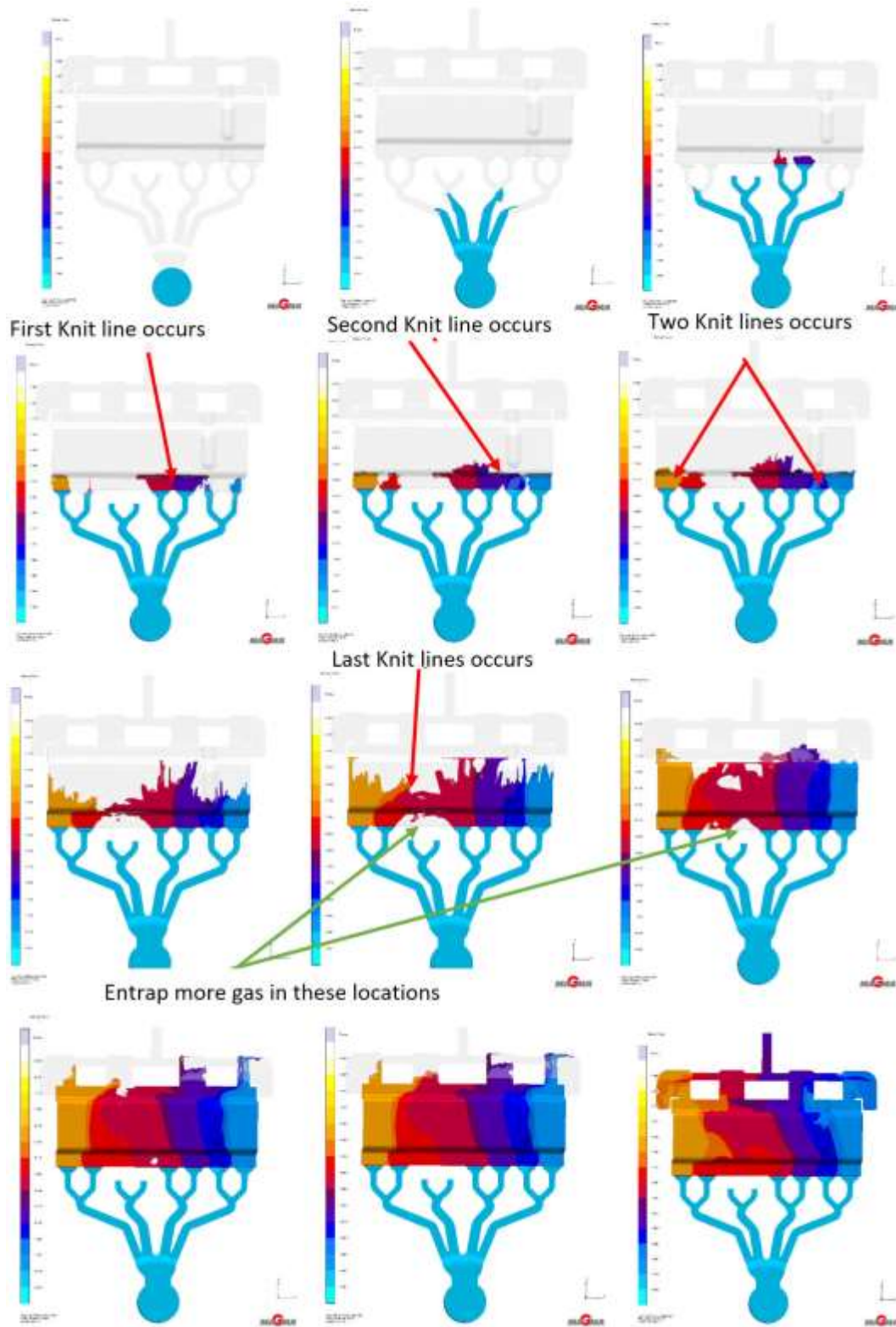


Figure 5.27: Simulation of mold filling top hat for Mode 2. Arrows show where knit line begins.

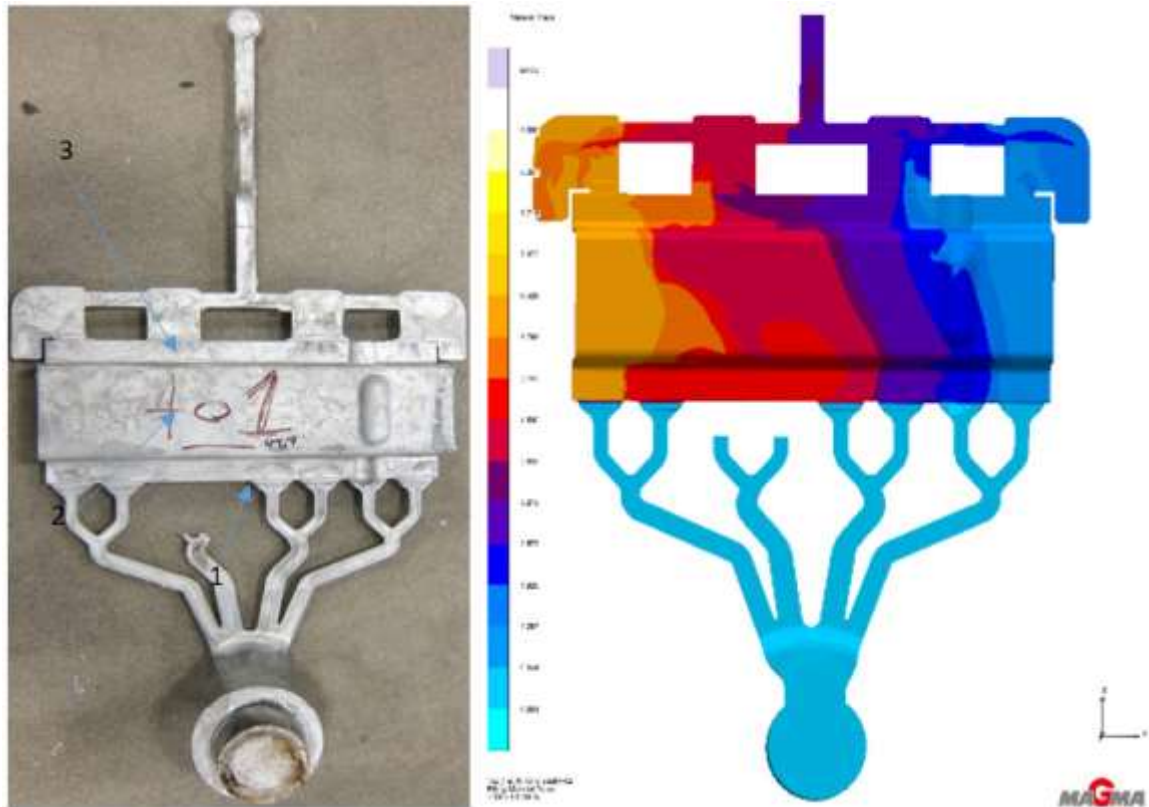


Figure 5.28: Top hat casting with three selected locations from flow direction including knit line between left runner and middle runner.

Based on the simulation results, three samples of 10mm×6mm×3mm were extracted from flow direction which might contain knit line between left runner and middle runner as shown in Figure 5.28. As illustrated in Figure 5.26, this knit line is not in the straight line. Figure 5.26 shows the profile of the area fraction of porosity in the direction parallel to the X- axis for locations 1 to 3.

Table 5.3 shows quantitative data on the porosity present in each location using X-ray tomography and optical metallography for locations which were extracted from casting of Mode 2. As indicated in Table 5.3, volumetric porosity in the locations 1 much higher than volumetric porosity in 3. As discussed, location 1 is filled after locations 2 and 3, as a result, more gas porosity located in location 1.

In Mode 2, area fraction of porosity decreases from gate to overflow which is in accordance with locations 4 to 6 in the case of Mode 1. This is due to the fact that the flow direction

including the knit line ends up overflow that reduces the amount of porosity in the locations close to overflow.

Comparison of data between Figures 5.26 and 5.29 indicates that the range of porosity level in the knit line among middle runners in Mode 2 is much higher than knit line among middle runners in Mode 1. This can be attributed that two flows meet each other in a position where far from gates in Mode 2 as compared with Mode 1.

Table 5.3: Quantitative data on the porosity presents in each location using X-ray tomography and optical microscope.

	Maximum area fraction of porosity (%)	Minimum area fraction of porosity (%)	Volumetric porosity (%)	Area fraction of porosity from optical micrograph (%)
Location 1	4.7	0.27	3.07	3.78
Location 2	3.5	0.31	2.24	3.49
Location 3	1.87	0.23	1.33	1.12

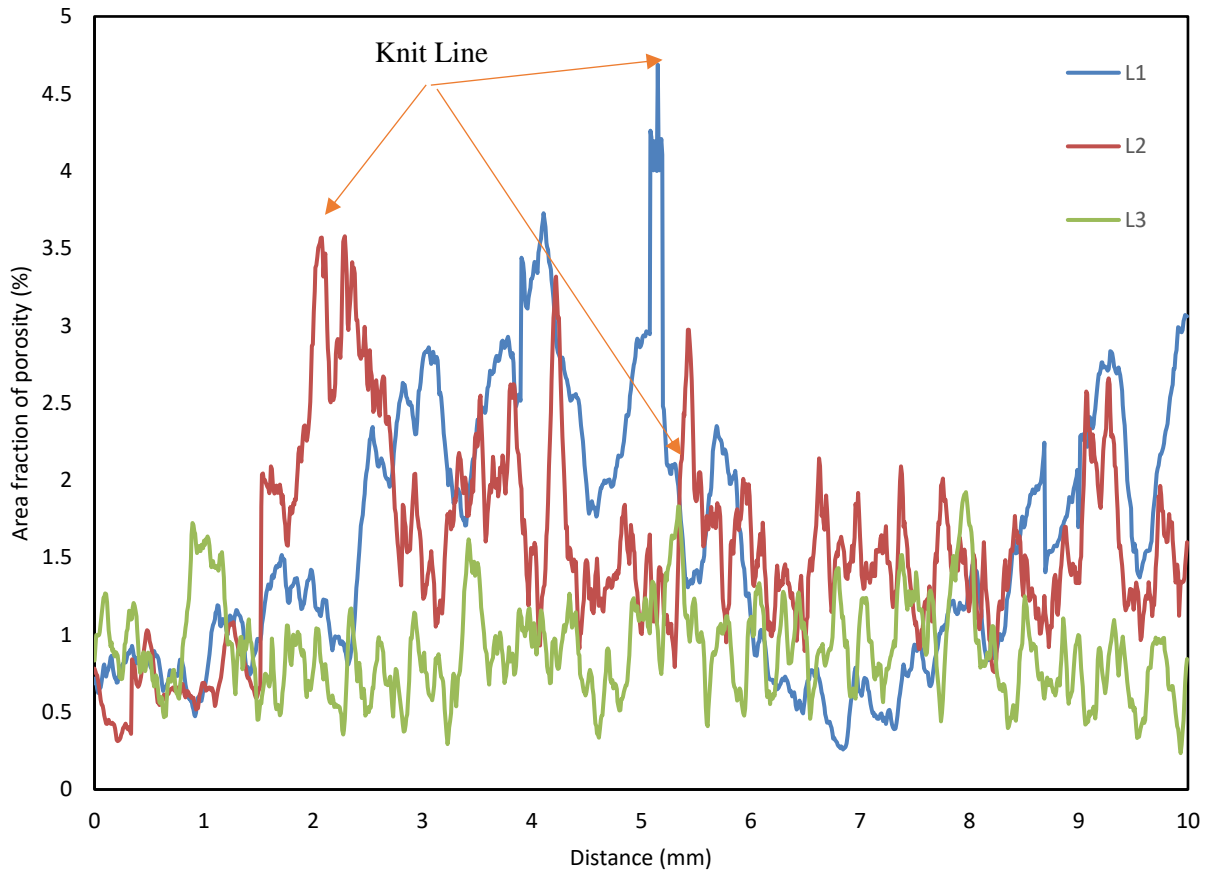


Figure 5.29: The area fraction of porosity along the X- axis of sample 1 to 3. Arrows indicates the predicted knit line locations.

Figure 5.30 shows the filling simulation conditions in the different selected time stages for Mode 3. The top hat is fed by two runners making it a casting with 3 distinct knit lines in the case of Mode 3, as shown in Figure 5.31. As illustrated in Figure 5.30, the knit line among middle gates earlier than knit line occurs among corner gates. There is a considerable delay to start knit line condition among runners. In addition, the position of two knit lines start near gates while third knit line starts far from gates, as shown in Figure 5.30.

Based on the simulation results, three samples of 10mm×6mm×3mm were extracted from flow direction which might contain knit line among two runners as shown in Figure 5.31. As illustrated in Figure 5.31, this knit line is not in the straight line. Figure 5.31 shows the profile of area fraction of porosity in the direction parallel to the X- axis for locations 1 to 3. As discussed the knit line probably happened in the location where shows maximum area fraction of porosity. As shown in Figure 5.31, arrows indicates the prediction of knit line locations.

Figure 5.33 shows a slice of tomography image for location 1. This image was selected from a location where knit line condition might occur. As illustrated in Figure 5.33, there are very big gas porosity and shrinkage porosity in the knit line region. It was observed that the majority of porosity, and in particular the larger pores are located in the interior region as compared with skin region. As mentioned the same distribution of porosity was observed for locations of Mode 1 and 2. This confirms that skin region is free porosity for die cast component and the most porosity is located in the core region even in the locations including knit line condition.

Table 5.4 shows quantitative data on the porosity present in each location using X-ray tomography and optical metallography for locations which were extracted from casting of Mode 3. As indicated in Table 5.4, volumetric porosity level in locations 1 is much higher than volumetric porosity in location 2. As shown in Figure 5.30, location 1 is filled after locations 2, as a result, more gas porosity located in location 1 as compared with location 2.

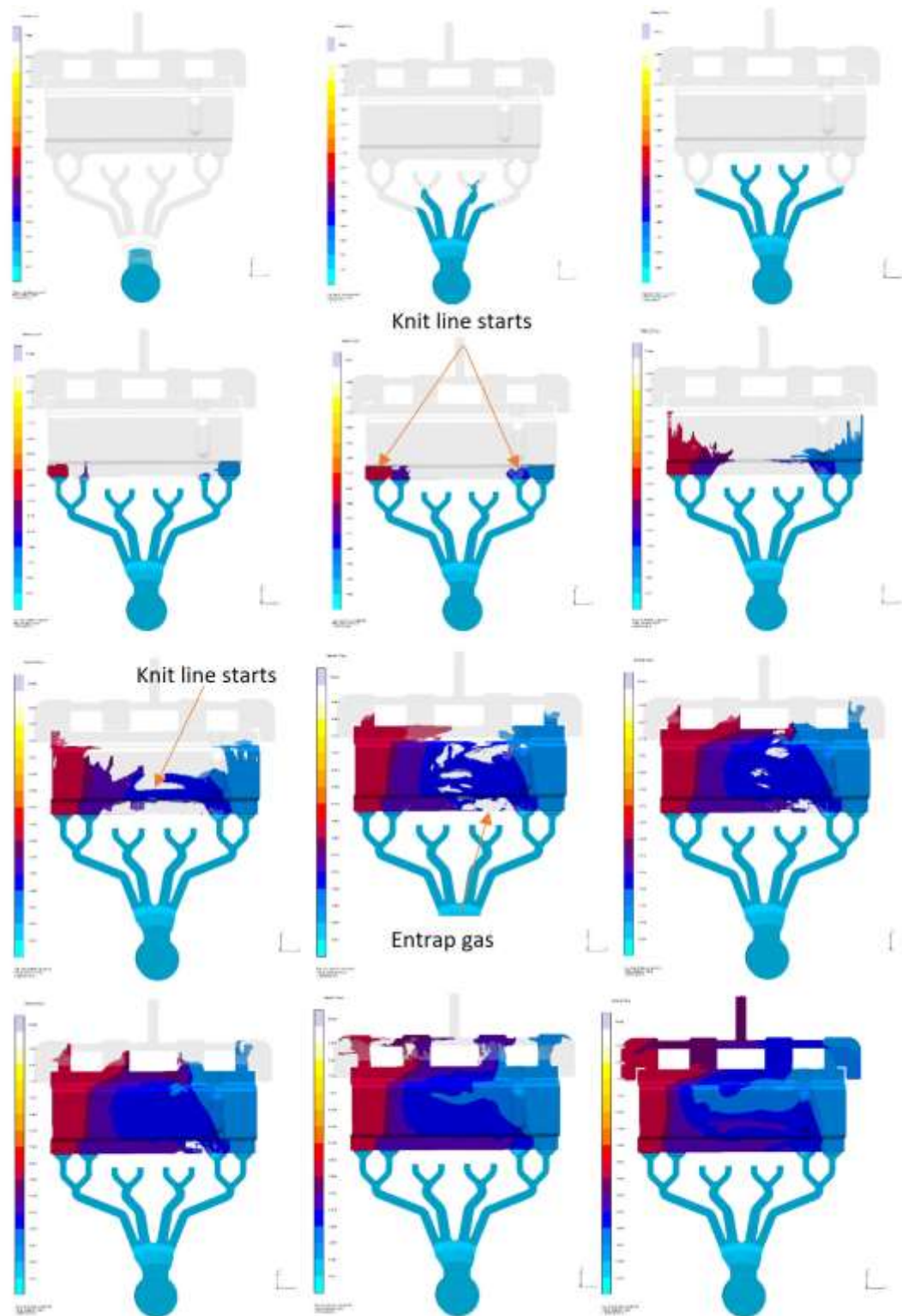


Figure 5.30: Simulation of mold filling top hat for Mode 3. Arrows show locations of knit line begins.

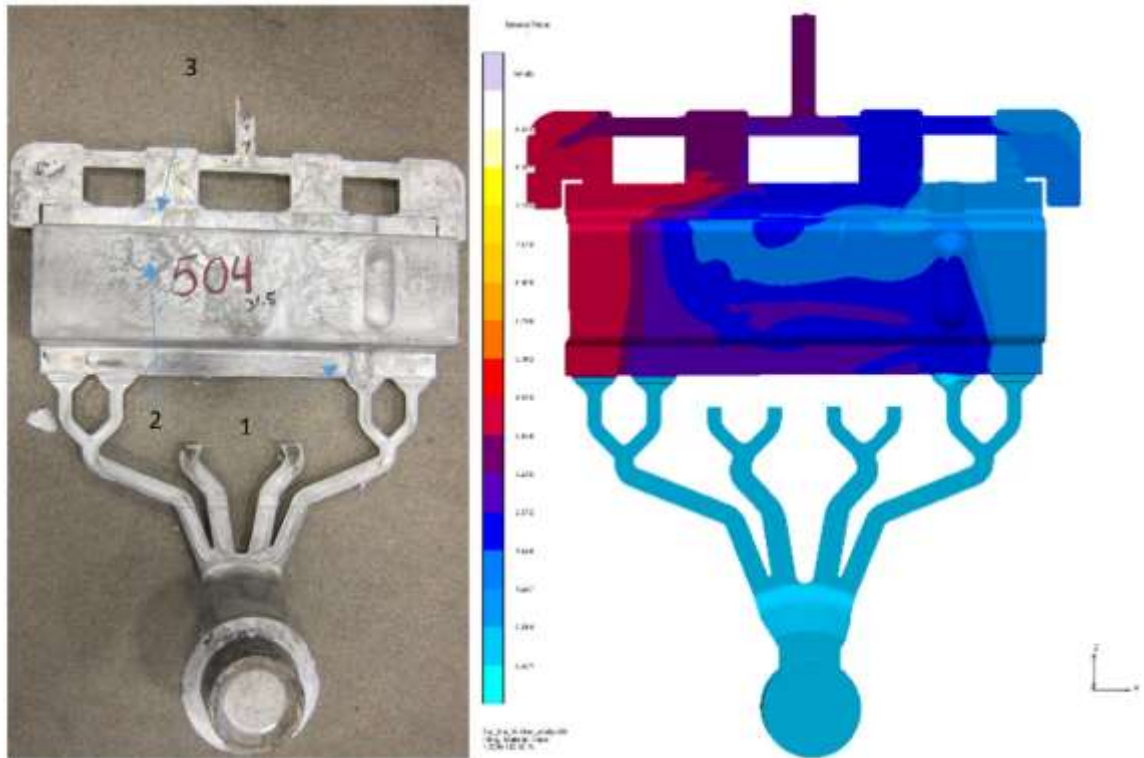
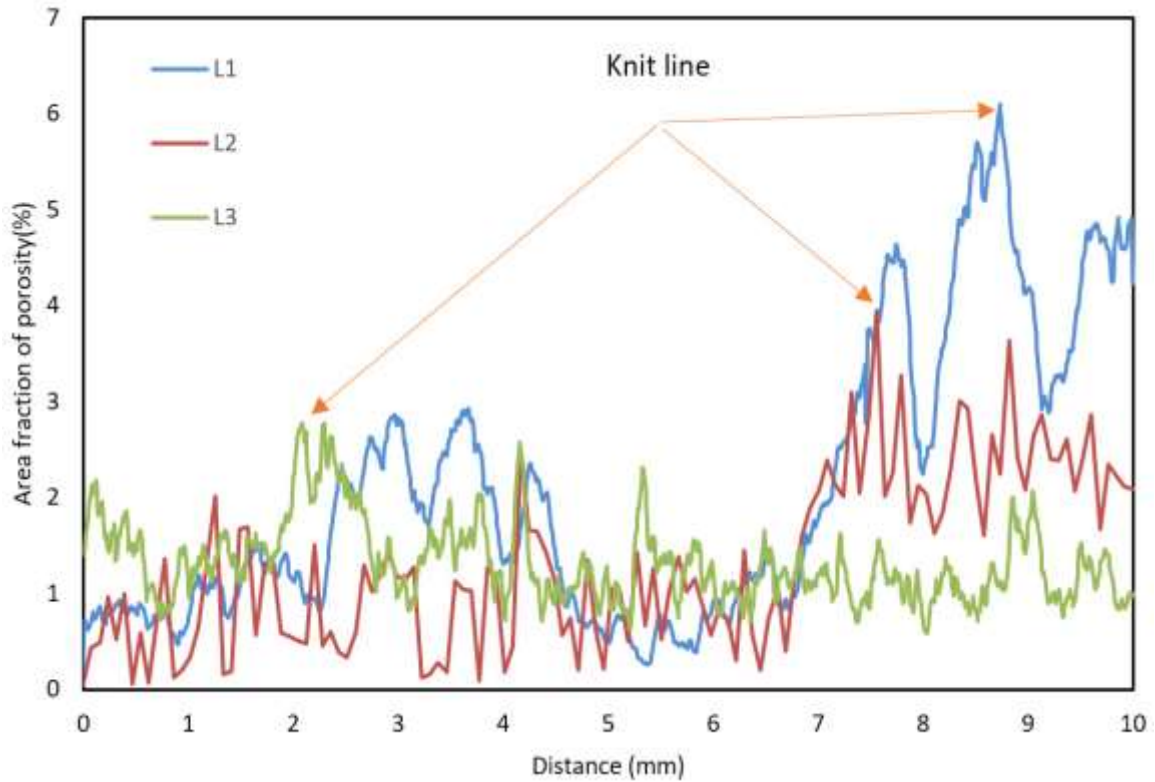


Figure 5.31: Top hat casting with three selected locations from flow direction including knit line between left runner and middle runner.

Like Modes 1 and 2, area fraction of porosity decreases from gates to overflow in Mode 3. This confirms that the flow direction including the knit line ends up overflow that reduce the amount of porosity in the locations close to overflow. In order to design the die cast component, the flow direction including knit line should insert in a pattern which reaches overflow during filling cavity.

Comparison of data in Figure 5.26, 5.29 and 5.31 shows that the range of porosity level in the knit line among middle runners in Mode 3 is much higher than the knit line among middle runners in Modes 1 and 2. This is because, removing of two runners in Mode 3 causes the start point of knit line to be far from gates. More turbulent might form into liquid when two flows meet each other, as a result, more gas forms in these locations. To prevent more formation of turbulence in the fluid, the start point of knit line should be close to gates.



**Figure 5.32: The area fraction of porosity along the X- axis of samples 1 to 3.
Arrows indicate the prediction of knit line locations**

Table 5.4: Quantitative data on the porosity presents in each location using X-ray tomography and optical microscope.

	Maximum area fraction of porosity (%)	Minimum area fraction of porosity (%)	Volumetric porosity (%)	Area fraction of porosity from optical micrograph (%)
Location 1	5.96	0.25	3.12	2.49
Location 2	3.95	0	2.4	1.89
Location 3	2.69	0.61	2.13	1.57

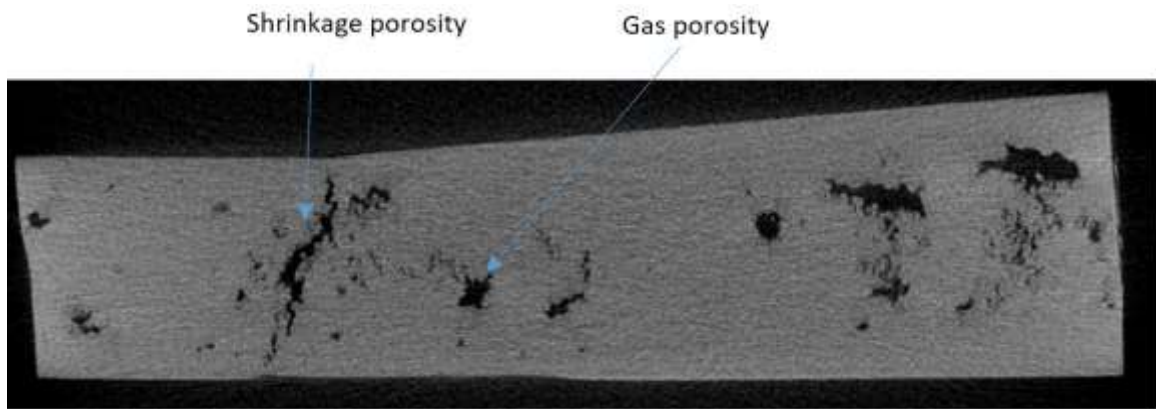


Figure 5.33: Tomography image showing the internal pores in cross section of casting, indicating a gas pore and the shrinkage pores.

Chapter 6

6 PREDICTION OF HEAT TRANSFER COEFFICIENT AT METAL/DIE INTERFACE

As discussed in Chapter 4, the heat transfer at the metal-mold interface plays a very important role in predicting the grain structure of castings. Also, determination of the interfacial heat transfer coefficient (IHTC) between molten metal and die surface is the most challenging issue in the numerical simulation of HPDC. The IHTC essentially quantifies the resistance to heat flow across the interface between the casting and the mold. Although many studies [33-40] have been undertaken to obtain the heat transfer coefficient for different kinds of casting processes, few attempts were carried out to predict the IHTC during the HPDC process, because, the operation procedure is complicated. In HPDC process, there are some limitations in the measurement of temperature such as high solidification rate, arrangement of thermocouples, high applied pressures and thermocouple response time.

Since reliable experimental values of (IHTC) are required for the prediction of solidification time and grain structure for HPDC processes, a new casting instrument was designed to simulate the important aspects of the HPDC process. In this chapter, variation of heat transfer coefficient at metal/die interface during solidification of magnesium alloy AM60 was analyzed by the inverse method. Also, effects of different pressure levels on the variation of IHTC were examined.

6.1 Experimental Procedure

In order to simulate the HPDC process, a new casting process instrument was designed by CanmetMaterials and Dr. Wood's research group at the University of Western Ontario. In this study, this instrument is called MiniCaster machine. The MiniCaster contains three main segments: hydraulic piston, die cavity and casting mold. As shown in Figure 6.1, the hydraulic piston and casting mold are in the two different sides which are locked after pouring molten metal into die cavity.

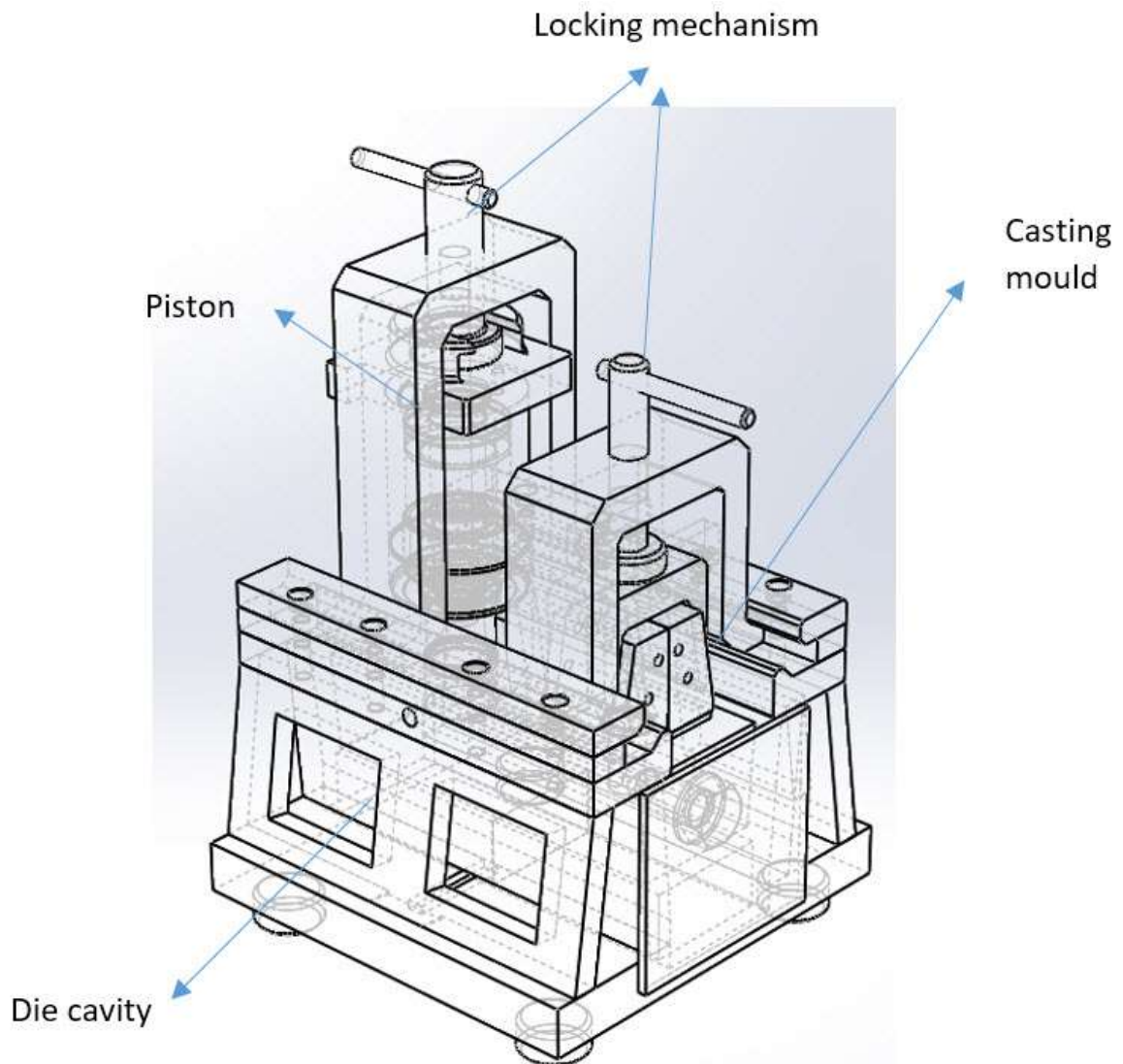


Figure 6.1: Schematic diagram of MiniCaster machine.

Figure 6.2 shows the configuration of the main part of MiniCaster. The diameter of piston, die cavity, and dimension of casting mold are shown in Figure 6.2. The mold casting shape is an inverted wedge. The alloy was melted in an electric resistance-type furnace up to a predetermined temperature. The thermocouple (K-type; chromel-alumel) is inserted into the pattern to measure temperature. The thermocouples report the local temperature at intervals of 0.1 ms.

Figure 6.3 shows the position of the thermocouples inside the casting and mold. The TC₁ installed inside the casting at center of wedge. The TC₂, TC₃ and TC₄ are located 1.5, 3 and 6 mm from the wall mold. During the casting process the thermocouples are connected to the data acquisition system as shown in Figure 6.4.

The alloy casted was AM60. The nominal chemical compositions of this alloy is given in Table 3.1. The alloys was melted in the electric resistance-type furnace and then poured alloy molten into the die cavity. The die cavity was preheated to 600 °C and, before pouring became stable using non-conductive materials. Pouring temperature was approximately 700 °C. The hydraulic piston was then installed. The pressure values of 100, 125, 150 and 175 bar were applied in this study.

After the completion of casting process, samples were sectioned at regular intervals along the height of casting, for metallographic analysis. Metallographic method was used same as procedure which was explained in the Section 3.1.3. Figure 6.5 shows a typical wedge casting poured under above mentioned process condition with applied hydraulic pressure of 175 bar.

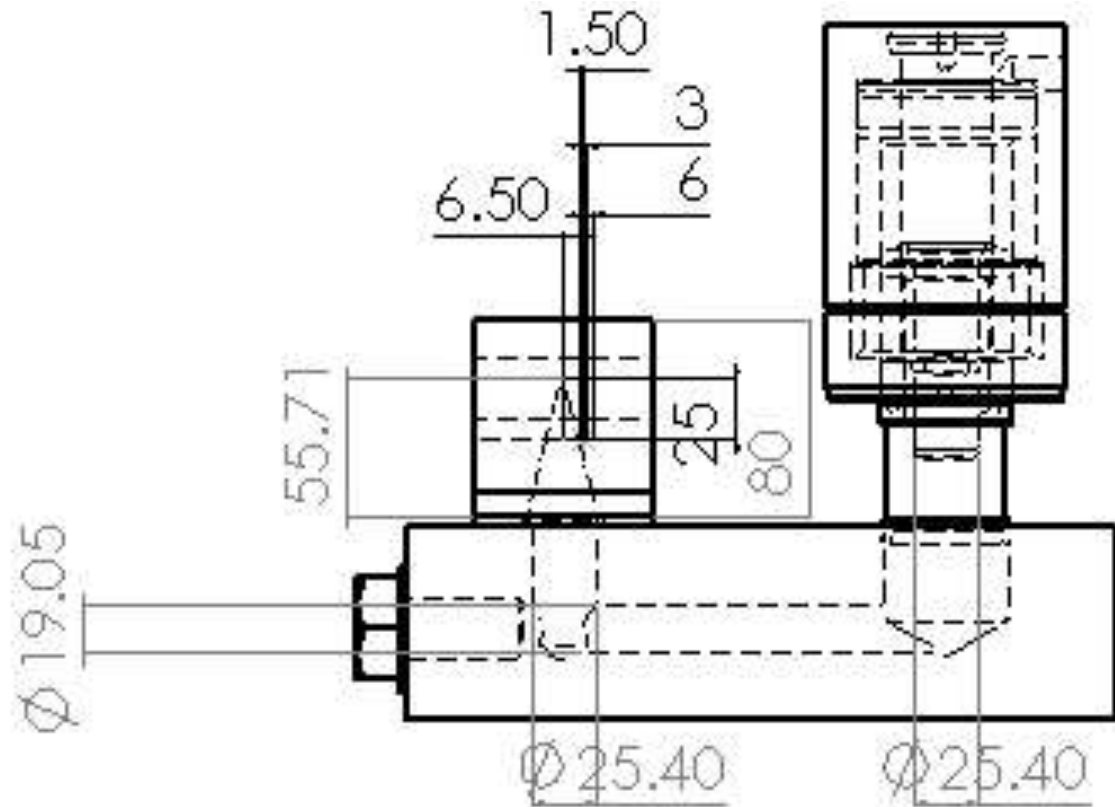


Figure 6.2: Configuration of the dies and adjustment of the thermocouples.

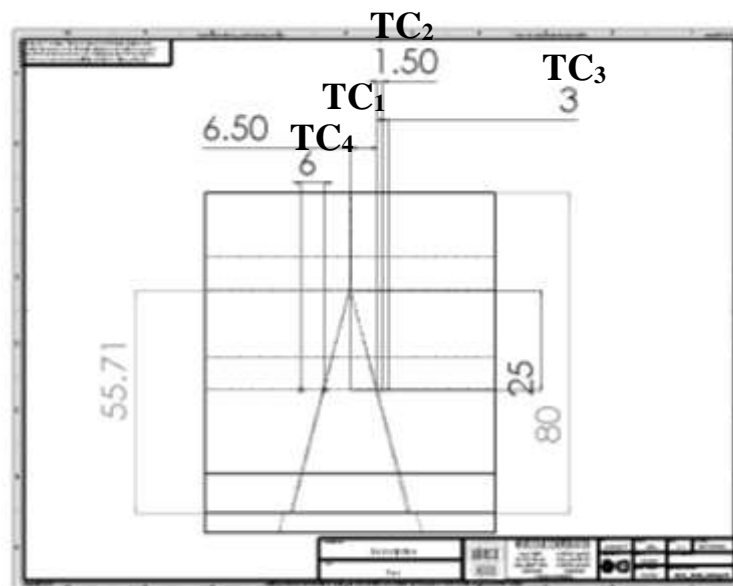


Figure 6.3: The position of thermocouples.

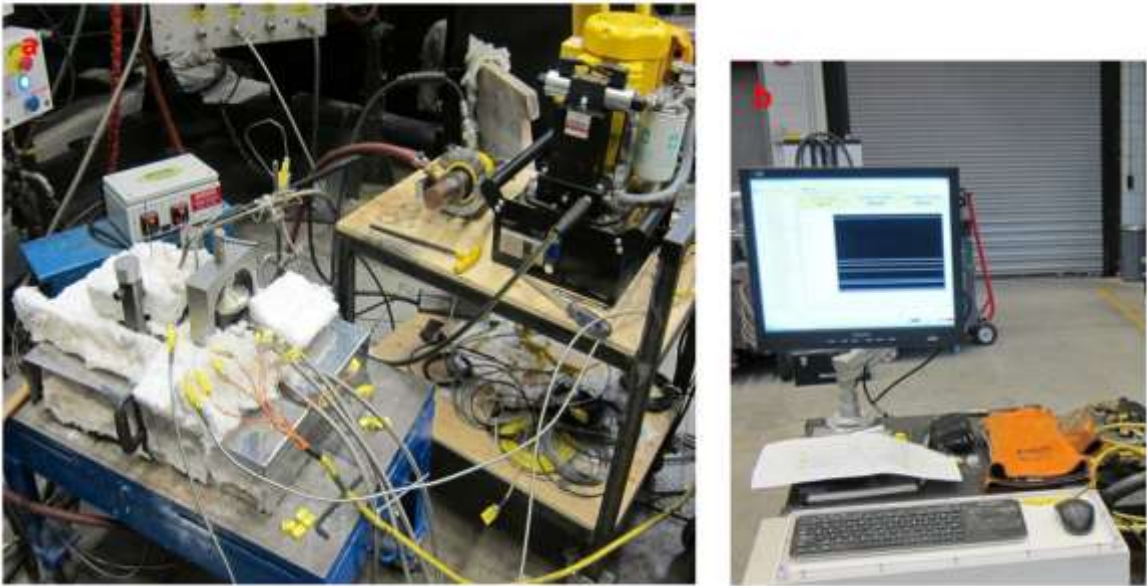


Figure 6.4: a) MiniCaster machine and b) the data acquisition system.



Figure 6.5: Wedge casting under applied pressure 175 bar.

6.2 Mathematical Modeling of Interfacial Heat Transfer Coefficient

As discussed in Chapter 2, the interfacial heat-transfer coefficient (IHTC) is defined by the heat flux per unit area at the metal/mold interface divided by the temperature difference between the alloy and the die surface, which is characterized by equation:

$$h(t) = \frac{q(t)}{T_{cs} - T_{ds}} \quad (6.1)$$

where q is heat flux at the metal–die interface; T_{cs} and T_{ds} are the casting surface temperature and die surface temperature, respectively. The heat flux at the metal/die interface can be determined from the gradient at the surface node and sub-surface node, as:

$$q(t) = -k \frac{dT}{dX} = -k \frac{T_n^t - T_{n-1}^t}{\Delta x} \quad (6.2)$$

where k is thermal conductivity of the casting or die materials and T_n^t is the temperature value on time t at the nodal point n .

Since solidification involves a phase change and thermal properties of magnesium are temperature dependent, the heat conduction is a non-linear problem. In order to predict the IHTC as a function of solidification time in this process, the finite difference method (FDM) was used based on the Beck's algorithm [41].

6.2.1 Heat Transfer Inside the Die

Since the solidification rapidly occurs in the MiniCaster process, it is assumed to be a purely transient conduction problem with negligible convection. Also, the heat transfer from the alloy towards the mold walls is assumed to be in one dimension. The heat transfer between the die surface and the last temperature measurement point is expressed by the general equation of heat conduction, as:

$$\rho C_p \frac{\partial T}{\partial t} = \frac{\partial}{\partial x} \left(k \frac{\partial T}{\partial x} \right) \quad (6.3)$$

where ρ is density, C_p is heat capacity,

The initial and boundary conditions are expressed by the following equations:

$$T(x,0)=T_i(x)$$

$$q(0,t)=-k(T)\frac{\partial T}{\partial X} \quad (x=0)$$

$$T(l, t)= Y(L, t)$$

where T_i is the initial temperature of the die. L is the distance from the last measured temperature point to the die surface and Y is the measured temperature at distance L from die surface. In this study, it is assumed that the value of those physical properties are constant

Using implicit finite difference method for the development of **Eq6.3**, we have:

$$\frac{T_n^{p+1}-T_n^p}{\Delta t} \cong k \frac{T_{n-1}^{p+1}-2T_n^{p+1}+T_{n+1}^{p+1}}{\Delta x^2} \quad (6.4)$$

The superscript p is referred to time dependence of T . The subscript n mean the number of the discrete nodal points. In order to calculate the temperature distribution, **Eq6.4** can be rewritten, as following equations:

- For the surface node of the die

$$(1+2r)T_0^{p+1} - 2rT_1^{p+1} = 2r \frac{\Delta x}{k} q + T_0^p \quad (6.5)$$

- For any interior node of the die

$$(1+2r)T_n^{p+1} - r(T_{n-1}^{p+1} + T_{n+1}^{p+1}) = T_n^p \quad (6.6)$$

where

$$r = \frac{k \Delta t}{c\rho(\Delta x)^2} \quad (6.7)$$

As discussed, the heat flow at the metal-die interface at each step time can be determined by solving the inverse method which was introduced by Beck [41]. This method focused on minimizing the following function:

$$\delta^{p+j-1} = \sum_{j=1}^J (T_{est}^{p+j-1} - T_{exp}^{p+j-1}) \quad (6.8)$$

where T_{est} and T_{exp} are, the estimated and experimentally measured temperatures at various thermocouple locations and times respectively and j is the integer subsequent future time steps. At the first time step, an appropriate initial value of q is assumed and with this value, the temperature distribution at each node of the next time step was calculated using **Eq6.5** to **Eq6.7**. The correction in heat flux (q) at each iteration step is made by εq value and new temperatures are calculated. The corrected heat flux of the same time step was obtained by following equations [32, 35]:

$$\Delta q^p = \frac{\sum_{j=1}^J (T_{est}^{p+j-1} - T_{exp}^{p+j-1})(\phi^{p+j-1})}{\sum_{j=1}^J (\phi^{p+j-1})} \quad (6.9)$$

$$\phi^{p+j-1} = \frac{\partial T}{\partial t} = \frac{\sum_{j=1}^J T_{est}^{p+j-1}(q_{corr}^p) - T_{est}^{p+j-1}(q^p)}{\varepsilon q^p} \quad (6.10)$$

$$q_{corr}^{p+1} = q^p \pm \Delta q^p \quad (6.11)$$

This procedure is repeated for a new h , and ε continues until $\Delta q^p / q^p \leq \varepsilon$. These previous equations, the heat flux at the metal-die interface and die temperature can be determined by the following iterative procedure:

- (1) The temperature distribution at each node is calculated by input experimental and thermophysical data and assume a suitable heat flux value (q) in **Eq6.6** to **Eq6.8**.
- (2) Calculate ϕ^{p+j-1} from **Eq6.10**
- (3) Calculate q_{corr}^{p+1} from **Eq6.9** and **Eq6.11**
- (4) Substitute ($q^{p+1} = q^p$) and repeat (1), (2) and (3) until $\Delta q^p / q^p \leq \varepsilon$
- (5) Substituted $p=p+1$ and repeat (1) to (4).

6.2.2 Heat Transfer Inside the Casting

Due to the phase change that occurs during the casting process, the latent heat of solidification must be taken into account. **Eq6. 3** is amended by adding the latent heat term (S_L), which is described by the heat source term related with the latent heat [32, 40], as:

$$\rho C_p \frac{\partial T}{\partial t} = \frac{\partial}{\partial x} \left(k \frac{\partial T}{\partial x} \right) + S_L \quad (6.12)$$

$$S_L = L \frac{\partial f_s}{\partial t} \quad (6.13)$$

L is the latent heat and f_s is the fraction of solid formed during the phase transformation.

Thus, **Eq6.12** is transferred into:

$$\rho \left(C_p - l \frac{\partial f_s}{\partial t} \right) \frac{\partial T}{\partial t} = \frac{\partial}{\partial x} \left(k \frac{\partial T}{\partial x} \right) \quad (6.14)$$

Where,

$$C = C_p - l \frac{\partial f_s}{\partial t} \quad (6.15)$$

The temperature profile of surface casting can be determined by applying **Eq6.5** to **Eq6.7**.

6.3 Results and Discussion

This section includes two segments. First, the heat flux and IHTC variation during solidification of magnesium alloys that associated via pressure is discussed. Second, the microstructural feature of wedge cast is described.

6.3.1 Heat Flux and IHTC Evaluation

Figure 6.6 shows typical set of measured temperature curves inside the casting and die for solidifying magnesium alloy AM60 and steel die respectively with applied hydraulic pressure of 150 bar. Figure 6.6 also shows the predicted die temperature and surface temperature which were determined based on the measured temperatures of die and center

of casting. As shown in Figure 6.6, the temperature curve at casting increases abruptly and drops faster than the measured temperature obtained at different locations on the mold wall. The same results can be observed for the predicted temperature at the metal-die interface.

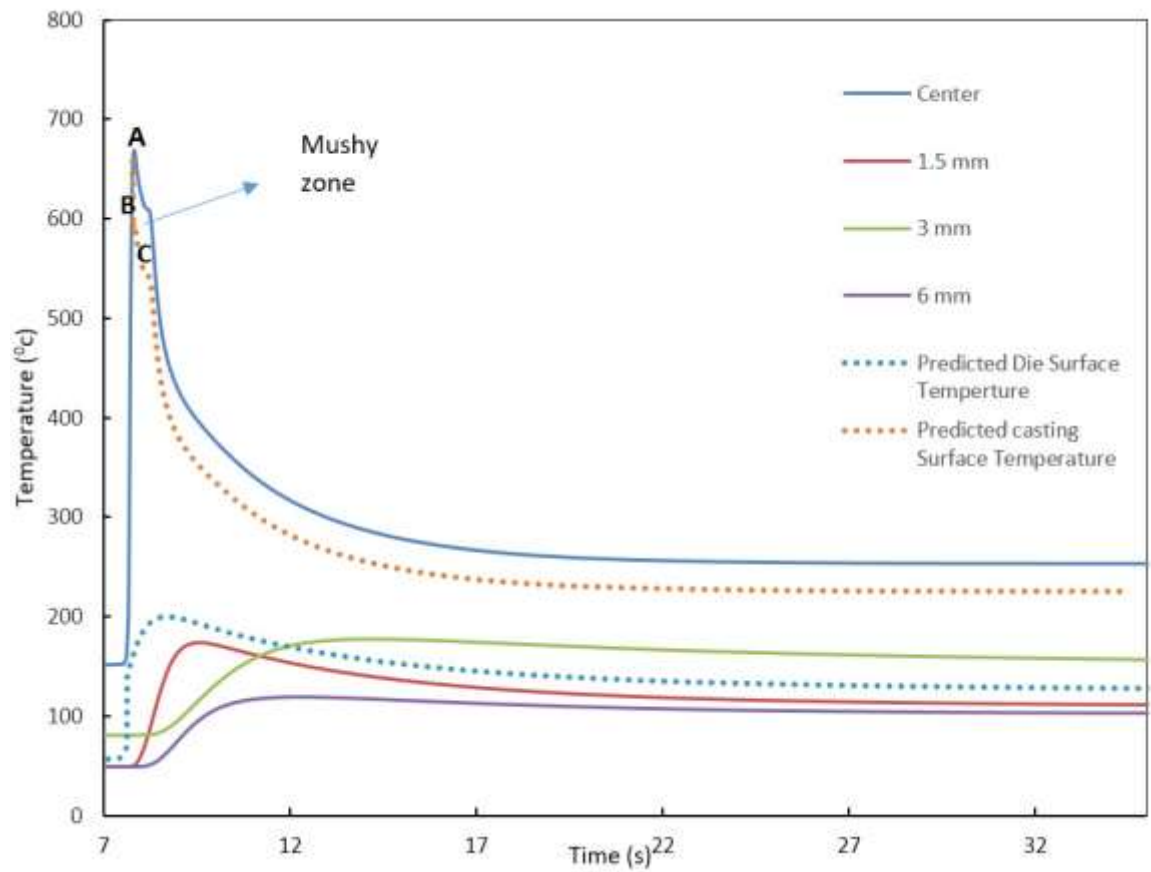


Figure 6.6: Measured temperatures in the casting and die and predicted surface casting die temperatures.

Figure 6.6 indicates the dynamic temperature variation at the metal-die interface. As shown in Figure 6.6, the rapid reduction of the predicted casting surface temperature occurred after metal pouring that indicates a high cooling rate near the mold wall. Since there is relatively cold mold wall, the cooling rate near wall is expected to be higher than that the cooling rate at center.

There are three segments in the cooling rate for casting surface temperature: high cooling rate from liquid state to mushy zone (A to B), middle cooling rate through mushy zone (B to C) and slow cooling rate in the solid state (after C).

It can be observed in Figure 6.6, that die surface temperature rises immediately corresponding to the decrease of the surface temperature in the high cooling rate segment. The die surface temperature reaches a maximum value while the casting surface temperature curve is still in the mushy zone with middle cooling rate. No die surface temperatures exceeded 200°C. The die surface temperature cools down when slow cooling rate of the casting surface temperature begins.

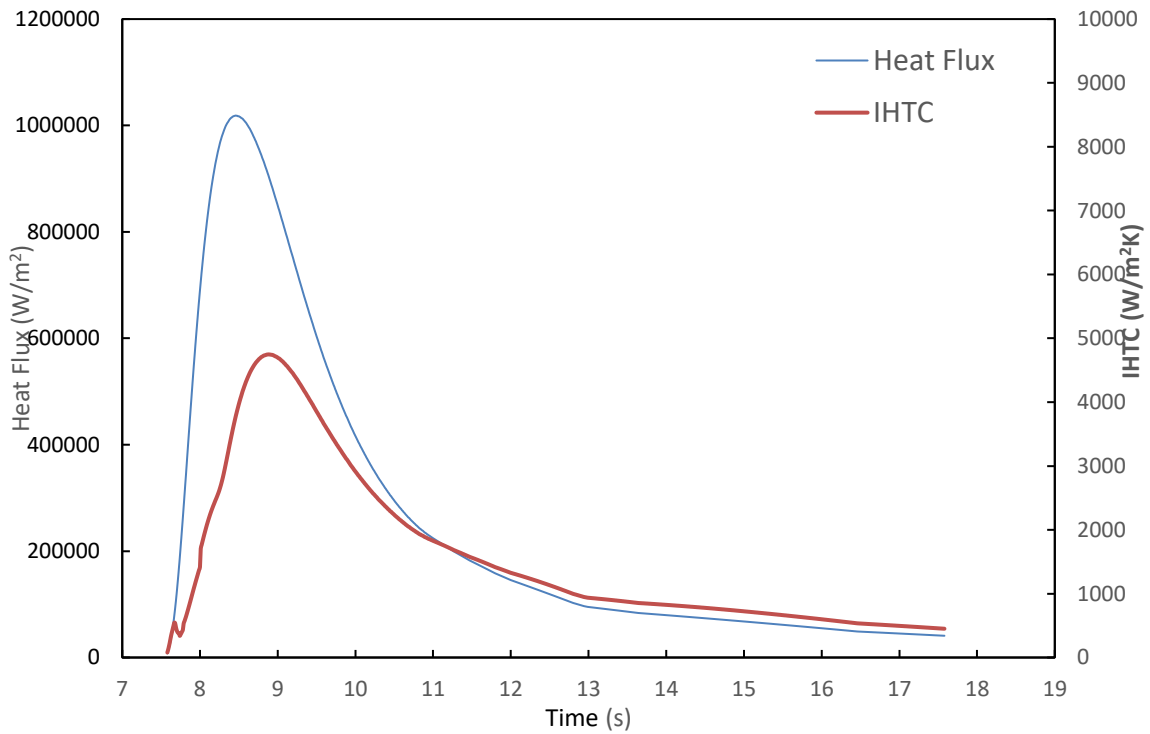


Figure 6.7: The predicted Heat flux and IHTC curves during solidification of magnesium alloys AM60 with applied pressure 150bar.

Based on the measured temperature at the center of the casting and 1.5, 3 and 6 mm from the die surface, heat flux and IHTC were determined using inverse method. Figure 6.7 shows the predicted IHTC (h) and heat flux (q) profiles with applied pressure 150 bar. The maximum heat flux value is $10.2E+04 \text{ Wm}^{-2}$, and the peak value of IHTC is $4747 \text{ Wm}^{-2} \text{ K}^{-1}$.

As shown in Figure 6.7, immediately after the filling cavity, the IHTC increases abruptly until reaching its peak value. This abrupt increase is explained by two reasons. First, the

rapid reduction of the casting surface temperature causes to transfer significant heat from casting immediately after filling. Second, the metal is completely liquid and has very good contact with mold.

After peak point, the IHTC curve drops rapidly until its value is less than $2000\text{Wm}^{-2}\text{K}^{-1}$ as shown in Figure 6.7. The same trend is observed for heat flux curve. The abrupt decrease of IHTC and heat flux take less than 2.5 second. The abrupt reduction of the IHTC or heat flux after peak point, can be explained by reduction close contact between the casting and die, due to the decrease of pressure effects as formation of the solid skin thickness.

The same trend in the IHTC curves observed for different level of pressure values. For all experiment, IHTC curves began with an increasing stage and reached their peak value, then dropped until the value became relative low level. The same behavior of IHTC profile have been reported by Gue et al. [40] who predicted the IHTC curves during HPDC process.

6.3.1.1 Effect of Pressure on the IHTC Value

Figures 6.8 and 6.9 show the predicted heat flux and IHTC during solidification of magnesium alloys AM60 with applied pressure 100, 125, 150 and 175bar. The peak value of heat flux is increased by increasing of pressure values. Also, the pressure has little effect on the shape of heat flux curves as shown in Figure 6.8. The application of different pressure values has considerable effects on the peak of heat flux curves while initial stage of heat flux is not affected by pressure. It is attributed to the initial stage of heat flux is affected by filling time, therefore, since these process parameters are relatively similar in all experiments, the initial stage of heat flux with application of various pressure values show the same behavior.

After filling stage, the pressure can affect the contact condition between the casting and mold. The effect of pressure reduces with the increasing of the solid skin thickness. It is due to the fact that contraction of the solidified layers that causes the perfect contact between the mold and the solidified casting no longer exists. Therefore, variation of pressure value mostly has influence on the shape and value of peak stage and first and last stage are affected by filling time and solidification process, respectively.

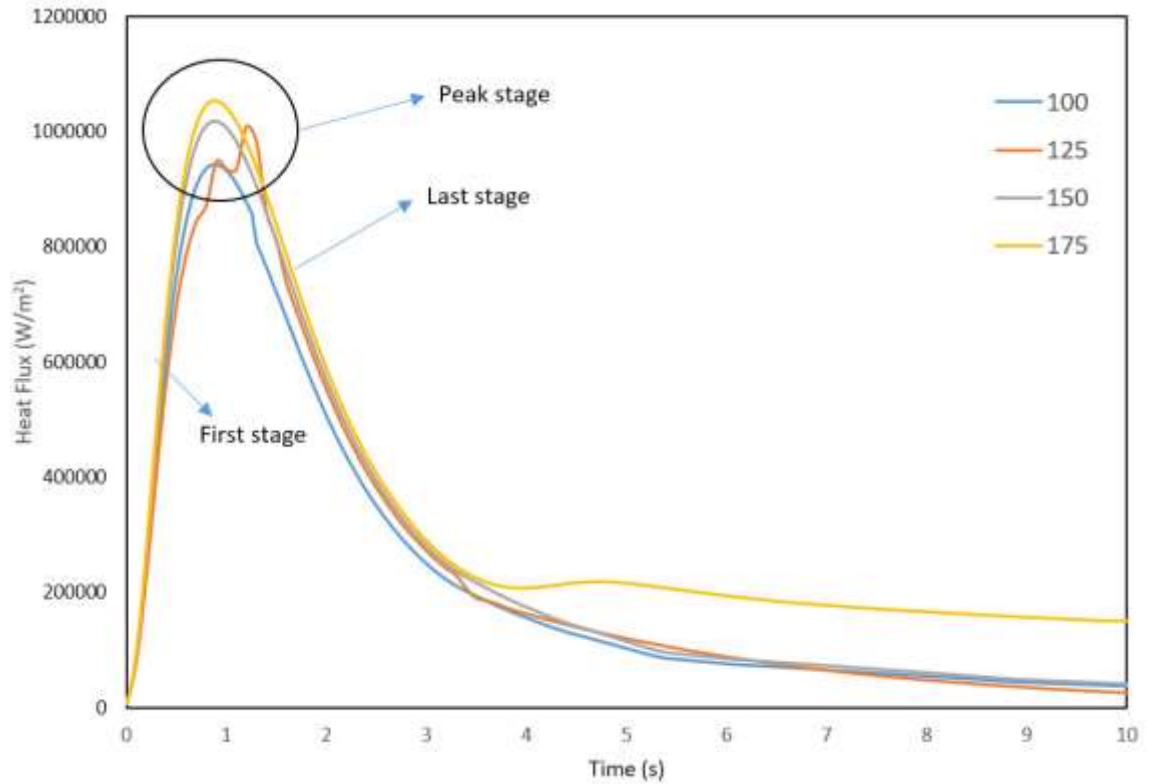


Figure 6.8: The predicted heat flux with applied pressure 100, 125, 150 and 175bar. Arrows indicate different stages of heat flux curves.

The IHTC values in the peak stage increase with increasing in pressure values which are in good agreement with the previous studies. Literature confirms that the higher level pressure increase the IHTC value in the casting process such as squeeze casting and high pressure die cast. It is attributed to higher level of pressure improves the contact between the castings and mold in the interface. As shown in Figure 6.8, the peak duration time reduces with increasing of applied pressure. The same results have been reported by Z. Sun [32] who investigated the impact of the variation of pressure values on the IHTC curves during solidification of magnesium alloys using squeeze casting.

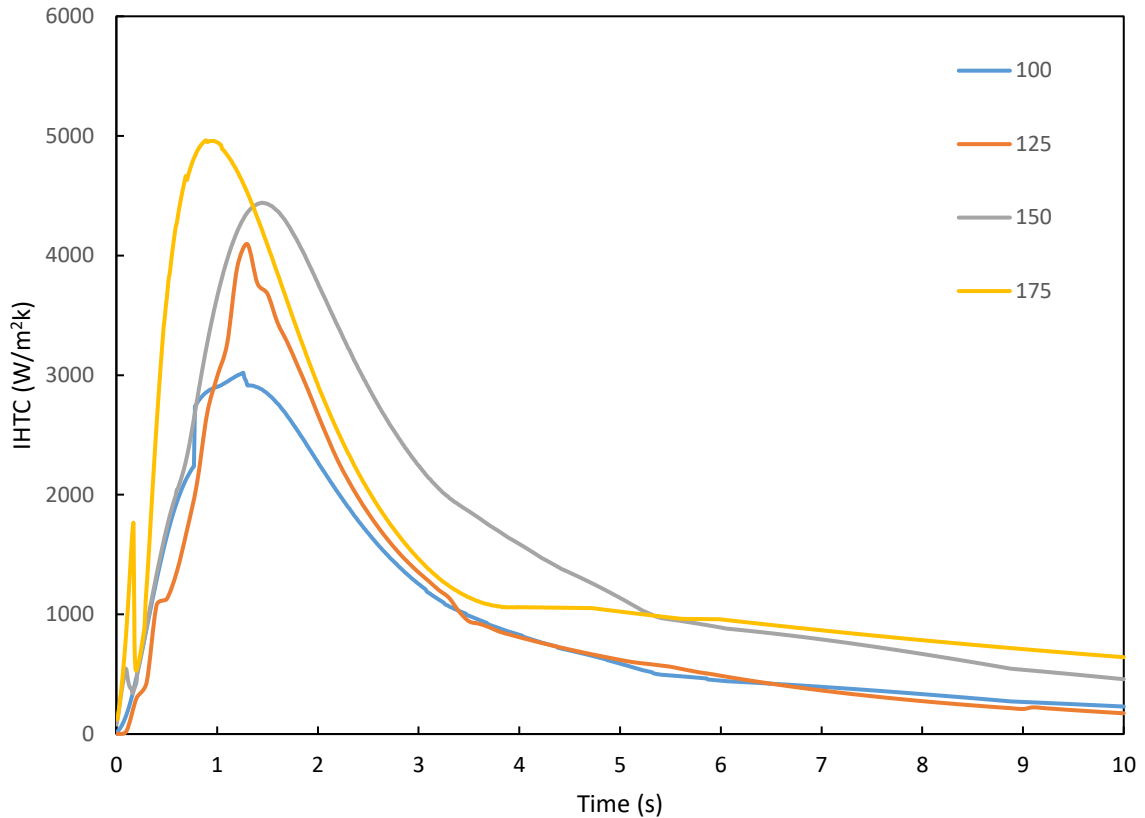


Figure 6.9: The predicted IHTC during solidification of magnesium alloys AM60 with applied pressure 100, 125, 150 and 175bar.

As illustrated in Figure 6.9, the variation of pressure values has significant effect on the shape of IHTC profile for three stages while the pressure has only effect on the peak stage of heat flux curves. This is attributed to the IHTC curve is affected by cooling rate, die surface temperature, casting surface temperature and heat flux. These factors generally depend on the variation of pressure values. However, it is reasonable that there should be difference between IHTC curves and heat flux curves in terms of pressure effects. Also previous studies indicated that the variation of IHTC depend on the other process parameters such as: the wettability of the liquid on the mold surface, pouring time, the amount of super heat, surface roughness, initial die temperature, thermal conductivity of mold, and turbulence of melt.

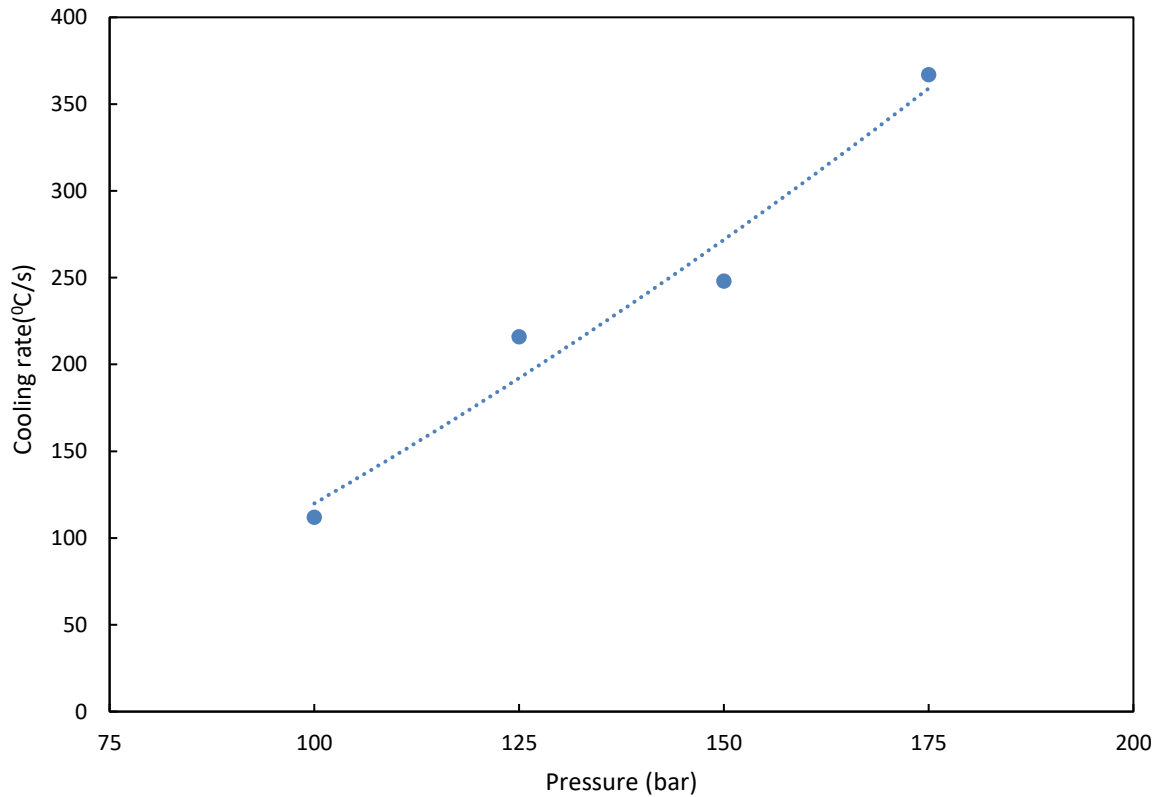


Figure 6.10: The dependency of cooling rate on the variation of pressure. Note that the cooling rate was measured by thermocouple which was located in the center.

Figure 6.10 shows the correlation between the applied pressure and the measurement of cooling rate. The cooling rate shows strong dependency on the variation of pressure. By the increase of pressure from 100 to 175 bar, the cooling rate is increased from 112 °C/s to 367 °C/s. This observation is consistent with finding of Z. Sun et al. [32] who reported that the cooling rate is increased by higher level of pressure during solidification of magnesium alloy AM60 using squeeze casting.

Figure 6.11 shows the correlation between the applied pressure and the peak of IHTC value. The IHTC shows strong dependency on the variation of the applied pressure. As shown in Figure 6.10, higher level of pressure leads to a higher IHTC peak value. By the increase of pressure from 100 to 175 bar, the amount of IHTC is increased from 3020 Wm⁻² K⁻¹ to 4963 Wm⁻² K⁻¹. The dependence of IHTC on the pressure can be described using the empirical equation, as given:

$$h = -0.344 P^2 + 120.66P - 5602.1 \quad (6.16)$$

P is the applied pressure and h is the peak value of IHTC.

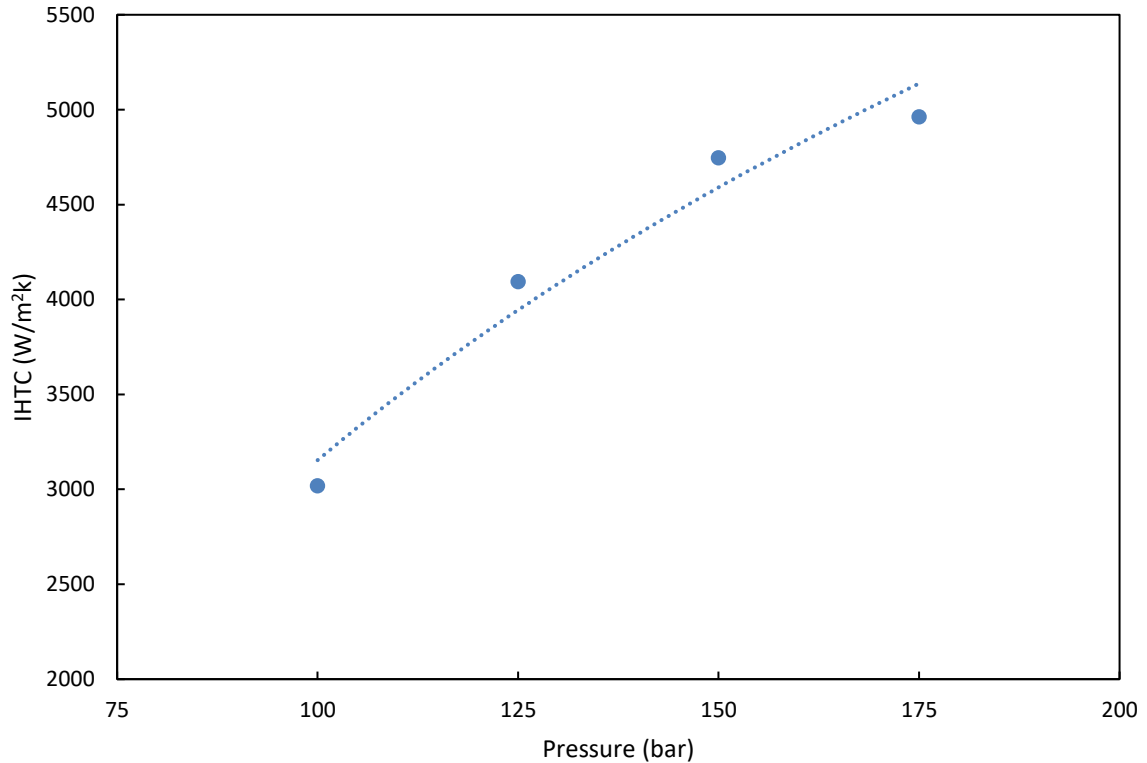


Figure 6.11: The maximum IHTC values as a function of the applied pressure.

The **Eq6.16** enable the predicting the peak values of IHTC for different levels of pressure. Note that this equation was determined for the inverted wedge produced by the MiniCaster.

In order to analyze the accuracy of IHTC evaluation by the inverse method, the peak IHTC value obtained from **Eq6.16** can be compared with the IHTC values which published in the literature [32, 40]. Figure 6.12 shows the predicted IHTC value determined based on the results of MiniCaster and the IHTC value were obtained during solidification of magnesium alloys AM60 and AM50 using squeeze casting and HPDC. These studies [32, 40] indicated that the peak value of IHTC show a strong dependency on casting thickness for squeeze or HPDC. Z. Sun et al. reported that the peak IHTC value increased as the thickness of step-cast increased for squeeze casting process. Gue et al [40] reported that

the IHTC value in a range from 10820 to 14,780 $\text{Wm}^{-2} \text{K}^{-1}$ for different thickness of step-shape die casting of magnesium. The IHTC data were extracted from casting sections whose thickness value is in correspondence with thickness of inverted wedge. As shown in Figure 6.12, the **Eq6.16** overestimates the peak IHTC values as compared with data extracted from literature, for squeeze casting.

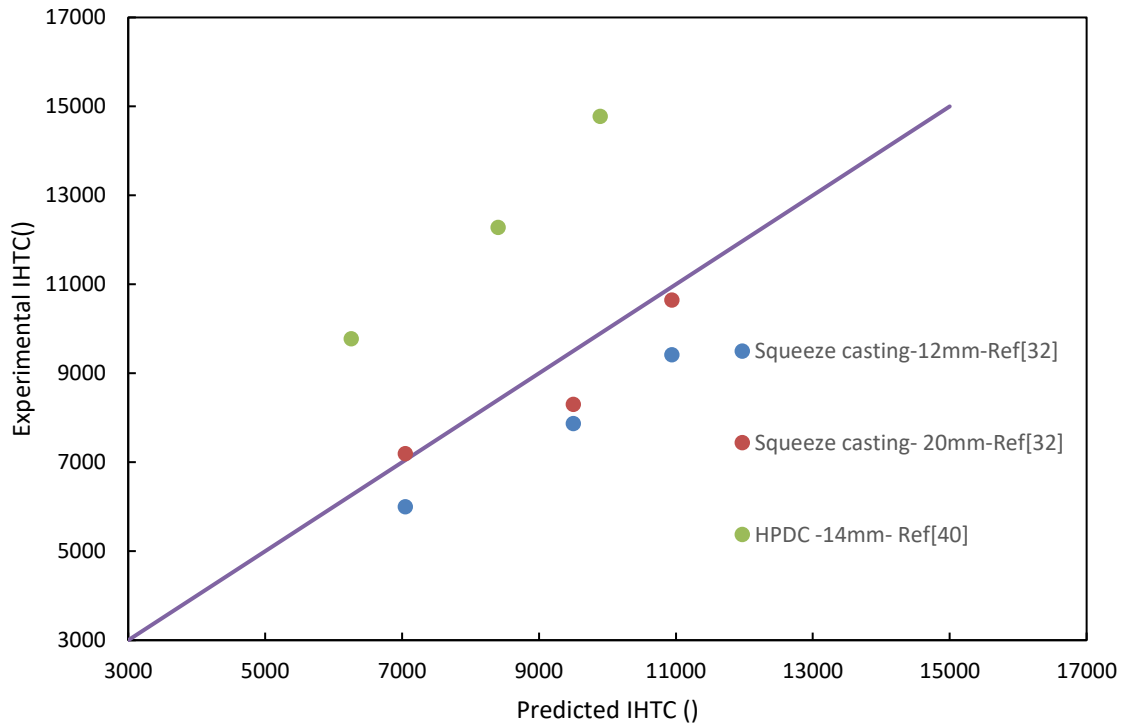


Figure 6.12: Comparison of the experimental results and predicted values determined from Eq.16.

There can be a significant difference between the local pressure in the casting and the external pressure in the squeeze casting process particularly as the fraction solid in the casting increases. Z. Sun et al. [32] reported the pressure drops at least 50% during filling cavity. However, the inverted wedge geometry employed in these experiments is expected to minimize this pressure drop and, therefore, the predicted IHTC value for MiniCaster process is expected to be higher than the results determined during the squeeze casting process.

As shown in Figure 6.12 the predicted IHTC from MiniCaster show lower values as compared with results determined from HPDC process. This can be explained by the filling time in HPDC process is much faster than the MiniCaster. As discussed in previous chapter, a higher fast shot velocity always lead to a higher IHTC peak value. However, the IHTC values predicted during HPDC process is expected to be higher than the results estimated by MiniCaster.

6.3.2 Microstructural Analysis

Figure 6.13 shows the typical microstructure along the casting, from the tip to the bottom of the wedge. The microstructure consists of a dendrite network with β -phase distributed uniformly in the interdendritic zone, as shown in Figure 6.13. The β -phase surround the dendrites which contain the primary or α -Mg phase.

The dendritic arms get coarser as we move away from the tip of the wedge. M.C.Flemings [15] proposed the theory of arm coarsening that the primary influencing factor behind dendrite arm spacing is the cooling rate. According to this theory a higher cooling rate will result in thinner arms and finer dendrites.

It was observed that there are two morphologies of dendrite grain structure in the middle and bottom of the casting. First, the middle of casting consists of branched dendrite arms which result from solidification of alloys in the mold. The second morphology of grains includes the globular-rosette which are same as externally solidified grains (ESGs) observed in the microstructure of HPDC.

The average size of pre-solidified grains in the MiniCaster is similar to the average size of ESGs in the microstructure of HPDC. As shown in Figure 6.13, the pre-solidified grains contain the thicker arms as compared with branched dendrite morphology.

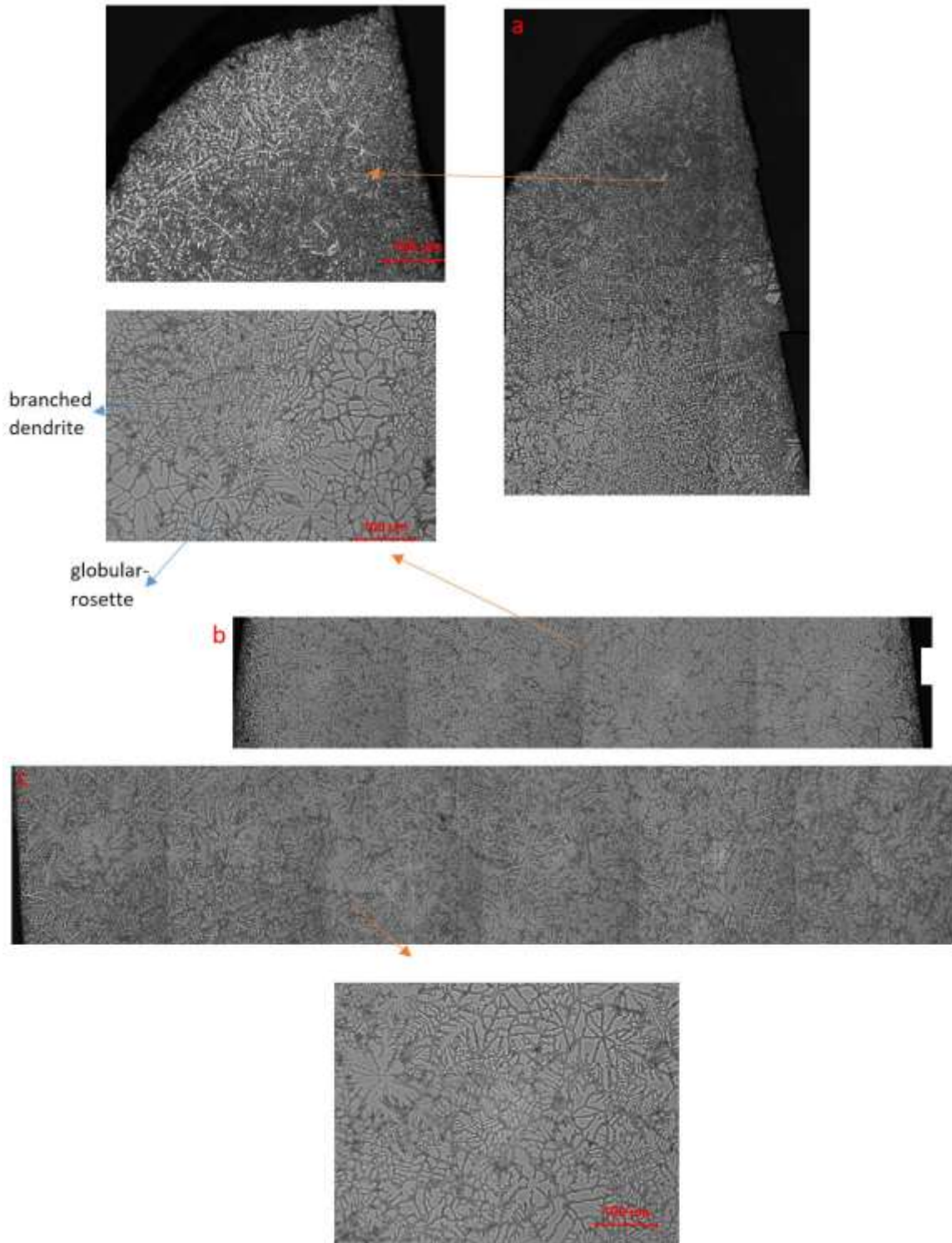


Figure 6.13: The typical microstructure of wedge cast from tip to bottom. a) tip b) middle c) bottom

Solidification begins when superheated metal impinges on the relatively cold wall cavity and piston. As a result, mixture of pre-solidified and liquid metal is injected into the mold when the plunger moves forward. The area fraction of pre-solidified material reduces with distance from the bottom toward middle of wedge cast. This is attributed to more pre-solidified form in the region near the cooled piston tip than in the region far away from the piston. Therefore, the first metal injected into the cavity contains a lower amount of pre-solidified grains, leading to the lower area fraction of these grains in the casting region far from the bottom of wedge. The decreasing volume fraction of pre-solidified grains far from bottom which is in agreement with our observation in the components which were produced by HPDC process.

The Average grain size shows reduction with distance from the tip to the base of the wedge. The average grain size, at the tip of wedge, ranged from 5-10 μm while the average grain size at bottom of wedge is higher than 30 μm . This is consistent with the decrease in cooling rate associated with the increase in section thickness. Also the presence of pre-solidified in the middle or bottom of wedge cast have significant contribution to increase average grain size in those locations.

Figure 6.14 shows typical grain structure through the cross section of castings which were produced by application of pressure 125 bar and 175 bar. This figure shows that the application of various level of pressure leads to differences in the grain structure. For 175 bar, the grain structure is very similar the microstructure of HPDC with a fine-grained microstructure near the surface (skin region) and coarser grained microstructure in the center (core region). Although the external pressure was applied, the grain structure for pressure 125 bar is more like the microstructure of gravity sand casting. Figure 6.15 shows variation of grain size with respect to distance from mold for different level of pressure. The grain size values show reduction with the higher level of applied pressure for all positions, as shown in Figure 6.15. As discussed higher level of pressure leads to a higher cooling rate, as a result, grain size is decreased. Also, variation of grain size between skin region and core region, is increased by higher level of pressure, as shown in Figure 6.15.

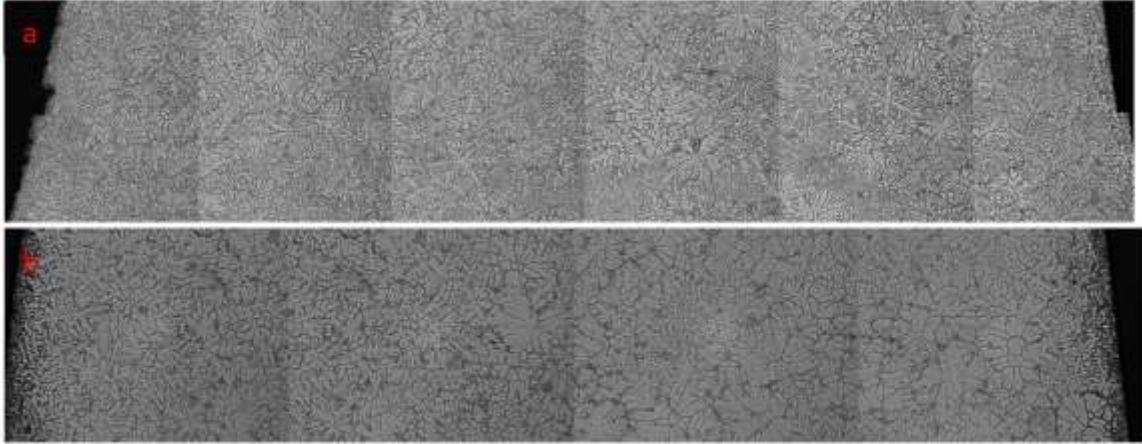


Figure 6.14: Typical grain structure through the casting cross section. a) 175 bar, b) 125 bar.

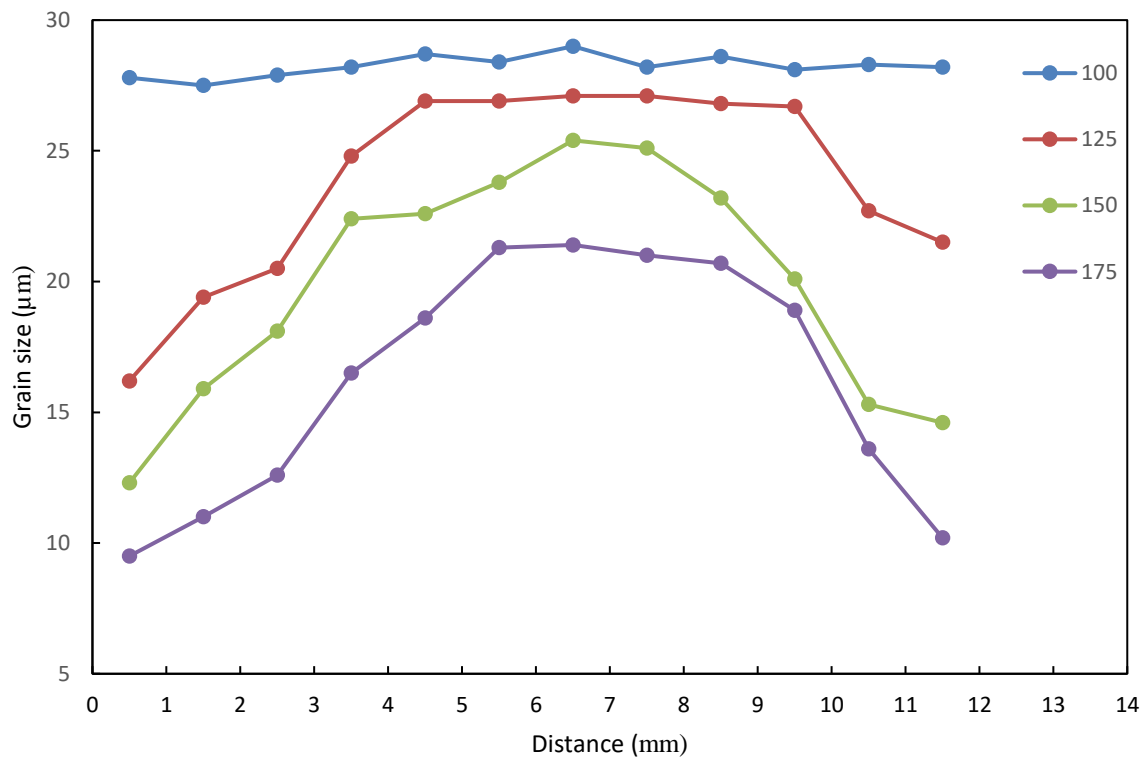


Figure 6.15: Variation of grain size with respect to distance for different level of pressure.

Figure 6.15 confirms that there is a significant difference between the skin region and core region in grain size for application of 175 bar while the grain size does not show any change from surface to center for the application of pressure 100 bar. At 175 bar, the skin and core regions were equally well differentiated, with a prevalence of small grains (lower than 12 μm) at the skin and large grains (15 to 20 μm) at the core. These ranges of grain size are relatively close to the grain size evaluation of HPDC. Laukl et al. [28] reported that the grain size in the skin region varied from 5 to 10 μm while the grain size is in range of 11 to 20 μm in the core region. Also, J.P. Weiler [5, 60] reported that the average grain size range from 5 to 9 μm in the skin region, and from 12 to 15 μm in the core region.

However, MiniCaster approach produces the grain structure that is very similar the microstructure of HPDC. The MiniCaster approaches enables researchers to simulate the die-casting procedure by accomplishing a solidification at laboratory scale while maintaining conditions that are representative of the HPDC process.

Chapter 7

7 SUMMARY AND FUTURE WORK

The objective of this study was to develop process-structure-mechanical property correlations for die cast magnesium alloys. The present study had four central aims: first, to characterize the cooling rate - grain size-local yield strength relationships; second, to predict heat transfer coefficient at metal/die interface for high pressure die cast (HPDC) process; third, to understand quantitatively the effects of process parameters and local solidification conditions on the amount of different kinds of defects; fourth to design and produce a new instrument of casting for simulating the HPDC process at the laboratory scale to investigate the effect of external pressure effects on the interfacial heat transfer coefficient between the cast metal and the die.

7.1 Cooling Rate - Grain Size-Local Yield Strength Relationships

In this contribution, a new method was developed which employs the knowledge of local cooling rates to predict the grain size and the skin thickness of HPDC magnesium components. The centreline cooling curve, together with the die temperature and the thermodynamic properties of the alloy were then used as inputs to find a solution to the Stefan problem of a moving phase boundary, thereby providing the through-thickness cooling curves at each chosen location of the casting. The local cooling rate was used to calculate the resulting grain size and skin thickness via the established relationships.

Spherical microindentation was used to analyze the influence of microstructural features on the flow stress for both skin (finer grain sizes) and core (larger grain sizes and dendrites) regions of HPDC, as well as different regions of gravity step-cast plate for all three magnesium alloys. It was observed that the local yield stress and flow stress of magnesium alloys depend on grain size. The Hall_Petch slopes determined from indentation testing were comparable to the results obtained from uniaxial tensile testing and the literature. The Hall_Petch equation was shown to be applicable for predicting the yield strength and the flow stress at several levels of plastic strains.

Finally, the locally varying yield strength was predicted using a modified Hall-Petch equation which takes into account the difference in grain size across the thickness of the die-cast samples. Compared to conventional Hall-Petch prediction, it was observed that the yield strength obtained by the modified Hall-Petch was in better agreement with the experimental results.

7.2 Prediction of Interfacial Heat Transfer Coefficient between Metal and Die

Multiple runs of the commercial casting simulation package, ProCAST™, were used to model the mold filling and solidification events employing a range of interfacial heat transfer coefficient values. The simulation results were used to estimate the centreline cooling curve at various locations through the casting. As discussed in Section 7.1, the local cooling rate and grain size distribution were predicted through the cross section of casting. The effects of die temperature, filling time and heat transfer coefficient on the grain structure in the skin region and core region were quantitatively characterized. It was observed that the grain size of the skin region strongly depends on these three factors, whereas the grain size of the core region only shows dependency on the interfacial heat transfer coefficient and the thickness of the sample. The grain size distribution from surface to center was estimated from the relationship between grain size and the predicted cooling rate. The average grain size of the skin region determined from this method compares well with the experimental results. Due to the presence of externally solidified grains (ESGs), this method underestimates the grain size value in the core region, as compared to the experiment.

The appropriate value of IHTC was estimated by comparing the predicted grain size and experimental data. It was found that the estimated IHTC value fluctuates for various locations. This was explained by the differences of the die surface temperature of each location and the local flow direction during filling cavity.

7.3 Quantitative Experimental Study of Defects Induced by Process Parameters in the High Pressure Die Cast Process

A quantitative experimental study of the effects of process parameters on the formation of defects during solidification of high pressure die cast magnesium alloy components was conducted. The parameters studied were slow stage velocity, fast stage velocity, intensification pressure and die temperature. The amount of various defects were quantitatively characterized. Multiple runs of the commercial casting simulation package, ProCAST™, were used to model the mold filling and solidification events. Several locations in the component including knit lines, last to fill and last to solidify are identified as the critical regions that have a high concentration of defects. The area fraction of total porosity, shrinkage porosity, gas porosity and externally solidified grains (ESGs) were separately measured.

It was observed that the area fraction of ESGs only depends on the residence time in the shot sleeve and is, therefore, controlled by the slow stage piston velocity. The percentage of gas porosity is affected by the fast stage of the piston velocity (affecting air entrapment) and intensification pressure (affecting the pressure balance at the void-metal interface). It was found that the area fraction of gas porosity at the knit line region was more sensitive to the fast stage of the piston velocity than the area fraction of porosity in other locations.

It was observed that the formation of the defect band is dependent upon the local solid fraction at the time the intensification pressure is applied and is, therefore, affected by the magnitude of the intensification pressure and the die temperature controlling local solidification conditions. It was observed that the application of higher intensification pressure significantly reduced the amount of gas porosity, but might also increase the total area fraction of porosity via defect band formation in some locations of a geometrically complex component. These observations highlight the significant role that the local solidification and filling conditions play in the formation of different kinds of defects.

7.4 Investigation of External Pressure Effects on the IHTC Variation

In order to simulate HPDC process a new casting instrument was designed by Canmet materials and Western University. The heat flux and IHTC profiles at the metal-die interface in the Mini Caster process have been successfully predicted based on the temperature measurements inside the die by solving the inverse thermal problem. It was observed that IHTC curves began with an increasing stage and reached their peak value, then dropped until the value reached a relatively low level.

The effects of pressure on the variation of IHTC was investigated. The variation of pressure values have significant effect on the shape of IHTC profile while the pressure has only impact on the peak stage of heat flux curves. It was observed that higher level of pressure leads to a higher heat flux and IHTC peak values. Also, it was found that the application of various levels of pressure leads to the difference in the grain structure. Higher level pressure produce a grain structure that is relatively the same as the microstructure of HPDC while lower level pressure produce the grain structure similar to the microstructure of a gravity sand casting. For the application of 175 bar casting pressure, the skin and core regions were equally well differentiated, with a prevalence of grains (less than 9 μm) at the skin and large grains (15 -20 μm) at the core. The MiniCaster gives researchers the opportunity to conduct further studies for the analysis of the HPDC process.

7.5 Future Work

In order to attain the ultimate purpose of this study, the following recommendations are suggested:

- 1) To predict the microstructural feature of HPDC, it is recommended to incorporate the developed cooling rate prediction method to the database of simulation software, such as Procast and MAGMASoft.
- 2) Further experiments are suggested to investigate the in-cavity pressure effects on the IHTC variation and grain size distribution during HPDC process.

- 3) Applying higher level of pressure, similar to HPDC in the MiniCaster process are suggested to approve method of IHTC calculations.
- 4) In the MiniCaster process, design of new mold shape is suggested to produce microstructural features (skin region or defect band) as same as microstructure of HPDC.

In order to simulate HPDC process, it is recommended to apply higher level of pressure during MiniCaster and investigate the effects of those on the IHTC variation.

References

- [1] E.F. Emley. Principals of magnesium technology. Pergamon Press Oxford, (1996).
- [2] B.L. Mordike, T. Elbert. Magnesium— applications — potential. *Materials Science and Engineering A*. 302, (2001), 37_45.
- [3] J.J. Kim. Recent Development and applications of magnesium alloys in the hyundai and Kia Motors Corporation. *Materials Transactions* 49, (2008), 894-897.
- [4] J. Campbell. *Complete Casting Handbook*, Elsevier, (2011).
- [5] J.P. Weiler. The development of comprehensive material models of the structure-property relationships for die-cast magnesium alloy AM60B. University of Western Ontario: London, Ontario, (2009). Doctor of Philosophy.
- [6] T. Aune, H. Westengen. Magnesium die casting properties. *Automotive Engineering* 1, (1995), 87-92.
- [7] J.P. Weiler, J.T. Wood, R.J. Klassen, E. Maire, R. Berkmortel, G. Wang. Relationship between internal porosity and fracture strength of die-cast magnesium AM60B Alloy. *Materials Science and Engineering A*, 395, (2005), 315-322.
- [8] P.Sharifi. Structure-Property relationships of Magnesium Alloys. University of Western Ontario: London, Ontario, (2012), M.E.Sc. Thesis.
- [9] J.P. Weiler, J.T. Wood, R.J. Klassen, R. Berkmortel, G. Wang: Variability of skin thickness in an AM60B magnesium alloy die-casting. *Materials Science and Engineering A*. 419, (2006), 297–305.
- [10] Y.C. Lee, A.K. Dahle, D.H. St.John. The Role of solute in grain refinement of magnesium. *Metallurgical and Materials Transactions A*. 31, (2000), 2895-2906.
- [11] M. M. Avedesian, H.Baker. Magnesium and magnesium alloys, ASM, International. Handbook Committee, (1999).
- [12] A.K. Dahle, Y.C. Lee, M.D. Nave, P.L. Schaffer and D.H. StJohn. Development of the as-cast microstructure in magnesium-aluminum alloys. *Journal of Light Metals*.1, (2001), 61-72.
- [13] S.Barbagallo, H.I.Laukli, O.Lohne, E. Cerri. Divorced eutectic in a HPDC magnesium –aluminum Alloy. *Journal of Alloys and compound*. 378, (2004), 226-232.
- [14] D.A. Porter. *Phase Transformation in Metals and Alloys*. (1981).

- [15] M.C. Flemings. Solidification Processing. (McGraw-Hill, 1974).
- [16]. Y. Tamura and J. Yagi. Observation of manganese-bearing particles in molten AZ91 magnesium alloy by rapid solidification. *Materials Transaction*. (2003), 552-557.
- [17] J.D. Hunt. Steady state columnar and equiaxed growth of dendrites and eutectic. (1983)
- [18] D.H. St John, A.K. Dahle and T. Abbott. Solidification of cast magnesium alloy (2003).
- [19] I. Basu. Effect of process variables on the microstructural features for As-Cast magnesium alloys, process-structure relationships in Mg Alloys, Western Ontario: London, Ontario, 2011, M.E.Sc. Thesis.
- [20] J.Campbell. The nonequilibrium freezing range and its relation to hydrostatic tension and pore formation in solidifying binary alloys. *Transaction of the metallurgical society of AIME*. 1969.
- [21] A. Bejan, A.D. Kraus. *Heat Transfer Handbook*, Wiley, 2003.
- [22] V.J. Lunardini, V. Nostrand, *Heat transfer in Cold Regions*, Reinhold, New York, 1981.
- [23] J. H. Weiner. *Transient heat conduction in multiphase media*, Columbia University, New York, 1955. Ph.D. Thesis.
- [24] S.C. Gupta, *The classical Stefan problem, basic concepts, modelling and analysis*. Indian Institute of Science, Bangalore, 2003. M.E.Sc.Thesis.
- [25] Z. Precision, <http://zitaitw.en.ec21.com>.
- [26] S. Otarawanna, H.I. Laukli, A.K. Dahle. Feeding mechanism in High Pressure Die Casting. *Metallurgical and Materials transactions A*. (2010), 1836-1846.
- [27] H.I. Laukli. *High Pressure Die casting of aluminium and magnesium alloys- grain structure and segregation characteristics*. Norwegian University of Science and Technology, 2004.Ph.D. Thesis.
- [28] X. Lia, S.M. Xiong, Z. Guo. Improved mechanical properties in vacuum-assist high-pressure die casting of AZ91D alloy. *Journal of Materials Processing Technology*. 231, (2016), 1-7.
- [29] A.K.Dahle, D.H.St.John: Rheological behavior of the mushy zone and its effect on the formation of casting defects during solidification. *Acta Material*. 47, (1999) 31-41.

- [30] MAGMASOFT® (version 4.4) Release Notes and Manual, (2006).
- [31] A. Banerjee. Process-Structure Relationships of Magnesium Alloys. University of Western Ontario: London, Ontario, 2013, M.E.Sc. Thesis.
- [32] Z.Z. Sun, H. Henry, X.P.Niu. Determination of heat transfer coefficients by extrapolation and numerical inverse methods in squeeze casting of magnesium alloy AM60. *J. Mater. Process. Technol.* 211, (2011). 1432-1440.
- [33] G. Dour, M. Dargusch, C. Davidson, A. Nef. Development of a Non-intrusive heat transfer coefficient gauge and its Application to High Pressure Die casting Effect of the Process Parameters. *Journal of Materials Processing Technology*, 169, (2005). 223–233.
- [34] T.G., Kim, Z.H. Lee. Time-varying heat transfer coefficients between tube-shaped casting and metal mold. *International Journal of Heat and Mass Transfer*. 40, (1997), 3513-3525.
- [35] J. A. Hines. Determination of interfacial heat-transfer boundary conditions in an aluminum low-pressure permanent mold test casting. *Metallurgical and materials transactions B*. 35, (2004), 299-311.
- [36] Z.P. Guo, S. Xiong, S. Cho, J. Choi. Heat transfer between casting and die during high pressure die casting process of AM50 alloy-modelling and experimental results. *Journal of Material Science Technology*. 24, (2008), 131-135.
- [37] S. Broucuret, A. Michrafy, G. Dour. Heat transfer and thermo-mechanical stresses in a gravity casting die influence of process parameters. *Journal of Materials Processing Technology*. 110, (2001), 211-217.
- [38] T.X. Hou, R.D. Pehlke. Determination of mold-metal interfacial heat transfer and simulation of solidification of an aluminum-13% Silicon casting. *AFS Transactions*. 96, (1988), 129-136.
- [39] P.T.S. Kumar, N. K. Prabhu, Heat flux transients at the casting/chill interface during solidification of aluminum base alloys. *Metallurgical Transactions B*. 22, (1991). 717-727.
- [40] Z. P. Guo, S.M. Xiong, B.C. Liu, M. Li and J. Allison. Determination of the heat transfer coefficient at metal–die interface of High Pressure Die Casting Process of AM50 alloy. *International Journal of Heat and Mass Transfer*. 51, (2008), 6032–6038.
- [41] J.V. Beck, B. Blackwell, Jr. St. Clair. Inverse heat conduction: ill-posed problems. Wiley Inter science, New York. (1985), 1-50.

- [42] M. Krishnan, D.G.R. Sharma. Determination of interfacial heat transfer coefficient in unidirectional heat flow by Beck's nonlinear estimation procedure. *International Comm. Heat and Mass Transfer*. 23, (1996), 203-214.
- [43] K. V. Yang, C.H. Caceres, A.V. Nagasekhara, M.A. Eastonb. The skin effect and the yielding behavior of cold chamber high pressure die cast Mg–Al alloys. *Materials Science and Engineering A*. 542, (2012), 49-55.
- [44] B.J. Coultres: Mechanical Property Variations in a Magnesium High-Pressure Die-Cast Component. University of Western Ontario: London, Ontario, 2003, M.E.Sc. Thesis.
- [45] D. Yin: Microstructural Characterization of a Magnesium Die-Casting. University of Western Ontario: London, Ontario, 2004, M.E.Sc. Thesis.
- [46] S.G. Lee, A.M. Gokhale, G.R. Patel, M. Evans: Effect of Process Parameters on Porosity Distributions in High-Pressure Die-Cast AM50 Mg-Alloy. *Materials Science and Engineering A*. 427, (2006), 99-111.
- [47] A. Balasundaram and A.M. Gokhale. Quantitative characterization of spatial arrangement of shrinkage and gas pores in cast magnesium alloys. *Materials Characterization*. 46 (2001), 419-426.
- [48] C. M. Gourlay and A. K. Dahle. Dilatant shear bands in solidifying metals. *Nature* 445, 70-73.
- [49] M. S. Dargusch, G. Dour, N. Schauer and C.M. Dinnis, G. Savage. The influence of pressure during solidification of high pressure die cast aluminum telecommunications components. *Journal of Materials Processing Technology*. 180, (2006), 37-43.
- [50] Y.J. Huang, B.H. Hu, I. Pinwill, W. Zhou, D.M.R. Taplin. Effects of process settings on the porosity levels of AM60B magnesium die castings. *Material Manufacturing Processes*. 15, (2000), 97-105.
- [51] V.D.Tsoukalas, S.A.Mavrommatis, N.G.Orfanoudakis and A. K.Baldoukas. A study of porosity formation in pressure die casting using the Taguchi approach. *Journal of Engineering Manufacture*. 218, (2004),77-86.
- [52] ProCAST 2011.User's Manual
- [53] E.O. Hall. The Deformation and ageing of mild steel, *Proceedings of the Physical Society*. B64, (1951), 747-753.

- [54] N.J. Petch, Cleavage Strength of Polycrystals. *Journal of the Iron and Steel Institute*. 174, (1953), 25-28.
- [55] G. Mima, Y. Tanaka. Grain Size dependence of yield stress and flow stress in the age-hardened magnesium-zinc Alloy. *Journal of the Japan Institute of Metals*. 35, (1971), 317-322.
- [56] J.P. Weiler: Structure Property relationships for die-cast magnesium Alloy AM60B. University of Western Ontario: London, Ontario, 2005, M.E.Sc. Thesis.
- [57] F.E. Hauser, P.R. Landon, and J.E. Dorn: Fracture of magnesium alloys at Low temperature. *Transactions of the American Institute of Mining, Metallurgical, and Petroleum Engineers*. 206 (1956). 589-593.
- [58] P. Andersson, C.H. Caceres, J. Koike. Hall-Petch Parameters for Tension and Compression in Cast Mg. *Materials Science Forum*. 419, (2003), 123-128.
- [59] W. P. Sequeira, G. L. Dunlop, M. T. Murray. In *Proceedings of the 3rd International Magnesium Conference*, G.W. Lorimer (ed.). Manchester, UK. (1996), 63-73.
- [60] J.P. Weiler, J.T. Wood, R.J. Klassen, R. Berkmortel . G. Wang. The effect of grain size on the flow stress determined from spherical microindentation of die-cast Magnesium AM60B alloy. *Journal of Materials Science*. 40, (2005), 5999-6005.
- [61] J.P. Weiler, J.T. Wood, J. Jekl and R. Berkmortel. Structure property relationships for die cast magnesium alloys. *Magnesium Technology*, The Minerals, Metals Society (TMS) (2010).
- [62] A. Wahlberg. Brinell's method of determining hardness and other properties of iron and steel. *The Journal of the Iron and Steel Institute*. 59, (1901), 243-298.
- [63] ASTM, Standard Test Method for Brinell Hardness of Metallic Materials, E10-96, *Annual Book of ASTM Standards*, Volume 03.01, 1997.
- [64] T.O. Mulhearn. The Deformation of Metals by Vickers-Type Pyramidal Indenters. *Journal of the Mechanics and Physics of Solids*. 7, (1959), 85-96.
- [65] D.M. Marsh: Plastic flow in glass. *Proceedings of the Royal Society of London, Series A*. 279, (1964), 420-435.
- [66] L.E. Samuels. *Microindentation Techniques in Materials Science and Engineering* ASTM STP 889. eds. P.J. Blau and B.R. Lawn. (1986), 5-25.

- [67] F.M. Haggag: Field Indentation Microprobe for Structural Integrity Evaluation. US Patent # 4,852,397, 1989.
- [68] H. O'Neill. The Significance of Tensile and Other Mechanical Properties of Metals. *Proceedings of the Institute of Mechanical Engineers*.151, (1944), 116-130.
- [69] D. Tabor: *The Hardness of Metals*. Oxford: Clarendon Press, 1951.
- [70] K.L. Johnson: The Correlation of Indentation Experiments. *Journal of the Mechanics and Physics of Solids*. 18, (1970), 115-156.
- [71] J.H. Ahn, D. Kwon. Derivation of plastic stress-strain relationship from ball indentations: Examination of strain definition and pileup effect. *Journal of Materials Research*. 16, (2001), 3170-3178.
- [72] W.C. Oliver, G.M. Pharr. An improved technique for determining hardness and elastic modulus using load and displacement sensing indentation experiments. *Journal of Materials Research*. 7, (1992), 1564-1583.
- [73] G. Chadha, J.E. Allison, and J.W. Jones. The role of microstructure and porosity in ductility of die cast AM50 and AM60 magnesium alloys. *Magnesium Technology 2004*, Ed. A.A. Luo, (TMS, 2004). 181-186.
- [74] J.P. Weiler, J.T. Wood. Modeling fracture properties in a die-cast AM60B magnesium alloy I—Analytical failure model. *Materials Science and Engineering A*. 527, (2009), 32–37.
- [75] J.P. Weiler, J.T. Wood. Modeling fracture properties in a die-cast AM60B magnesium alloy II .The effects of the size and location of porosity determined using finite element simulations. *Materials Science and Engineering A*. 527, (2009), 37-47.
- [76] C.D. Lee. Dependence of tensile properties of AM60 magnesium alloy on microporosity and grain size. *Materials Science and Engineering A*. 455, (2007), 575–580.
- [77] C. D. Lee, K.S. Shin. Effect of microporosity on the tensile properties of AZ91 magnesium alloy. *Acta Materialia*. 55, (2007), 4293-4303.
- [78] C.D. Lee. Tensile properties of high-pressure die-cast AM60 and AZ91 magnesium alloys on microporosity variation. *Journal of Material Science*. 42, (2007), 1032-1039.
- [79] S.G. Lee, G.R. Patel, A.M. Gokhale. Quantitative fractographic analysis of variability in the tensile ductility of high-pressure die-cast AE44 Mg-alloy. *Materials Science and Engineering A*. 427, (2006), 255-262.

- [80] W.F. Hosford, R.M. Caddell. *Metal Forming*. Third Edition Cambridge. 2007
- [81] C.H. Caceres, B.I. Selling. Casting defects and the tensile properties of an Al-Si-Mg alloy. *Materials Science and Engineering A*. 220, (1996), 109-116.
- [82] Q.Z. Wang. Simple formulae for the stress concentration factor for two- and three dimensional holes in finite domains. *Journal of Strain Analysis*. 37, (2002), 259-264.
- [83]. E.Z. Stowell. Stress and strain concentration at a circular hole in an infinite plate. National Advisory Committee for Aeronautics, Technical Note 2073. (1950).
- [84] H.F. Hardrath, L. Ohman. A Study of elastic and plastic stress concentration factors due to notches and fillets in flat plates. National Advisory Committee for Aeronautics, Report 1117. (1951).
- [85] J.P. Weiler, J.T. Wood. Modeling the tensile failure of cast magnesium alloys. *Journal of Alloys and Compounds*. 5, (2012), 133-140.
- [86] N. Hansen. Hall–Petch relation and boundary strengthening. *Scripta Materialia*. 51, (2004), 801-806.
- [87] G. Nussbaum, P. Bridot, T.J. Warner, J. Charbonnier, G. Regazzon. New Mg-Al based alloys with improved casting and corrosion properties[C]//MORDIKE B L, HEHMANN F. *Magnesium Alloys and their Application*. In: B.L. Mordike, F. Hehmann, (Eds.), DGM, Germany. (1992), 351-358.
- [88] G. Nussbaum, P. Sainfort, G.Regazzoni. Strengthening mechanisms in the rapidly solidified AZ 91 magnesium alloy. *Scripta Metallurgica*. 23, (1989), 1079-1084.
- [89]Y. Chino, M. Mabuchi. Influences of Grain Size on Mechanical Properties of Extruded AZ91 Mg Alloy after Different Extrusion Processes. *Advance Engineering Materials*. 3, (2001), 981-983.
- [90] M.F. Ashby. The deformation of plastically non-homogeneous materials.21, (1970), 399-424.
- [91] H. Jind, J. Lloyd. The tensile response of a fine-grained AA5754 alloy produced by asymmetric rolling and annealing. *Metallurgical and Materials Transactions A*.35 (2004), 997–1006.
- [92] S. Savović, J. Caldwell. Finite difference solution of one-dimensional Stefan problem with periodic boundary conditions. *International Journal of Heat and Mass Transfer*. 46, (2003). 2911–2916.

- [93] P. Sharifi, Y. Fan, J.P. Weiler, J.T. Wood. Predicting the flow stress of high pressure die cast magnesium alloys. *Journal of Alloys and Compounds*. 605, (2014), 237–243.
- [94] Z.W. Chen. Skin solidification during high pressure die casting of Al-11Si-2Cu-1Fe alloy. *Materials Science and Engineering A*. 348, (2003), 145-153.
- [95] P. Sharifi, Y. Fan, H.B. Anaraki, A. Banerjee, K. Sadayappan, J.T. Wood. Evaluation of cooling rate effects on the mechanical properties of die cast magnesium alloy AM60. *Metallurgical and Materials Transactions A*. 47, (2016). 5159-5168.
- [96] H.B. Anaraki. Characterization of High-Pressure-Die-Cast Magnesium Alloy AM60. University of Western Ontario: London, Ontario, (2015), M.E.Sc. Thesis.
- [97] P.D.D. Rodrigo and V. Ahuja: Proc. 2nd Israeli Conf. on Magnesium Science and Technology, Dead Sea, Magnesium Research Institute, Beer-Sheva, Israel, 2000, E. Aghion and D. Eliezer, eds. (2000), 97–104.
- [98] C.M. Gourlay, H.I. Laukli, K. Dahle. Defect Band characteristics in Mg-Al and Al-Si High-Pressure Die Castings. *Metallurgical and Materials Transactions A*. 38, (2007), 1833-1844.
- [99] B. Meylan, S. Terzi, C.M. Gourlay, M. Suéry, A.K. Dahle. Development of shear bands during deformation of partially solid alloys. *Scripta Materials*. 63, (2010), 1185-1188.

Curriculum Vitae

Pouya Sharifi

Education

- M.E.Sc. Mechanical Engineering Sep. 2010-Aug 2012
University of Western Ontario, London, Ontario, Canada
- B.E.Sc. Metallurgy Engineering Sep. 2004- Aug. 2009
University of Science and Technology, Tehran, Iran

Teaching Professional Development

- Teaching Assistant, "Materials Engineering Sep. 2010- Dec. 2016

Publication

Peer-Reviewed Journal Papers:

- P. Sharifi, J. Jamali, K. Sadayappan, J.T. Wood.**
Quantitative experimental study of defects induced by Process Parameters in the High Pressure Die Cast process. (submitted)
- P. Sharifi, J. Jamali, K. Sadayappan, J.T. Wood.**
Journal of Materials Science & Technology (accepted 2016)
'Grain size distribution and interfacial heat transfer coefficient under solidification of magnesium alloys during high pressure die casting process'
- P. Sharifi, Y. Fan, H.B. Anaraki, A. Banerjee, K. Sadayappan, J.T. Wood.**
Metallurgical and Materials Transactions A. 47, (2016). 5159-5168.
Evaluation of cooling rate effects on the mechanical properties of die cast magnesium alloy AM60.
- P. Sharifi, Y. Fan, J.P. Weiler, J.T. Wood.**
Journal of Alloys and Compounds. 605, (2014). 237-243.
Predicting the flow stress of high pressure die cast magnesium alloys.

Peer-Reviewed Conference Papers

- P. Sharifi, K. Sadayappan, J. Wood.**
Materials Science Forum, 879. 2017.
The Effects of Interfacial Heat Transfer Coefficient on the Microstructure of High-Pressure Die-Cast Magnesium Alloy AM60B
- P. Sharifi, Y. Fan, K. Sadayappan, G. Birsan, J.T. Wood**
Magnesium Technology 2015, 349-356.
Process-Structure-Property Correlations for HPDC AM60B

Honors, Awards and Grants

- Western Graduate Research Scholarship (W.G.R.S.) Sep. 2010- Aug. 2016
School of Graduate and Postdoctoral Studies, University of Western Ontario,
- Western GTA Union Outstanding Research Contributions Scholarship 2012